Characterisation of strontium-containing apatite-wollastonite porous scaffolds

Lucia Pontiroli

Submitted in accordance with the requirements for the degree of
Doctor of Philosophy

The University of Leeds
School of Dentistry

July 2018

The candidate confirms that the work submitted is her own and that appropriate credit has been given where reference has been made to the work of others.

In memory of
Daniel

Acknowledgments

First of all, I have to thank my supervisors David Wood, Thuy Do and Xuebin Yang for giving me the opportunity to carry out this work. Thank you to the University of Leeds for funding my research through the 110th Anniversary Scholarship.

A huge thank you to Jackie Hudson and Sarah Myers, for all the technical support and the training over the past 3 years, and to Matty Percival for the precious help in keeping the labs running. To Shabnum Rashid, thank you for all the advice for my microbiology work. Thank you to Scott Finlay for training me on the mechanical testing machine and to Steve Brooks for letting me use the micro CT. Thanks to Phil Davies for helping me organise the biweekly Biomaterials meetings. An enormous thank you to Greg Baugh for your incredible work behind the scenes, nothing would have happened without you.
Thanks to everyone in Oral Biology for your kindness and friendship.

I am immensely grateful to Maria Katsikogianni for finding time to come all the way to Leeds and train me on the DSC. Thank you for all the advice on the glass making procedures: your help has been invaluably precious.

I would also like to thank Faye Esat and Jenny Forrester for the training and support with the XRD measurements and analysis, Susanne Patel and Ben Douglas for the training in the Particles lab and Rachel Gasior for carrying out the ICP-OES measurements. Thank you to Michael Misson from Almath Crucibles Ltd for his technical support, critical for the glass production.

To all my PhD colleagues in Oral Biology, an immense thank you: your friendship made the difference every day. Thank you to Monika for all our lunch chats and your kindness; thanks Claire for all the great laughs (and the cheese and wine!) and Sam W for all the pragmatic advice and for listening to all my complaining; thank you to Ali for always being available to help me no matter how busy you were and to Róisín for reminding me of the life outside the lab. Thank you to Fatima, Rachael, Shane, Zijian, Lizzie K, Rasha and Fahad for being the best companions I could ask for during this tough journey.
To Heather, Oscar, Erin, Neil, Martin, Rui, Emanuelle and Lizzie: you welcomed me since the first day we met and have been the greatest of friends.

To David K, thank you so much for hosting me for longer than expected and for all the amazing food, music and board game nights. You helped turning a stressful transition period into a time dense with great memories.
To all of you, thank you for keeping me sane and making me survive these crazy four years.

To Emanuela, Alessandro, Susanna, Diego, Alessia, Francesca B and Daniele: thank you for your support over these years I have been away and sorry for not coming back often enough. I cannot wait to finally have the chance to spend more time with you all again.
To Silvia “The Boxmate”, Francesca T and Marta, thank you for being great examples and always cheering for me.

An enormous thank you to Imran for choosing me for his fantastic team and patiently waiting for me to complete this thesis. Thank you to Elaine, Tony, Gil, Ahmed, Yousaf: I am hugely grateful for all the moral support you have given me every day and for your understanding in these very hard last seven months.

To Sam, I do not have enough words to thank you for all the help, advice, support, patience, friendship, encouragement and love you have given me every day. You have seen the worst of me and every time you brought me back on track. I would not have made it to the end of this without you at my side.

Finally, the biggest thank you and endless gratitude to all my family for teaching me the importance of hard work, responsibility, generosity and respect. Thank you to my parents for always supporting me in all my choices, no matter how far they have taken me and how hard they have been to accomplish; thank you for your help the one time I would not have made it on my own. And thank you to the most wonderful person that is my sister, for always believing in me with no hesitation and for putting up with me all these years; to you and Simone, I wish you all the happiness you deserve for your new life together.

Abstract

Porous strontium-doped apatite-wollastonite scaffolds were evaluated as potential substitutes for enhanced bone regeneration and the prevention of peri-prosthetic infections.

Parent glasses of composition $35.5SiO_2$-$7.1MgO$-$0.4CaF_2$-$7.1P_2O_5$-(49.9-x)CaO-xSrO mol%, where x = 0, 6.2, 12.5, 18.7, 24.9 or 37.4, were produced via the melt-quench route, ground and sieved <45 µm. Porous scaffolds were obtained following the foam-replication method and heat-treated at 1050 °C for 2 h for controlled nucleation and growth of the crystal phases.

All six glasses produced were amorphous. Differential scanning calorimetry showed that the formation of the calcium silicate phase strongly depended on the amount of strontium contained in the parent glass, linearly moving to higher temperatures with increasing strontium.

Morphological evaluation (scanning electron microscopy and micro-computed tomography) proved that the obtained scaffold porosity, about 55 vol%, did not depend on the strontium content. X-ray diffraction showed that strontium preferentially substituted in apatite, while only higher strontium compositions formed a strontium magnesium calcium silicate phase. Compressive and biaxial flexural strength were both comparable to cancellous bone. Compositions containing 0 %, 6.2 % and 12.5 % strontium showed excellent apatite forming ability when submerged in simulated body fluid, which then decreased with increasing strontium for the three higher-strontium compositions.

Microbiological tests carried out on strontium-containing salts showed no effective antibacterial properties for strontium as a free element. Amongst the six strontium-containing glasses, only the 37.4 % strontium oxide glass showed antimicrobial effects against *Pseudomonas aeruginosa* in broth dilution tests.

Proliferation and osteogenic differentiation of porous scaffolds were tested on human bone cells. No conclusive results were obtained for the G292 cell line. When scaffolds were tested with human primary mesenchymal stromal cells, an increase in DNA content was observed with increasing strontium, while enhanced alkaline phosphatase activity and increased collagen production were found for low strontium compositions.

Table of contents

List of Figures

List of Tables

List of Equations

Abbreviatons

α-MEM Alpha-modified minimum essential medium
ADSC Adipose-derived stem cell
ALP Alkaline phosphatase
ANOVA Analysis of variance
ASTM American society for standards and materials
ATCC American type culture collection
AWGC Apatite-wollastonite glass-ceramic
BHI Brain Heart Infusion
Bmp2 Bone morphogenetic protein 2
BSE Backscattered electrons
BSI British standard institution
BSP Bone sialoprotein
CaSR Calcium sensing receptor
CECT Coleccíon española de cultivos tipo (Spanish type culture collection)
CFU Colony forming unit
CT Computed tomography
CTAn CT-Analyser software
DMEM Dulbecco's modified Eagle's medium
DMSO Dimethyl sulphoxyde
DSC Differential scanning calorimetry
E Young's elastic modulus
EDS Energy dispersive x-ray spectroscopy
EDTA Ethylenediaminetetraacetic acid
EMA European medicines agency
EPS Extracellular polymeric substance
ERK1/2-MAPKEextracellular signal-regulated kinase – Mitogen-activated protein kinase
EUCAST European committee on antimicrobial susceptibility testing
FBS Foetal bovine serum
FTIR (Fourier-Transform Infrared spectroscopy
GNB Gram-negative bacilli
HAp Hydroxyapatite
hBM-MSCs Human bone marrow-derived mesenchymal stromal cells
HCA Hydroxyl-carbonate-apatite

HSM Hot stage microscopy

ICDD International centre for diffraction data

ICP-OES Inductively coupled plasma – Optical emission spectrophotometer

LB Lysogeny broth

MAS NMR Magic angle spinning nuclear magnetic resonance

MBC Minimum bactericidal concentration

MH Mueller-Hinton

MIC Minimum inhibitory concentration

MSC Mesenchymal stromal cell

NBO Non-bridging oxygen

NC Network connectivity

NCTC National collection of type cultures

NF-κB Nuclear factor kappa-light-chain-enhancer of activated B cells

OCN Osteocalcin

PBS 1x Phosphate buffered saline

PJI Peri-prosthetic joint infections

PKCβII Protein kinase C βII

PMMA Poly-methylmethacrylate

pNPP p-Nitrophenyl phosphate

PPI Pores-per-inch

PVA Poly-vinyl alcohol

ROI Region of interest

Rpm Revolutions per minute

RT-PCR Reverse transcriptase-Polymerase chain reaction

Runx2 Runt-related transcription factor 2

$S_{\%}$ Percentage of shrinkage

SBF Simulated body fluid

SEM Scanning electron microscope

TCP Tricalcium phosphate

T_g Glass transition temperature

T_m Melting temperature

T_{on} Onset of peak temperature

T_p Peak temperature

TRIS Tris(hydroxymethyl)aminomethane

VEGF Vascular endothelial growth factor

VOI Volume of interest

Vol_f Final volume

Vol_i Initial volume

XRD X-ray diffraction

Y-TZP Yttria-stabilised tetragonal zirconia polycrystal

Chapter 1
Introduction

1.1 Background to the project

Bone defects can derive from trauma, diseases such as osteoporosis and osteoarthritis, surgery (for example after the removal of a tumour) or infections. They represent one of the major clinical challenges in orthopaedics, especially those defects that are above a critical size, i.e. more than 2 cm long with more than 50 % of lost bone (1, 2). Non-unions, which are fractures that do not present signs of healing after 6 months, occur in 5-20 % of all traumatic fractures (3, 4). About 1 million bone reconstructions are performed in Europe every year (5) and this number is constantly increasing due to the ageing of population. In fact, bone is already the second most transplanted tissue after blood (6), with musculoskeletal grafts representing the 71 % of total grafts distributed in the U.S. in 2015 (7).
The current gold standard for the treatment of large bone defects and non-unions is the use of autografts, followed by allografts and xenografts. However, all these present relevant drawbacks such as donor site morbidity, lack of donor tissue and disease transmission (8-10). In addition, the incidence of infections in the orthopaedic field is becoming a growing issue, further aggravated by the increasing antibiotic resistance of pathogenic bacteria, with heavy economic consequences. For this reason, extensive research has been carried out since the 1970s around the design of synthetic substitutes that could support, guide and stimulate bone regeneration and, more recently, also present antimicrobial properties (11).

The work presented in this thesis concerns the production and characterisation of porous scaffolds for enhanced bone regeneration. The material chosen for the scaffolds is the apatite-wollastonite glass-ceramic (AWGC), which has improved mechanical properties in comparison to other bioactive glass or glass-ceramic materials, making it a good candidate for load-bearing sites (12, 13). Its composition was then modified so that strontium oxide was substituted for calcium oxide. In fact, strontium is a chemical element well known for its ability to induce bone regeneration and it is used in clinic for the treatment of severe osteoporosis (14-16). In addition, interest is growing on whether this element could possess antibacterial features that could thus be imparted to the material that contains it (17, 18).

The present Chapter will provide some background to the work reported in this thesis: a summary on bone tissue and its characteristics (Section 1.2) and an overview on bone grafts (Section 1.3) and on bioactive glass and glass-ceramic materials (Section 1.4) will be provided, before focussing on the AWGC system used for the work presented here (Section 1.5); then orthopaedic post-operative infections will be introduced (Section 1.6) and finally the use of strontium as a therapeutic agent and in bone substitutes will be described (Section 1.7). The aim and objectives of the research presented in this thesis will also be presented (Section 1.8).

1.2 Bone tissue

The human body is composed of 206 bones that form the skeleton, which provides mechanical stability, protects the internal organs, takes part in the formation of blood cells (haematopoiesis) and maintains ion homeostasis, in particular calcium and phosphorus (19, 20).
When designing artificial constructs for the repair of a portion of the body, it is important that the architecture and biology of the original sound tissue and organs are known and understood, so that properties of the new implant can match those of the surrounding tissue once implanted.
In the following Sections, bone tissue characteristics will be presented and described: composition and structure (Section 1.2.1), mechanical properties (Section 1.2.2) and the mechanisms of bone remodelling and healing (Section 1.2.3).

1.2.1 Bone composition and structure

Bone is essentially a composite material, made of an organic collagen-based matrix (25 wt%), a mineral apatite dispersed phase (65 wt%) and about 10 wt% of water (21). These phases are organised in ordered structures, with the apatite crystals disposed along the collagen fibrils.
The molecule of collagen consists of a repetitive sequence of aminoacids –(Glycine-X-Y)$_n$–, where usually X is proline and Y is hydroxyproline, which allows the protein to form a triple helix called tropocollagen (21), about 300 nm long (20). Molecules of tropocollagen are then organised in staggered arrays, where molecules are parallel, but offset by about 67 nm in respect from the next molecule and disconnected from the following molecule by a gap of approximately 40 nm (20-22); this structure gives fibrils, which are then organised in fibres. Each fibril is filled and surrounded by nanocrystals that constitute the mineral phase of bone (23, 24). Bone mineral crystals nucleate within the gaps of the collagen fibrils, as represented in Figure 1.1, giving platelets that

are 15-200 nm long, 10-80 nm wide and 2-10 nm thick (21, 23). It is a form of hydroxyapatite (HAp), $Ca_{10}(PO_4)_6(OH)_2$, with a Ca:P ratio lower than the stoichiometric value of 1.67 because of the presence of impurities such as carbonate, fluorine, sodium and magnesium (21, 23). It crystallises in the hexagonal system, with Ca^{2+} ions and PO_4^{3-} tetrahedrons arranged around a column of OH^- ions along the c-axis (Figure 1.2).

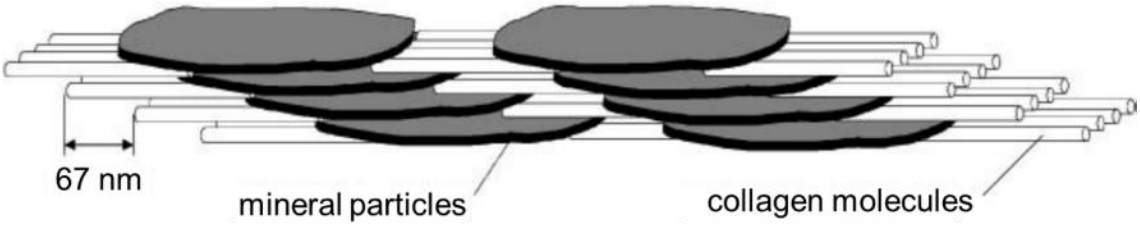

Figure 1.1: Schematic representation, not in scale, of the structure of bone at the nanoscale, with molecules of tropocollagen (the collagen molecules) organised in a staggered array and thin mineral crystals (mineral particles) nucleating within the 67 nm gap between tropocollagen molecules and growing along the fibril axis. Reproduced with permission from (23).

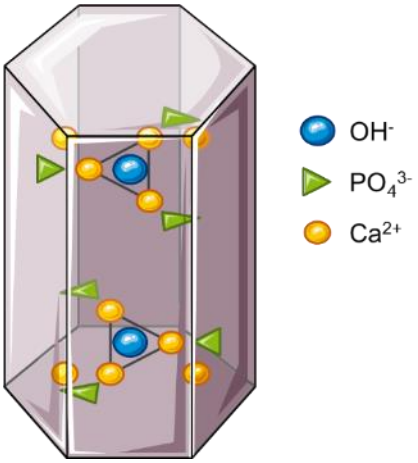

Figure 1.2: Simplified representation of the crystal structure of hydroxyapatite. Drawn using Servier Medical Art, https://smart.servier.com/.

Four main types of cells can be found in bone tissue: osteoclasts, osteoblasts, osteocytes and osteoprogenitors. Osteoclasts are large, multinucleated cells that resorb bone through the production of acids and enzymes. Osteoblasts are the bone-producing cells: they deposit new bone matrix and control mineralisation during remodelling, until they remain embedded in the tissue and enter a quiescent status, becoming osteocytes. Osteocytes maintain the mineral homeostasis and act as

mechano-transducers. Osteoprogenitor cells derive from the differentiation of mesenchymal stromal cells (MSCs) and will mature into osteoblasts (25). All these cells take part into bone formation and regeneration, the mechanisms of which will be explained in Section 1.2.3.

At the macroscale, bone can be divided into two types: cortical (or compact) and cancellous (or spongious or trabecular) bone. Cortical bone is found on the outside of long bones and in flat bones; it is dense and formed by regular, cylindrical lamellae that form the Haversian system: a cylindrical structure with blood vessels in the middle and osteocytes in between layers (22, 26). Cancellous bone is a porous structure that is usually found within the epiphysis of long bones, within short bones and a small amount in flat bones and it is filled with bone marrow. Its porosity is higher than 50 % and it is formed by interconnected lamellar plates and cylindrical trabecular struts. In general, it consists of struts, about 100 μm in diameter, which extend for about 1 mm before making a connection (27). Where high loads are involved, trabeculae tend to orient along the lines of principal stress so that loads are transferred to cortical bone (28).

1.2.2 Bone properties

The two types of bone described in Section 1.2.1 differ not only in their macrostructure, but also in their porosity and mechanical behaviour. When designing artificial constructs, it is important to match the characteristics of the native tissue as much as possible, so that the optimal integration of the implant can be achieved. However, it is also important to note that, when it comes to living tissues, variability in their properties is very high and therefore only ranges of values can be given when describing them.
As mentioned before, cortical and cancellous bone can be distinguished by eye by their porosity. While the porosity of cortical bone has been estimated as 3-12 % (29), that of trabecular bone can range between 50 % to 90 % (30), with pore size at the order of 1 mm, depending on species, anatomical site considered, age and health of the subject and, partially, also on method of measurement used.
Like any other material, bone can be characterised for its elastic properties, strength, fracture mechanism, creep and fatigue resistance. However, since bone structure depends on the function it exerts in a specific anatomical region of the body, its architecture is optimised to obtain the best mechanical properties with the least amount of material; as a consequence, the mechanical properties of bone are highly anisotropic, i.e. they highly depend on the direction in which they are tested. An

example is given in Table 1.1, where properties of human cortical bone are listed. Average Young's modulus for cortical bone is 19.3 GPa (31).

Table 1.1: Mechanical properties of Haversian cortical bone, measured longitudinally and circumferentially (22). All strength values are in MPa ± standard deviation.

	Longitudinal	Circumferential
Tension		
Strength	133 ± 15.6	53 ± 10.7
Yield stress	114 ± 7.1	-
Ultimate strain	0.031 ± 0.006	0.007 ± 0.0014
Compression		
Strength	205 ± 17.3	131 ± 20.7
Ultimate strain	0.019 ± 0.003	0.050 ± 0.011
Shear		
Strength	67 ± 3.5	

For human cancellous bone, its mechanical properties highly depend on its porosity. Its compressive strength can vary between 2 and 12 MPa and Young's modulus between 50 and 500 MPa (32-35), with power law relationships to apparent density for both parameters (22).

Toughness has been estimated as 2-12 $MPa \cdot m^{1/2}$ for cortical bone and 0.1-0.8 $MPa \cdot m^{1/2}$ for cancellous bone (35). Cortical bone has also been shown to be more fatigue-resistant than cancellous bone, although the latter can undergo much higher deformations before fracture (36).

1.2.3 Bone remodelling and healing

In 1892, Wolff published a treatise on the influence of mechanical stress on bone structure, in particular trabecular bone, known as "Wolff's Law" (37). Now generally summarised as "bone functional adaptation", it provided a mathematical model for bone remodelling in cancellous bone trabeculae as a function of their loading history. Although some of the premises for his theory have now been disproved, the general conclusion that bone adapts to the direction and pattern of the applied mechanical load is still valid. This is particularly evident, as displayed in Figure 1.3, in the proximal portion of the femur, where trabeculae are oriented along the axis of principal stresses, thus resembling, as Wolff showed, the stress trajectories derived by Culmann in a curved crane (38).

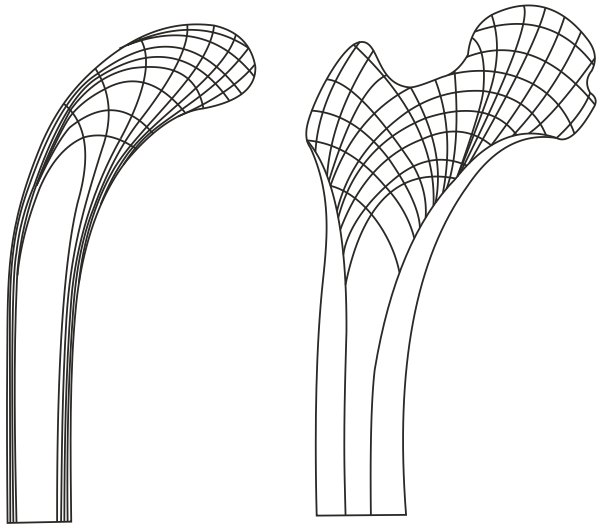

Figure 1.3: Comparison between the principal stress trajectories in Culmann's crane (left) and the orientation of trabeculae of cancellous bone of the proximal femur (right). Drawing based on (38, 39) .

At the cellular level, bone remodelling is controlled and managed by the four types of cells described in Section 1.2.1. It is a continuous process that develops in a cycle, displayed in Figure 1.4. The cycle is initiated by microdamage of the matrix and osteocyte apoptosis. First, osteoclast precursors are recruited from the blood stream to the site of remodelling, where they differentiate into mature osteoclasts, adhere to the bone surface and excrete acids and enzymes that degrade the matrix. Macrophages clear the area from debris before osteoblasts, differentiated from mesenchymal stromal cells, deposit new collagen and induce its mineralisation. Osteoblasts then either mature into osteocytes or bone lining cells, which reside embedded in the bone matrix or on its surface, respectively (40-42).

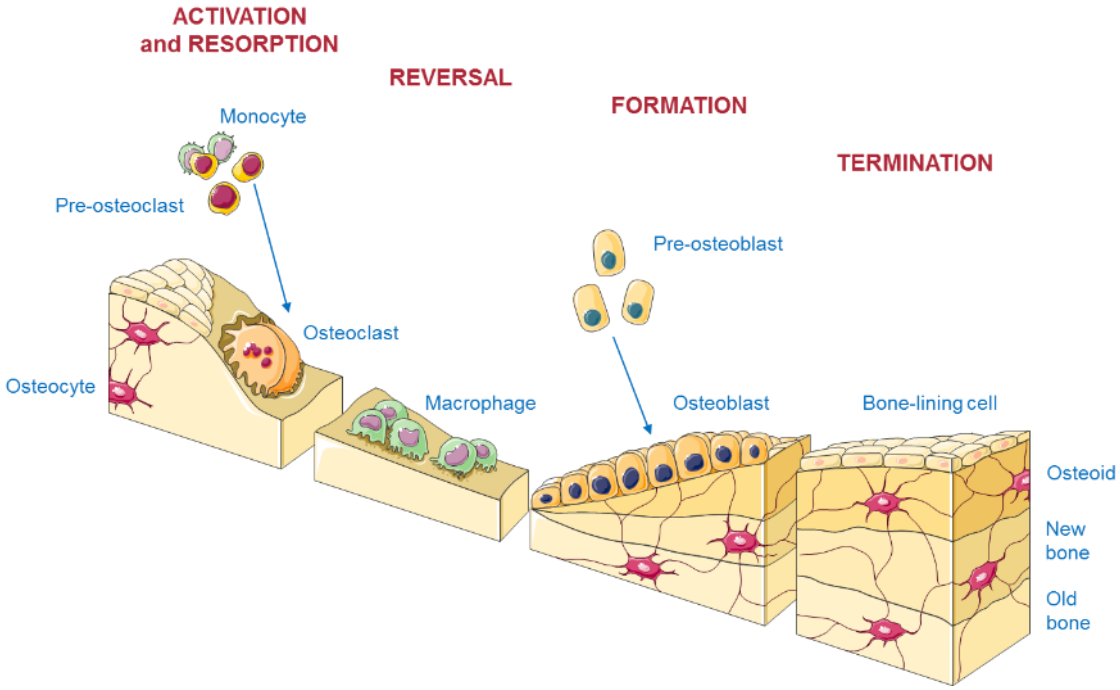

Figure 1.4: Stages of bone remodelling. Activation: osteoclast precursors are recruited. Resorption: osteoclasts demolish old bone matrix. Reversal: macrophages process the debris left by the osteoclasts. Formation: osteoblast precursors are recruited, mature into osteoblasts and deposit new bone matrix, inducing its mineralisation. Termination: osteoblasts mature into osteocytes or bone-lining cells and new bone tissue is formed. Drawn using Servier Medical Art, https://smart.servier.com/.

Bone healing is the process of repairing fractured bones. Depending on the type of fracture, it can happen as primary healing or secondary healing. Primary healing occurs when the two fractured surfaces are maintained in contact; osteoclasts resorb the fractured tissue, osteoblasts deposit new matrix and the fracture is repaired through bone remodelling. Secondary healing occurs when a gap is created between the two fracture surfaces. The process takes longer and involves, in chronological sequence, hematoma formation and inflammation, granulation (formation of a soft callus), callus mineralisation, callus remodelling and bone remodelling (43-46).

1.3 Bone substitutes

When repairing a non-healing fracture or filling a bone defect, it is necessary to implant some material (a graft or a scaffold) that can provide mechanical support to the regenerating tissue, integrate with the native tissue (bioactivity) and, ideally, undergo remodelling, so that the defect can be filled and repaired by the body. The way and

extent at which this happens depends on which of these characteristics the construct presents (47, 48):

- Osteconduction describes the ability of a material to bind to native bone and guide bone regeneration, without the formation of fibrous tissue at the interface.
- Osteoinduction is the formation of new bone through the recruitment of mesenchymal stromal cells and their differentiation into osteoblasts, even in heterotopic tissues; growth factors are required for this process.
- Osteogenicity is the capacity of the construct itself to form new bone tissue, deposited by osteoblastic cells.

The various options of materials and constructs that are now available for surgeons will be illustrated in the following Sections. One category of these grafts is represented by bone tissue-derived grafts, described in Section 1.3.1, while a second option is the use of synthetic materials for the production of fillers, granules, cements or solid scaffolds and is illustrated in Section 1.3.2. The requirements for the ideal bone scaffold will then be presented in Section 1.3.3.

1.3.1 Bone grafts

Currently, the gold standard for the repair of bone defects is the use of autografts: pieces of bone removed from one site and implanted in another site of the same patient's body. Usually, they are harvested from the iliac crest, they provide immediate stability and perfectly integrate with the native tissue. However, they have limited availability, require longer surgery time, cause donor site morbidity and increase the risk of infections (47-49).

The second option is the use of allografts: bone pieces taken from a different donor or a cadaver, processed and then implanted. Although they eliminate the risk of second site morbidity and are readily available during surgery, often they lose their mechanical stability through sterilisation; they are also not osteogenic and they can cause an immune response or, rarely, transmit diseases to the recipient (48, 49).

Xenogenic scaffolds are mainly used in dentistry and maxillofacial surgery in the form of granules; they usually derive from bovine bone tissue that has been treated to remove all its organic components. Also in this case, the material is always available at the time of surgery, but presents reduced mechanical stability, is not osteogenic and has reduced osteoinductivity (50).

1.3.2 Synthetic bone substitutes

Because of the risks and drawbacks associated with the use of natural bone grafts, grafts based on synthetic materials represent an appealing alternative for repairing large defects. In this case, apatite or calcium phosphate substitutes are the most obvious choice, due to their similarity with the native bone mineral phase. They are often used as granules or powder fillers or, sometimes, as 3D constructs. The most common are hydroxyapatite (HAp) and β-tricalcium phosphate (β-TCP). HAp is the closest to the original bone apatite, it is osteoconductive and integrates very well with the native tissue. β-TCP is also resorbable, but at a higher rate than HAp; resorption rate can be controlled by mixing HAp and β-TCP (8, 49, 51).

Another class of materials that can be used to fill bone gaps is cements. Inorganic cements are obtained from either calcium phosphates, which give a carbonated apatite once cured *in vivo*, or calcium sulphates (gypsum). Both are implanted, or sometimes injected, as a paste, they solidify in the body within few minutes and then slowly resorb while new bone tissue forms (9, 52).

A different material commonly used to fill bone voids is PMMA (poly-methylmethacrylate) cement. It is mainly used in combination with joint replacement implants, to fix them in place and provide immediate stability. It is often used also in the case of prosthetic revisions due to peri-prosthetic infections: a temporary spacer is created with antibiotic-loaded PMMA and implanted to maintain the functionality of the treated bone or joint, until the infection is under control and the final revision implant can be placed (53, 54).

One more class of materials suitable for bone implants is represented by bioactive glasses and glass-ceramics, which will be more extensively described in Section 1.4.4.

A summary of the characteristics of the different types of graft is reported in Table 1.2.

Table 1.2: Properties of bone grafts and substitutes. Adapted from (8, 9, 52).

Grafting material	Osteo-conduction	Osteo-induction	Osteo-genicity	Immuno-genicity	Donor site morbidity	Comments
Autograft	++++	++	+++	-	+	Gold standard
Allograft	+	+/-	-	+	-	Available in many forms
Xenograft	+	+/-	-	+	-	Different resorption
HAp	+	-	-	-	-	Biocompatible
β-TCP	+	-	-	-	-	Resorbable
Inorganic cements	+	-	-	-	-	Initial support; resorbable
PMMA	-	-	-	-	-	Primary stability
Bioactive glasses	+	+/-	-	-	-	Anti-infective potential

1.3.3 The diamond concept and the ideal scaffold

To obtain bone repair, four factors are considered fundamental for the healing of a fracture or a defect. These have been combined in the so-called diamond concept, where each of them builds one side of a diamond, as shown in Figure 1.5. These four requirements are (55, 56):

- The recruitment and action of osteogenic cells, in particular mesenchymal stromal cells.
- The presence of growth factors and proteins, which control the different stages of tissue repair.
- The presence of a structure (a scaffold) that can provide mechanical support and guide the healing process.
- The transmission of mechanical loads and stresses from the surrounding tissues to the healing region, to provide the required mechanical stimulation.

Once these four factors are in place, the success of an implant will also depend on its vascularisation and the general health condition of the host (57).

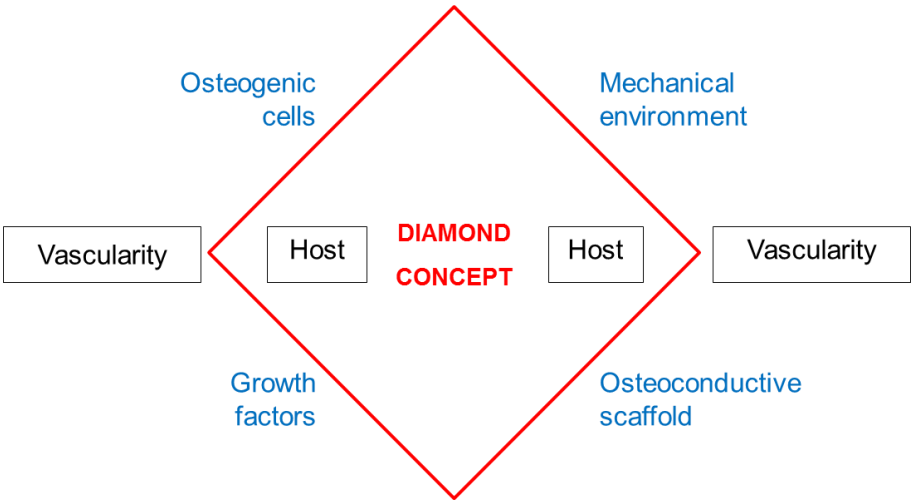

Figure 1.5: The diamond concept for bone repair. The four sides correspond to the fundamental requirements necessary to obtain bone regeneration, which is also influenced by the factors in the black boxes. Reproduced with permission from (57).

This diamond concept thus provides the general requirements for the success of a bone implant aimed at bone regeneration. It therefore follows that the ideal bone scaffold possesses numerous properties (9, 34, 58):

- It is biocompatible, so it does not induce an inflammatory response;
- It is bioactive, connecting to the surrounding tissues (osteoconduction) and stimulating the differentiation of osteoprogenitor cells (osteoinduction);
- It guides the formation of new sound tissue;
- Its mechanical properties match those of the host tissue;
- Its nanotopography supports cell attachment, while its porosity, with at least 100 µm pore size (30), favours bone ingrowth and angiogenesis for better integration of the construct within the tissue;
- Its resorption rate matches the rate of new tissue formation and its degradation products are not toxic nor cause any inflammatory response;
- It is easy to sterilise, its shape can be tailored to the defect shape and is cost-effective;
- It allows and promotes angiogenesis.

Although a construct that presents all these characteristics does not exist yet, some materials can be tailored and used to design implants that cover most of the requirements listed above, thus giving scaffolds that possess great potential for a future clinical use. Amongst these are bioactive glasses and glass-ceramics, which will be described later in Sections 1.4.4 and 1.5.

1.4 Glasses and glass-ceramics

The concept of bioglass was first introduced by Larry Hench in 1971, when he described a glass composition that could interact and bond to living bone (59). Since then, many other compositions have been proposed with the intent of designing the optimal material for bone regenerating constructs, which include the apatite-wollastonite glass-ceramic (AWGC) chosen for the present thesis.
In order to better understand what a glass and a glass-ceramic material is, Section 1.4.1 will describe the structure of a glass and its formation, Section 1.4.2 will describe the crystallisation process in glass-ceramics and Section 1.4.3 will explain the mechanisms of sintering of glass powders. Section 1.4.4 will then present the most common bioglass and bioglass-ceramic compositions, while the AWGC will be more extensively presented in Section 1.5.

1.4.1 Glass formation

A glass can be defined as an amorphous solid that lacks long-range, periodic atomic structure and exhibits a temperature region of glass transformation (60). Its characteristics can be described in terms of enthalpy (or volume) to temperature relation, as represented in Figure 1.6, as the final atomic structure of the material depends on the cooling rate used after melting. When a small volume of material is brought to a temperature well above the melting temperature T_m, it will be in its liquid state. If the material is then cooled down slowly, its atomic structure will re-arrange to form crystals, which causes the enthalpy of the system to drop. However, if the molten glass is cooled down quickly, crystals will not form and a supercooled liquid will be obtained; its enthalpy will gradually decrease, while its viscosity will increase until atoms will not be able to rearrange to the equilibrium order. The range of temperature between the deviation from the supercooled liquid to the frozen liquid represents the glass transformation region. If a lower cooling rate is used, the conversion from supecooled to frozen liquid will begin at a lower temperature. The atomic structure of the final glass will be the one of the equilibrium liquid at the fictive temperature T_f, which is the temperature where the lines of the supercooled liquid and frozen liquid intersect (60).
Since this change of state, from liquid to frozen liquid, happens over a range of temperatures, the glass transition temperature T_g cannot be uniquely defined and depends on the measurement method. However, it is used as an indication for the change in behaviour of the material: below T_g, the glass behaves as a solid, above T_g it behaves as a liquid (60).

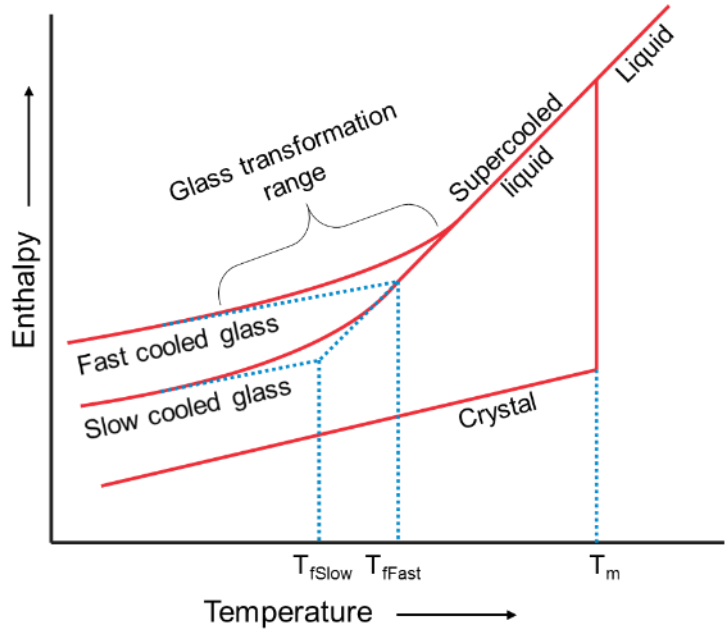

Figure 1.6: Effect of temperature on the enthalpy of a glass forming from its liquid molten state. Reproduced with permission of The Royal Society of Chemistry, http://dx.doi.org/10.1039/9781847551160-00001 (60).

The atomic structure of a glass can be easily exemplified with silica, which is the most common glass former for bioactive glasses used in bone applications. Silica tends to form tetrahedrons where the silicon atom is in the centre, surrounded by four oxygen atoms. As shown in Figure 1.7, in the case of a crystalline structure (quartz) all the tetrahedrons are connected in an ordered regular structure. For an amorphous silica glass, the tetrahedral unit is still present, but the long-range order is lost. This irregular network can be further modified by the introduction of other elements, for example calcium, sodium and potassium, that interrupt the silica network by creating non-bridging oxygens (NBO). While silicon, boron and phosphorus are glass network formers, ions such as sodium, potassium, calcium, strontium and barium are considered network modifiers, whereas aluminium, magnesium and titanium are intermediate oxides, because their role in the structure depends on the overall composition of the glass (61).

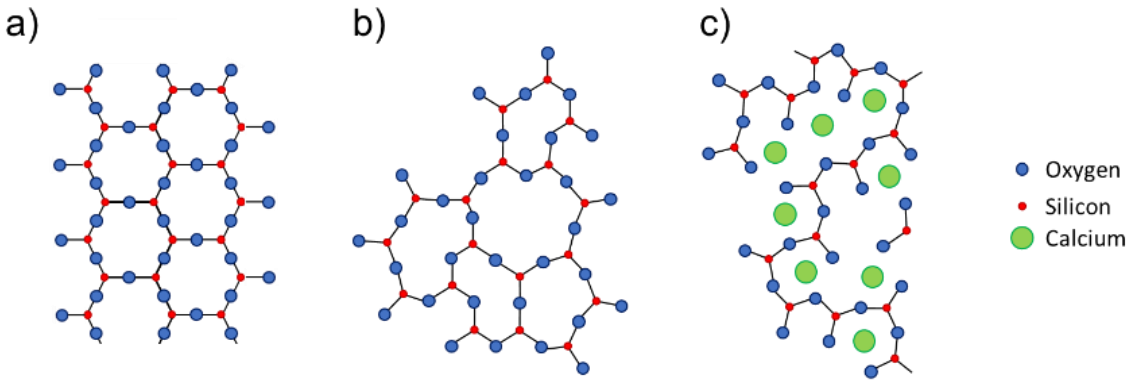

Figure 1.7: Schematic representation of the atomic structure of a) crystalline silica, b) glassy silica and c) silicate glass with calcium as network modifier and non-bridging oxygens. Adapted with permission from (61).

A measure of the amount of non-bridging oxygens is given by a parameter called network connectivity (NC). It describes the average number of bridging oxygens per [SiO_4] tetrahedron and, consequently, the mobility of ions and solubility of the glass: the higher the NC, the more the network modifier ions are locked within the glass structure and therefore the less they are likely to be released when in solution (62). The formula for calculating NC, displayed in Equation 1.1, depends on the concentration of network formers present in the glass (63). In the case of a silico-phosphate glass like the composition chosen for this thesis, where phosphorus acts as a modifier and silicon is the only network former (Hollings, personal communication), the formula for calculating NC is (64):

$$NC = 4 - 2 * \left(\frac{C_O - 4C_P}{C_{Si}} - 2\right)$$

Equation 1.1: General formula for the network connectivity of a glass (64).

Where C_O, C_P and C_{Si} are the atomic concentrations of oxygen, phosphorus and silicon, respectively. It has been shown that, for most bioactive glasses, the NC is below or close to 2 (65, 66). In the case of the strontium AW parent glasses described in this thesis, it was calculated to be 1.98 (Hollings, personal communication).

1.4.2 Crystallisation

Glass-ceramics derive from glasses that have undergone a controlled thermal treatment, which induced the formation of crystal phases (crystallisation or

devitrification). Through this process, a specific microstructure is created and desired properties are imparted to the initial glass such as mechanical strength and controlled solubility (13, 67). The crystallisation of a glass takes place in two stages: nucleation, described in Section 1.4.2.1, and crystal growth, explained in Section 1.4.2.2.

1.4.2.1 Nucleation

A nucleus is an entity that belongs to the crystal phase, but is in unstable equilibrium with respect to the parent glass (13). Nucleation is regulated by the difference in free energy (enthalpy) between the glass and the crystal; it is called homogenous nucleation if the development of a new crystal phase happens without foreign boundaries, while if boundaries are involved, for example in the presence of substrates or grain boundaries, it is referred to as heterogeneous nucleation. In the case of homogenous nucleation, if spherical particles with radius *r* are considered, the free enthalpy of the system ΔG can be modelled as shown in Equation 1.2:

$$\Delta G = -\frac{4}{3}\pi r^3 \Delta G_V + 4\pi r^2 \gamma + \Delta G_E$$

Equation 1.2: Free enthalpy of phase transition in a glass (13).

Where ΔG_V is the change in free enthalpy per unit volume caused by the formation of crystal nuclei, γ is the required energy for the formation of the surface of the new nucleus and ΔG_E represents the energy of the elastic distortion caused in the system, which can usually be neglected in the case of crystallisation of glasses (13). Nucleation occurs if the thermodynamic barrier ΔG^* (Equation 1.3) is overcome and the variation in ΔG becomes negative, which happens if the radius of the forming crystal is larger than the size of the critical radius r* (Equation 1.4) (13, 68, 69):

$$\Delta G^* = \frac{16\pi\gamma^3}{3(\Delta G_V)^2}$$

Equation 1.3: Critical free energy required for the nucleation of stable crystals in a glass (13).

$$r^* = \frac{2\gamma}{\Delta G_V}$$

Equation 1.4: Minimum critical radius of a crystal nucleus required for the formation of stable crystals in a glass (13).

For heterogeneous nucleation, the critical enthalpy ΔG_H^* depends on the interaction between the substrate and the material, in particular their contact angle θ (13, 70), as shown in Figure 1.8 and Equation 1.5.

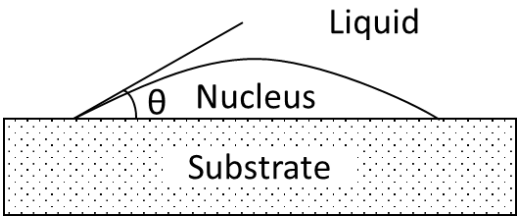

Figure 1.8: Heterogeneous nucleation of a crystal on a substrate, with contact angle θ. Drawn based on (13) and (70).

$$\Delta G_H^* = \Delta G^* \frac{(2 + cos\theta)(1 - cos\theta)^2}{4}$$

Equation 1.5: Critical enthalpy in heterogeneous nucleation of crystals in a glass (13, 70).

The theory of kinetics for crystal nucleation and growth was developed by Johnson, Mehl and Avrami and Kolmogorov and is known as the JMAK theory or the Avrami theory (71). Their equation for describing an isothermal transformation, reported in Equation 1.6, can be applied also to glass-ceramics:

$$X(t) = 1 - \exp[-X_e(t)], \; X_e(t) = kt^n$$

Equation 1.6: The JMAK equation for crystal nucleation and growth kinetics.

Where t is time, X is the volume fraction of transformed material, X_e is the extended volume fraction (the theoretical fraction of new phase that would form if the different growing crystals would not affect each other), k is a constant and n is the Avrami coefficient; for continuous, homogenous nucleation and spherical crystal growth, k equals $\pi/3$ and n equals 4, while for fast, heterogeneous nucleation n equals 3 (13, 71, 72).

Depending on the composition of the glass, the thermal treatment and the time, nucleation can happen homogenously in the bulk of the material or on its surface. In the first case, a neat sharp exothermal peak is found when the thermal characteristics of the material are tested, for instance using differential thermal analysis or differential

scanning calorimetry. In the case of surface nucleation, a broad and smaller peak is generated (73).

1.4.2.2 Crystal growth

Once the nuclei have reached their critical value r*, crystals start to grow. The rate of crystal growth depends on the material transport from the glass matrix to the interface with the new crystal, where the driving force is the entropy change at this interface (13). For a microscopically rough interface, the growth rate *V* deriving from continuous crystal growth is given by Equation 1.7 (13, 74).

$$V = \nu a \left(1 - \exp\left(\frac{-\Delta G}{\kappa T}\right)\right)$$

Equation 1.7: Growth rate for continuous crystal growth (13, 74).

Where ν is the frequency factor for material transport to the interface, a is a distance factor, ΔG is the change in free enthalpy at the interface, κ is the Boltzmann's constant and T is the temperature.
In the case of surface crystallisation, the model is based on a smooth surface and *V* is obtained according to Equation 1.8 (13):

$$V = \left(C\nu \cdot \exp\left(\frac{-B}{T \cdot \Delta T}\right)\right)$$

Equation 1.8: Crystal growth rate for surface crystallisation (13).

Where C and B are parameters that depend on the time necessary for the formation of a nucleus and on that necessary for its growth at the interface.
Crystal growth can be classified as primary growth, anisotropic growth, surface growth and secondary growth. In primary growth, crystals grow through an isotropic process from the nucleus until secondary growth starts. In anisotropic growth, crystals grow preferentially in certain directions through diffusion processes, imparting distinct properties to the material. Surface growth derives from surface nucleation; it begins at the surface and then continues into the volume of crystal. Secondary grain growth occurs after the maximum crystallinity has been reached and leads to an increase in crystal size; it is due to a reduction in energy deriving from the reduction in surface area and may cause a deterioration of the material properties (13).

1.4.3 Sintering

Sintering (or firing) is a processing technique that uses powders to produce dense bodies with controlled microstructure through temperature. Powder is first compacted into a green body, shaped and then an appropriate thermal treatment is applied. There are four categories of sintering (75, 76):

- Solid-state sintering: the green body is densified only in the solid state, through atomic diffusion at a temperature of 0.5 to 0.9 times the melting temperature.
- Liquid-phase sintering: a liquid phase is formed during heating, although not enough to fill all the pores so other processes are necessary to reach complete densification.
- Vitrification: a liquid phase is formed that is sufficient to fill all the pores, after which either crystallisation or vitrification of this liquid phase occurs.
- Viscous flow sintering: glass particles are heated above or near their softening temperature and densification is caused by surface tension forces.

The main two mechanisms are solid-state sintering and liquid-phase sintering. Solid-state sintering can be divided into three stages. During the initial stage, necks form between particles through atom diffusion mechanisms and about 5 vol% shrinkage is obtained. At the intermediate stage, the body has become a three-dimensional network of interpenetrating particles and continuous porosity, with grain growth becoming significant. At the final stage, grain growth becomes more important and the network of pores is converted into isolated closed voids. The sintering rate increases with decreasing particle size and with increasing sintering temperature and time (75, 76).

Liquid-phase sintering is usually achieved through the use of additives that induce the formation of a liquid phase and increase the degree of densification of the initial particles. In this case, the processing factors are the heating rate, holding time, peak temperature, cooling rate, green density and particle size. Material transport is facilitated by capillary forces that induce a liquid flow. However, some properties such as creep or fatigue resistance may be reduced in the final solid (75-77).

1.4.3.1 Foam replication method

A particular technology that makes use of sintering is the foam (or sponge) replication method, through which 3D highly porous structures can be produced. The process requires the preparation of a ceramic slurry, which usually contains a polymeric binder; an open-cell polymeric (normally polyurethane) sponge is then impregnated through cyclic soaking and removal of the excess slurry, before it is let dry and finally thermally

treated so that the polymers are burnt out and the ceramic particles sinter, leaving a positive replica of the initial template.

This technique was first described in 1963 (78), but it is only in more recent years that it has been applied to medical materials, hydroxyapatite first in 2001 (79) and bioactive glasses later in 2006 (80, 81), due to the similarity between the foam porous structure and cancellous bone.

With this method, it is possible to tailor the shape of the scaffold, for example to the shape of a bone defect, and the porosity and pore size can be controlled through the choice of the initial template. An adequate thermal treatment, which is highly dependent on the material used and the particle size of the initial slurry, is then necessary to control the densification of the material and the formation of crystal phases. For example, hydroxyapatite with average particle size around 1-5 μm is sintered at 1200 °C for 1 h, with a step at 600 °C for 1 h to burn the polymers (79, 82). Bioglass 45S5 scaffolds prepared with <5 μm particles are either sintered at 1000 °C for 5 h or 1100 for 1 h and combeite $Na_2CaSi_2O_6$ crystallises (80, 83). Apatite-wollastonite is sintered at 1050 °C for 30 min on hydroxyapatite foam-replicated scaffolds (84), which is the same temperature used to crystallise apatite-wollastonite in <45 μm compacted powder (85).

Because of the similarity of the final product with trabecular bone, the possibility of tailoring the final shape of the implant and the low costs of production, foam replication was the method of choice for the porous strontium-containing apatite-wollastonite scaffolds studied in this thesis.

1.4.4 Bioactive glasses and glass-ceramics

As explained in Section 1.3.3, a material is defined as bioactive if, once implanted *in vivo*, it reacts with surrounding fluids and tissues; in the case of materials for bone regeneration, this reaction leads to the spontaneous precipitation of apatite and the formation of a chemical bond between the implant and bone.

The first bioactive glass composition was invented by Larry Hench in 1971; it is known as Bioglass 45S5 and it is a sodium-calcium-phosphorus-silicate glass with composition $45SiO_2$-$24.5CaO$-$24.5Na_2O$-$6P_2O_5$ wt% (59). The proposed mechanism of Bioglass bioactivity, summarised in Figure 1.9, is composed of 12 steps: the first 5 are inorganic reactions that occur between the glass surface and the surrounding fluids, while the remaining 7 steps describe the interactions with cells up to the formation of new bone tissue. First, Na^+ ions go in solution and are exchanged with H^+ ions; this leads to the formation of Si-OH (silanol) groups on the glass surface, which condense and form a layer of hydrated silica gel. This silica gel is then enriched with other ionic

species, forming an amorphous $CaO-P_2O_5$-rich film that subsequently crystallises in hydroxyl-carbonate-apatite (HCA). The regeneration of bone tissue is then initiated with the adsorption of proteins, which then triggers, along with other cellular processes, osteogenesis and osteoblast differentiation so that new bone tissue is formed (86-88). This bioactive response is controlled genetically: seven families of genes are activated and up-regulated in osteoprogenitor cells, thus inducing osteostimulation through the rapid proliferation and differentiation of osteoblasts (89-92). Bioglass 45S5 products are now commercially available under the brand name of NovaBone for bone grafts and NovaMin as an additive in toothpaste (93).

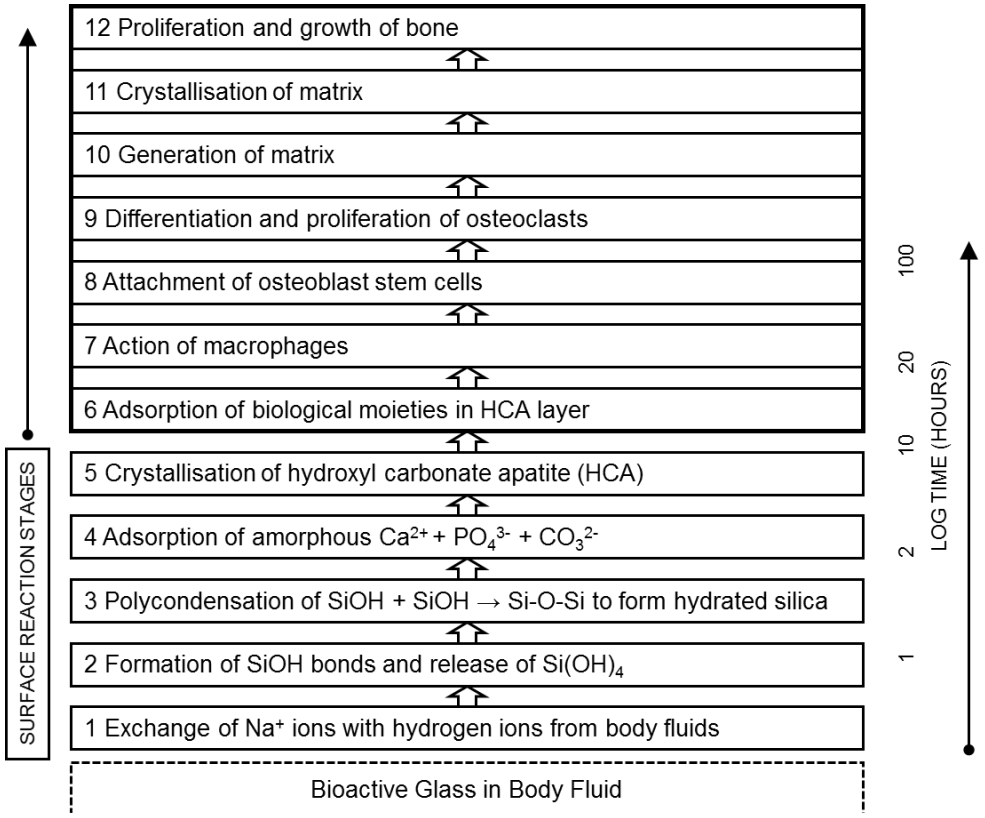

Figure 1.9: Sequence of reactions in the bioactivity mechanism of Bioglass 45S5. Reproduced with permission from (88).

After Bioglass 45S5, many other compositions of bioactive glasses and glass-ceramics have been introduced and studied over the last 40 years, based on the phase diagram shown in Figure 1.10. One example is the bioactive glass S53P4, a variation of Bioglass 45S5 that proved good osseointegration and antimicrobial properties, now sold with the brand name of BonAlive® (93, 94). BioMin® also derives from Bioglass 45S5; it contains CaF_2 and higher phosphate and it is also used in toothpaste (93). 13-93 is another silica-based bioactive glass, specifically designed to undergo sintering

without forming crystal phases (95, 96). Bioverit I and Bioverit II are machinable bioactive glass-ceramics (13, 97), while CEL2 and ICEL2 are a silica-based and a phosphate-based glass-ceramics, respectively; the former contains combeite and akemanite, while the latter contains sodium/magnesium phosphate and calcium pyrophosphate and they both have been studied as materials for porous bone substitutes (98, 99). Apatite-wollastonite is a high strength bioactive glass-ceramic, commercially sold as Cerabone® (13, 97); it is the base material chosen for the work described in the present thesis and will be fully described in Section 1.5.
Table 1.3 compares the composition of some of the glasses and glass-ceramics described above.

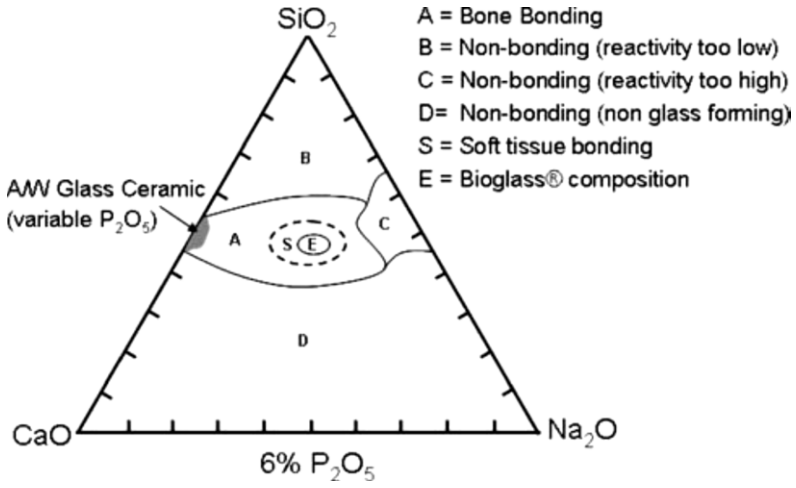

Figure 1.10: Diagram showing the bone bonding ability of different glass compositions, amounts in wt%. Bioglass 45S5 is in region E, glasses in region S are osteoinductive (they also bond to soft tissues and are gene activating), glasses in region A are osteoconductive (they bond to bone tissue), compositions in regions B, C and D are non-bonding. AWGC has a higher amount of P_2O_5 and no Na_2O. Reproduced with permission from (100).

Table 1.3: Molar composition of some bioactive glasses and glass-ceramics described in the literature and commercially available (all values in mol%).

	SiO_2	CaO	Na_2O	P_2O_5	MgO	K_2O	CaF_2
Bioglass 45S5	46.1	26.9	24.4	2.6			
BonAlive S53P4	53.8	21.8	22.7	1.7			
13-93	54.6	22.1	6.0	1.7	7.7	7.9	
CEL2	45	26	15	3	7	4	
ICEL2	3	26	15	45	7	4	
Cerabone AW	35.5	49.9		7.1	7.1		0.4

1.5 The apatite-wollastonite system

The apatite-wollastonite glass-ceramic (AWGC) material was first described by Kokubo and co-workers in 1982 (85). Thanks to the controlled crystallisation of fine-grained apatite and fibrous β-wollastonite, it proved to have superior mechanical properties compared to other bioactive glass and glass-ceramic compositions, while still retaining excellent apatite-forming and bone-bonding ability (12, 101, 102). For these properties, AWGC was chosen as the reference material for the addition of strontium and the production of foam-replicated scaffolds presented in this thesis. Its production is described in Section 1.5.1, before its mechanical properties are presented in section 1.5.2 and apatite-forming ability in Section 1.5.3; its commercial form Cerabone® is described in Section 1.5.4.

1.5.1 Production

AWGC is prepared by melting its precursors and then either pouring the melt on platinum or quenching it in cold water. Its molar composition is listed in Table 1.3. The reagents used for its preparation are MgO, $CaCO_3$, SiO_2, $CaHPO_5{\bullet}2H_2O$ (or P_2O_5) and CaF_2, which are mixed and then melted at 1450 °C for 2 h (85, 103). In order to better control the nucleation and growth of wollastonite, the glass obtained is ground and its powder compacted, before being treated at 1050 °C for 2h (usual heating rate 5 °C/min) (104). A glass-ceramic is thus formed that contains 36 wt% of $3CaO{\bullet}P_2O_5$, 40 wt% of $CaO{\bullet}SiO_2$ and 24 wt% of $CaO{\bullet}MgO{\bullet}2SiO_2$. As shown in Figure 1.11, the $3CaO{\bullet}P_2O_5$–$CaO{\bullet}SiO_2$ system has a eutectic point at 36 wt% $3CaO{\bullet}P_2O_5$ – 64 wt% $CaO{\bullet}SiO_2$ at a temperature of 1420 °C, which is decreased through the partial substitution of $CaO{\bullet}SiO_2$ with $CaO{\bullet}MgO{\bullet}2SiO_2$ in the AWGC system (103).

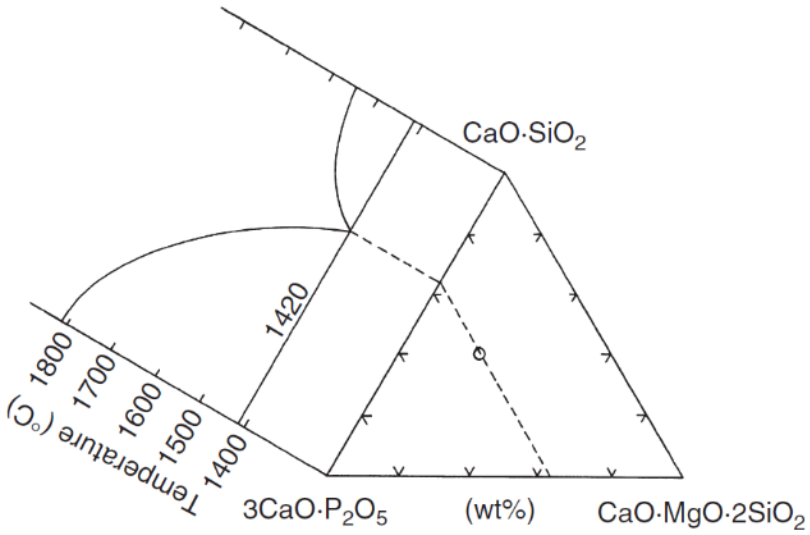

Figure 1.11: Pseudo-ternary system of $3CaO•P_2O_5$ – 64 wt% $CaO•SiO_2$ – $CaO•MgO•2SiO_2$, where a small circle indicates the base composition of AWGC. Reproduced with permission from (103).

The system can precipitate three crystal phases, depending on the temperature at which the powder compact is treated: as summarised in Table 1.4, apatite forms first, at about 870 °C, then wollastonite precipitates at about 900 °C; if the material is heated above 1050 °C (the temperature used to obtain AWGC), the apatite crystals disappear and whitlockite (β-$3CaO•P_2O_5$) forms at about 1100 °C (85).

Table 1.4: Crystalline phases found in AWGC, depending on the temperature of the applied thermal treatment (85).

Crystalline phase	Temperature (°C)	Composition
Oxyfluoroapatite	870	$Ca_{10}(PO_4)_6(O,F_2)$
β-Wollastonite	900	$CaO·SiO_2$
Whitlockite	1100	β-$3CaO·P_2O_5$

1.5.2 Mechanical properties

The composition of AWGC was specifically designed to improve the mechanical properties of Bioglass. This was obtained by producing a material that contained fine-grained apatite and wollastonite, homogenously dispersed in the glass matrix (105). Kokubo and co-workers showed how the precipitation of wollastonite in particular brought a significant improvement in the bending strength and fracture toughness of the material, making it comparable to human bone (Figure 1.12) (106).

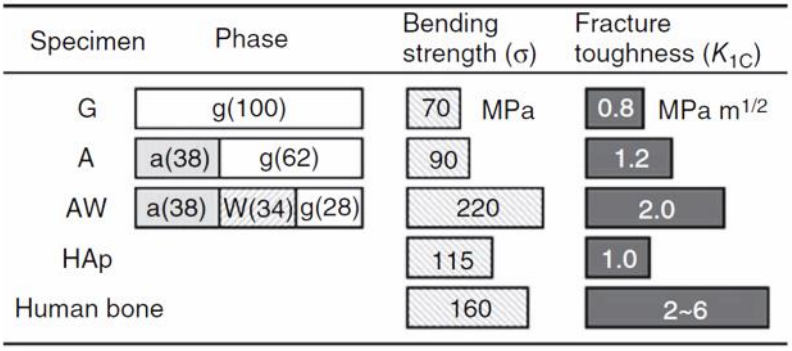

Figure 1.12: Comparison of the mechanical properties of AWGC (AW) with its parent glass (G), its glass with only apatite (A), sintered hydroxyapatite (HAp) and human bone. a: apatite, g: glass, W: wollastonite. Reproduced with permission from (106).

AWGC also showed improved compressive strength, compared to sintered HAp, and Young's modulus, compared to both Bioglass 45S5 and sintered HAp (12, 13, 107), as summarised in Table 1.5.

Table 1.5: Comparison of the mechanical properties of AWGC, Bioglass 45S5, sintered hydroxyapatite and human cortical bone (107).

Property	AWGC	Bioglass	HAp	Bone
Density (g/cm^3)	3.07	2.66	3.16	1.6-2.1
Flexural strength (MPa)	220	42 (tensile)	115-200	50-160
Compressive strength (MPa)	1060		500-1000	100-230
Young's modulus (GPa)	118	35	80-110	7-30
Hardness (Vickers)	680	458	600	
Fracture toughness (MPa•m$^{1/2}$)	2.0		1.0	2-6

In terms of fatigue strength, it was estimated a life-time of 10 years when AWGC was subjected to a bending stress of 65 MPa in simulated body fluid (SBF) at 36.5 °C, with the lowest dependence on the stress rate compared to its parent glass and the same glass with only apatite (108).

1.5.3 Apatite forming mechanism and *in vivo* behaviour

Kokubo and co-workers also studied the apatite forming ability of AWGC and they observed that it did not form an intermediate silica-gel layer between the sample and the deposited apatite, thus differing from the bioactivity mechanism of Bioglass 45S5 proposed by Hench (86) and summarised in Section 1.4.4. As displayed in Figure

1.13, when AWGC is put in contact with SBF, calcium and silicon ions are released from wollastonite and from the glassy phase; calcium induces a local supersaturation of the solution for apatite, while on the AWGC surface silanol groups are formed that provide nucleation sites for the precipitation of apatite. The preferential dissolution of wollastonite and of the glassy phase also causes the formation of a rough surface, mainly composed of the remaining apatite crystals, which provides further nucleation sites for the deposition of HAp (109). The precipitated apatite is a calcium-deficient, carbonated hydroxyapatite (Ca/P ratio 1.46), which incorporates also small amounts of magnesium and silicon and is composed of needle-like nano-crystals, randomly oriented (105, 106). The absence of the silica gel allows AWGC to get in direct contact with bone when implanted *in vivo* (105), thus giving a very high bonding strength with bone tissue (101).

Animal testing of AWGC samples demonstrated the excellent ability of the material to bond to bone, with the apatite layer precipitated on the surface of the implanted samples providing the substrate for its integration with the newly formed bone tissue (110). AWGC showed the highest failure load 8 weeks after implantation when compared to alumina, Bioglass 45S5 and hydroxyapatite, with samples fracturing either at the interface with bone or within the bone (85, 101). AWGC porous intramedullary plugs (70 % porosity, 200 μm mean pore size) were tested in dogs and rabbits and showed bone-bonding at 1 month and bone remodelling at 24 months (111, 112). AWGC granules were used during arthroplasty in humans, as bone fillers during total hip replacements, with excellent outcomes: direct bonding with bone and bone tissue remodelling were observed in all patients, when followed-up for up to 9 years (113).

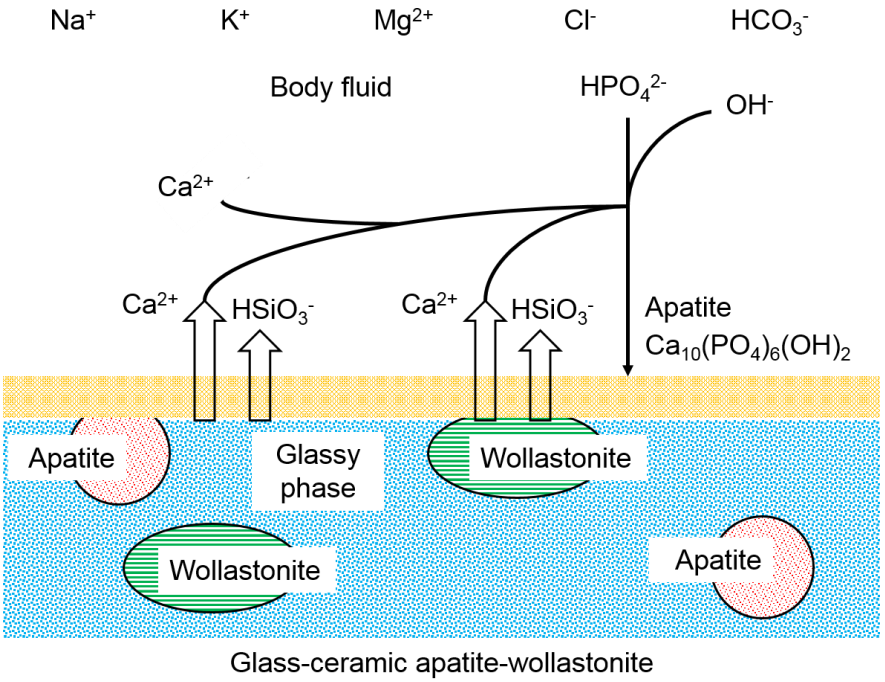

Figure 1.13: Scheme of the bioactivity mechanism for apatite-wollastonite glass-ceramic, as proposed by Kokubo. Adapted with permission from (109).

1.5.4 Cerabone® and recent studies

Thanks to its excellent mechanical properties and bone-bonding ability, AWGC has been made into a commercial product called Cerabone®, produced by Nippon Electric Glass Co Ltd and sold in Japan as granules and porous or solid spacers until December 2000 (Figure 1.14) (97, 114). It has been estimated that, in Japan, more than 60,000 patients have been treated with AWGC bone substitutes between 1990 and 2000 (115).

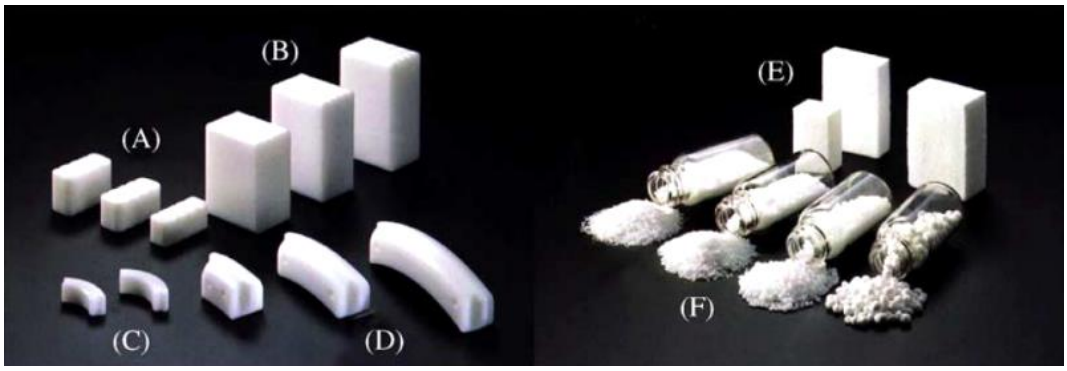

Figure 1.14: Examples of Cerabone® products: (A) intervertebral disc spacers, (B) artificial vertebrae, (C) spinous process spacers, (D) iliac crest spacers, (E) porous spacers and (F) granular bone filler. Reproduced with permission from (116).

Improvements for the AWGC material have also been proposed in the literature. Ono et al. studied the mechanical properties of implanted AWGC-fibrin mixtures in rats and observed that the fracture toughness was comparable to that of cancellous bone after 24 weeks (117). Magallanes-Perdomo et al. proved the citocompatibility of an AW glass-ceramic composition, crystallised with a different thermal treatment than that of Kokubo's AWGC, by studying its effect on human bone-marrow mesenchymal stromal cells (hBM-MSCs) (118). Xiao et al. produced AWGC porous scaffolds using selective laser sintering, which maintained excellent mechanical properties and apatite-forming ability (119); Dyson et al. showed that the same scaffolds were also biocompatible and osteo-supportive when tested with hBM-MSCs (120). Serna proved the feasibility of foam-replication for the production of porous AWGC scaffolds, which showed mechanical properties similar to cancellous bone (121).

1.6 Post-operative and peri-prosthetic bone infections

One of the reasons for a fracture or a bone defect to not heal is represented by the presence of an infection at the site, one of the current major orthopaedic challenges. They are often the consequence of an open traumatic fracture or a surgical intervention; especially when an implant is inserted inside the body, for instance a joint replacement implant or a plate or a nail for reducing a fracture, it provides a surface onto which bacteria can attach and proliferate, making the infection more difficult to eradicate. Some background on bacterial growth and biofilm formation is provided in Section 1.6.1, before the impact of infections in the orthopaedic field is discussed in Section 1.6.2.

1.6.1 Bacterial proliferation

Bacteria are prokaryotic, mono-cellular organisms; they do not possess a contained nucleus and present a cell wall around their cell membrane. Their size ranges in general between 1 and 10 µm and they come in different shapes: for example, cocci are spherical, while bacilli are rod-shaped. Depending on the type of cell wall they present, they can be divided into two main groups: Gram-positive and Gram-negative. Gram-positive bacteria present a thick cell wall, mainly composed of peptidoglycans, while Gram-negative bacteria have a thinner peptidoglycan layer and a further outer membrane that contains liposaccharides, proteins and phospholipids (122, 123). This classification derives from the outcome of Gram staining: Gram-positive bacteria retain the stain within their thick wall, while the outer membrane of Gram-negative bacteria prevents the staining from interacting with the peptidoglycan membrane. This difference in wall morphology, along with allowing for a simple morphological identification, is also the reason for Gram-negative bacteria to be more resistant to antibiotics and antimicrobial agents (124).

When cultured *in vitro* in liquid media, a typical bacterial growth curve is composed of four different phases, although the time-scale for the growth is species-specific. These four phases are represented in Figure 1.15 and are (122):

- Lag phase: when few bacterial cells are added to the media, they initially adapt to the new environment without increasing in number.
- Log phase: the cell number increases quickly because of their exponential proliferation; the media turns from clear to cloudy.
- Stationary phase: the cell number stops increasing because nutrients become exhausted or the pH has decreased due to the high concentration of metabolic waste products.
- Decline phase: the media does not contain enough nutrients to sustain cell survival and cells die; while the optical density of the culture does not change at this stage, the viable count decreases.

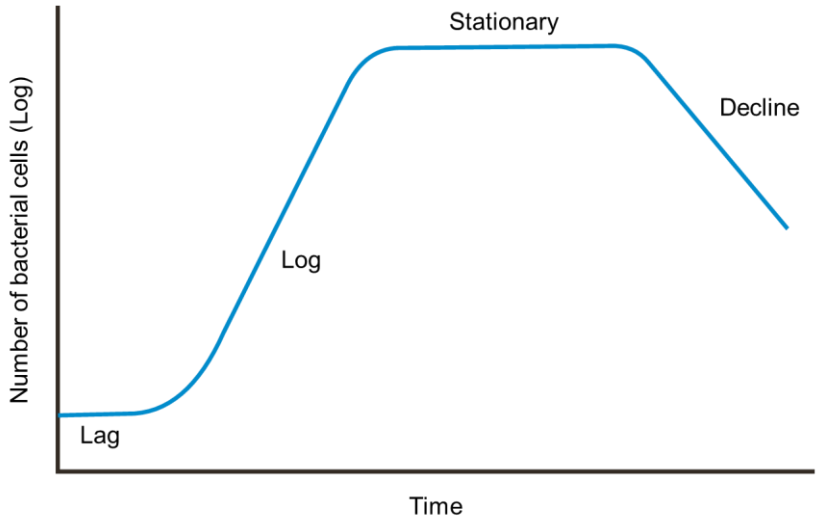

Figure 1.15: Typical bacterial growth curve. Reproduced from (125).

In the presence of a surface, bacteria usually adhere and form a thick layer of cells called biofilm. Biofilms contain a high concentration of cells of one or more species, which are embedded in a self-produced extracellular polymeric substance (EPS) that is made of polysaccharides, proteins, lipids and extracellular DNA (126). It protects bacteria from antimicrobial agents and mechanical stresses, thus making them more difficult to eradicate and therefore representing a major issue for the treatment of infections (127), as it will be discussed in Section 1.6.2.

The formation of a biofilm, shown in Figure 1.16, begins with bacterial cells attaching to the surface and starting to produce the EPS. At this point, cells begin to proliferate and aggregate, forming microcolonies first, which then develop into a mature biofilm. The biofilm is then maintained and evolves by releasing cells and fragments of EPS into the medium or surrounding environment, while the EPS matrix is constantly remodelled (123, 127).

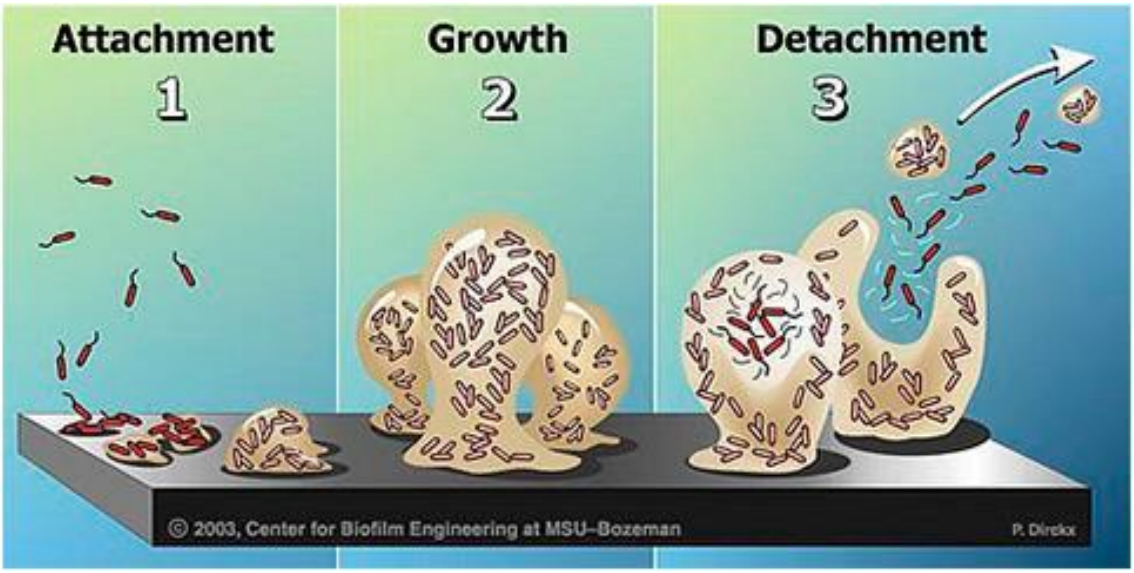

Figure 1.16: Phases of biofilm formation on a surface. Source: Montana State University Center for Biofilm Engineering, http://www.biofilm.montana.edu.

Both Gram-positive and Gram-negative bacteria can form biofilms on various surfaces, including surgical sutures, catheters and orthopaedic implants and this causes the development of post-operative and peri-prosthetic infections, which are presented in the following Section 1.6.2.

1.6.2 Impact of orthopaedic infections

Bone implant-related infections generally occur in 1-2 % of primary joint replacement procedures (128, 129), but numbers can increase to 4-5 % for secondary procedures and depending on the hospital and the inclusion criteria considered (127, 130), or even up to 30 % in the case of treatment of open traumatic fractures (131). They tremendously hinder the quality of life of patients and have very high associated costs for their treatment. It has been shown that a septic revision can cost 2-4 times more than a primary procedure and 1.5-3 times more than an aseptic revision surgery (132). In the U.S., it has been calculated that in 2009 the average cost for the revision of an infected hip prosthesis was $ 93,600 and $ 74,900 for an infected knee (133); if explant surgery, medical treatment and re-implantation procedure are considered, costs can even exceed $ 500,000 per patient (127). In the case of traumatic fractures, it has been estimated that the total cost of treatment for a fracture that becomes infected is twice the cost of the initial treatment, estimated as about $ 109,000 per infected patient compared to about $ 57,000 per patient without infection (134). In a recent study carried out in Belgium, the average cost for a deep infection after tibial

fracture was calculated to be about 6.5 times higher than uninfected cases, with about € 44,500 spent compared to about € 7,000 without infection (135).

The presence of biofilms can further complicate the detection of infections. In fact, current diagnostic methods rely on the collection of planktonic microbes in the tissue, blood or synovial fluid, while when pathogens are embedded in the EPS of a biofilm they are more difficult to retrieve, they tend to not grow using standard laboratory techniques and are more resistant to antibiotics; in addition, bacteria can also colonise cells, especially osteoblasts, which protects them from antimicrobial agents and further complicates their detection (136, 137). Because of all these reasons, it has been argued that, of all the revisions of orthopaedic implants that are ascribed to aseptic loosening, about 20 % are actually due to infections that could not be diagnosed (128, 138, 139), making the actual rate of post-operative infection increase dramatically.

The bacterial species usually detected in orthopaedic peri-prosthetic joint infections (PJI) and their incidence are summarised in Table 1.6. Aerobic Gram-positive cocci account for 65-78 % of infections, with *Staphylococcus aureus* and *Staphylococcus epidermidis* being the most frequently detected. Aerobic Gram-negative bacilli are found in less than 10 % of cases, while anaerobic bacteria are involved in 7 % of infections (133, 140). Depending on the timing and type of infection, the most commonly species found are (133, 141):

- *S. aureus* (36 %), *S. epidermidis* (16 %), *E. coli* (15 %) and *P. aeruginosa* (15 %) in early post-operative infections;
- *S. epidermidis* (33 %), *S. aureus* (20 %), other *Staphylococci* (17 %) and *P. acnes* (5 %) in chronic infections;
- *S. aureus* (39 %), *E. coli* (13 %), *S. agalactiae* (11 %) and other *Streptococci* (5 %) in acute haematogenous infections.

Most infections involve only one species, although about 20 % of infections are polymicrobial, i.e. are caused by more than one species.

Currently, treatments include the use of antibiotics, irrigation and debridement of the affected site and revision of the implant, either in one stage or two stages with the use of a temporary antibiotic-loaded cement spacer (133, 142, 143). However, concerns around antibiotic resistance are constantly increasing: multidrug-resistant species are found in 14 % of PJI, where 8 % are due to methicillin-resistant *S. aureus* and 6 % to multidrug-resistant Gram-negative bacilli (133). In addition, in 4-12 % of cases no pathogens are detected despite some of the symptoms being present (133).

It is therefore of primary importance that new ways of preventing and treating infections, especially alternatives to antibiotics, become available.

Table 1.6: Bacterial species identified in culture-positive peri-prosthetic joint infections. Adapted from (141).

Microorganism or group	% of infections
Aerobic Gram-positive cocci	**77.7**
Coagulase-negative staphylococci	39.6
Staphylococcus epidermidis	23.3
S. lugdunensis	1.9
S. capitis	1.5
S. hominis	1.3
Staphylococcus aureus	28.1
Methicillin-resistant *S. aureus*	7.9
Streptococcus species	9
S. agalactiae	2.8
Viridans group	2
S. mitis group	1.4
S. anginosus group	1
Enterococcus species	8
E. faecalis	6.9
Aerobic Gram-negative bacilli (GNB)	**27.6**
Enterobacteriaceae	20.4
Escherichia coli	9.1
Proteus species	4.8
Enterobacter species	4.2
Klebsiella species	2.5
Morganella morganii	1.9
Non-fermenting GNB	9.5
Pseudomonas species	8.8
Aerobic Gram-positive bacilli	**2.4**
Corynebacterium species	2.2
Anaerobic bacteria	**6.8**
Anaerobic Gram-positive bacilli	5.1
Cutibacterium species	4.9
Anaerobic Gram-positive cocci	1.4
***Mycobacterium* species**	**0.4**
Fungi	**1.3**
Candida species	1.2

1.7 Strontium

Strontium, symbol Sr and atomic number 38, is the fourth alkaline-earth metal in the periodic table of chemical elements, between barium and calcium. Its atomic weight is 87.62 u (144), 2.2 times that of calcium, and its ionic radius is 1.13 Å, 1.14 times that of calcium (145).
Traces of strontium are found in the human body, 98 % of which deposited in bone and teeth where it substitutes for calcium in the atomic structure of hydroxyapatite (146). Normally, the strontium/calcium ratio in bones and serum varies between 1:1000 and 1:2000, with the highest concentration of strontium being found in newly formed bone and in calcified bone near the mineralisation front (147-149).
Oral administration of this element has been shown to induce higher bone formation rate and higher density in trabecular bone and is therefore used in clinic to treat osteoporosis. The following Sections will provide an overview on its effects on bone cells (Section 1.7.1), the use of strontium ranelate as a drug for treating osteoporosis (Section 1.7.2), its use as a doping agent in bioactive glasses and glass-ceramics for bone substitutes (Section 1.7.3) and more recent investigations on its potential antimicrobial effect (Section 1.7.4).

1.7.1 Effect of strontium on bone cells

Strontium has been shown to enhance bone deposition and, at the same time, inhibit bone resorption (15, 150, 151). This is due to the fact that strontium can be considered an uncoupling agent, for its dual action on osteoblasts and osteoclasts (14, 15), as it can be seen in Figure 1.17.

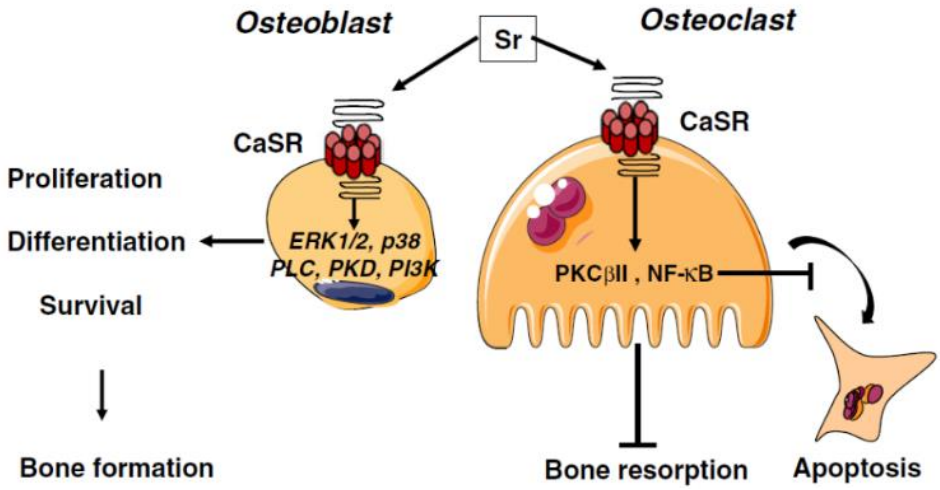

Figure 1.17: Action of strontium as an uncoupling agent for osteoblasts and osteoclasts. Through the calcium sensing receptor (CaSR), osteoblasts and their precursors are induced to increase their proliferation, differentiation and survival, thus enhancing bone formation, while osteoclast activity is inhibited so that bone resorption is reduced and apoptosis is increased. Reproduced with permission from (152).

It has been shown that strontium can interact with both osteoblasts and osteoclasts through their calcium sensing receptors (CaSRs), although the whole mechanism of action of strontium on bone cells and the way it can be distinguished from calcium is still not fully understood.

In osteoblasts, strontium can enhance the differentiation of osteoblast precursors, their proliferation and the production of osteoblast markers such as alkaline phosphatase (ALP), bone sialoprotein (BSP) and osteocalcin (OCN), which altogether can increase bone deposition (153-156). CaSRs control the activation of the ERK1/2-MAPK pathway (extracellular signal-regulated kinase – mitogen-activated protein kinase), which regulates proliferation, and of the Wnt pathways, which regulate differentiation (157, 158).

In osteoclasts, strontium has been shown to disrupt the actin network that allows these cells to attach to bone and resorb it (16) and to modulate the NF-κB (the nuclear factor kappa-light-chain-enhancer of activated B cells) and the PKCβII (protein kinase C βII) signalling pathways, thus reducing their differentiation and inducing their apoptosis, respectively (159, 160).

1.7.2 Use of strontium in medicine: Strontium ranelate

After the discovery of the bone regenerative properties of strontium described above in Section 1.7.1, Marie and co-workers developed an organic divalent strontium salt that could be used to treat osteoporosis: strontium ranelate, S12911 (15). It was shown that, like other strontium salts, strontium ranelate could promote bone formation, increase trabecular bone volume and decrease bone resorption (14, 16, 161). Clinical trials in humans proved its efficacy at preventing vertebral and non-vertebral fractures and bone loss in postmenopausal women and osteoporotic men (162-167).
The use of strontium ranelate as a drug was approved in Europe in 2004 and is currently utilised in 70 countries as a drug for the treatment of osteoporosis and the prevention of fractures, with the commercial names of Protelos and Osseor (145, 168). However, concerns increased in 2012 about the potential cardiovascular side effects of this drug (169-171). As a result, in 2013 and again in 2014 the European Medicines Agency (EMA) set stricter recommendations and new contraindications for its systemic use (172-175), so that it is now prescribed only to patients who do not have a history of heart or circulatory conditions and are unable to take any other medication for severe osteoporosis (168, 176). It is therefore clear that the systemic delivery of this drug is not advisable and other routes of administration would be preferable to avoid its contraindications. The use of bioactive glasses and glass-ceramics for the local delivery of low doses of strontium, as investigated in the work presented in this thesis, would be therefore ideal for the safe treatment of a larger number of patients that would benefit from the bone regenerative properties of this element.

1.7.3 Use of strontium as a doping agent in bone substitutes

With the increase in interest for the bone regenerative properties of strontium, numerous solutions have been proposed for the addition of this element into the glass network of bone scaffolds, so that their bioactivity could be improved.
The first composition that was modified, as it is also the most studied, was Bioglass 45S5. 0 to 100 mol% of its CaO has been substituted with SrO and the dual action of strontium in inhibiting osteoclasts and promoting osteoblast activity *in vitro* was further confirmed, with the best results obtained for the 10 mol% SrO composition (151, 177). *In vivo* tests then proved the osteoconductivity of the material (178). In sol-gel glass systems, the dissolution rate of strontium-doped bioactive glasses showed faster dissolution kinetics (179), while still promoting osteoblast differentiation (180, 181). Similar results were also observed when strontium was added to glass-ceramics such as calcium silicates, calcium phosphates and hydroxyapatite, where changes in the

dissolution rate and an increase in osteoblast proliferation and differentiation were found, with the optimal amount of strontium depending on the initial composition of the starting material (182-185). In particular, Vickers first developed the strontium AWGC compositions studied in this thesis and found that the best composition in terms of bioactivity and osteogenic properties was the one containing 6.2 mol% of SrO (186) for samples prepared from compacted powders.
3D porous scaffolds containing strontium were also described in the literature, produced following different techniques such as the use of a polymeric porogen (183, 187), foam replication (188, 189), foam replication combined with sol-gel (190-192), electrophoretic deposition of strontium-containing glass particles (193) and 3D printing (194). In the case of the work described in present thesis, the strontium-doped AW glass was produced via melting and quenching, then the porous scaffolds were fabricated following the foam replication technique utilising a single thermal treatment to obtain both sintering of the glass particles and controlled nucleation and growth of the crystal phases.

1.7.4 Antibacterial activity of strontium

In more recent years, interest has increased around the possibility that strontium could have some antimicrobial properties. Investigations started in 2003, when Guida et al. hypothesised a synergistic effect of strontium and fluoride when combined in glass ionomer cements for dental applications (17), later observed also by Dabsie et al. (195). Afterwards, further studies described the improved loading and release of antibiotics from a strontium-substituted calcium phosphate cement (196), the bactericidal effect of a strontium-doped bioactive glass in a composite cement (197), the antibacterial properties of strontium-modified bioactive glasses against sub-gingival bacteria (18) or of borosilicate bioactive glasses against common bone pathogens (198) and the antimicrobial properties of strontium-substituted hydroxyapatite nanoparticles (199). Some authors combined strontium with silver in antibacterial glasses and glass-ceramics; although generally no enhancement was found in their antimicrobial action when strontium was added to silver, a reduction in cytotoxicity was observed, therefore allowing enhanced bone regeneration while maintaining the same antimicrobial effect (200-202).
Whether strontium can be considered a bactericidal or bacteriostatic agent is still not clear, as well as its interaction and mode of action with bacterial cells is still under investigation. It must be noted that it has been observed that not only strontium glasses can present an antibacterial behaviour, but also Bioglass 45S5 itself (203, 204) and, more distinctively, Bioglass S53P4 (BonAlive®) (94, 205-207). In addition,

two publications studied different compositions of bioactive glasses against numerous aerobic and anaerobic bacterial species, observing growth inhibition for all samples (208, 209). Some authors ascribed the observed antibacterial effect to the presence of calcium (210, 211), while others to phosphorus (212, 213). Proposed mechanisms of action include the decrease in zeta potential when strontium is added (199), the increase in local pH and osmolarity caused by the dissolution of the glass (94, 206-208), the formation of debris that can damage the bacterial cell membrane (204) and disturbance to the membrane potential by the increase of calcium ions (208, 209). Certainly, the induction of antimicrobial properties adds very high value to materials designed for bone repair, turning them into potential tools for the prevention and treatment of post-operative and peri-prosthetic infections.

1.8 Thesis aim and objectives

The overall aim of the work presented in this thesis was to investigate the feasibility of the production of bone porous substitutes that, through the addition of strontium to AWGC, could enhance bone tissue regeneration and, at the same time, provide antibacterial features for the prevention and treatment of infections.
The investigation was therefore divided into different objectives, which will be addressed in the following Chapters 2 to 5:

- Production and characterisation of the glass powders used for the fabrication of the porous scaffolds.
- Production of porous scaffolds through the foam replication method and their characterisation, including the assessment of their crystallinity, morphology, mechanical properties, *in vitro* apatite forming ability and radiopacity.
- Investigation of the antibacterial properties of strontium and of the strontium-containing glass powders produced.
- Investigation of the *in vitro* biological properties of the porous scaffolds, in terms of effect on proliferation and osteogenic differentiation of bone cell precursors.

Chapter 2
Production and characterisation of strontium glasses

2.1 Introduction

Substitution of strontium for calcium in bioactive glasses and glass-ceramics has been widely described in the literature, based on different glass compositions: from Bioglass 45S5 (151, 177), to boron-containing 13-93 (214), to hydroxyapatite (184). Vickers first studied the substitution of strontium for calcium in the apatite-wollastonite glass-ceramic (AWGC) system: substitutions up to 50 mol% of the initial calcium oxide amount were described and 45-90 μm powders were used to produce microporous scaffolds from compacted powders (186).
In the work presented in this thesis, substitutions up to 75 mol% of calcium oxide were produced and powders <45 μm were used for the fabrication of macroporous scaffolds, as it will be described in Chapter 3. Before the strontium-containing glass-ceramic porous scaffolds under study could be produced, parent glasses of the desired composition were prepared. These glasses were produced via the melt-quench route and then processed in order to obtain glass powders in the desired range of particle size. Powders were also characterised to ensure that strontium had been substituted for calcium in the desired proportion for each desired composition and to study the thermodynamic effects of this substitution.
The aim of this chapter was therefore to describe the six strontium glasses produced, assess the strontium substitution and study the effects of this substitution. In this chapter, the methods used for producing the six strontium glasses will be presented, along with their processing steps and their characterisation in terms of density, morphology, composition, particle size distribution, thermal behaviour and atomic structure.

2.2 Materials and methods

2.2.1 Production of strontium-containing AW parent glasses

Basing on the original AWGC composition first described by Kokubo and co-workers (85) and later studied by Xiao and co-workers (119), six different glass compositions were produced by substituting an increasing amount of strontium oxide for calcium oxide on a molar basis. The general formula for the six compositions under study is:

35.5 SiO_2 – 7.1 MgO – 0.4 CaF_2 – 7.1 P_2O_5 – (49.9-x) CaO – x SrO mol %,

where x = 0, 6.2, 12.5, 18.7, 24.9, 37.4.
The six compositions were named after the molar amount of SrO they contained and are listed in Table 2.1.

Table 2.1: Composition of the six strontium AW glasses under study. Amounts in mol%.

Glass	SiO_2	MgO	CaF_2	P_2O_5	CaO	SrO
AW 0%	35.5	7.1	0.4	7.1	49.9	0
AW 6.2%	35.5	7.1	0.4	7.1	43.7	6.2
AW 12.5%	35.5	7.1	0.4	7.1	37.4	12.5
AW 18.7%	35.5	7.1	0.4	7.1	31.2	18.7
AW 24.9%	35.5	7.1	0.4	7.1	25.0	24.9
AW 37.4%	35.5	7.1	0.4	7.1	12.5	37.4

All glasses were produced through melting and quenching. The reagents listed in Table 2.2 were first weighed in the specified amounts and then mixed for 1 hour on a roller mixer, then carefully packed in alumina crucibles (Almath Crucibles Ltd). These were placed inside bigger mullite crucibles (Magma Ceramics & Catalysts) containing calcined alumina powder and, with their lid on, placed in a furnace (Elite, BCF13/12-2416); temperature was brought to 500 °C and held for 15 min. The big crucibles were then transferred to a Pyro Therm furnace, pre-heated at 1400 °C, and its temperature was further raised to 1450 °C. After 2 h, the big crucibles were taken out of the furnace, the alumina crucibles extracted and the molten glass poured in cold tap water. The frit obtained was then rinsed under running water and dried overnight in a drying cabinet. Table 2.2 lists the amounts necessary for making 100 g of glass frit.

Table 2.2: Details of the reagents and relative amounts necessary for producing 100 g of glass frit for the six compositions under study. All data in g.

	SiO_2 Tilcon Sands	MgO Sigma Aldrich	CaF_2 VWR Int.	P_2O_5 Fisher Scientific	$CaCO_3$ Fisher Scientific	$SrCO_3$ Fisher Scientific
AW 0%	34.1	4.6	0.5	16.1	79.8	0.0
AW 6.2%	32.6	4.4	0.5	15.4	66.8	14.0
AW 12.5%	31.1	4.2	0.5	14.7	54.6	26.9
AW 18.7%	29.9	4.0	0.4	14.1	43.7	38.6
AW 24.9%	28.7	3.8	0.4	13.5	33.6	49.4
AW 37.4%	26.5	3.6	0.4	12.5	15.6	68.7

After drying, the glass frit was ground for 15 min with a Gyro-mill percussion mill (Glen Creston Ltd), using a small puck with 20 g of frit at a time. The powder so obtained was then sieved with an automatic siever (Octagon Digital, Endecotts), run for 30 min at intermittent mode and amplitude 9 and fitted with the following stack of sieves: 45 µm, 90 µm, 125 µm, 1 mm, 2 mm. Glass powders were collected separately for the different size ranges and the fraction <45 µm (about 50% of the starting load) was used for producing porous scaffolds, following the methods described in Chapter 3.

2.2.2 Characterisation of the strontium-containing AW parent glass powders

2.2.2.1 Density of strontium AW glass powders

The density of the six glass powders was measured using a Micromeritics AccuPyc 1330 pycnometer. Given the weight of the sample, the machine used helium to measure the volume occupied by the powder and calculate its density; the machine performed up to 50 measurements until five of them had a standard deviation below 0.005 % of their average.

About 1.4 g of glass powder <45 µm were tested for each composition; the exact weight was recorded, as well as their single measurements, average and standard deviation.

2.2.2.2 Morphology and composition of ground strontium AW glass powders

Glass powder particles sieved <45 µm were checked for their morphology and composition using a Hitachi S-3400N scanning electron microscope (SEM), coupled with a Bruker XFlash detector for energy dispersive x-ray spectroscopy (EDS). Powders were attached to aluminium stubs using adhesive carbon tape, sputtered with gold to enhance their conductivity and analysed at 30 kV to allow for a better detection of strontium, whose K_α signal is at 14.16 keV. Micrographs were taken at about 5 mm working distance, while EDS data were collected at 10 mm from areas magnified 200 times.
Elemental analyses were performed with Quantax Esprit 1.9.4 analysis software, on three different batches of glass for each composition.

2.2.2.3 Particle size distribution of ground strontium AW glass powders

After grinding and sieving the glass frit as described in Section 2.2.1, the particle fraction <45 µm was analysed for particle size distribution via laser light scattering using a Malvern Mastersizer 2000, to verify that the powders produced were consistent across compositions. Powders were dispersed in ultrapure water and modelled as glass beads; the refractive index was set to 1.33 for water and to 1.52 for the glass particles. Before each sample was suspended in water, a background measurement was recorded. The glass powders were kept suspended in the dispersant by maintaining a stirring speed around 2000 revolutions per minute (rpm) on the dispersion unit. For each sample, 10 measurements were taken and automatically averaged by the Mastersizer 2000 software.

2.2.2.4 Thermal behaviour of the strontium AW parent glasses

The thermal behaviour of all six glass compositions was tested using a Netzsch DSC 404 *F3 Pegasus* differential scanning calorimetry (DSC) machine.
20 mg of sample (fraction tested <45 µm) were placed in a platinum-rhodium crucible with a lid and the measurement was conducted against an empty crucible, upon recording of the baseline signal using the same two crucibles, both empty. During the analysis, the glass powder was heated at 10 °C/min from room temperature to melting, maximum temperature 1300 °C, and the signal produced by the sample recorded in a graph.

After the measurement, Proteus Analysis software was used to identify the characteristic temperatures: glass transition temperature (T_g), onset of peak temperature (T_{on}), top of peak temperature (T_p) and melting temperature (T_m).
For each glass composition, three batches were tested and averaged using OriginPro 2015 to verify the consistency of production.

2.2.2.5 Verification of the amorphous nature of strontium AW glass powders

The amorphous nature of the six compositions was verified by means of x-ray diffraction (XRD): if a sample was amorphous, it did not produce any XRD peak, but gave a broad halo instead. In general, for silicon-based glasses, the characteristic halo has a broad hump centred at about 2θ = 30 °.
All six strontium glasses were tested with a Bruker D8 Advance diffractometer, working with Bragg-Brentano geometry and copper-K alpha radiation. The diffractometer was set to 40 kV and 40 mA, the required amount of <45 µm powder was compacted in the sample holder and the analysis run from 10 ° to 70 ° 2θ, step size 0.033 °, time/step 0.6 s.

2.3 Results

2.3.1 Strontium increases the density of AW glass powders

The density measured for the six glasses is reported in Table 2.3 and shown in Figure 2.1. Average and standard deviation were given as output from the Micromeritics AccuPyc 1330 pycnometer measurements.

Table 2.3: Density of the six strontium-containing AW glasses.

	Average (g/cm^3)	**Standard deviation (g/cm^3)**
AW 0%	2.9372	0.0065
AW 6.2%	3.0915	0.0103
AW 12.5%	3.1925	0.0042
AW 18.7%	3.2849	0.0082
AW 24.9%	3.3538	0.0139
AW 37.4%	3.5796	0.0102

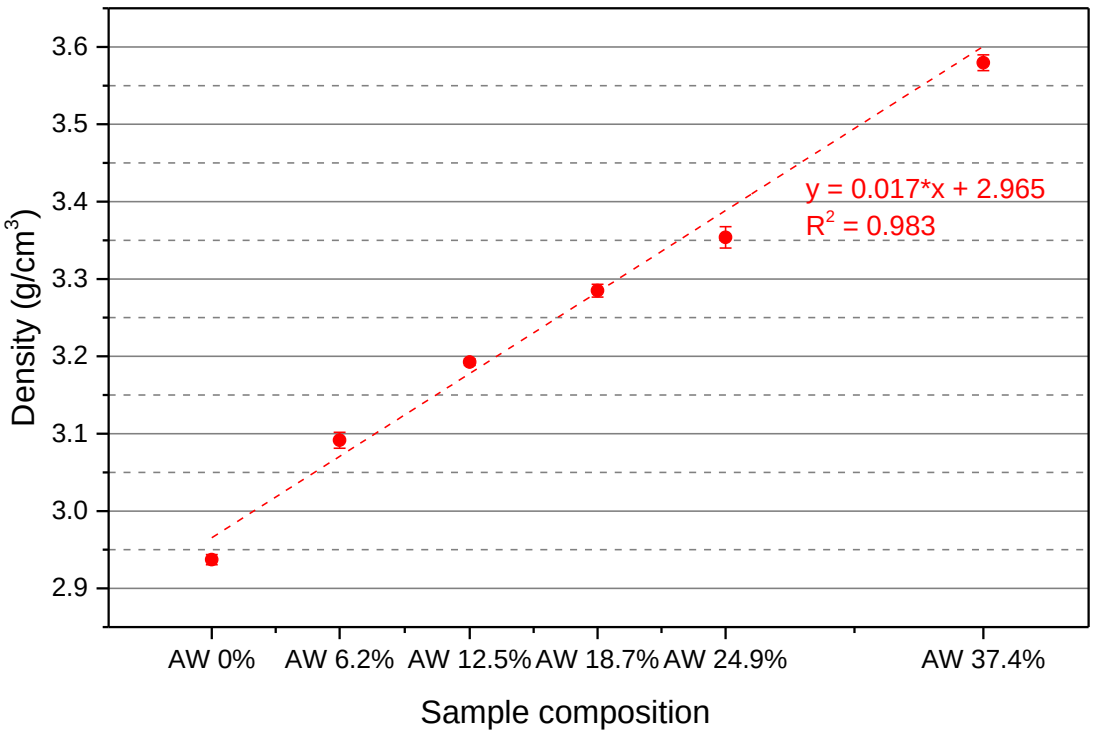

Figure 2.1. Density of the six strontium-containing AW glasses, with fitting trendline. Error bars indicate the standard deviation from 5 measurements performed by the Micrometrics AccuPyc 1330 helium pycnometer for each sample.

As expected from the substitution, on a molar basis, of a heavier element for a lighter element, it was found that the density of the six glasses linearly increased with the increasing amount of strontium.

These results were used, as described in Chapter 3, to calculate the (water + PVA)-to-glass ratio of the slurry used for the production of solid discs and porous scaffolds.

2.3.2 Effect of strontium on morphology and composition of ground AW glass powders

SEM micrographs of particles of the six strontium AW glasses, ground and sieved <45 μm, are shown in Figure 2.2 and Figure 2.3.

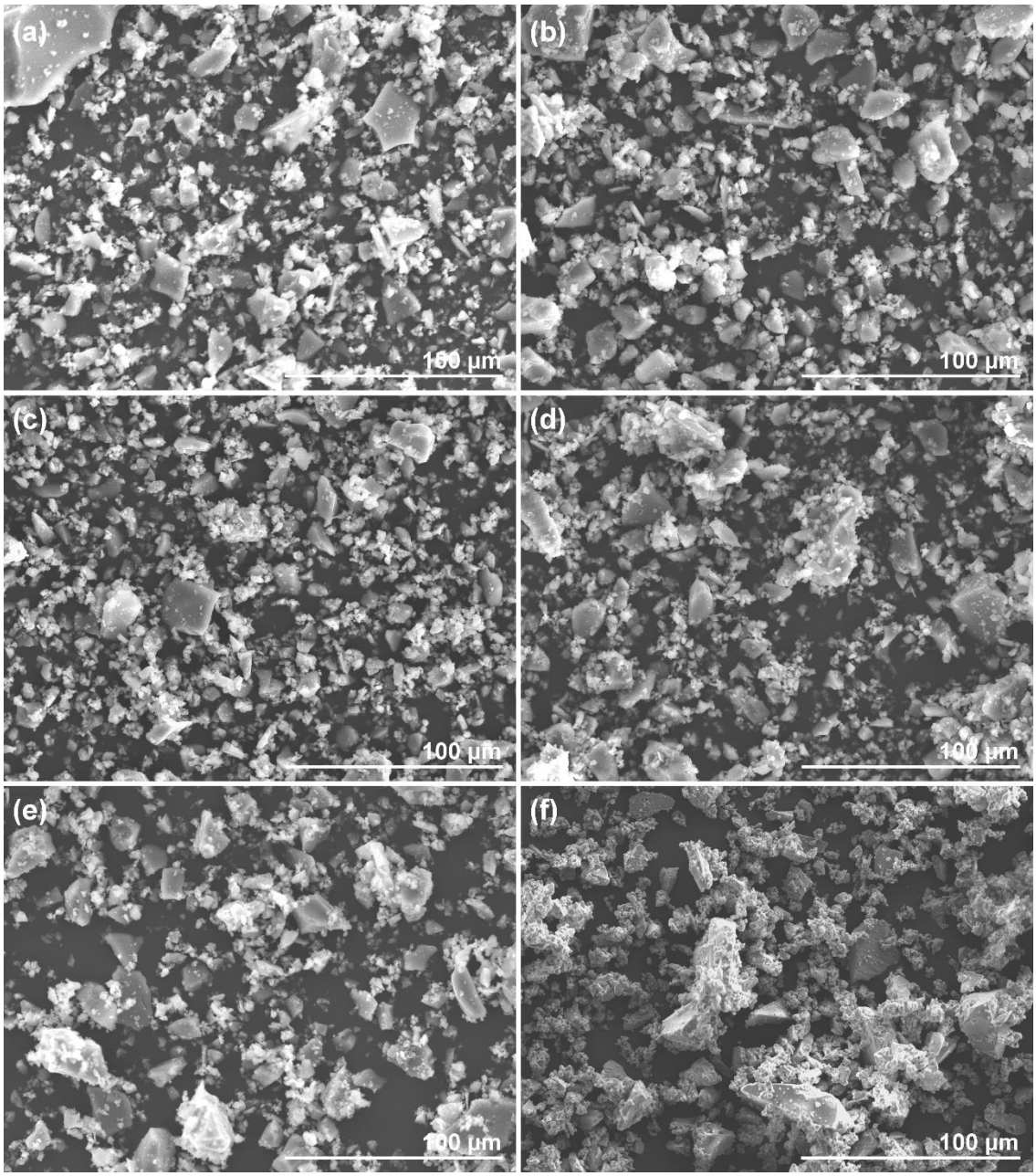

Figure 2.2: SEM micrographs at low magnification of the glass powders sieved <45 µm, imaged from secondary electrons. (a) AW 0%, (b) AW 6.2%, (c) AW 12.5%, (d) AW 18.7%, (e) AW 24.9%, (f) AW 37.4%. Scale bars represent 100 µm.

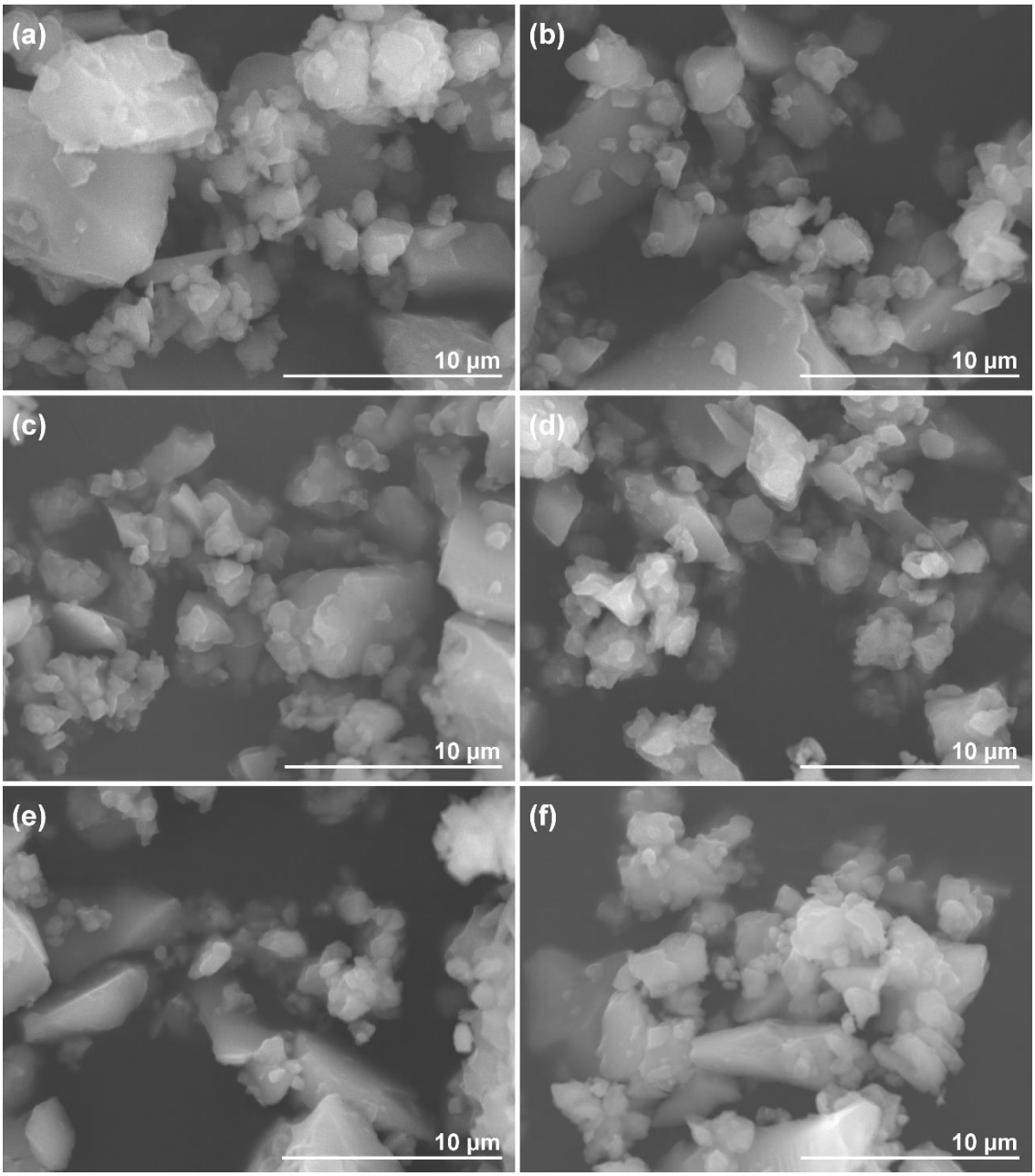

Figure 2.3: SEM micrographs, at higher magnification and imaged from secondary electrons, of the glass powders sieved <45 µm shown in Figure 2.2. (a) AW 0%, (b) AW 6.2%, (c) AW 12.5%, (d) AW 18.7%, (e) AW 24.9%, (f) AW 37.4%. Scale bars represent 10 µm.

All samples presented particles with an irregular shape, as expected from the grinding process of a glass frit. For all compositions, most particles were within the required size, with few particles bigger than 45 µm in only one of their dimensions, which let them still pass through the mesh of the sieve. As better shown in Figure 2.3, all samples contained an important fraction of small particles, about 1 µm large or less.

EDS data were taken in order to confirm the composition of powders, from areas of the samples magnified 200 times.

Table 2.4 shows the expected theoretical values for the elements of interest, while Table 2.5 reports the results of the quantitative analysis of the powder samples, expressed as average ± standard deviation of three batches of glass for each composition.

Table 2.4: Theoretical atomic percentages of the elements of interest for the glass and glass-ceramic samples, which correspond to the expected EDS values.

Elem.	AW 0%	AW 6.2%	AW 12.5%	AW 18.7%	AW 24.9%	AW 37.4%
Si	32.90	32.90	32.90	32.90	32.90	32.90
Mg	6.58	6.58	6.58	6.58	6.58	6.58
F	0.74	0.74	0.74	0.74	0.74	0.74
Ca	46.62	40.87	35.03	29.29	23.54	11.96
P	13.16	13.16	13.16	13.16	13.16	13.16
Sr	0.00	5.75	11.59	17.33	23.08	34.66

Table 2.5: Average atomic percentage and standard deviation of the elements of interest in the glass powder samples, as measured by EDS from three batches for each composition.

Elem.	AW 0%	AW 6.2%	AW 12.5%	AW 18.7%	AW 24.9%	AW 37.4%
Si	30.50 ± 0.73	28.35 ± 0.85	27.79 ± 1.49	26.63 ± 1.72	25.71 ± 1.39	26.17 ± 2.66
Mg	4.84 ± 0.08	4.76 ± 0.02	5.04 ± 0.23	5.44 ± 0.90	5.06 ± 0.24	5.11 ± 0.37
F	2.29 ± 2.12	2.41 ± 1.64	2.28 ± 2.37	2.86 ± 2.52	5.06 ± 1.48	5.53 ± 0.28
Ca	47.59 ± 0.80	42.65 ± 0.63	36.69 ± 0.29	30.36 ± 0.75	24.47 ± 1.08	12.45 ± 0.77
P	14.33 ± 0.44	13.64 ± 0.39	13.68 ± 0.32	13.50 ± 0.67	12.83 ± 0.39	12.04 ± 0.80
Sr	0.00 ± 0.00	7.12 ± 0.34	13.62 ± 0.28	19.97 ± 1.05	26.05 ± 1.71	38.27 ± 2.07
Al	0.45 ± 0.16	1.07 ± 0.35	0.91 ± 0.20	1.25 ± 0.50	0.83 ± 0.09	0.42 ± 0.57

For all compositions, the atomic percentage of calcium, phosphorus and strontium was very close to the theoretical values, within the limits of the technique. The element that presented the highest deviation from its theoretical value was fluorine, which was found higher in all compositions: about 2 at% for compositions AW 0%, AW 6.2%, AW 12.5% and AW 18.7%, while about 5 at% for compositions AW 24.9% and AW 37.4%. This was likely due to the intrinsic error of the analysis, for which it was not possible to precisely detect amounts below 1 at% (the theoretical value is 0.74 at%) and, in fact, the standard deviations for fluorine were the highest amongst all the elements. The higher fluorine was compensated by lower amounts of silicon and magnesium. A small amount of aluminium (around 1 at%) was detected in all samples, which was likely due to an ionic exchange, occurring at high temperature, with the alumina crucibles used to produce the glass samples.

2.3.3 Particle size distribution of strontium AW glass powders for scaffold production

Laser light scattering was used for the six strontium AW glasses, <45 µm fraction, in order to ensure that the powders used for producing the scaffolds presented comparable particle size distributions. Results are displayed in Figure 2.4.

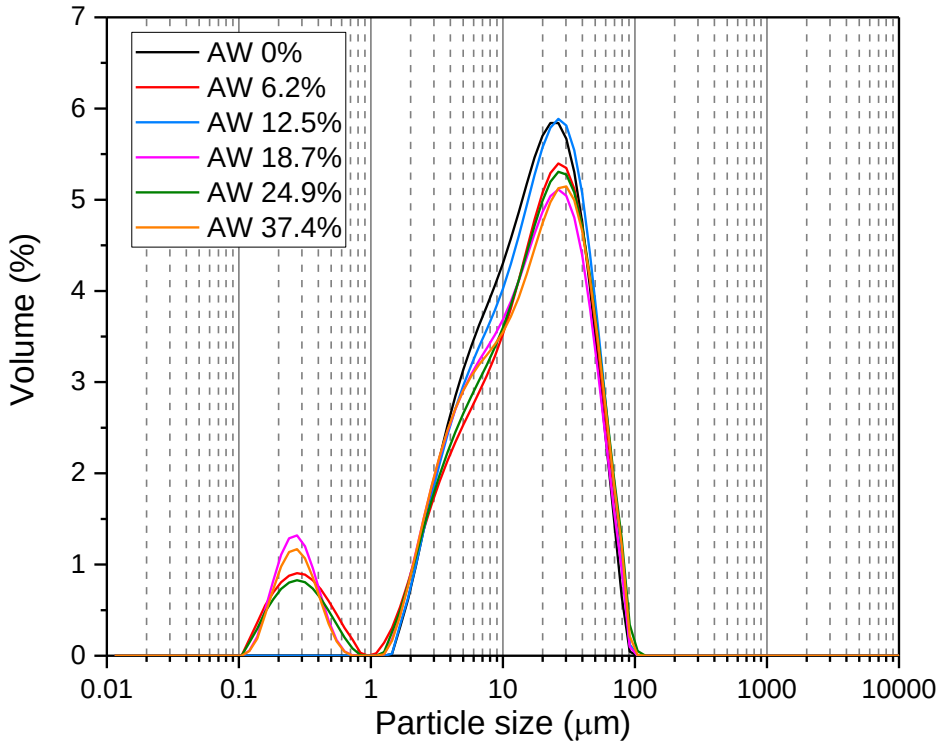

Figure 2.4: Particle size distribution of the six strontium AW glass powers, ground and sieved <45 µm.

All six samples gave very similar results. Each particle size distribution presented two main peaks: the first peak centred around 250 nm and the second peak at about 25 µm; for all glasses, the second peak also showed a hump around 6 µm. The minimum detected size was 100 nm, while the maximum detected size was 100 µm, thus indicating that some larger particles passed through the sieve. Because all compositions showed the same distribution, particle size was not considered a variable in the foam replication production of porous scaffolds, described in Chapter 3.

2.3.4 Effect of strontium on the thermal characteristics of AW glass powders

Thermal analyses were run at 10 °C/min on three batches of <45 µm glass powder per each composition. Average graphs for the whole range of tested temperatures are shown in Figure 2.5, then reproduced with their standard deviations represented in grey and within the temperatures of interest in Figure 2.6.

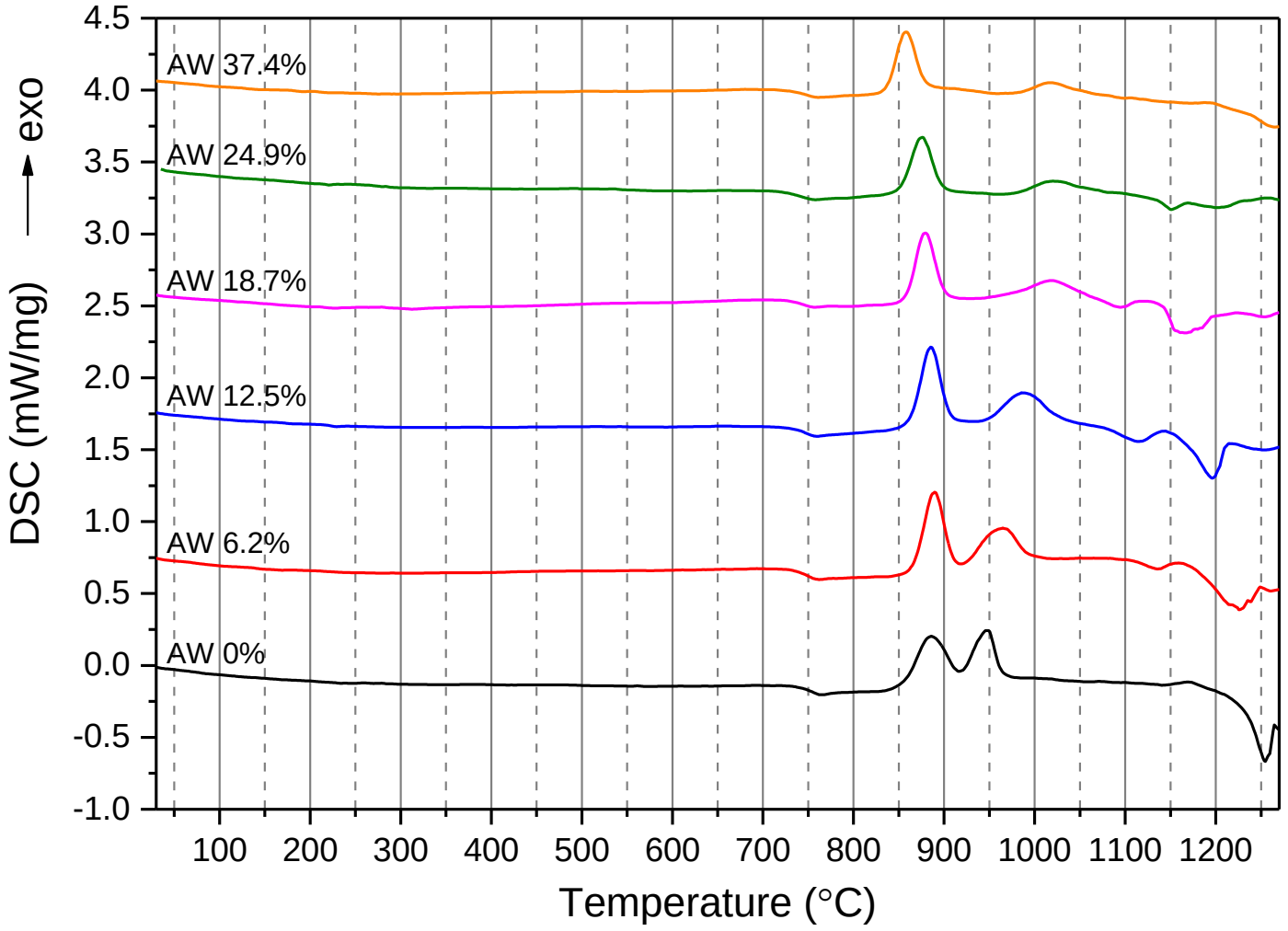

Figure 2.5: DSC average traces of the strontium AW glass compositions, for powders <45 µm heated at 10 °C/min.

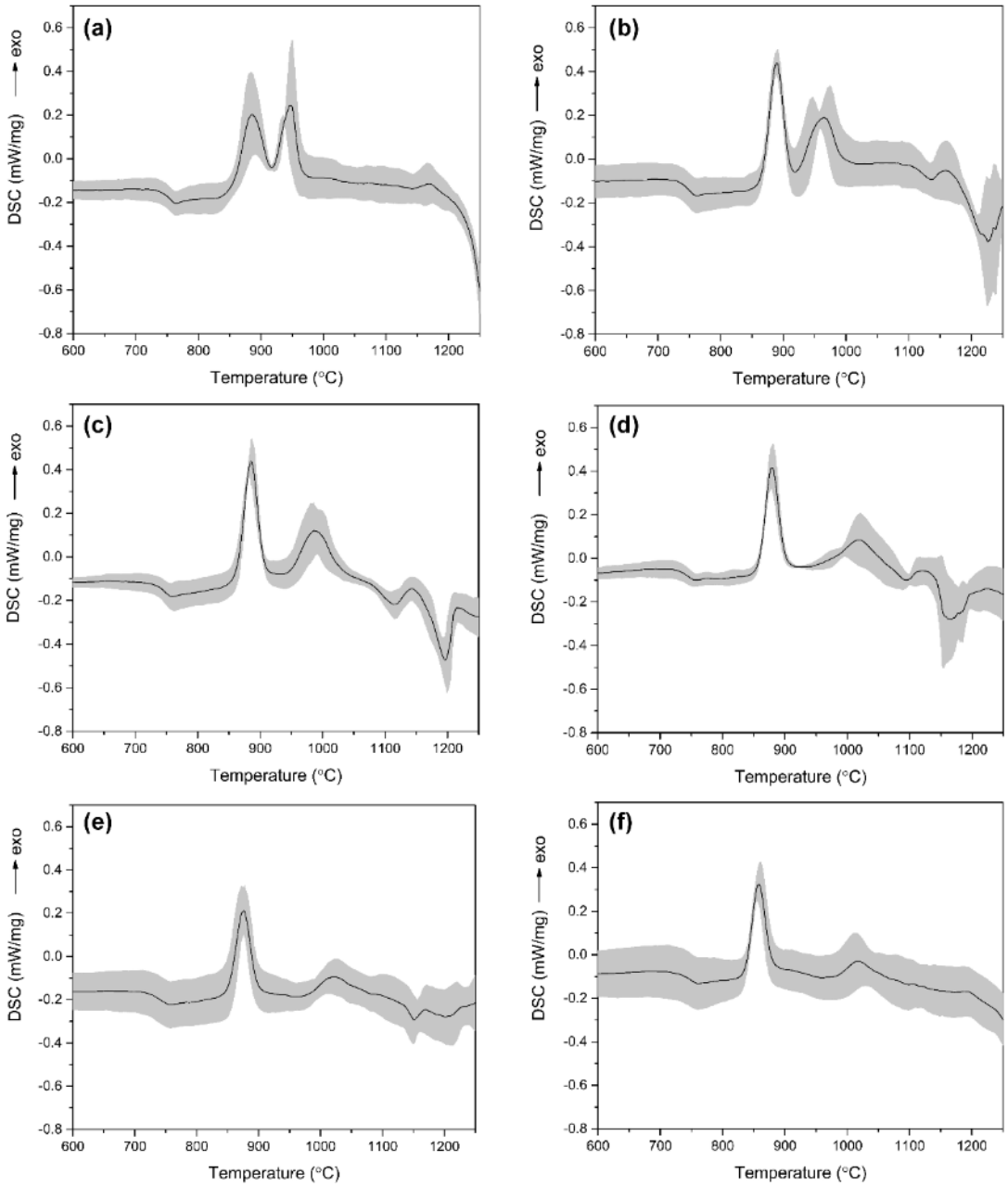

Figure 2.6: Average DSC traces of the <45 µm powders heated at 10 °C/min, with standard deviations in grey (n=3). (a) AW 0%, (b) AW 6.2%, (c) AW 12.5 %, (d) AW 18.7%, (e) AW 24.9%, (f) AW 37.4%.

The thermal trace for all compositions presented an inflection between 700 and 750 °C, representing their glass transition temperature T_g. Two exothermic peaks followed at higher temperature. The first peak appeared around 850 °C for all glasses, indicating the formation of apatite as described in the literature (85, 104, 186). The temperature of the second peak varied from about 950 °C for AW 0% to 1020 °C for AW 37.4%, representing the formation of the wollastonite phase according to the

literature (85, 104, 186). It was therefore evident that the formation of the calcium silicate phase strongly depended on the strontium content.

To better visualise the temperatures of interest across the glass compositions, Figure 2.7 summarises the behaviour of the characteristic temperatures depending on the strontium content: glass transition (T_g), onset of peaks (T_{on}), top of peaks (T_p) and melting (T_m).

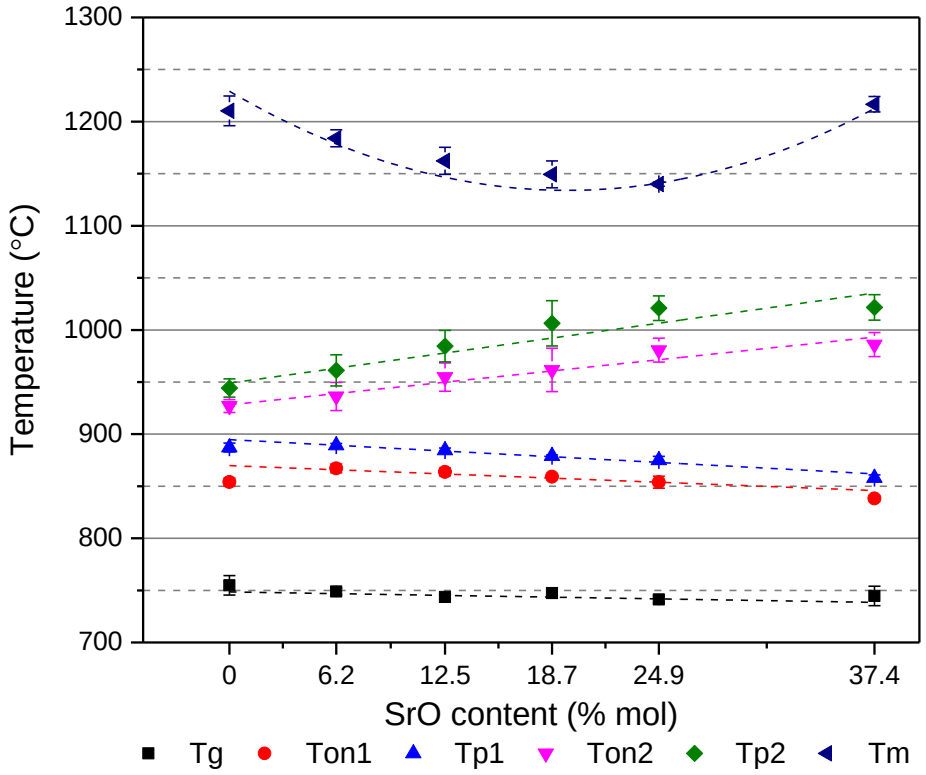

Figure 2.7: Characteristic temperatures of the strontium glasses depending on their strontium content, with fitting trendlines. T_g: glass transition temperature; T_{on1}: onset of the first exothermic peak; T_{p1}: first exothermic peak temperature; T_{on2}: onset of the second exothermic peak; T_{p2}: second exothermic peak temperature; T_m: melting temperature. Error bars indicate standard deviations (n=3).

The graph in Figure 2.7 confirmed that the glass transition temperature (T_g) did not change considerably with the amount of strontium, while the position of the first exothermic peak was slightly shifted towards lower temperatures with increasing strontium. On the contrary, the nucleation and growth of the second crystal phase was directly proportional to the strontium content. The melting temperature followed a

second order curve with AW 24.9% melting at the lowest temperature. Data are summarised in Table 2.6, reported as mean ± standard deviation.

Table 2.6: Average ± standard deviation of the characteristic temperatures of the strontium glasses. T_g: glass transition temperature; T_{on1}: onset of the first exothermic peak; T_{p1}: first exothermic peak temperature; T_{on2}: onset of the second exothermic peak; T_{p2}: second exothermic peak temperature; T_m: melting temperature. All data in °C.

	T_g	T_{on1}	T_{p1}	T_{on2}	T_{p2}	T_m
AW 0%	754.8 ± 9.3	854.0 ± 3.8	887.2 ± 4.2	927.0 ± 6.2	944.3 ± 8.7	1210.3 ± 14.2
AW 6.2%	748.9 ± 3.3	867.1 ± 4.2	889.2 ± 1.8	936.2 ± 13.5	961.2 ± 14.9	1184.0 ± 8.2
AW 12.5%	743.7 ± 1.8	863.7± 3.7	884.4 ± 2.2	954.7 ± 13.5	984.4 ± 15.1	1162.3 ± 13.0
AW 18.7%	747.5 ± 4.8	859.2 ± 0.9	879.0 ± 1.1	961.6 ± 20.8	1006.4 ± 21.7	1149.3 ± 12.9
AW 24.9%	741.3 ± 3.1	853.9 ± 5.8	874.9 ± 3.7	980.6 ± 11.4	1020.9 ± 11.8	1140.0 ± 2.0
AW 37.4%	744.7 ± 9.3	838.3 ± 2.7	857.9 ± 3.0	986.0 ± 11.5	1021.6 ± 12.3	1216.7± 7.4

All fitting curves shown in Figure 2.7, described by Equation 2.1 to Equation 2.6, were obtained using Origin Pro 2015.

$$T_g = 748.52 - 0.27 * SrO\%$$

Equation 2.1: First order regression curve for the glass transition temperature.

$$T_{on1} = 869.75 - 0.64 * SrO\%$$

Equation 2.2: First order regression curve for the onset temperature of the first crystal phase.

$$T_{p1} = 894.72 - 0.88 * SrO\%$$

Equation 2.3: First order regression curve for the peak temperature of the first crystal phase.

$$T_{on2} = 928.15 + 1.74 * SrO\%$$

Equation 2.4: First order regression curve for the onset temperature of the second crystal phase.

$$T_{p2} = 948.95 + 2.31 * SrO\%$$

Equation 2.5: First order regression curve for the peak temperature of the second crystal phase.

$$T_m = 1229.26 - 9.72 * SrO\% + 0.25 * (SrO\%)^2$$

Equation 2.6: Second order regression curve for the melting temperature.

While the glass transition temperature only slightly decreased with the increase of strontium, the formation of the first crystal phase (apatite) linearly tended to lower temperatures with a shift of about 30 °C between AW 0% and AW 37.4%; this difference was not detected from the qualitative assessment of the DSC graphs shown in Figure 2.5 and Figure 2.6. The formation of the second crystal phase (calcium silicate) also depended linearly on the amount of strontium oxide in the starting glass powder, but its onset and peak temperature increased with increasing strontium, with a shift of about 80 °C between the lowest and the highest strontium composition. The melting temperature, however, presented a minimum for the AW 24.9% composition, while AW 0% and 37.4% melted at about the same temperature, around 1200 °C.

2.3.5 Amorphous nature of the strontium AW glass powders

Glass powders sieved <45 μm were tested to verify that no crystalline phases formed during the melting and quenching of the six glasses; in fact, the starting materials had to be amorphous glasses, so that the formation of crystal phases could be controlled through appropriate thermal treatments.
Figure 2.8 shows the resulting XRD spectra for the six samples.

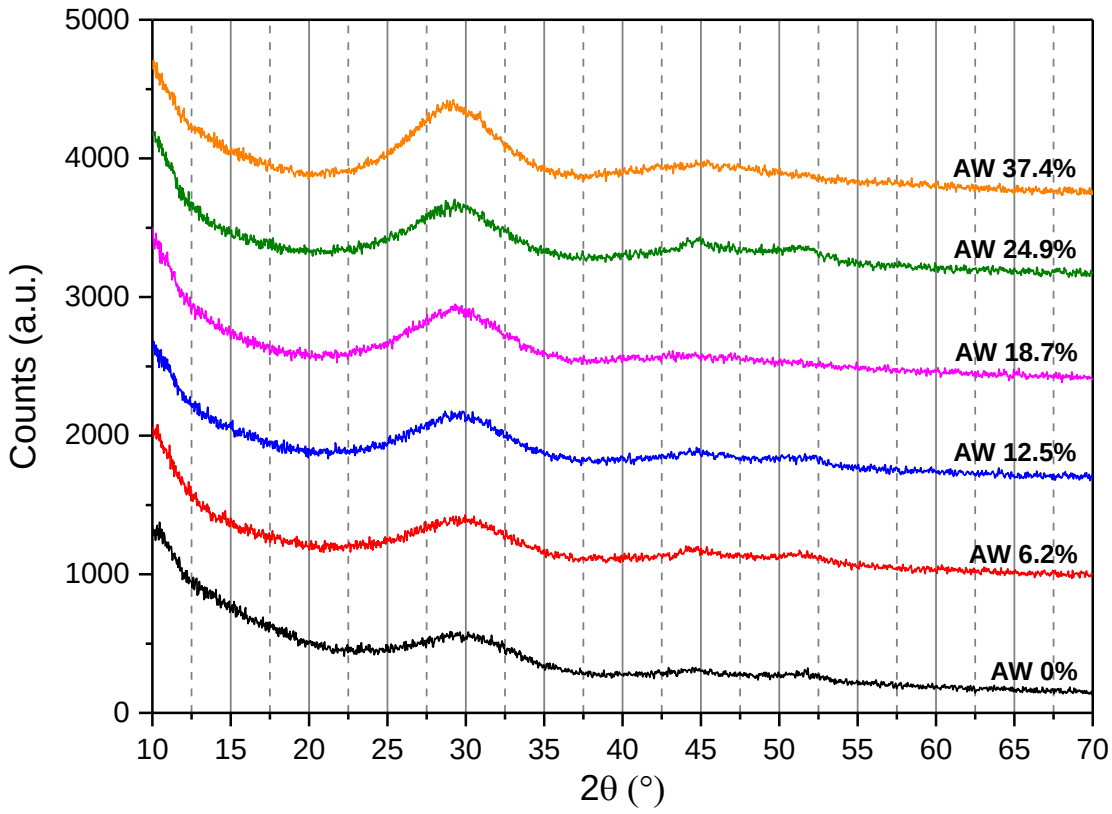

Figure 2.8: XRD traces of the six strontium AW parent glass compositions, ground and sieved <45 µm before sintering and controlled devitrification.

All samples presented only the amorphous hump expected for silica-based glasses and no peaks could be detected. This confirmed that the six starting materials were amorphous, thus the formation of crystals in the final scaffolds could be induced by subsequently applying an appropriate thermal treatment. The peak of the hump progressively moved towards lower angles with increasing strontium, from around 2θ = 30 ° for AW 0%, to around 2θ = 27 ° for AW 37.4%.

2.4 Discussion

This chapter investigated the six strontium apatite-wollastonite parent glasses, which will be used for producing the porous scaffolds described in Chapter 3, and showed that the substitution was feasible via a melt-quench route.

Similar substitutions were widely described in the literature for other bioactive glasses and glass-ceramics: Bioglass 45S5 has been modified via a melt-quench route by different authors so that up to 100 % of its calcium oxide was substituted with strontium oxide (177, 178), as well as other glasses belonging to the same SiO_2-CaO-Na_2O-P_2O_5 system (18, 63, 151); Lao et al. substituted up to 5 wt% of calcium oxide

with strontium oxide in sol-gel SiO_2-CaO-SrO and SiO_2-CaO-P_2O_5-SrO glasses (215); Kargozar et al. produced melt-quenched glasses in the system SiO_2-P_2O_5-CaO-SrO-Na_2O-MgO-K_2O-CoO by replacing 6 mol% of CaO with SrO (216); Yin et al. studied the effect of strontium substitution on foam-replicated scaffolds in the borate glass 13-93B2 (214). Strobel et al. obtained strontium-doped nanoparticles (5 wt%) by flame-spraying (217); Wu et al. produced strontium-containing mesoporous scaffolds with 5 and 10 mol% strontium oxide (191); strontium hydroxyapatite was studied in the form of microspheres (184), nanowires (218), powder (185) and single-crystal nanorods (219). In addition, the same substitution in apatite-wollastonite presented in this thesis was described by Vickers in previous work (186): compositions up to AW 24.9%, which corresponds to 50 mol% of calcium oxide being substituted with strontium oxide, were produced and fraction 45-90 μm was used to obtain microporous scaffolds from compacted powders. In this work, the <45 μm fraction was studied for the fabrication of foam-replicated macroporous scaffolds.

2.4.1 Strontium determines the density of AW glasses

As expected from the substitution of a heavier element (strontium) for a lighter element (calcium), not only the molecular weight of the glasses increased with increasing strontium, but also their density. As highlighted in Table 2.7, where the theoretical molecular weight ratio of the glasses is compared with the ratio of the measured densities (derived from Table 2.3), the density of the glass powders increased with the increase of strontium content. However, the increase in density was smaller than the increase in weight and this was due to the fact that strontium is 2.2 times heavier than calcium, but only 1.14 times bigger (144, 145). Hence, not only the molar weight of the strontium glasses is higher, but also the molar volume, which consequently slows down the increase in density. The effect of the enlarged glass network is also evident in the XRD results of the tested glasses (Figure 2.8) and it has been reported in the literature (220), as it will be further discussed in Section 2.4.4 and in Chapter 3.

Table 2.7: Comparison between the molecular weight ratio and the density ratio of the strontium glasses compared to the no-strontium control AW 0%.

	Mol. weight (g/mol)	Weight ratio	Density ratio
AW 0%	62.5645	1.0000	1.0000
AW 6.2%	65.5121	1.0471	1.0525
AW 12.5%	68.5073	1.0950	1.0869
AW 18.7%	71.4549	1.1421	1.1184
AW 24.9%	74.4025	1.1892	1.1418
AW 37.4%	80.3452	1.2842	1.2187

2.4.2 Final morphology and composition of the strontium AW glass powders

The glass particles produced by grinding and sieving the glass frit presented sharp edges and a broad range of dimensions, from 45 µm to less than 1 µm, as assessed with SEM imaging. Particle size distributions were found similar for all compositions, with two main peaks at about 250 nm and 25 µm. The smaller fraction around 250 nm is of particular interest for the foam replication method of scaffold production and their subsequent treatment. In fact, it has been shown that the particles size distribution can affect the final sintering process of ceramic materials, for which broader distributions tend to lead to higher bulk densities, reduce the shrinkage needed to reach the desired density and present a higher densification rate at the initial stages of sintering (221-223). This is due to the smaller particles filling the bigger pores left by larger particles; as a consequence, it provides better mechanical properties, for example in the case of 3D printed scaffolds (224).

The EDS analysis of the sieved powders confirmed that the substitution was effective and all six glasses reached the expected composition. About 1 at% of aluminium was detected in all samples; this could be explained by the use of alumina crucibles for the production of the glasses, causing an ionic exchange from container to molten glass at high temperatures. Although aluminium has been proven in the literature to be cytotoxic (225-228), the amount found in the samples is very low and similar materials have been successfully used in cell culture in previous work (186) and in the work presented in this thesis, as it will be presented in Chapter 5. In addition, Ohgushi et al. reported that an alumina-containing apatite-wollastonite glass ceramic better stimulated the osteogenic differentiation of rat bone-marrow derived stem cells compared to standard apatite wollastonite and hydroxyapatite-coated apatite-

wollastonite (229), thus confirming that the amount found in the samples prepared in the present work did not reach concerning levels.

2.4.3 Dependence of characteristic temperatures of AW glass powders on the strontium content

The DSC results showed that the thermal properties of the six produced glasses varied with their composition: with increasing strontium, the glass transition temperature and the formation of the first crystal phase moved slightly towards lower temperatures, while the formation of the second crystal phase moved more significantly towards higher temperatures, thus the two main peaks moved apart. The crystal phases formed in the strontium glasses were tested and results are presented and discussed in Chapter 3.

The effect on the glass transition temperature can be explained by the fact that the glass network expands in order to accommodate a bigger ion. This has been shown already by O'Donnell et al. (177), Fredholm et al. (230) and Yin et al. (214) when doping Bioglass, a Bioglass-derived glass and a borate-based glass with strontium, respectively, as well as by Vickers for apatite-wollastonite parent glasses (186). The same effect has also been described by Brink for bioglasses in the system Na_2O-K_2O-MgO-CaO-B_2O_3-P_2O_5-SiO_2 when doped with magnesium (231); as later explained by Watts et al. using magic angle spinning nuclear magnetic resonance (MAS NMR), although magnesium is a smaller ion than calcium, it partially behaves as an intermediate oxide instead of a network modifier, leading to the formation of Mg-O bonds that are weaker than Si-O bonds (66). This has also been observed by Linati et al. when adding zinc, which caused T_g to decrease for compositions containing up to 15 mol%, while higher percentages made T_g increase due to the polymerisation of the glass network with the increasing amount of interconnected Si-Zn-P tetrahedra (232). The other two thermal events evidenced by the DSC analysis are two exothermic peaks, which correspond to the nucleation and growth of two crystal phases. As described in the literature for composition AW 0%, the first peak corresponds to the formation of fluoro/oxyapatite and the second peak to wollastonite (85, 104, 186, 233, 234). In the present thesis, it was found that apatite precipitated at (887.2 ± 4.2) °C, while wollastonite precipitated at (944.3 ± 8.7) °C. This is close to what described in the literature: Kokubo et al., when they first described the material, found that apatite formed at 870 °C and wollastonite at 900 °C (85, 104) for particles <44 µm heated at 5 °C/min. Cannillo et al. found that particles <38 µm gave apatite at 887 °C and wollastonite at 927 °C for a heating rate of 10 °C/min (233). Likitvanichkul and

Lacourse described crystallisation peaks for apatite and wollastonite at 880 °C and 1008 °C, respectively, for glass particles in the range 1-2 mm and heated at 5 °C/min (234). Vickers observed that apatite precipitated at 892.7 °C and wollastonite at 955.2 °C, when particles were <45 μm and heated at 10 °C/min (186). While the formation temperature of apatite is comparable across the literature, differences in the formation temperature of wollastonite can be found. This is due to the different formation mechanism of the two crystal phases: in fact, while apatite follows a bulk nucleation mechanism, wollastonite has a surface nucleation mechanism that makes it strongly dependent on the particle size and the particle size distribution of the powders chosen for the analysis (186).

The effect of the substitution of strontium for calcium on the formation of the crystal phases can therefore be due to a combination of factors. First of all, as it will be shown in Chapter 3, the crystal phases that formed in each sample changed with the increase of strontium, eventually becoming strontium-apatite and strontium-wollastonite, which likely require different energies for initiating their transformation. Secondly, the expansion of the glass network could facilitate the migration of ions, so the energy barrier necessary for initiating the phase transformation was reduced; this in particular could be the case for apatite, for which calcium ions could have been more easily available, thus explaining the decrease of its peak temperature with the increase in strontium. Hill et al. suggested that the substitution of strontium for calcium in a SiO_2-Al_2O_3-P_2O_5-CaO-CaF_2 glass caused the apatite to turn from bulk nucleation to a surface nucleation mechanism (235). However, this was not observed by Vickers for the strontium apatite-wollastonite parent glasses up to composition AW 24.9%, where the peak temperature for apatite remained constant with varying particle size, within the same composition (186). Thirdly, it is possible that the facilitated formation of apatite depleted the remaining material of most of the calcium and strontium ions, so the wollastonite phase presented a higher energy barrier, i.e. required a higher temperature, to gather all the necessary atoms before the phase could precipitate.

The melting temperature of the glasses under study was the only characteristic with a clear non-linear behaviour: as shown in Figure 2.7, the melting temperature decreased with increasing strontium until composition AW 24.9%, but for composition AW 37.4% it was as high as for the starting AW 0%, so that the fitting curve became a second-order equation. This could mean that substituting 50 mol% of calcium with strontium, or an amount around 50%, might give a eutectic composition for the class of glasses under study. Since this is the first time that composition AW 37.4% is produced and studied, it is also the first time that this behaviour is observed and therefore further studies are required to confirm this hypothesis.

It is important to note that all compositions formed both crystal phases before the temperature of 1050 °C, which was the temperature chosen for treating all samples and producing the porous scaffolds described in Chapter 3.

2.4.4 Atomic organisation of the strontium AW glasses

The XRD analysis showed that all the produced powder samples were amorphous glasses, as their traces gave only the broad hump typical of silicate-based glasses. The amorphous hump moved towards lower angles with the increasing amount of strontium in the glass. This effect of strontium substitution in bioactive glasses has been observed in previous work (186) and in the literature (63, 236, 237) and it is due to strontium atoms expanding the glass network, thus increasing its d-spacing. In fact, according to Bragg's law (Equation 2.7), when the interatomic distance *d* increases the incident angle *θ* decreases, for a constant wavelength:

$$n\lambda = 2d * sin\theta$$

Equation 2.7: Bragg's law for x-ray diffraction.

Where *n* is an integer number and *λ* is the wavelength of the x-ray radiation used for the analysis: 0.154056 nm for Cu-K alpha radiation. This effect was also confirmed with other techniques by Hollings et al. (personal communication), who drew the same conclusion from the results of neutron diffraction and Raman spectroscopy analyses run on the same glasses.
These results therefore confirmed that the starting glasses were amorphous, which was essential for the purposes of the work presented in this thesis: in fact, only if the starting glasses were amorphous, their crystallisation could then be controlled by the thermal treatments applied when producing the scaffolds, as described in Chapter 3.

Chapter 3
Production and characterisation of strontium AW scaffolds

3.1 Introduction

When materials are developed to support bone repair, it is important to consider the form in which these materials are intended to be used, for instance granules, putty or solid and porous scaffolds. If the implant is to be used in load-bearing regions, then its structural and mechanical properties are key to the success of the implant integration in the native bone tissue for an effective repair of the defect. Different methods have been described in the literature for the fabrication of 3D porous scaffolds, from the use of organic porogens (238-241) to freeze-casting (242, 243), sol-gel foaming (244-247) or 3D printing (119, 248-250). For the strontium-doped AW porous scaffolds produced in the present thesis, the foam (or sponge) replication method was chosen, which was first applied to hydroxyapatite in 2001 by Tian and Tian (79) and then developed for bioactive glasses in 2006 by Chen et al. (80) and Park et al. (81).
Chapter 2 presented the production and characterisation of the strontium-containing glass powders used for the scaffold production. The present chapter will first describe the steps of the sponge replication method followed for the production of the strontium AW scaffolds. Then the glass-ceramic samples, in the form of solid discs and porous scaffolds, will be characterised in terms of volumetric shrinkage upon treatment, crystal phases, morphology, mechanical properties, apatite-forming ability and radiopacity.
The aim of this chapter was therefore to assess the effects of substituting strontium for calcium in apatite-wollastonite when 3D porous construct, intended as bone substitutes for large bone defects, are produced by the foam replication method.

3.2 Materials and methods

3.2.1 Glass-ceramic scaffold production

Porous scaffolds were produced following the sponge/foam replication method (80, 81).
A slurry was prepared using ultrapure water, high molecular weight poly-vinyl alcohol (PVA, Mowiol® 56-98, Mw ~195000, Aldrich) and the <45 µm glass powder produced as described in Chapter 2. The composition of the slurry used in this work was based

on the results of Serna, who optimised it for the AW 0% glass as 55:3:42 wt% water:PVA:glass powder (121). As shown in Chapter 2, the different strontium glasses had different densities. To take this into account when preparing the slurry, the water:PVA:volume of glass (instead of mass) ratio was kept constant. Table 3.1 shows the resulting slurry compositions for the six glasses under study.

Table 3.1: Composition of the slurry for the fabrication of foam-replicated scaffolds, depending on the glass used and starting from 10 mL of ultrapure water.

	Water (mL)	PVA (g)	Glass powder (g)
AW 0%	10.0	0.53	7.88
AW 6.2%	10.0	0.53	8.30
AW 12.5%	10.0	0.53	8.57
AW 18.7%	10.0	0.53	8.82
AW 24.9%	10.0	0.53	9.00
AW 37.4%	10.0	0.53	9.61

To prepare the slurry, the first step was to dissolve the PVA in ultrapure water. As all the glasses required the same water-to-PVA ratio, stocks of 500 mL of water (26.70 g of PVA) were prepared and the required amount was weighed out at the time of making the samples. For dissolving the PVA, first the required amount of ultrapure water was heated up to 92°C in a water bath on a stirring hot plate. Then the PVA flakes were added to the water and kept stirring until the polymer was completely dissolved.

Once the polymer solution was cooled down to room temperature, the required amount was weighed in a beaker and the corresponding amount of glass powder was added. The mixture was then vigorously stirred for 1 h so that a stable suspension, the slurry, was obtained.

Polyurethane foams with porosity of 90 pores-per-inch (PPI) were used. The shape and dimensions of the foams, manually cut, differed depending on the application and will be specified case by case in this thesis. Each foam was soaked and squeezed in the slurry for 1 minute, in order to ensure the complete coating of the porous structure and, at the same time, avoid the occlusion of pores. All coated foams were then let dry overnight on a bench, periodically turning them for the first hour to remove the excess slurry and maintain the slurry evenly distributed. For making solid discs, the same slurry was used, but poured on greased 96 well-plates lids using a micropipette, 83 µL of slurry per sample, and then dried overnight.

All samples were finally treated in a furnace at 1050°C for 2 hours, heating rate 10°C/min (186), in order to burn all the polymers (PVA and foams), sinter the glass particles and induce the nucleation and growth of the crystal phases. The final samples were thus obtained, the porous ones being a replica of the polyurethane template.

3.2.2 Glass-ceramic sample characterisation

3.2.2.1 Shrinkage of 3D porous scaffolds

The sintering of glass particles and densification of the material during thermal treatment caused the samples to shrink, so their dimensions decreased after the treatment and the final samples were smaller replicas of the original template.
In order to measure this shrinkage, dimensions were taken of specimens produced with cubic foams, 5.0 mm side. The three dimensions were measured using a digital calliper and volumes calculated. Measurements were performed before the thermal treatment, on air-dried coated foams, and after it. The shrinkage was calculated as a percentage of the initial volume, according to Equation 3.1:

$$S_{\%} = \frac{\left(Vol_i - Vol_f\right)}{Vol_i} * 100$$

Equation 3.1: Volume shrinkage of porous scaffolds.

where $S_{\%}$ is the percentage of volume shrinkage, while Vol_i and Vol_f are the initial and the final volume, respectively. 30 samples per composition were tested and the average and standard deviation of their shrinkage were calculated.

3.2.2.2 Density of strontium AW glass-ceramics

Fragments of the porous scaffolds tested for compression (Section 3.2.2.6.1) were ground for 2 min using a Gyro-mill percussion mill, Glen Creston Ltd, and the powders obtained were used to measure the density of the final glass-ceramic materials. About 4.5 g of glass-ceramic powder were poured in the measuring vessel, previously tared, and a Thermo Scientific Pycnomatic ATC helium pycnometer was used to measure the density. After 3 cleansing cycles, the machine automatically performed up to 20 measurements until the standard deviation of 3 measurements was 0.400 % of their average density. The result of the measurements was provided as the average density and the standard deviation of the sample.

3.2.2.3 X-ray diffraction for crystal phase identification

In order to detect the crystal phases nucleated in the samples, porous scaffolds were ground using the Gyro-mill percussion mill (Glen Creston Ltd) using a small puck for 15 min. These were tested using a Bruker D8 Advance diffractometer, set on the same parameters used for the glass powders (Section 2.2.2.5), i.e. from 10 ° to 70 ° 2θ, step size 0.033 °, time/step 0.6 s and run at 40 kV and 40 mA.
The collected data were analysed using the software X'Pert Highscore Plus and crystal phases checked against the last updated International Centre for Diffraction Data (ICDD) database.

3.2.2.4 Scanning Electron Microscopy and Electron Dispersive x-ray Spectroscopy for assessing scaffold morphology and composition

Solid discs and porous scaffolds were observed under a Hitachi S-3400N SEM for a qualitative assessment of their morphology, after sputtering them with gold. In order to improve sample conductivity, solid discs were fitted to aluminium stubs using a silver paint (Agar Scientific), while the top and bottom surfaces of porous scaffolds (derived from 5.0 mm-side foams) were manually polished before fitting them to stubs with conductive carbon tape.
The composition of samples was verified using EDS quantitative analysis, performed using a Bruker XFlash detector and Quantax Esprit 1.9.4 analysis software.

3.2.2.5 Micro Computed Tomography for assessing the 3D scaffold architecture

For each composition, four scaffolds, derived from 5 mm side cubic foams, were tested using the micro computed tomography (CT) system Bruker Skyscan 1172 scanner. A 0.5 mm aluminium filter was used, 9 µm resolution was set, which gave a pixel size of 8.88 µm, and scans were performed at 100 kV and 100 µA. Before each scan, the flat field was recorded and then applied. The four samples were scanned together setting an automated oversize scan, averaging was set to 3, rotation step to 0.6 ° and random movement to 1 to reduce the ring artifact. Reconstruction of slices was performed using the Bruker NRecon software: after previewing a slice, the greyscale histogram was set between 0 and 10 % above the value of the last bar, then the beam hardening artifact was reduced using the fine tuning function.

3D rendered pictures of the scanned samples were created using the software CTvox, after adapting the opacity and luminance of the object basing on its intensity histogram.

3.2.2.5.1 Scaffold porosity evaluation

Micro CT images of the strontium AW scaffolds, collected as described in Section 3.2.2.5, were analysed for porosity using the Bruker CT-Analyser (CTAn) software. For the analysis of the open and closed porosity of samples, at first a cylindrical volume of interest (VOI) was created by selecting its top and bottom slice and then applying a circular region of interest (ROI) to all the slices in the selected stack. The images of the VOI were binarised by selecting the threshold automatically calculated by CTAn on the base of the entire dataset. Then an automated task list was set up, as shown in Figure 3.1, by using CTAn plugin functions so that the general, open and closed porosity of each sample could be calculated, along with their pore size distributions. Porosity $P_{\%}$ was defined, according to Equation 3.2, as the portion of the total volume of sample V_{Tot} that was due to voids, V_p:

$$P_{\%} = \frac{V_p}{V_{Tot}} * 100$$

Equation 3.2: Definition of porosity for a scaffold.

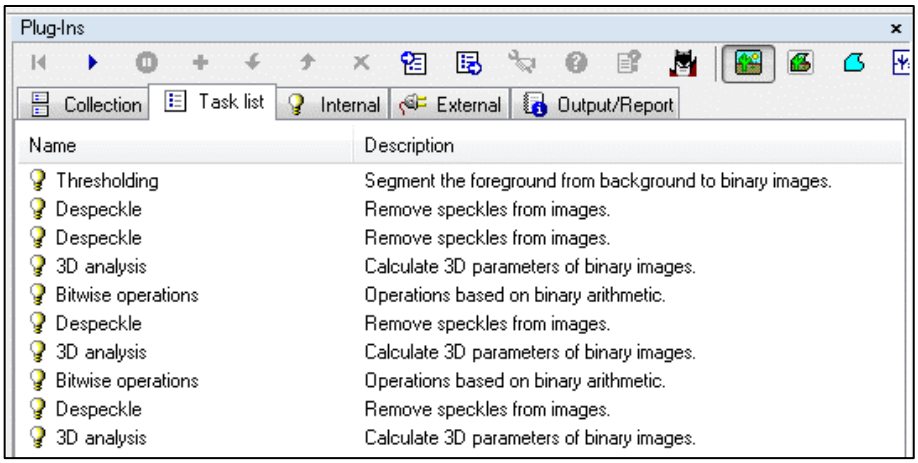

Figure 3.1: Task list used for the calculation of sample porosity in CTAn.

In the task list, first the chosen threshold was applied to all slices. Then, Despeckle was performed twice: the first time to remove the black noise (volumes of less than 10 voxels) and making it white, the second time to remove the white noise by sweeping

every white voxel except the largest object (the scaffold). This was followed by the 3D analysis of the object for calculating the general porosity.
The following Bitwise operation saved the stack before performing a further Despeckle that deleted all the closed pores in the VOI, so that the next 3D analysis calculated the open porosity.
Finally, with the last Bitwise operation, the saved VOI was loaded back, the open pores were removed with the Despeckle function and the closed porosity calculated with the last 3D analysis. All the results were automatically recorded in the same Excel file.
Results for the open porosity were summarised as average ± standard deviation and tested with ANOVA using OriginPro 2015.
Pore size distributions were also plotted, represented as volume percentage against pore range.

3.2.2.5.2 Comparison with experimental porosity

Porosity could also be calculated from the volume and mass of samples after thermal treatment. In fact, using data collected from the samples tested for shrinkage (Section 3.2.2.1), knowing the final density of the glass-ceramic materials (Section 3.3.2) and starting from the definition of porosity represented in Equation 3.2, the porosity $P_{\%}$ of scaffolds could be calculated as shown in Equation 3.3:

$$P\% = \left(1 - \frac{Vol_{mat}}{Vol_{Tot}}\right) * 100 = \left(1 - \frac{m_{mat}}{d * Vol_{Tot}}\right) * 100$$

Equation 3.3: Formula for calculating the porosity of scaffolds from their experimental mass, volume and density.

where Vol_{mat} is the volume of the actual material that makes the scaffold, Vol_{Tot} is the total volume of the scaffold (in cm^3), m_{mat} is the experimental mass of the sample (in g) and d is the measured density of the material (in g/cm^3).

3.2.2.6 Mechanical testing of porous scaffolds

Cylindrical porous scaffolds were prepared using 90 PPI foams, diameter 20 mm and height 15 mm, and tested for compressive strength (Section 3.2.2.6.1) and biaxial flexural strength (Section 3.2.2.6.2).

3.2.2.6.1 Measurement of scaffold compressive strength

Eight samples for each composition were tested for compression using an Instron 3365 universal testing machine, fitted with a 5 kN load cell and controlled via the Instron Bluehill 3 software. Height and diameter of each sample were manually added to the software, then the load was applied at 1.0 mm/min and recorded, along with the displacement of the loading head.
After the measurement, the compressive strength was calculated from the maximum load reached according to Equation 3.4:

$$\sigma_c = \frac{L_{max}}{A} = \frac{L_{max}}{\pi\left(d/2\right)^2}$$

Equation 3.4: Compressive stress of cylindrical porous scaffolds.

where L_{max} is the maximum load recorded for the sample, A is its resisting area and d its mid-height diameter. The Young's elastic modulus, E, was derived as the slope of the linear region of the stress-strain curve, using the *Linest* function in Microsoft Excel. For each set of eight samples, average and standard deviation were calculated and results compared using the ANOVA test in OriginPro 2015, upon checking for the normality of distributions of values.

Fracture surfaces were observed by performing SEM imaging on fragments of tested samples, attaching them to aluminium stubs using carbon tape and silver paint and sputtering them with gold to increase their conductivity.

3.2.2.6.2 Measurement of scaffold biaxial flexural strength

The biaxial flexural strength of porous scaffolds was tested on thin circular slices obtained from cylindrical samples like those described above in Section 3.2.2.6.1. Samples were cut using a Struer Accutom-5 cutting machine, fitted with a 350 µm diamond-coated blade fed at 0.1 mm/min; the obtained slices were 1.5 mm thick. Each slice was measured prior to testing using a digital calliper. The Instron 3365 universal testing machine, fitted with a 500 N load cell, was used to perform the piston-on-three-ball test described in the standard BS EN ISO 6872 (251). The apparatus consisted of three stainless steel balls, diameter (4.5 ± 2) mm, positioned at 120 ° on a support circle of (11 ± 1) mm diameter. As shown in Figure 3.2, during the test samples were positioned concentrically to the circle, then a flat punching pin, diameter (1.4 ± 0.2) mm, was lowered in the middle of the sample at 1.0 mm/min and the load recorded until failure. For each composition of scaffold, 15 slices were tested.

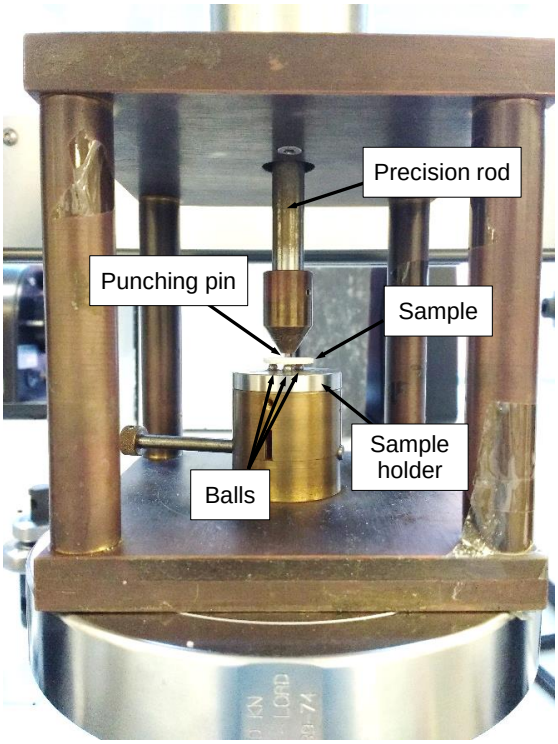

Figure 3.2: Apparatus used for the biaxial flexural strength test of slices of porous scaffolds.

The biaxial flexural strength was calculated according to the standard BS EN ISO 6872, following Equation 3.5 (251).

$$\sigma = -0.2387P\frac{(X-Y)}{b^2}$$

Equation 3.5: Formula for calculating the biaxial flexural strength (251).

where σ is the biaxial flexural strength of the sample, in MPa, P is the maximum load at fracture, b is the specimen thickness and X and Y are described by Equation 3.6 and Equation 3.7, respectively:

$$X = (1+\nu)ln\left(\frac{r_2}{r_3}\right)^2 + \frac{(1-\nu)}{2}\left(\frac{r_2}{r_3}\right)^2$$

Equation 3.6: Formula for the calculation of *X* in Equation 3.5 (251).

$$Y = (1+\nu)\left[1 + ln\left(\frac{r_1}{r_3}\right)^2\right] + (1-\nu)\left(\frac{r_1}{r_3}\right)^2$$

Equation 3.7: Formula for the calculation of *Y* in Equation 3.5 (251).

where v is the Poisson's ratio of the material, estimated as 0.25, r_1 is the radius of the support circle, r_2 is the radius of the loaded area (i.e. the radius of the punching pin) and r_3 is the radius of the specimen.
Results were reported as average ± standard deviation and tested for ANOVA using OriginPro 2015.

As 15 samples for each composition were tested, the Weibull statistics could also be calculated, according to the standard BS EN ISO 6872 (251). The Weibull distribution is a two-parameter statistical distribution frequently used to describe the dispersion in fracture strength of brittle materials; it links the cumulative probability of failure P_f to the tensile stress σ as described in Equation 3.8 (251-253).

$$P_f = 1 - exp\left[-\left(\frac{\sigma}{\sigma_0}\right)^m\right]$$

Equation 3.8: Weibull distribution (251-253).

where m and σ_0 are the two Weibull parameters: the Weibull modulus and the Weibull characteristic strength, respectively. The Weibull modulus m is a shape parameter and describes how steep the function is, thus how dispersed the fracture stresses are, while the Weibull characteristic σ_0 determines the location of the distribution; σ_0 is related to the mean fracture stress and represents the strength that has 63.2 % probability of causing failure (251, 252).
In order to calculate the Weibull parameters for the biaxial flexural strength of the six compositions of scaffolds, first the flexural strengths that were calculated according to Equation 3.5 were ranked in ascending order and their probability of failure P_f assigned as per Equation 3.9:

$$P_f = \frac{i - 0.5}{N}$$

Equation 3.9: Probability of failure of the i^{th} sample.

where i is the rank of the specimen and N the total number of tested specimens in the batch. Variables P_f and σ were then transformed in lnln[1/(1-P_f)] and lnσ and plotted as the y and x axis, respectively. The linear regression parameters were calculated using the function *Linest* in Excel: if the linear fit was represented as y = mx + constant, the Weibull modulus corresponded to the slope m of the fitting line, while the Weibull characteristic strength σ_0 was obtained by setting y = 0 and calculating the natural exponential of the so-derived x_0, $\sigma_0 = e^{x_0}$, which corresponded to P_f = 63.2 %.

SEM micrographs of fracture surfaces were obtained by attaching the slices to aluminium stubs using carbon tape and silver paint so that the fractured side was exposed, then samples were sputtered with gold to increase their conductivity.

3.2.2.7 Apatite-forming ability of strontium AW glass-ceramic samples

An important requirement for a biomaterial for bone regeneration is its ability to induce the formation, when in contact with body fluids, of hydroxyapatite (HAp), a crystal phase very close to the natural mineral phase found in bone tissue (see Chapter 1). In this thesis, both solid discs and porous scaffolds were used to test the bioactivity of the six materials under study. Following the ISO standard 23317 (254), specimens were immersed in simulated body fluid (SBF) solution: this is a solution, as described by Kokubo and Takadama (255), that simulates the inorganic composition of human blood plasma. Table 3.2 compares the ion composition of SBF with human plasma.

Table 3.2: Comparison of the ion concentration in SBF and in human blood plasma (255).

	Concentration (mM)	
Ion	**SBF (pH 7.40)**	**Blood plasma (pH 7.2 to 7.4)**
Na^+	142.0	142.0
K^+	5.0	5.0
Mg^{2+}	1.5	1.5
Ca^{2+}	2.5	2.5
Cl^-	147.8	103.0
HCO_3^-	4.2	27.0
HPO_4^{2-}	1.0	1.0
SO_4^{2-}	0.5	0.5

SBF was prepared following the above mentioned standard (254). First, 700 mL of ultrapure water were heated in a water bath and temperature was brought to (36.5 ± 1.5) °C. Then the reagents listed in Table 3.3 were added. The first eight reagents were dissolved one by one, and granule by granule if necessary, ensuring that temperature was always in the range (36.5 ± 1.5) °C, rinsing every weighing container with ultrapure water and adding the washings to the solution. A pH meter was then inserted and the pH checked, which was expected to be in the range of 2.0 ± 1.0; then the volume of water was brought to 900 mL and its temperature kept at (36.5 ± 1.5) °C. While measuring the pH and keeping the temperature of the solution always at

(36.5 ± 0.5) °C, TRIS was slowly added until the pH raised to 7.45 ± 0.01. At this point, HCl 1 M was added dropwise until the pH decreased to 7.42 ± 0.01 and this process was repeated until all the TRIS was completely dissolved. The pH was finally adjusted to 7.40 at exactly 36.5°C, the pH probe was removed, rinsed with ultrapure water and the washing added to the solution. Once at room temperature, the final volume of SBF was brought to 1 L and the solution stored at 4 °C until use for up to 30 days.

Table 3.3: Reagents used for preparing SBF.

Reagent	Formula	Amount
Sodium chloride	NaCl	8.035 g
Sodium hydrogen carbonate	$NaHCO_3$	0.355 g
Potassium chloride	KCl	0.225 g
Di-potassium hydrogen phosphate trihydrate	$K_2HPO_4 \cdot 3H_2O$	0.231 g
Magnesium chloride	$MgCl_2$	0.143 g
Hydrochloric acid, 1 M	HCl	39 mL
Calcium chloride	$CaCl_2$	0.292 g
Sodium sulphate	$NaSO_4$	0.072 g
Tris-hydroxymethyl aminomethane	TRIS	6.118 g
Hydrochloric acid, 1 M	HCl	0 to 5 mL

The minimum required volume of SBF per each sample was calculated according to Kokubo and Takadama (255), with Equation 3.10:

$$v_s = S_a/10$$

Equation 3.10: Volume of SBF required for testing one sample.

where v_s is the volume of SBF (mL) and S_a is the apparent surface of the sample (mm^2).

When testing the thin solid discs, the required volume of SBF was calculated from their average diameter of 6.4 mm: considering their exposed surface as twice their area, the minimum required volume was found to be 6.4 mL. However, as samples had some residual porosity and their surface presented some degree of roughness (see SEM results in Section 3.3.4), the volume of SBF used was 10 mL per sample. Specimens, marked on their top surface, were placed at the bottom of 15 mL Falcon tubes (Corning) as shown in Figure 3.3a, SBF was added and then all the tubes were placed in an oven kept at 37 °C. Samples were collected after 1 day, 3 days, 7 days and 14

days, in triplicate. At the time of collection, the final pH of the solution was recorded, 1 mL was taken for ion release testing and the sample was carefully extracted, rinsed with ultrapure water and placed in a desiccator for drying.

When the porous scaffolds were tested, samples were put in 50 mL Falcon vials as shown in Figure 3.3b and 30 mL of 37 °C SBF added, according to literature (256-258). Vials were kept in a 37 °C oven for 1 day, 7 days and 14 days. At collection, the pH of the solution was measured and samples were extracted, rinsed with ultrapure and left drying in a desiccator until analysed.

Once dried, as shown in Figure 3.3 and described in the standard ISO 23317 (254), the bottom side of solid discs was analysed with SEM and EDS (see details of the machine in Section 3.2.2.4), fixed to the stubs using conductive silver paint and sputtered with gold. The ion release of samples was tested at the School of Geography (University of Leeds) using a Thermo Scientific iCAP7600 Inductively Coupled Plasma – Optical Emission Spectrophotometer (ICP-OES) equipped with a 240-position Cetac auto-sampler, which is a simultaneous analyser with the capability to view in axial or radial mode. The 1 mL of sample that was collected at each time-point was diluted in 9 mL of ultrapure water and then frozen until the day of the analysis. All samples were tested for Si, Mg, P, Ca and Sr and standards were run with the samples for calibration. The wavelength, revolutions per minute (rpm) and mode used for the final calculations were chosen basing on the best calibration.

Porous scaffolds extracted from SBF and dried were fitted, prior to testing, to SEM stubs using carbon tape and sputtered with gold. As the apatite found was only inside their pores and not on their surface (see results in Section 3.3.7.2), EDS analysis was not feasible and therefore only SEM imaging was performed on one of their lateral sides, as required by the ISO standard 23317 (254) and depicted in Figure 3.3b.

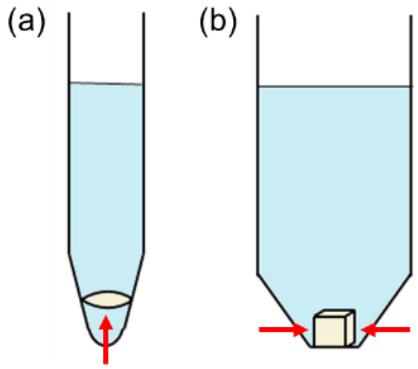

Figure 3.3: Sample configuration for SBF testing, as specified in the ISO standard 23317 (254); (a) solid disc, in a 15 mL Falcon tube and (b) porous scaffold, in a 50 mL Falcon tube. Red arrows indicate the surfaces investigated for apatite deposition.

3.2.2.8 Radiopacity assessment through x-ray imaging of porous scaffolds

As strontium is known to be a radiopaque agent for glasses and cements (259), porous samples produced using the six strontium compositions studied in this work were pictured using x-rays and the obtained radiographs analysed for radio-density. X-ray pictures were taken using the dental radiography system Carestream CS 2200, coupled with CS 7600 film reader for the digitalisation of images. The machine was operated at 70 kV, 7 mA, large-adult and molar tooth mode. Two sets of samples were tested, in triplicate: pieces of circular slices previously tested for biaxial flexural strength (Section 3.2.2.6.2), all 1.5 mm thick, and small cubic scaffolds obtained from 5 mm-side foams. Pictures were automatically saved as DICOM and were then converted to TIFF using the software ImageJ.

ImageJ was also used to calculate the average optical density of samples: polygonal and square regions of interest (ROI) were drawn for the slices and the cubic samples, respectively, as shown in Figure 3.4. Exactly the same ROI shape was used for all the samples in each picture and radiopacity was measured using the function “Measure”, which provides the average intensity of the selected area, where 0 = black and 255 = white. Three pictures per set were tested and the average and standard deviation were calculated for each composition of sample.

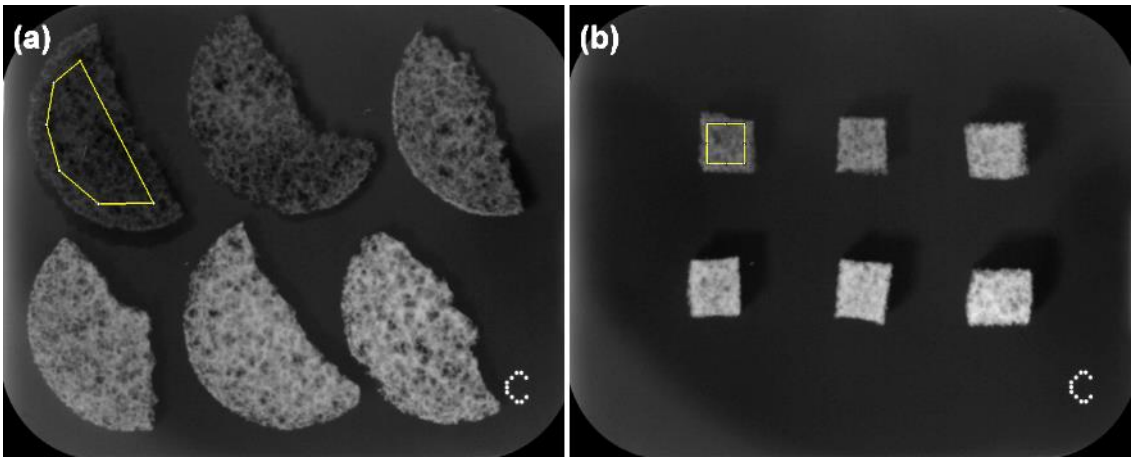

Figure 3.4: Example of regions of interest (ROIs) selected for (a) the scaffold slices and (b) the cubic scaffolds.

3.3 Results

3.3.1 Effect of strontium addition to AW on scaffold shrinkage

The shrinkage of samples upon thermal treatment was measured for cubic samples and results, averaged from 30 samples for each composition, are reported in Table 3.4.

Table 3.4: Average and standard deviation of volume shrinkage of porous scaffolds.

	Shrinkage (%)	Standard deviation (%)
AW 0%	58.2	2.7
AW 6.2%	56.8	2.8
AW 12.5%	54.5	3.0
AW 18.7%	53.4	3.0
AW 24.9%	50.5	2.6
AW 37.4%	48.5	2.5

As better shown in Figure 3.5, shrinkage of cubic porous scaffolds decreased with increasing strontium, with a difference of about 10 % between sample AW 0% and sample AW 37.4%.

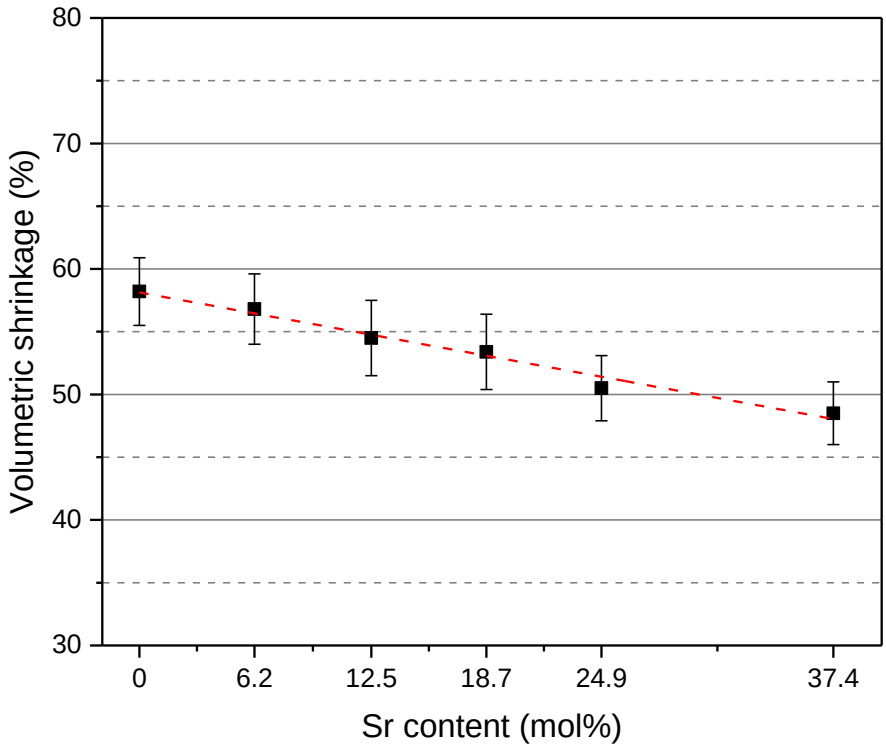

Figure 3.5: Volumetric shrinkage of cubic porous scaffolds, with trendline dashed in red, y = -0.27x + 58.13, R^2 = 0.98. Error bars indicate the standard deviation (n=30).

Using OriginPro 2015, data could be fit to a line with slope -0.27, R^2 0.98. This meant that the addition of strontium reduced the degree of sintering of glass particles, or that the different compositions followed different sintering mechanisms, or that the crystal phases forming in strontium-containing samples had a bigger volume, or a combination of these effects.

3.3.2 Effect of strontium addition to AW scaffolds on material density

Glass-ceramic samples were ground and tested for density using a helium pycnometer (Thermo Scientific Pycnomatic ATC). Results of the measurements are presented in Table 3.5, along with the standard deviations calculated by the machine, and summarised in Figure 3.6.

Table 3.5: Density of ground glass-ceramic scaffolds.

	Density (g/cm^3)	Standard deviation (g/cm^3)
AW 0%	3.00157	0.00405
AW 6.2%	3.10460	0.00235
AW 12.5%	3.23409	0.00439
AW 18.7%	3.29850	0.00211
AW 24.9%	3.32916	0.00099
AW 37.4%	3.47934	0.00129

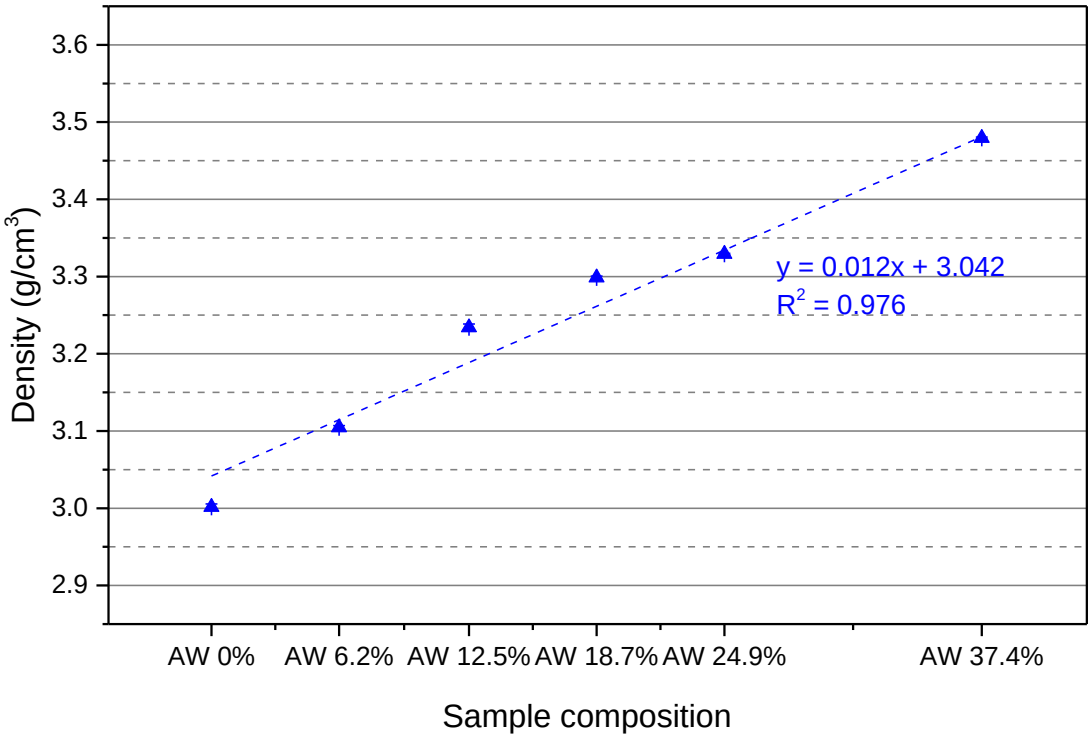

Figure 3.6: Density of the six strontium-containing AW porous scaffolds, with fitting trendline. Error bars indicate the standard deviations, as calculated by the Thermo Scientific Pycnomatic ATC helium pycnometer.

As expected, the density of the glass-ceramic materials that constituted the porous scaffolds increased with the increasing amount of strontium, as strontium is a heavier ion than calcium. In particular, the increase was found to be linear, with a slope of 0.012 and R^2 of 0.976 for the fitting line. The same trend was already observed with the parent glasses, as shown in Chapter 2, and results were similar for each composition. Therefore, despite the rearrangement of ions during crystallisation, the overall density of the material did not change significantly with the thermal treatment.

3.3.3 Identification of crystal phases formed in strontium-containing AW porous scaffolds

XRD traces of ground porous scaffolds are compared in Figure 3.7, with their peaks assigned to ICDD crystal phases. Each trace is then shown individually in Figure 3.8 to Figure 3.13, where the stick patterns of the selected phases are also displayed.

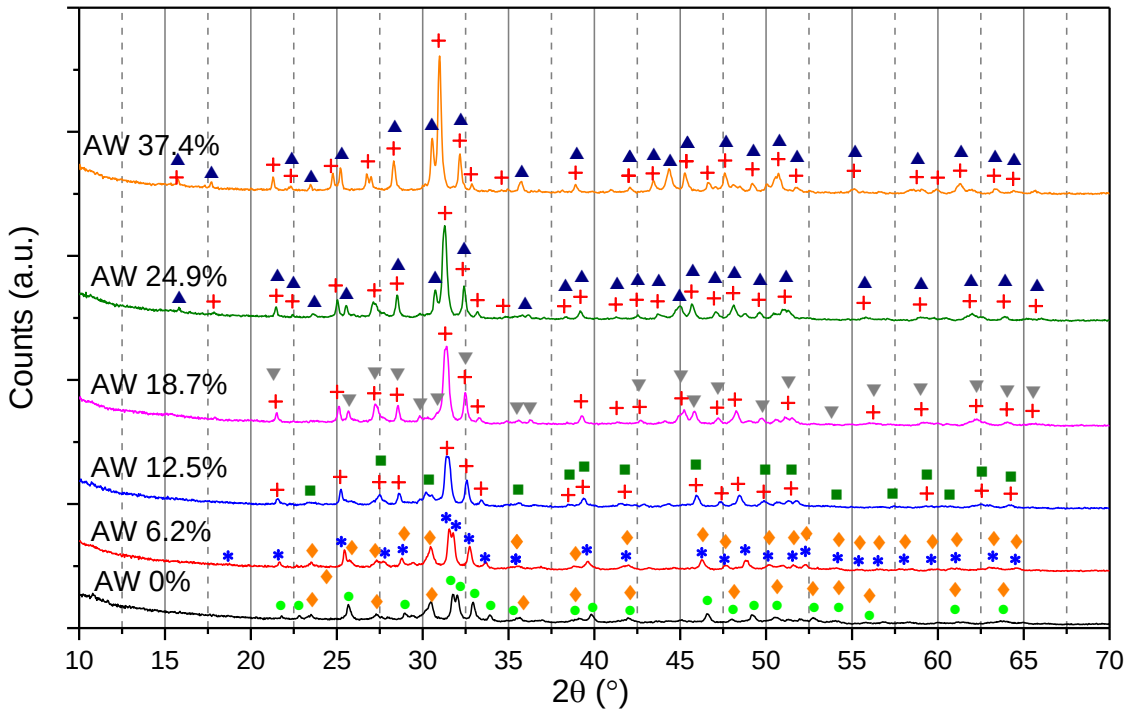

Figure 3.7: XRD traces of ground porous scaffolds, with peaks assigned to matching ICDD crystal phases. ● 00-064-0738 Hydroxyapatite, ♦ 00-066-0271 Wollastonite 2M, * 01-089-5632 Strontium hydroxyapatite $(Ca_{7.7}Sr_{2.3})(PO_4)_6(OH)_2$, + 01-089-5633 Strontium hydroxyapatite $(Ca_{3.6}Sr_{6.4})(PO_4)_6(OH)_2$, ■ 04-011-6810 Calcium magnesium silicate $CaMgSi_2O_6$, ▼ 04-012-1764 Pseudowollastonite, ▲ 01-083-5061 Calcium magnesium strontium silicate $(CaSr)Mg(Si_2O_7)$.

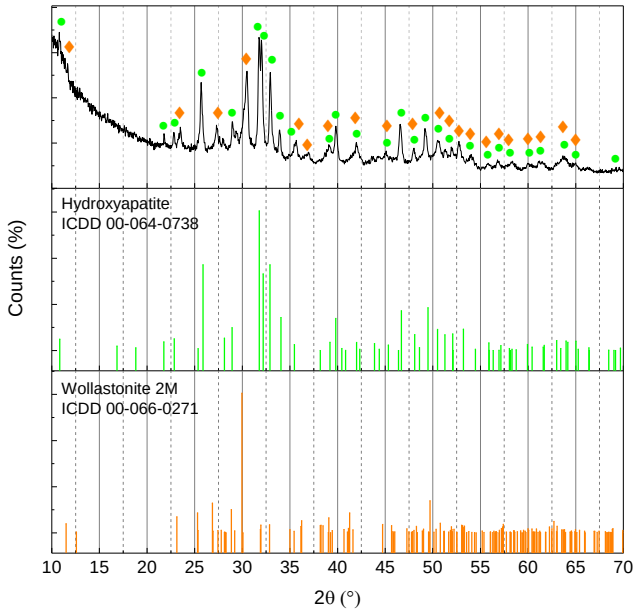

Figure 3.8: Detail of the XRD trace derived from ground AW 0% porous scaffolds shown in Figure 3.7, with corresponding peak assignment: ● 00-064-0738 Hydroxyapatite, ♦ 00-066-0271 Wollastonite 2M (upper panel). Stick patterns of the selected crystal phases as provided by the ICDD database (middle and lower panel).

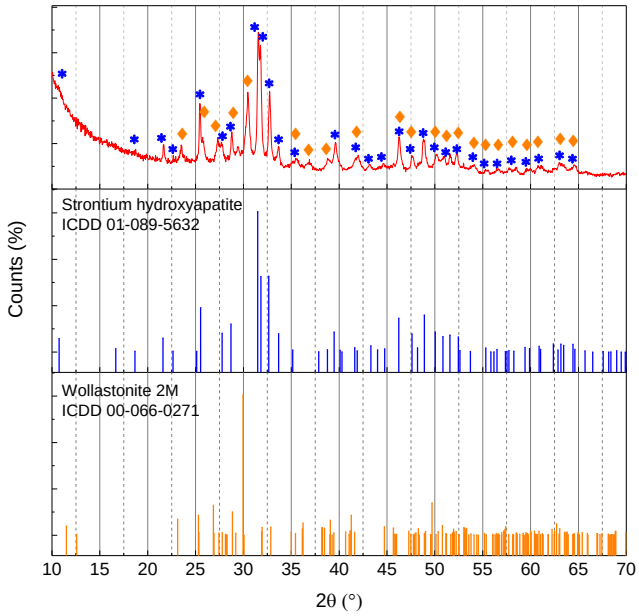

Figure 3.9: Detail of the XRD trace derived from ground AW 6.2% porous scaffolds shown in Figure 3.7, with corresponding peak assignment: * 01-089-5632 Strontium hydroxyapatite $(Ca_{7.7}Sr_{2.3})(PO_4)_6(OH)_2$, ♦ 00-066-0271 Wollastonite 2M (upper panel). Stick patterns of the selected crystal phases as provided by the ICDD database (middle and lower panel).

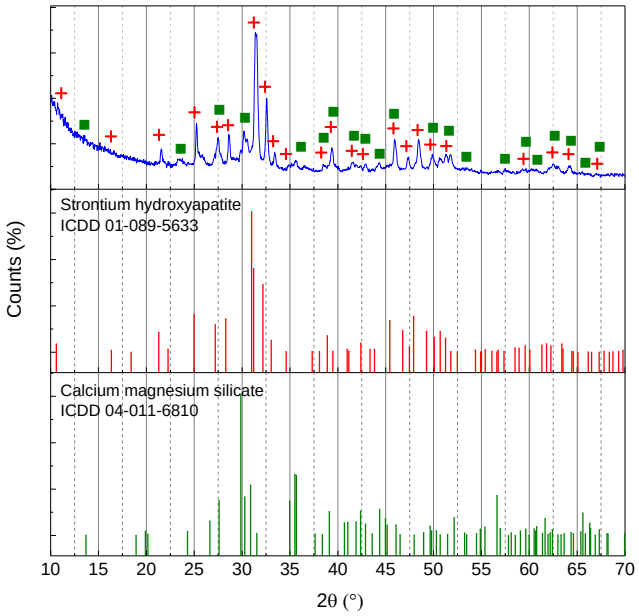

Figure 3.10: Detail of the XRD trace derived from ground AW 12.5% porous scaffolds shown in Figure 3.7, with corresponding peak assignment: + 01-089-5633 Strontium hydroxyapatite $(Ca_{3.6}Sr_{6.4})(PO_4)_6(OH)_2$, ■ 04-011-6810 Calcium magnesium silicate $CaMgSi_2O_6$ (upper panel). Stick patterns of the selected crystal phases as provided by the ICDD database (middle and lower panel).

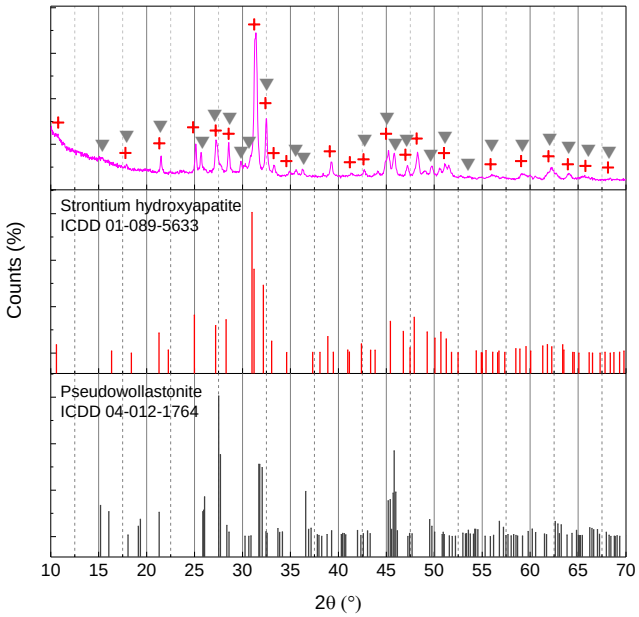

Figure 3.11: Detail of the XRD trace derived from ground AW 18.7% porous scaffolds shown in Figure 3.7, with corresponding peak assignment: + 01-089-5633 Strontium hydroxyapatite $(Ca_{3.6}Sr_{6.4})(PO_4)_6(OH)_2$, ▼ 04-012-1764 Pseudowollastonite (upper panel). Stick patterns of the selected crystal phases as provided by the ICDD database (middle and lower panel).

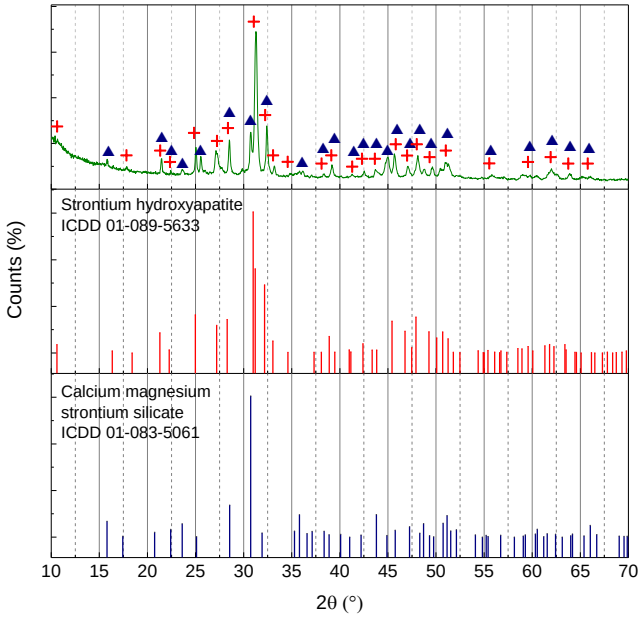

Figure 3.12: Detail of the XRD trace derived from ground AW 24.9% porous scaffolds shown in Figure 3.7, with corresponding peak assignment: ▲ 01-083-5061 Calcium magnesium strontium silicate (CaSr)Mg(Si_2O_7) (upper panel). Stick patterns of the selected crystal phases as provided by the ICDD database (middle and lower panel).

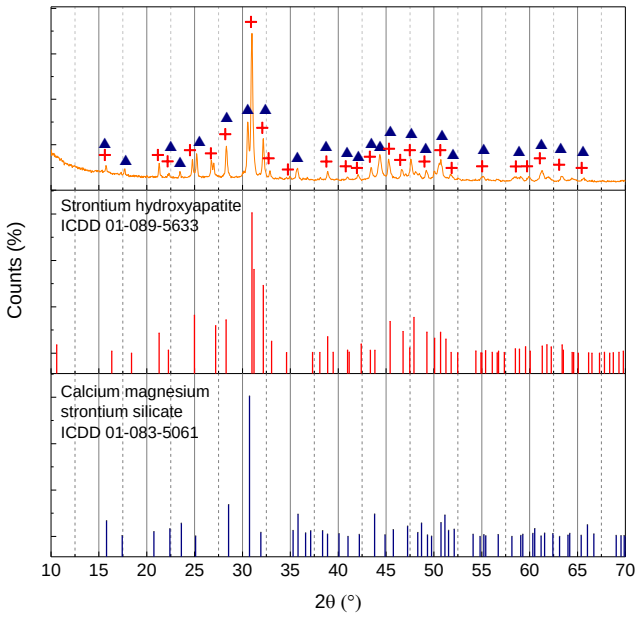

Figure 3.13: Detail of the XRD trace derived from ground AW 37.4% porous scaffolds shown in Figure 3.7, with corresponding peak assignment: ▲ 01-083-5061 Calcium magnesium strontium silicate (CaSr)Mg(Si_2O_7) (upper panel). Stick patterns of the selected crystal phases as provided by the ICDD database (middle and lower panel).

From the comparison between compositions summarised in Figure 3.7, it was observed that the main apatite peak moved towards lower angles with the increase in strontium in the sample composition, as a consequence of its crystal lattice being enlarged by the presence of the bigger ion. In addition, the main peaks, in particular the two apatite peaks around 32 °, became higher and narrower with the increase in strontium.

All scaffold compositions matched two phases: an apatite and a calcium silicate. AW 0% samples contained the two expected phases described in the literature (85), hydroxyapatite (ICDD: 00-064-0738) and wollastonite 2M (ICDD: 00-066-0271). With the increase in strontium content in the samples, apatite prevalently acquired strontium in respect to wollastonite. In fact, strontium-apatite, with chemical formula $(Ca_{7.7}Sr_{2.3})(PO_4)_6(OH)_2$ (ICDD: 00-066-0271), was matched for scaffolds AW 6.2% and a different strontium-apatite with a higher strontium content, chemical formula $(Ca_{3.6}Sr_{6.4})(PO_4)_6(OH)_2$ (ICDD: 01-089-5633), was then matched for compositions AW 12.5% and higher. On the contrary, the wollastonite phase maintained the same 2M structure (ICDD: 00-066-0271) for samples AW 0% and AW 6.2% and then evolved into different phases with the increase of strontium: it was found to contain magnesium in composition AW 12.5 %, matching diopside $CaMgSi_2O_6$ (ICDD: 04-011-6810), then it became pseudowollastonite for AW 18.7% scaffolds and acquired strontium only with samples AW 24.9% and 37.4%, matching with a calcium magnesium strontium silicate (ICDD: 01-083-5061).

3.3.4 Effect of strontium addition to AW glass-ceramic samples on surface morphology and elemental composition

Both solid discs and porous scaffolds were observed under the SEM to investigate their surface morphology.

Micrographs of the surface of discs were taken at 5 mm working distance and two different magnifications, 1000x shown in Figure 3.14 and 5000x shown in Figure 3.15.

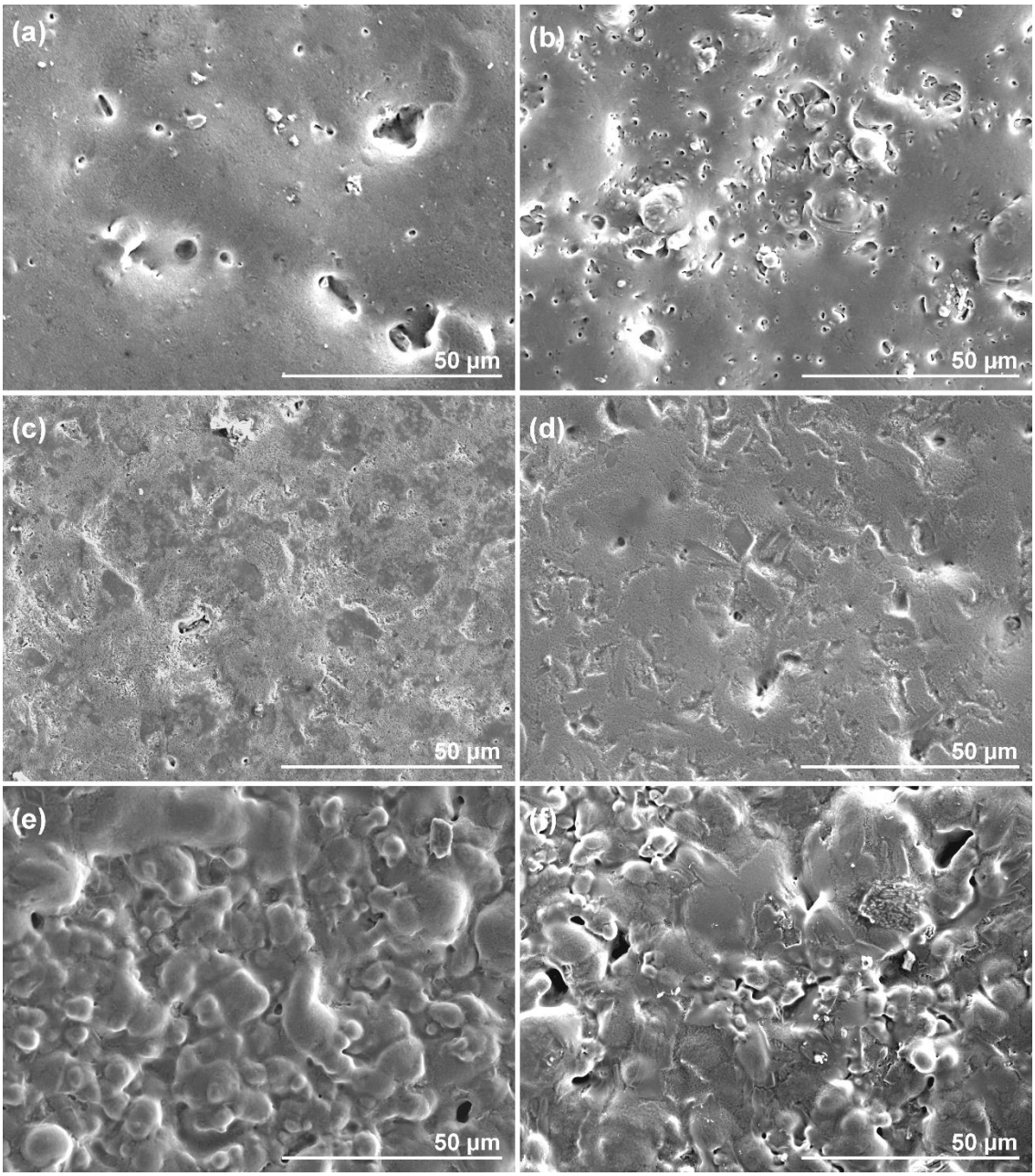

Figure 3.14: SEM micrographs, imaged from secondary electrons, of the surface of solid discs at lower magnification, 1000x. (a) AW 0%, (b) AW 6.2%, (c) AW 12.5 %, (d) AW 18.7%, (e) AW 24.9%, (f) AW 37.4%. Scale bars represent 50 µm.

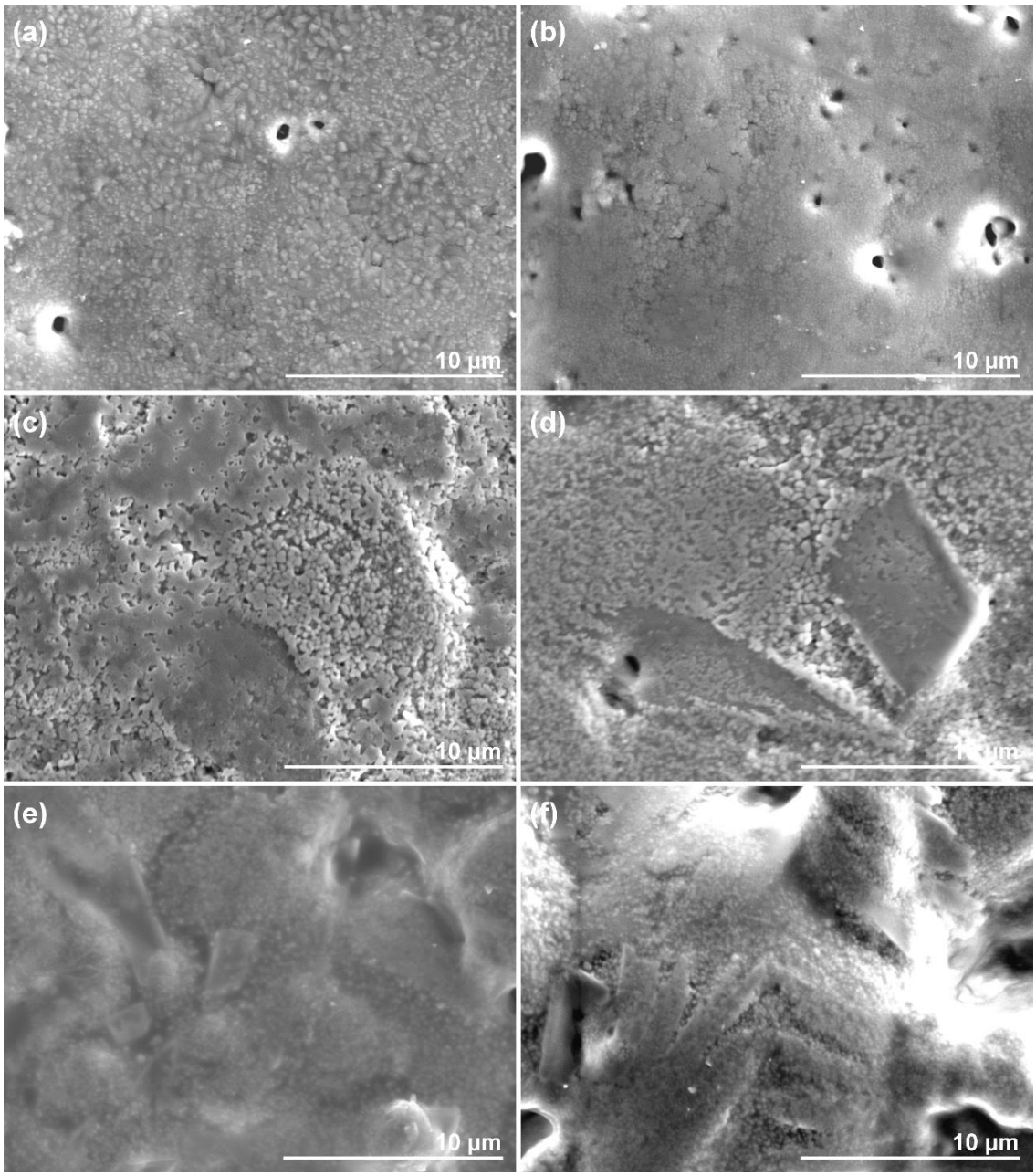

Figure 3.15: SEM micrographs, imaged from secondary electrons, showing details of the solid discs displayed in Figure 3.14 at higher magnification, 5000x. (a) AW 0%, (b) AW 6.2%, (c) AW 12.5 %, (d) AW 18.7%, (e) AW 24.9%, (f) AW 37.4%. Scale bars represent 10 µm.

As seen in Figure 3.14, all samples appeared well sintered, with the presence of rounded protrusions only for discs AW 24.9% and AW 37.4% deriving from the original glass particles, thus indicating a lower degree of sintering for these two phases.
In Figure 3.15, areas with different morphologies and bigger crystals were observed for samples containing 12.5 mol% strontium oxide and higher, signifying a different distribution and growth of the crystal phases.

Figure 3.16 and Figure 3.17 show micrographs of the porous scaffolds and details of the sintered struts, respectively, taken at different magnifications.

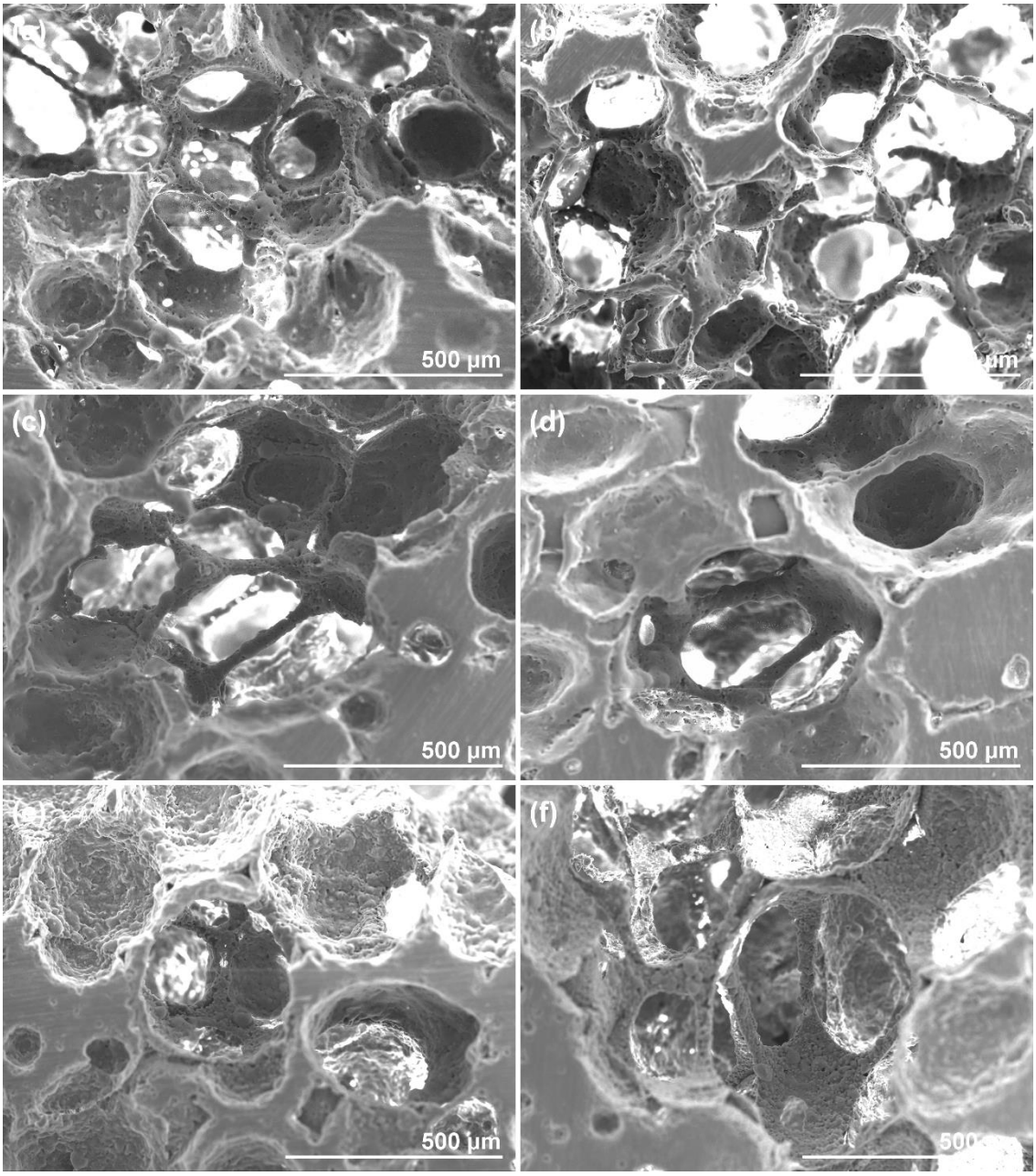

Figure 3.16: SEM micrographs, imaged from secondary electrons, of porous scaffolds taken at magnification 100x. (a) AW 0%, (b) AW 6.2%, (c) AW 12.5 %, (d) AW 18.7%, (e) AW 24.9%, (f) AW 37.4%. Scale bars represent 500 µm.

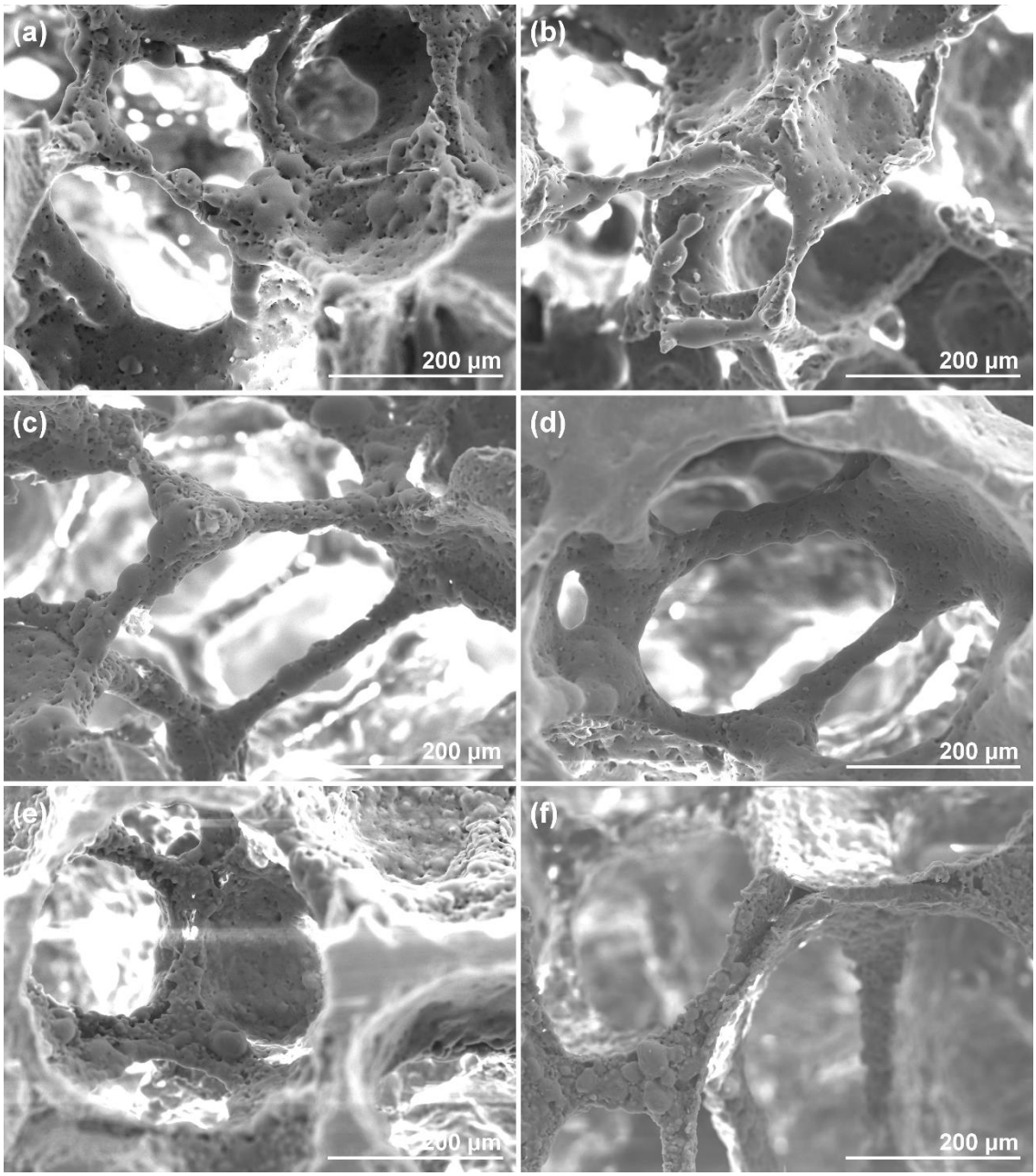

Figure 3.17: SEM micrographs, imaged from secondary electrons, of the porous scaffolds displayed in Figure 3.16 at higher magnification (200x), showing details of the struts. (a) AW 0%, (b) AW 6.2%, (c) AW 12.5 %, (d) AW 18.7%, (e) AW 24.9%, (f) AW 37.4%. Scale bars represent 200 µm.

After their thermal treatment, scaffolds maintained the porous structure of the template, with struts forming an interconnected network of pores for all the compositions. All scaffolds presented a residual microporosity where sintered glass particles did not fuse completely. It could also be observed that samples sintered differently, especially compositions AW 24.9% and 37.4% where the trace of the

original glass particles remained evident. Sintering defects were also present for all the compositions, with hollow struts that derived from the templating polyurethane foam.

3.3.4.1 Effect of strontium addition on the elemental composition of discs and porous scaffolds

The composition of discs and scaffolds was verified using EDS from the same samples observed under SEM.

Table 3.6 reports the results of data collected at 30 kV, magnification 1000x for discs and 200x for scaffolds. Figure 3.18 to Figure 3.23 show, for each composition, selected EDS points and their corresponding spectra for solid discs; data were collected at 5000x magnification and 10 kV, as a lower voltage allowed for a better identification of the sample topography.

Table 3.6: EDS quantification of relevant atoms for solid discs (D.) and porous scaffolds (Sc.), compared to the theoretical values (Th.). All data in at%.

	AW 0%			AW 6.2%			AW 12.5%			AW 18.7%			AW 24.0%			AW 37.4%		
Atom	**Th.**	**D.**	**Sc.**	**Th.**	**D.**	**Sc.**	**Th.**	**D.**	**Sc.**	**Th.**	**D.**	**Sc.**	**Th.**	**D.**	**Sc.**	**Th.**	**D.**	**Sc.**
Si	32.90	29.30	29.65	32.90	24.15	25.01	32.90	24.93	24.01	32.90	24.83	23.42	32.90	23.46	22.03	32.90	23.96	20.25
Mg	6.58	4.67	4.32	6.58	4.29	3.77	6.58	4.35	4.07	6.58	5.17	4.30	6.58	4.68	4.56	6.58	5.34	4.21
F	0.74	2.12	4.22	0.74	2.65	4.62	0.74	2.52	4.91	0.74	0.80	4.20	0.74	2.19	3.84	0.74	0.26	4.62
Ca	46.62	50.65	47.84	40.87	46.54	41.84	35.03	38.79	35.38	29.29	31.54	30.09	23.54	26.02	22.98	11.96	14.23	11.84
P	13.16	13.25	13.97	13.16	12.82	13.47	13.16	14.11	13.39	13.16	14.98	12.74	13.16	13.90	12.60	13.16	14.10	11.48
Sr	0.00	0.01	0.00	5.75	9.55	11.29	11.58	15.30	18.24	17.33	22.68	25.25	13.08	29.75	33.99	34.66	42.11	47.60

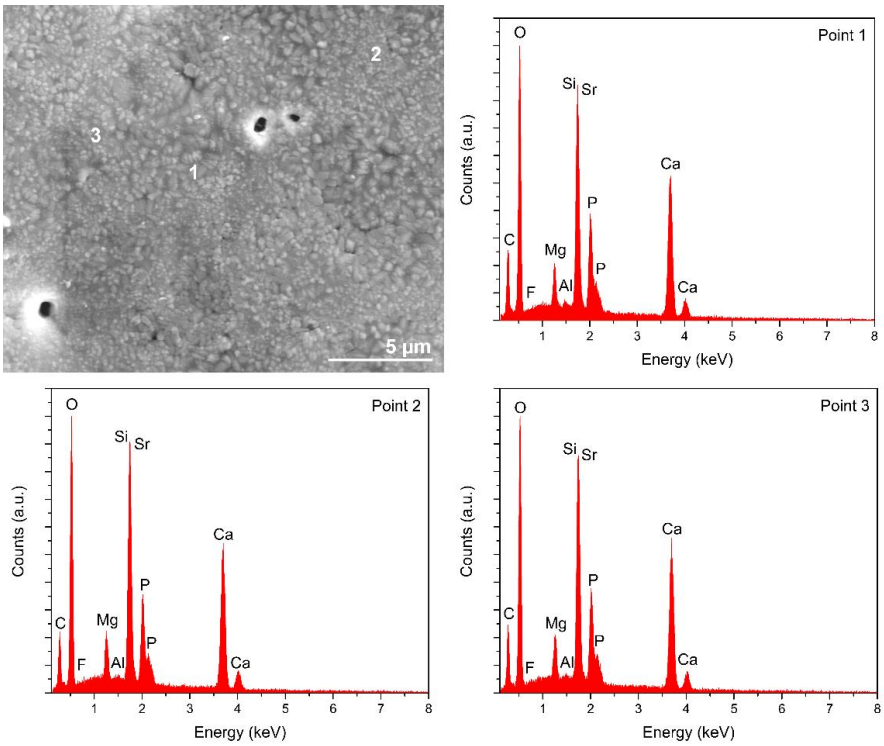

Figure 3.18: EDS results of three point areas on an AW 0% disc. Secondary electron image of the analysed area (top left). EDS spectrum of Point 1 (top right), Point 2 (bottom left) and Point 3 (Bottom right).

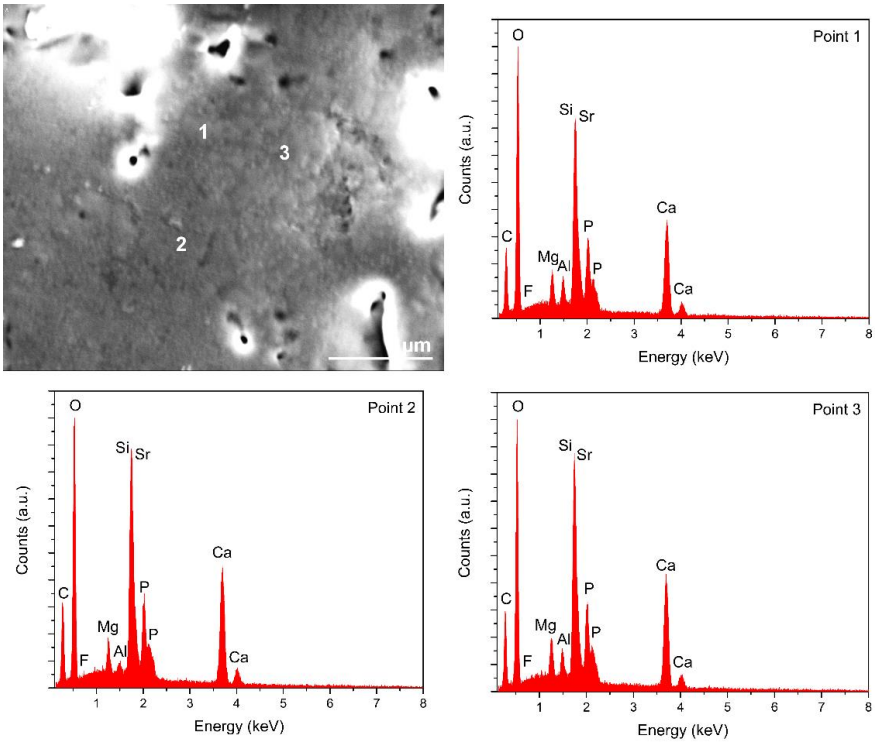

Figure 3.19: EDS results of three point areas on an AW 6.2% disc. Secondary electron image of the analysed area (top left). EDS spectrum of Point 1 (top right), Point 2 (bottom left) and Point 3 (Bottom right).

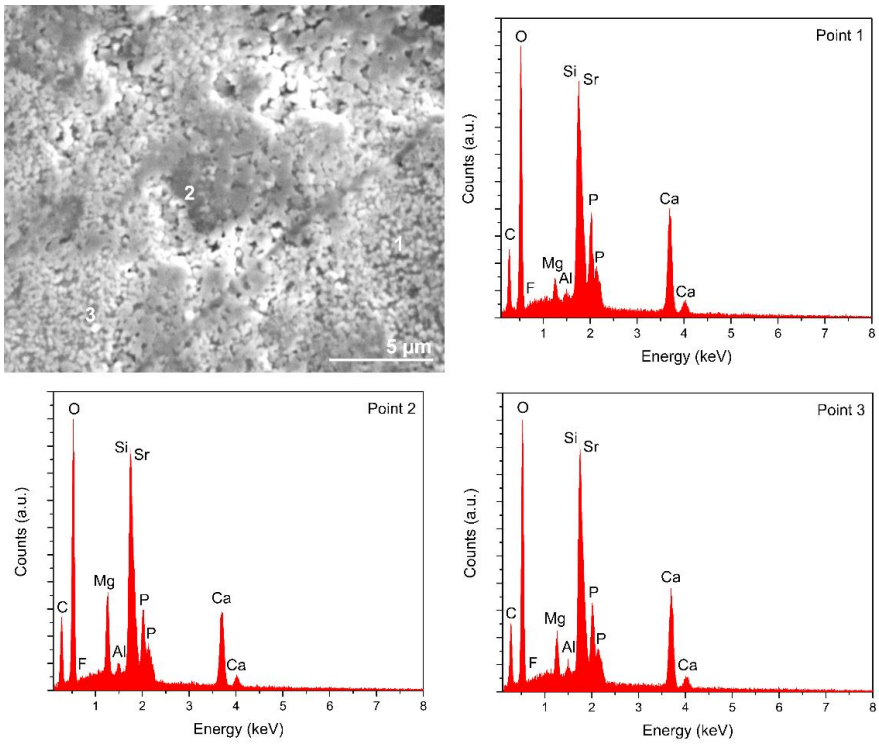

Figure 3.20: EDS results of three point areas on an AW 12.5% disc. Secondary electron image of the analysed area (top left). EDS spectrum of Point 1 (top right), Point 2 (bottom left) and Point 3 (Bottom right).

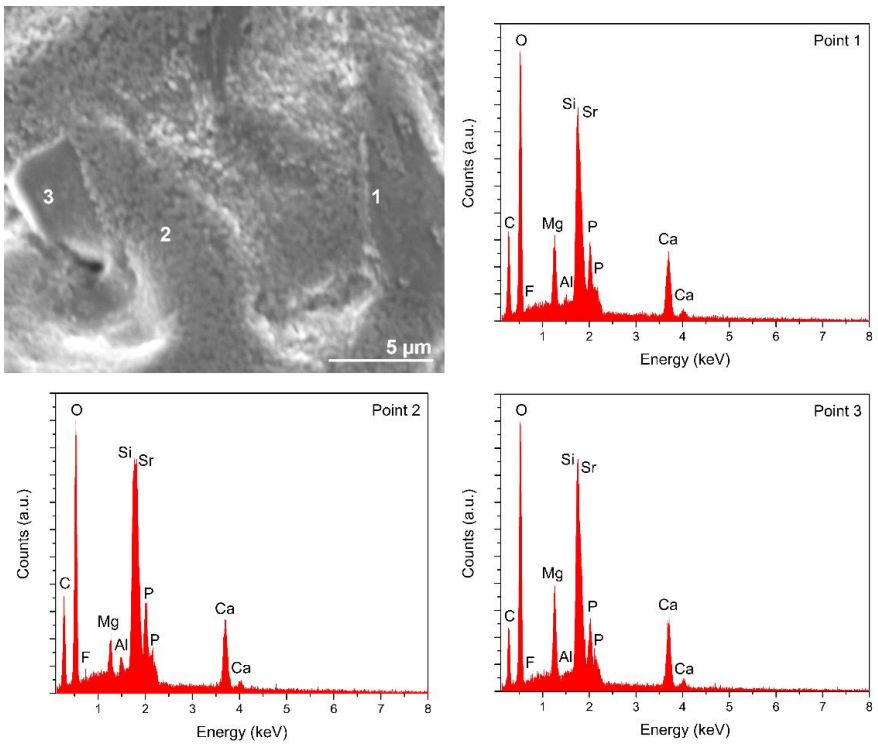

Figure 3.21: EDS results of three point areas on an AW 18.7% disc. Secondary electron image of the analysed area (top left). EDS spectrum of Point 1 (top right), Point 2 (bottom left) and Point 3 (Bottom right).

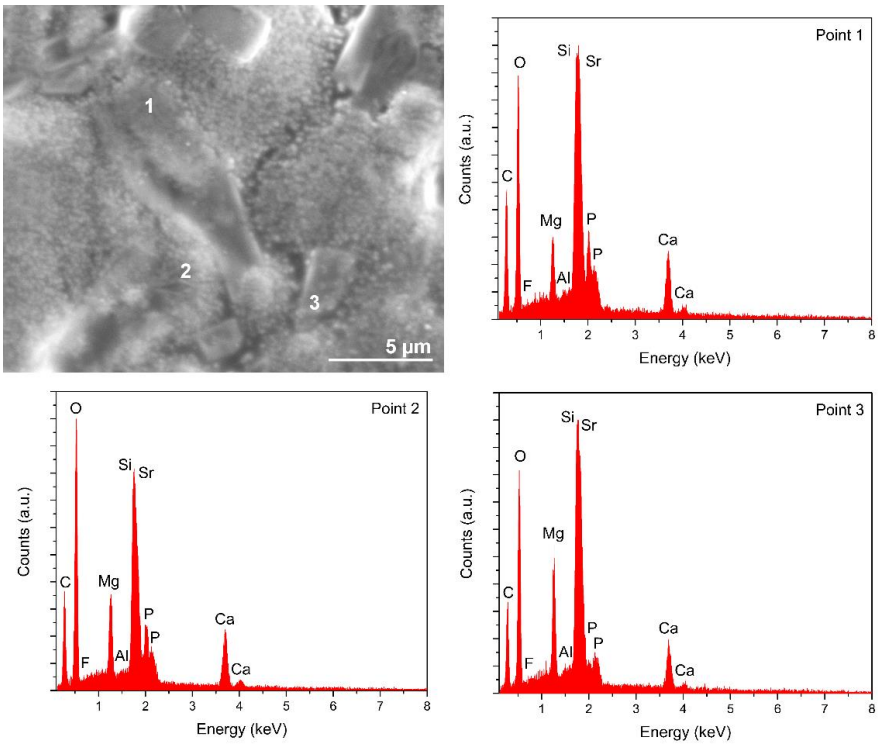

Figure 3.22: EDS results of three point areas on an AW 24.9% disc. Secondary electron image of the analysed area (top left). EDS spectrum of Point 1 (top right), Point 2 (bottom left) and Point 3 (Bottom right).

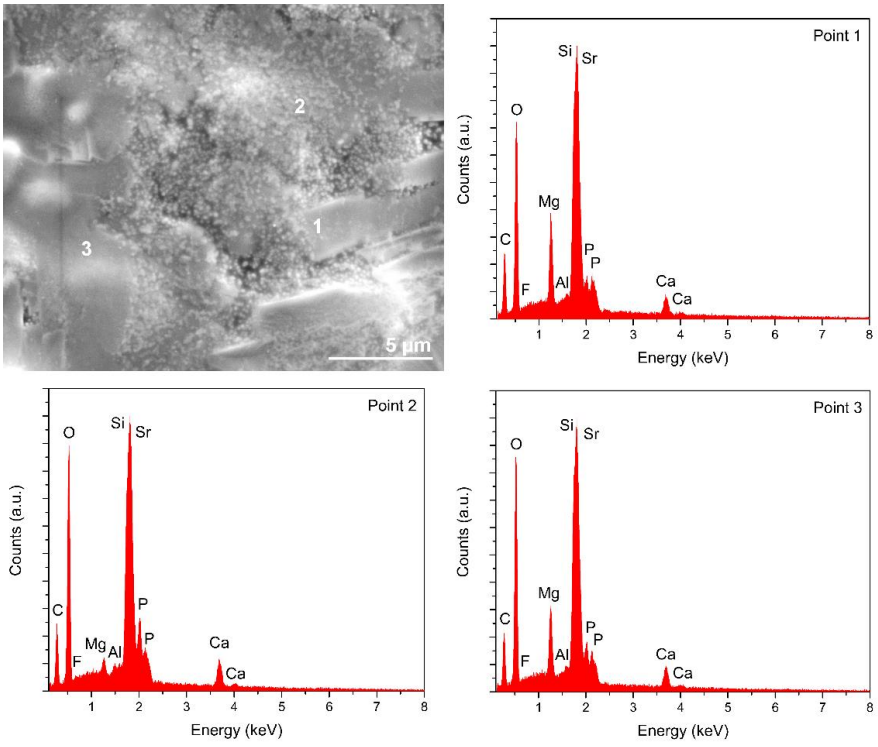

Figure 3.23: EDS results of three point areas on an AW 37.4% disc. Secondary electron image of the analysed area (top left). EDS spectrum of Point 1 (top right), Point 2 (bottom left) and Point 3 (Bottom right).

Table 3.6 showed that both forms of glass-ceramic samples, solid discs and porous scaffolds, maintained all the atomic elements they contained before their thermal treatment. However, both discs and even more the porous scaffolds had a higher percentage of strontium compared to the theoretical values, always balanced by a lower amount of silicon. Since this result was not found for the parent glasses (Chapter 2), it is likely that this change in composition was an effect of the thermal treatment and the formation of crystal phases in the samples. In particular, it is possible that the apatite phase (more specifically, a strontium-substituted apatite) tended to emerge to the outer surface of samples, thus segregating the silicate phase deeper in the bulk. Therefore, a surface investigation of samples such as the EDS described here would preferentially detect only the outer apatite phase, but an analysis of ground or sectioned samples would be necessary to confirm this hypothesis. Fluorine was also found to be higher than its theoretical values by a few percent units in all samples, as already observed with the parent glasses, and higher in scaffolds than discs. As explained in Chapter 2, this result could derive from the intrinsic error of the machine and probably did not represent an actual increase in fluorine.

As far as the sample topography was concerned, as also shown previously in Figure 3.14 and Figure 3.15, different crystal phases could not be clearly identified in discs AW 0% and AW 6.2%. This was confirmed by the EDS spectra taken in different areas of these samples, which appeared similar in the three selected points. For composition AW 12.5% and above, the morphology of the surface of discs indicated the formation of areas with different crystal compositions. In particular, smoother areas tended to be richer in magnesium and poorer in phosphorus, indicating that the specific crystal phase could be the magnesium-calcium silicate identified during the XRD analysis (Section 3.3.3). On the contrary, dotted areas were identified as apatite. It was not possible to visualise the increase in strontium in these spectra, as its K_α and K_β signals are at about 14 and 16 keV, respectively, and therefore a higher voltage would have been required that, however, would have hindered the quality of the topography investigation. However, the silicon+strontium peak at about 1.8 keV increased with the increase in strontium; since silicon was constant throughout the six sample compositions, the increase was therefore due to the increased amount of strontium.

3.3.5 Effect of strontium addition to AW glass-ceramic on the 3D architecture and porosity of porous scaffolds

Micro CT data were used to reconstruct 3D models of the scanned scaffolds. Images were created using the software CTvox and Figure 3.24 shows pictures of one sample

per composition, where their front side was virtually cut with a plane so that the internal structure could be seen.

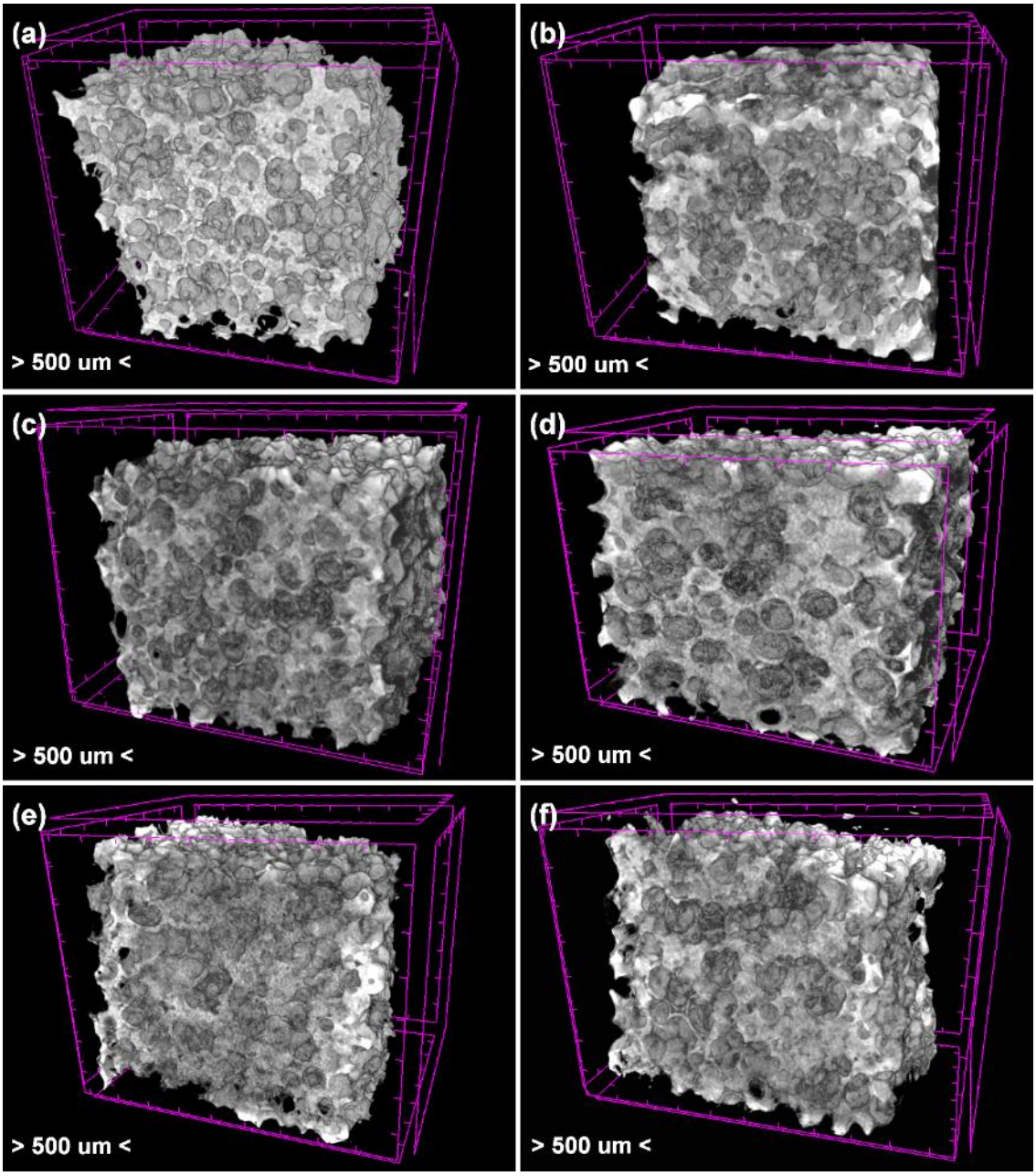

Figure 3.24: Micro CT images of porous samples, sectioned with a cutting-through plane for visualising their internal structure. (a) AW 0%, (b) AW 6.2%, (c) AW 12.5 %, (d) AW 18.7%, (e) AW 24.9%, (f) AW 37.4%. Marks on the axes of purple boxes indicate 500 μm.

All samples maintained their porous structure throughout their volume. Pores looked interconnected, with the presence of some bigger pores where struts failed to form due

to incomplete coating from the slurry. Struts of varying thickness could be observed for all samples. No difference could be observed between compositions.

3.3.5.1 Effect of strontium addition to AW scaffolds on porosity from micro CT imaging

Micro CT post-processing analysis was then used to study the porosity of the scaffolds. Table 3.7, Table 3.8 and Table 3.9 report the resulting general, open and closed porosity, respectively, calculated from 4 scaffolds for each composition.

Table 3.7: General porosity of scaffolds as measured by µCT, n=4.

	Average (%)	**Standard deviation (%)**
AW 0%	63.07	3.50
AW 6.2%	57.15	2.13
AW 12.5%	56.70	3.82
AW 18.7%	57.00	4.56
AW 24.9%	50.45	3.05
AW 37.4%	57.31	2.30

Table 3.8: Open porosity of scaffolds as measured by µCT, n=4.

	Average (%)	**Standard deviation (%)**
AW 0%	62.92	3.58
AW 6.2%	57.00	2.14
AW 12.5%	56.55	3.79
AW 18.7%	56.84	4.58
AW 24.9%	50.02	3.02
AW 37.4%	57.01	2.35

Table 3.9: Closed porosity of scaffolds as measured by μCT, n=4.

	Average (%)	Standard deviation (%)
AW 0%	0.15	0.08
AW 6.2%	0.15	0.02
AW 12.5%	0.16	0.06
AW 18.7%	0.16	0.04
AW 24.9%	0.43	0.03
AW 37.4%	0.29	0.11

For all the six compositions of scaffold tested, most of the general porosity derived from open porosity. In fact, values in Table 3.8 were very close to values in Table 3.7, while less than 1% of the general porosity was due to closed porosity (Table 3.9). This meant that, for all the compositions under study, most of the porosity of samples derived from an interconnected network of pores, therefore the foam replication method followed in this thesis allowed the final scaffolds to preserve the structure of the template, without a relevant amount of obstructed pores.
The open porosity of scaffolds is also represented in Figure 3.25, where significance was tested using one-way ANOVA in OriginPro 2015.

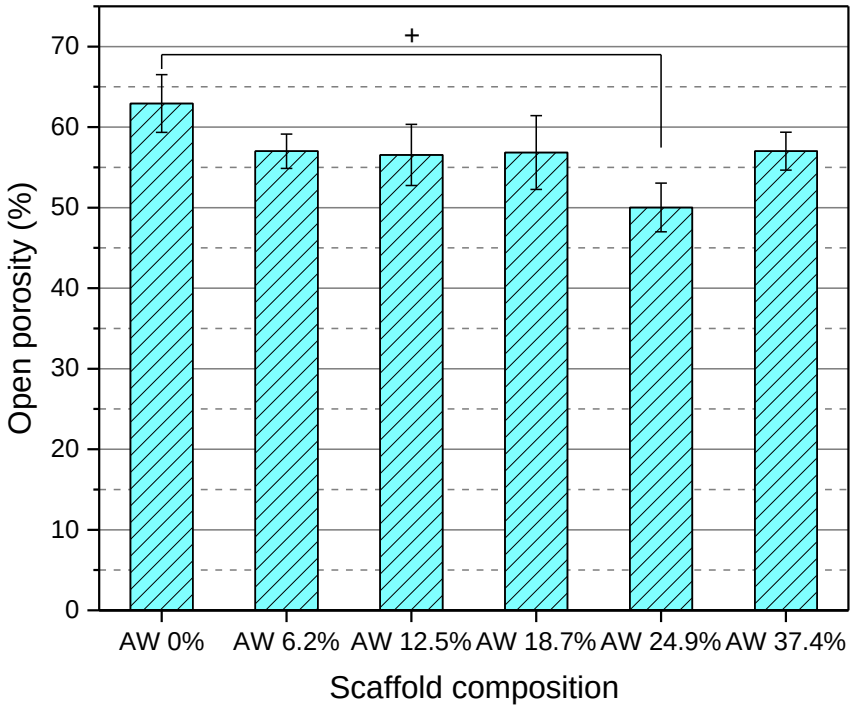

Figure 3.25: Open porosity of strontium scaffolds (n=4), as measured from the post-processing of micro CT data, +p<0.001. Error bars indicate the standard deviation (n=4).

All scaffolds had an open porosity of 50 to 60 % of their total volume. Only compositions AW 0% and AW 24.9% were found significantly different ($p<0.001$). However, only one batch of samples per composition was tested and therefore results did not include inter-batch variability. Because all samples were handmade, it could be concluded that, on average, all samples had a porosity of about 55 % independently of their composition.

3.3.5.2 Comparison with experimental porosity

Porosity measurements for the scaffolds could be derived also from the experimental mass and volume data collected for their shrinkage measurements (Section 3.3.1) and their measured density (Section 3.3.2). Table 3.10 compares the general porosity measured by the micro CT post-analysis with the porosity calculated from the experimental masses, volumes and densities.

Table 3.10: Comparison between the total porosity calculated by micro CT (µCT porosity, n=4) and the porosity calculated from measured mass, volume and density (Exp. Porosity, n=30).

	µCT porosity (%)	**Exp. porosity (%)**
AW 0%	63.07 ± 3.50	60.80 ± 2.34
AW 6.2%	57.15 ± 2.13	66.31 ± 2.97
AW 12.5%	56.70 ± 3.82	62.92 ± 2.22
AW 18.7%	57.00 ± 4.56	59.46 ± 3.08
AW 24.9%	50.45 ± 3.05	61.14 ± 2.82
AW 37.4%	57.31 ± 2.30	68.04 ± 3.54

Porosities calculated from the experimental mass, volume and density of samples tended to be higher than those calculated computationally from the micro CT data. This could depend on the inter-batch variability of specimens, as scaffolds in the two groups were taken from different batches. Another reason for this difference could be the fact that, for the experimental calculations, samples were approximated as cuboids (a linear measure was taken for each dimension using a calliper), but their shapes were actually irregular as each foam was cut manually: this could have caused an under-estimation of their volume and, consequently, an over-estimation of their porosity. Because the micro CT analysis made use of ROIs all contained within the volume of samples, the micro CT porosity results could be considered closer to the actual porosity of scaffolds.

3.3.5.3 Effect of strontium addition to AW scaffolds on trabecular thickness and spacing

CTAn also provided the overall mean trabecular thickness (Tr.Th.) and trabecular spacing (pore size, Tr.Sp.). These values are reported in Table 3.11.

Table 3.11: Overall trabecular thickness (Tr.Th.) and trabecular spacing (Tr.Sp.), as calculated in CTAn from the micro CT data. Values are average ± standard deviation from 4 scaffolds per composition.

	Tr.Th. (µm)	Tr.Sp (µm)
AW 0%	96.29 ± 4.14	250.15 ± 11.77
AW 6.2%	123.02 ± 4.45	247.77 ± 12.92
AW 12.5%	103.45 ± 5.18	223.38 ± 28.44
AW 18.7%	138.09 ± 8.52	274.88 ± 26.55
AW 24.9%	130.10 ± 5.95	244.55 ± 13.97
AW 37.4%	126.08 ± 3.80	268.84 ± 5.15

The average trabecular thickness ranged from 96.29 µm for scaffolds AW 0% to 138.09 µm for scaffolds AW 18.7%, while the overall mean pore size, indicated as trabecular spacing, ranged from 223.38 µm for scaffolds AW 12.5% to 274.88 µm for scaffolds AW 18.7%. Although often reported as the parameters that characterise a scaffold, these values strongly depend on the strut thickness distribution and pore size distribution, respectively, so it must be taken into account that, in the present case, values do not present Gaussian distributions, as it will be shown in Figure 3.26. In addition, as mentioned previously, these results were obtained from 4 scaffolds that belonged to the same batch for each composition, therefore inter-batch variability was not taken into account.

3.3.5.4 Effect of strontium addition to AW scaffolds pore size distribution

Figure 3.26 shows the pore size distributions of scaffolds as calculated by CTAn for their open porosity. The CTAn software automatically outputs distributions dividing the pore size in fractions that are twice the pixel size: since, for the scaffolds tested here, the pixel size was 8.88 µm, the width of each pore size fraction of the distribution was 17.76 µm.

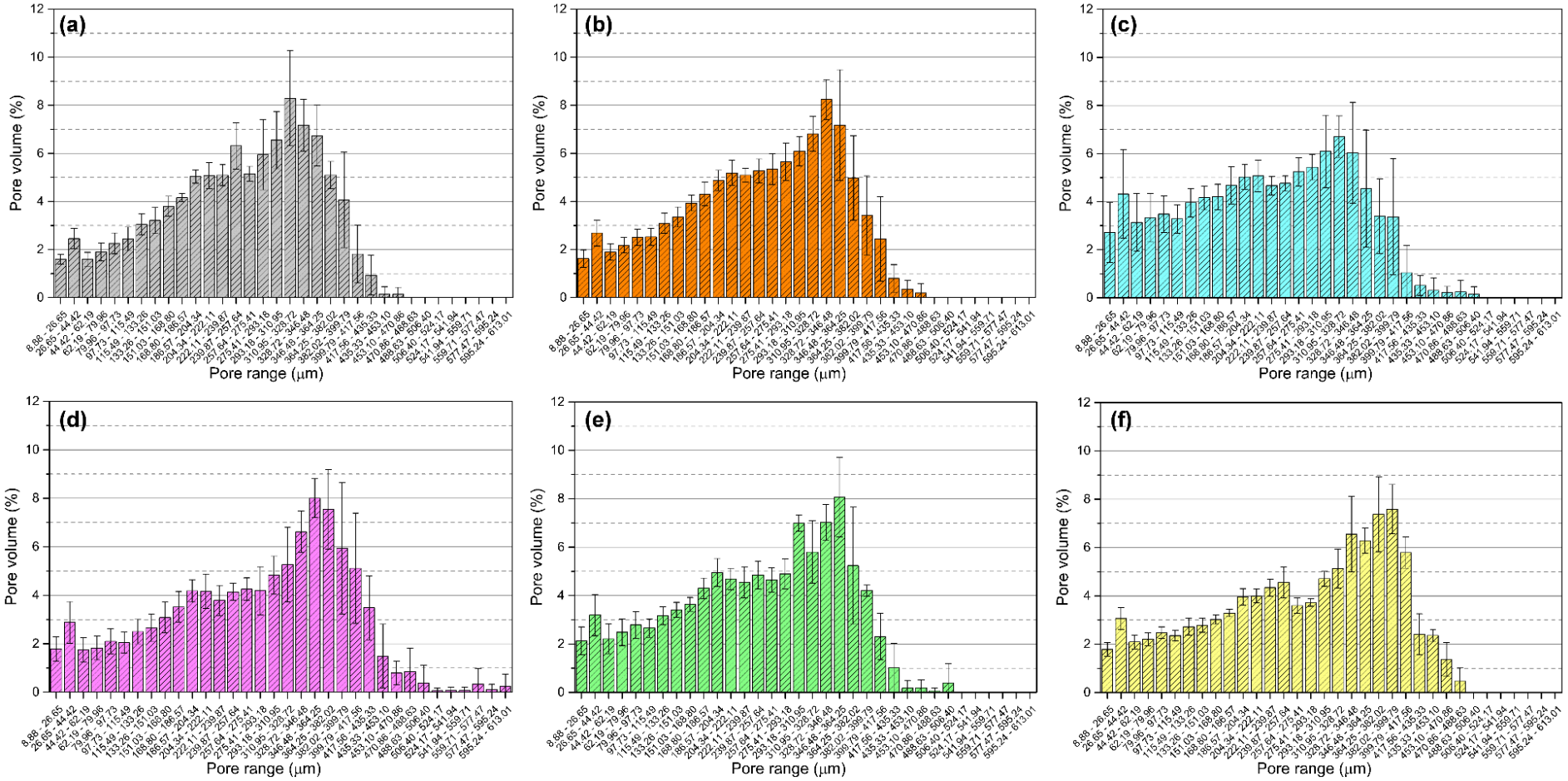

Figure 3.26: Pore size distributions of strontium scaffolds as calculated from micro CT data, n=4. (a) AW 0%, (b) AW 6.2%, (c) AW 12.5 %, (d) AW 18.7%, (e) AW 24.9%, (f) AW 37.4%. Error bars indicate the standard deviation .

For all samples, most pores were included in the range 100-400 µm, which is the range recommended for bone scaffolds, as it allows for cell colonisation and bone ingrowth (30, 260). All compositions presented a bimodal distribution, with the first peak at around 200 µm and the second peak between 310 µm and 380 µm; the second peak moved towards bigger pore sizes for samples containing a higher amount of strontium. While pores around 200 µm derived from the 90 PPI foam template used for producing the scaffolds, the second peak probably derived from defects created by uncomplete struts due to uneven coating of foams with the slurry during the preparation of samples, as also observed in micro CT images in Figure 3.24 and SEM images in Figure 3.16. The fact that the bigger pores were larger for higher strontium compositions could be the consequence of the different shrinkages that samples underwent during their thermal treatment (Section 3.3.1): the smaller their shrinkage, the bigger the final pores, with the effect being more evident for larger diameters. All compositions also presented a smaller peak in the region 25-45 µm, likely deriving from the incomplete fusion of glass during sintering already observed in the SEM micrographs in Figure 3.17.

3.3.6 Effect of strontium addition on the mechanical properties of porous scaffolds

Porous scaffolds were tested for compression and biaxial flexural strength. Results are presented in Section 3.3.6.1 and 3.3.6.2, respectively.

3.3.6.1 Effect of strontium on compressive strength and elastic modulus

Figure 3.27 shows the average compressive strength of porous cylindrical scaffolds, while Figure 3.28 displays their average Young’s modulus.

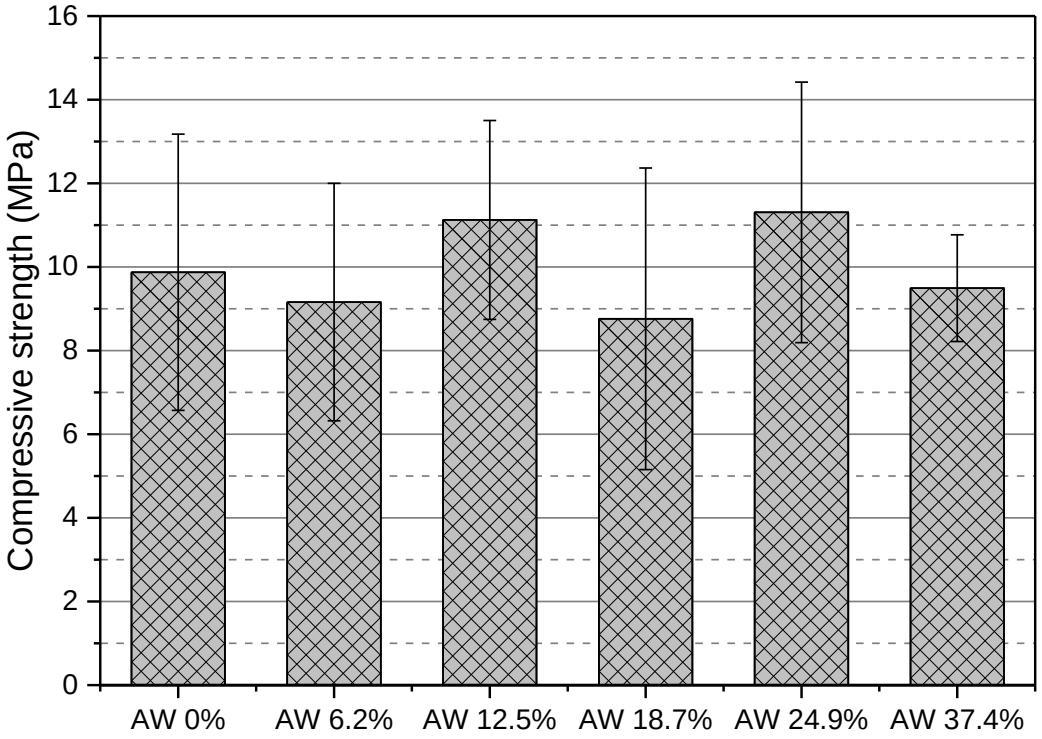

Figure 3.27: Average compressive strength of porous scaffolds (n=8). Error bars represent the standard deviation. No significant difference was found between samples (p>0.05).

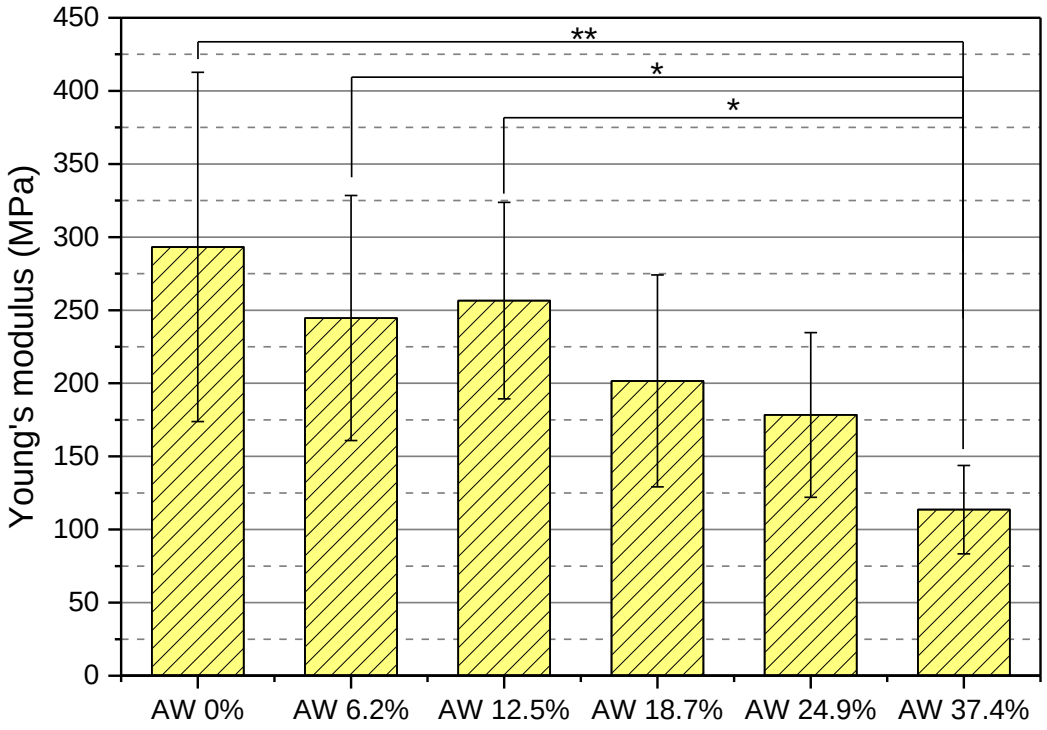

Figure 3.28: Young's modulus of porous scaffolds (n=8). Error bars indicate the standard deviation. *p<0.05, **p<0.005.

All samples presented an average compressive strength of about 10 MPa, which is within the range suggested for cancellous bone (34, 35). Data were tested for significance using one-way ANOVA in OriginPro 2015, but no difference could be found ($p>0.05$). High standard deviations derived from the intrinsic variability of scaffolds and their highly porous nature. However, all compositions seemed to possess a similar resistance to compression. Considering that samples contained different crystal phases depending on their composition (Section 3.3.3), it is possible that differences in compressive strength for the six materials under study were overcome by their porous structure.

On the contrary, the Young's modulus of samples decreased with increasing strontium, being about 300 MPa for samples AW 0% and about 120 MPa for samples AW 37.4%. Composition AW 37.4% was found significantly different from AW 0% and AW 6.2% ($p<0.05$) and AW 12.5% ($p<0.005$). This suggested that porous samples, despite being able to withstand similar stresses in compression, resisted to the application of load in a different way, with samples with increasing strontium undergoing a larger deformation before fracturing.

3.3.6.1.1 Effect of strontium addition to AW porous scaffolds on fracture mechanism in compression

Figure 3.29 and Figure 3.30 show SEM micrographs of fracture surfaces of samples tested for compression, at lower and higher magnification, respectively.

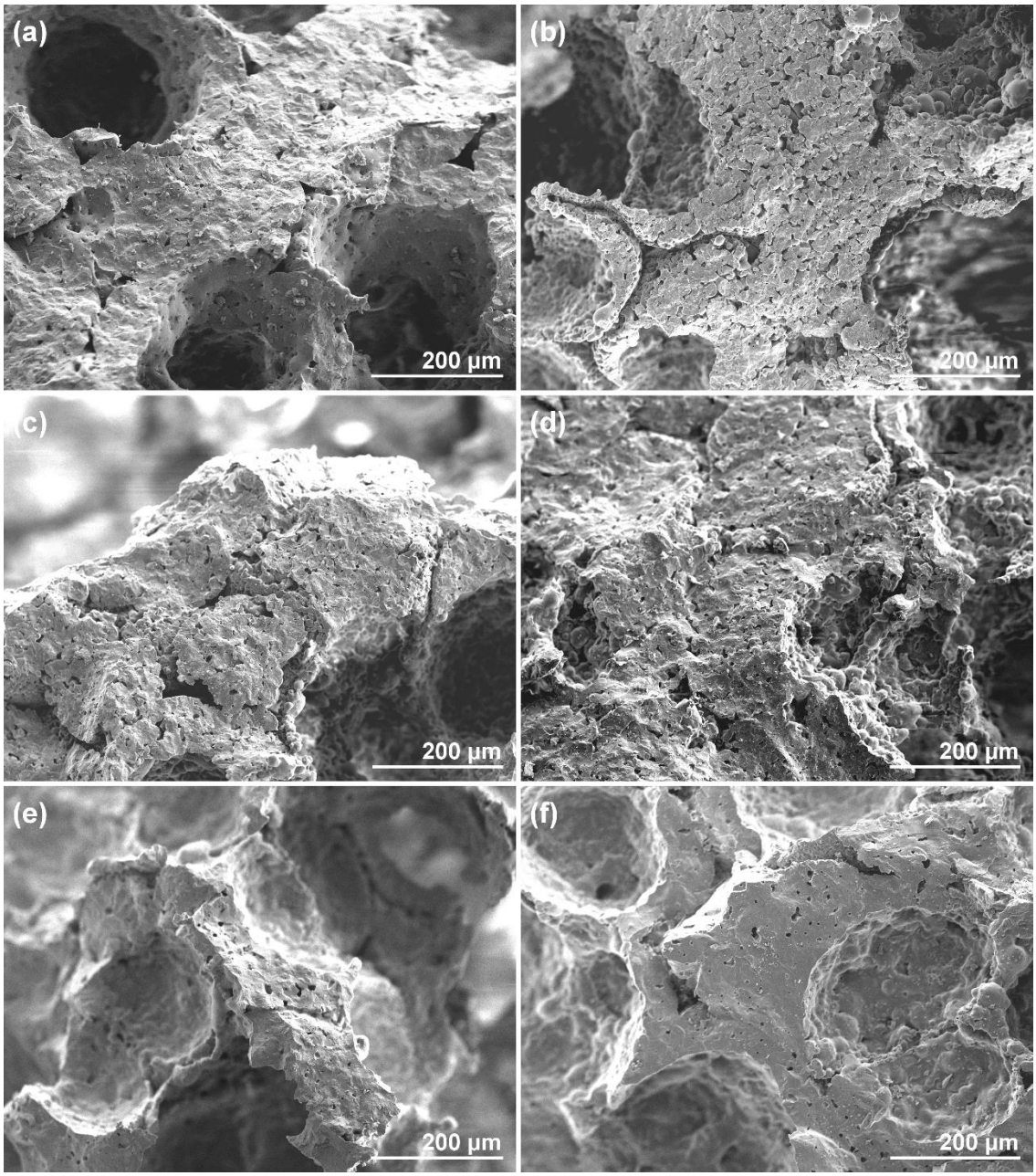

Figure 3.29: SEM micrographs, imaged from secondary electrons, of the fracture surfaces of samples tested for compression, low magnification. (a) AW 0%, (b) AW 6.2%, (c) AW 12.5 %, (d) AW 18.7%, (e) AW 24.9%, (f) AW 37.4%. Scale bars represent 200 µm.

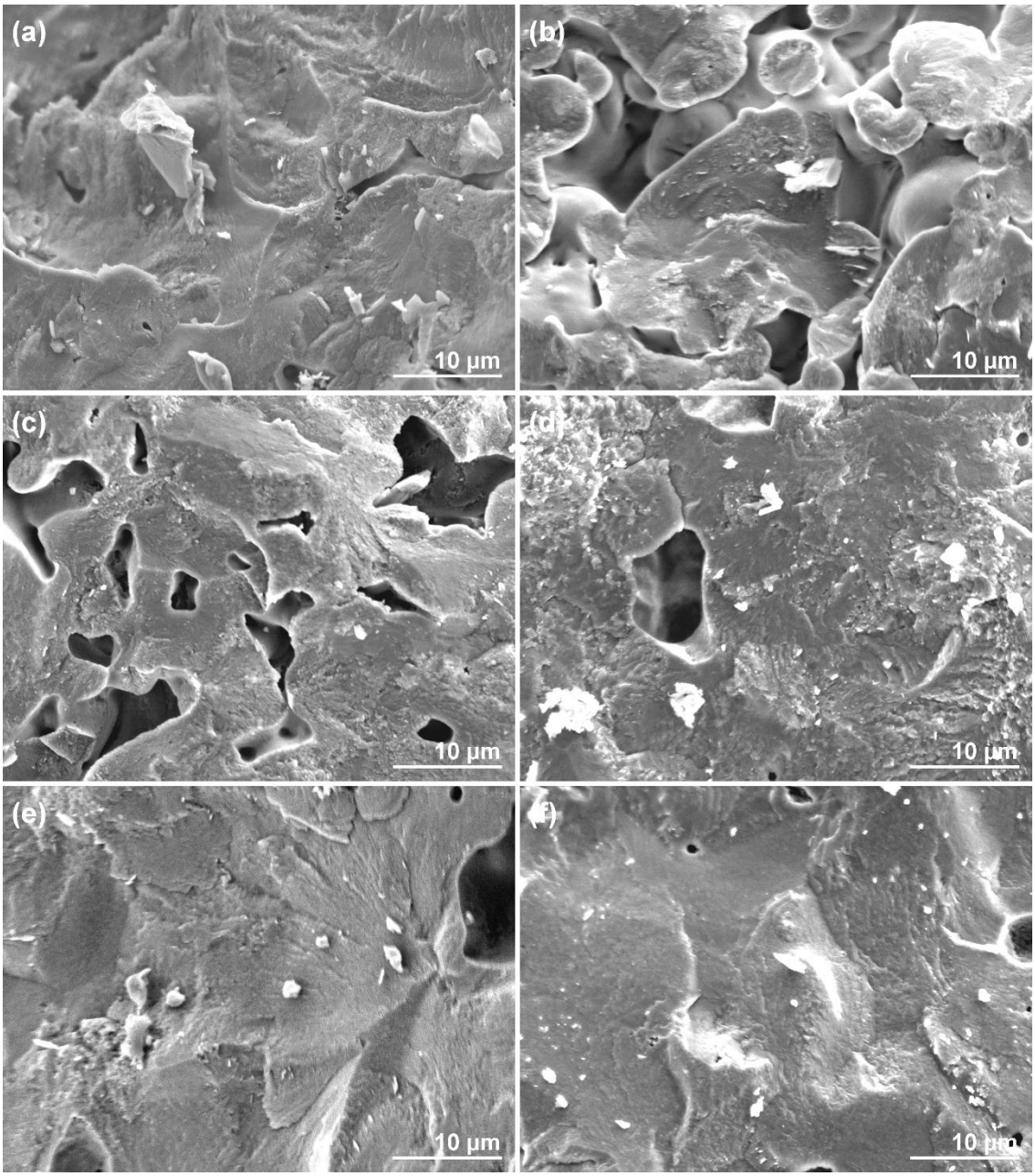

Figure 3.30: SEM micrographs showing details, at higher magnification, of the fracture surfaces of the samples displayed in Figure 3.29. Samples imaged from secondary electrons. (a) AW 0%, (b) AW 6.2%, (c) AW 12.5 %, (d) AW 18.7%, (e) AW 24.9%, (f) AW 37.4%. Scale bars represent 10 µm.

Sintering necks could be identified for all samples, but fracture surfaces propagated through the densified material. In Figure 3.30, where surfaces are shown at a higher magnification, it was possible to observe smoother and rougher areas, which could correspond to areas of different crystalline composition or indicated the areas of mirror, mist and hackle typical of ceramic fracture. As expected from a ceramic

sample, no signs of plastic deformation were visible and cracks likely propagated through the crystal grains rather than at grain boundaries.

3.3.6.2 Effect of strontium on biaxial flexural strength

Figure 3.31 reports the average biaxial flexural strength, measured from slices obtained from the strontium AW porous scaffolds, 15 specimens tested per composition. Their Weibull distributions are then shown in Figure 3.32 and their Weibull characteristics summarised in Table 3.12.

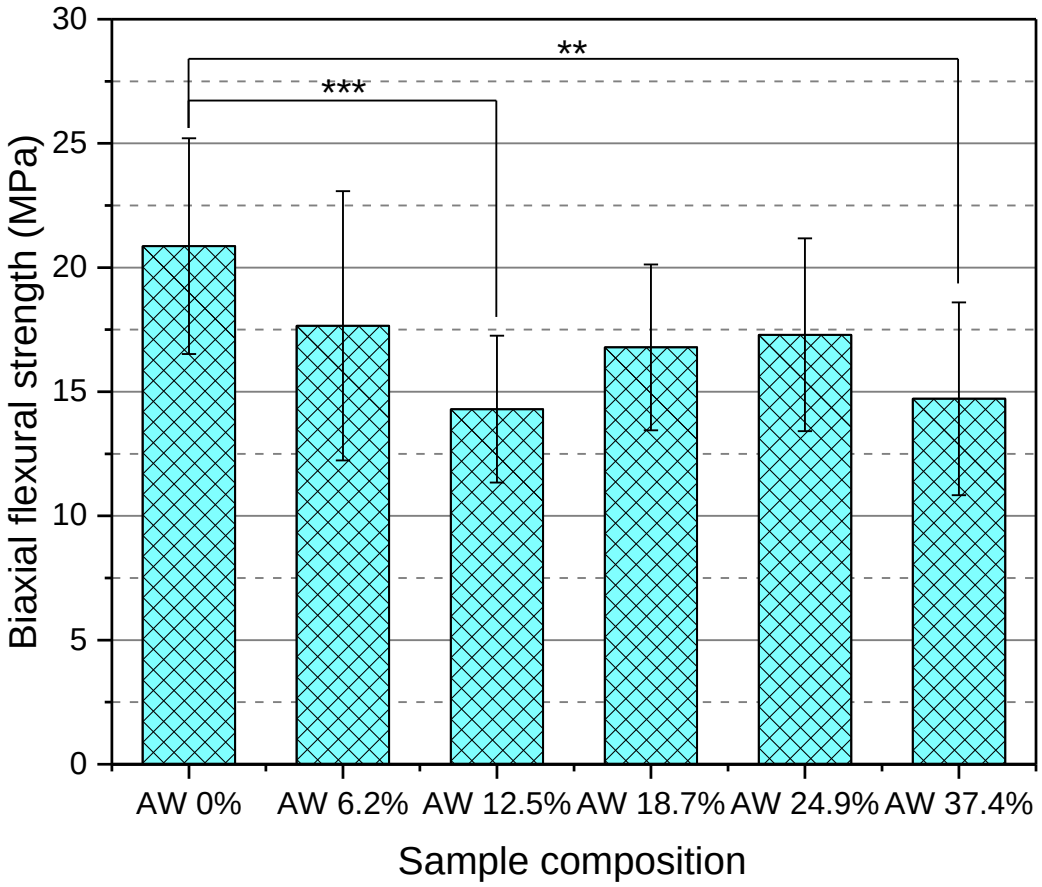

Figure 3.31: Average biaxial flexural strength of porous scaffolds. Error bars indicate the standard deviation (n=15). **p<0.005, ***p<0.0005.

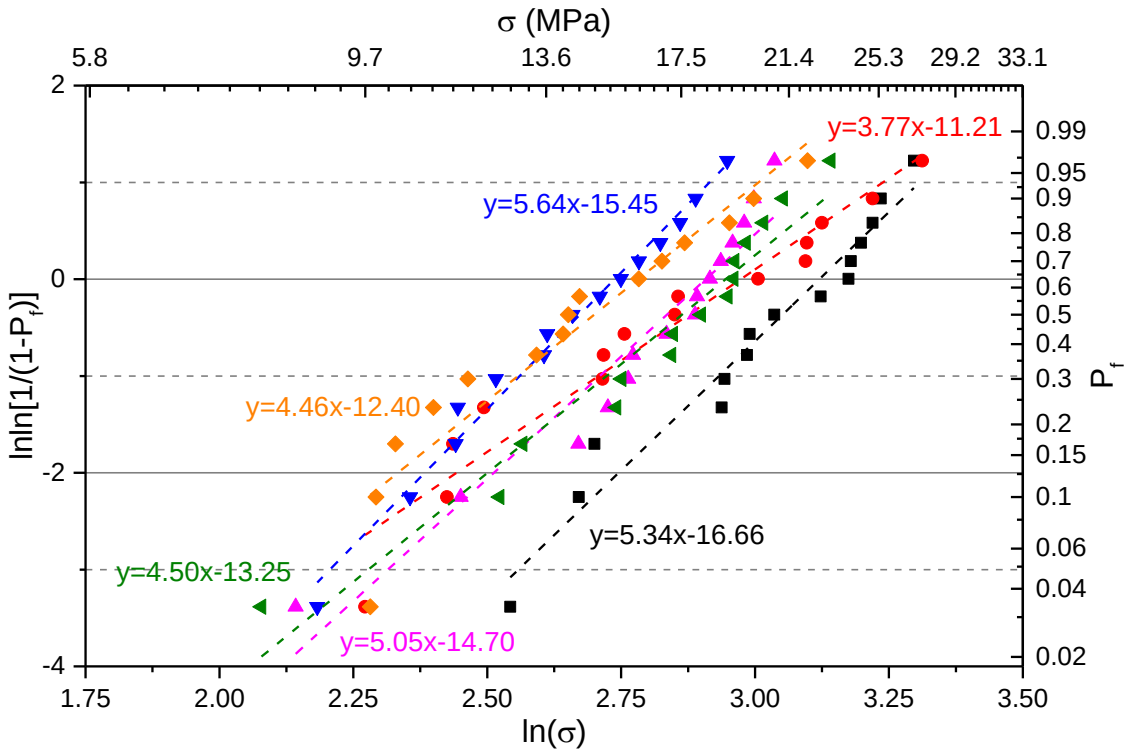

Figure 3.32: Weibull distributions and fitting trendlines for porous scaffolds tested for biaxial flexural strength (n=15). ■ AW 0%, ● AW 6.2%, ▼ AW 12.5%, ▲ AW 18.7%, ◄ AW 24.9%, ♦ AW 37.4%.

Table 3.12: Weibull characteristics for porous scaffolds tested for biaxial flexural strength, Weibull modulus *m* and characteristic strength σ_0.

	m	**σ_0 (MPa)**
AW 0%	5.3397	22.6483
AW 6.2%	3.7692	19.5558
AW 12.5%	5.6440	15.4532
AW 18.7%	5.0540	18.3212
AW 24.9%	4.4983	19.0132
AW 37.4%	4.4561	16.1502

The biaxial flexural strength for all compositions was between 14 and 21 MPa, thus higher than the corresponding compressive strengths. Samples AW 12.5% and AW 37.4% had significantly lower strength than AW 0% ($p<0.0005$ and $p<0.005$, respectively). This could be also seen from their Weibull distributions, for which these two compositions had lower Weibull characteristic strength, while AW 0% had the highest: 22.6 MPa. On the contrary, the Weibull moduli ranged from 3.7 to 5.6, with samples AW 6.2% showing the lowest and samples AW 12.5% giving the highest. Therefore, scaffolds AW 6.2% had the highest dispersion of values for their biaxial

flexural strength results and scaffolds AW 12.5% were the least dispersed, but samples AW 0% had the lowest probability of failure at a set flexural stress.

3.3.6.2.1 Effect of strontium addition to AW porous scaffolds on fracture mechanism in flexure

SEM micrographs of the fracture surfaces of samples tested for biaxial flexural strength are shown in Figure 3.33 and Figure 3.34, at lower and higher magnification, respectively.

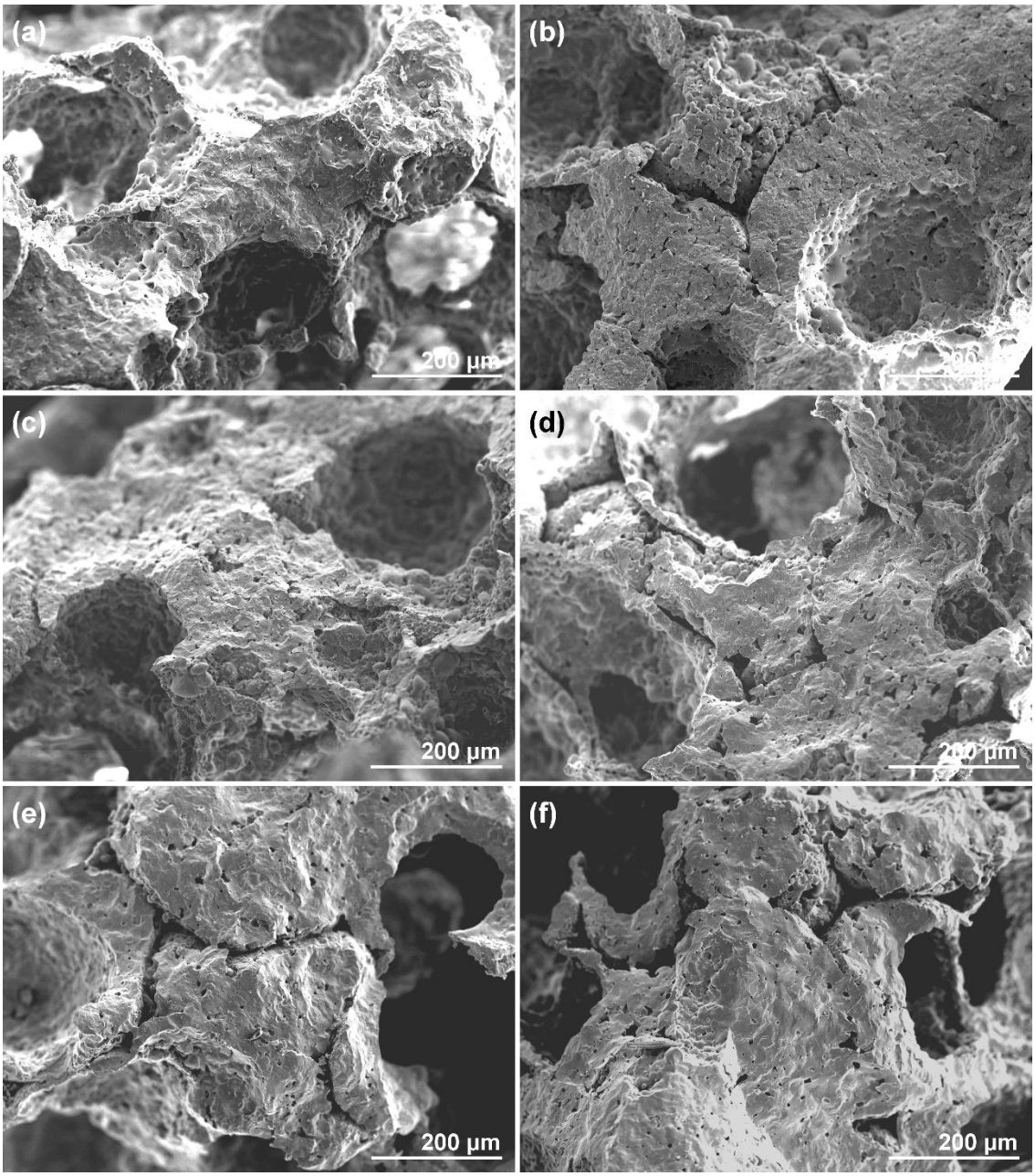

Figure 3.33: SEM micrographs, imaged from secondary electrons, of the fracture surfaces of samples tested for biaxial flexural strength, taken at low magnification. (a) AW 0%, (b) AW 6.2%, (c) AW 12.5 %, (d) AW 18.7%, (e) AW 24.9%, (f) AW 37.4%. Scale bars represent 200 µm.

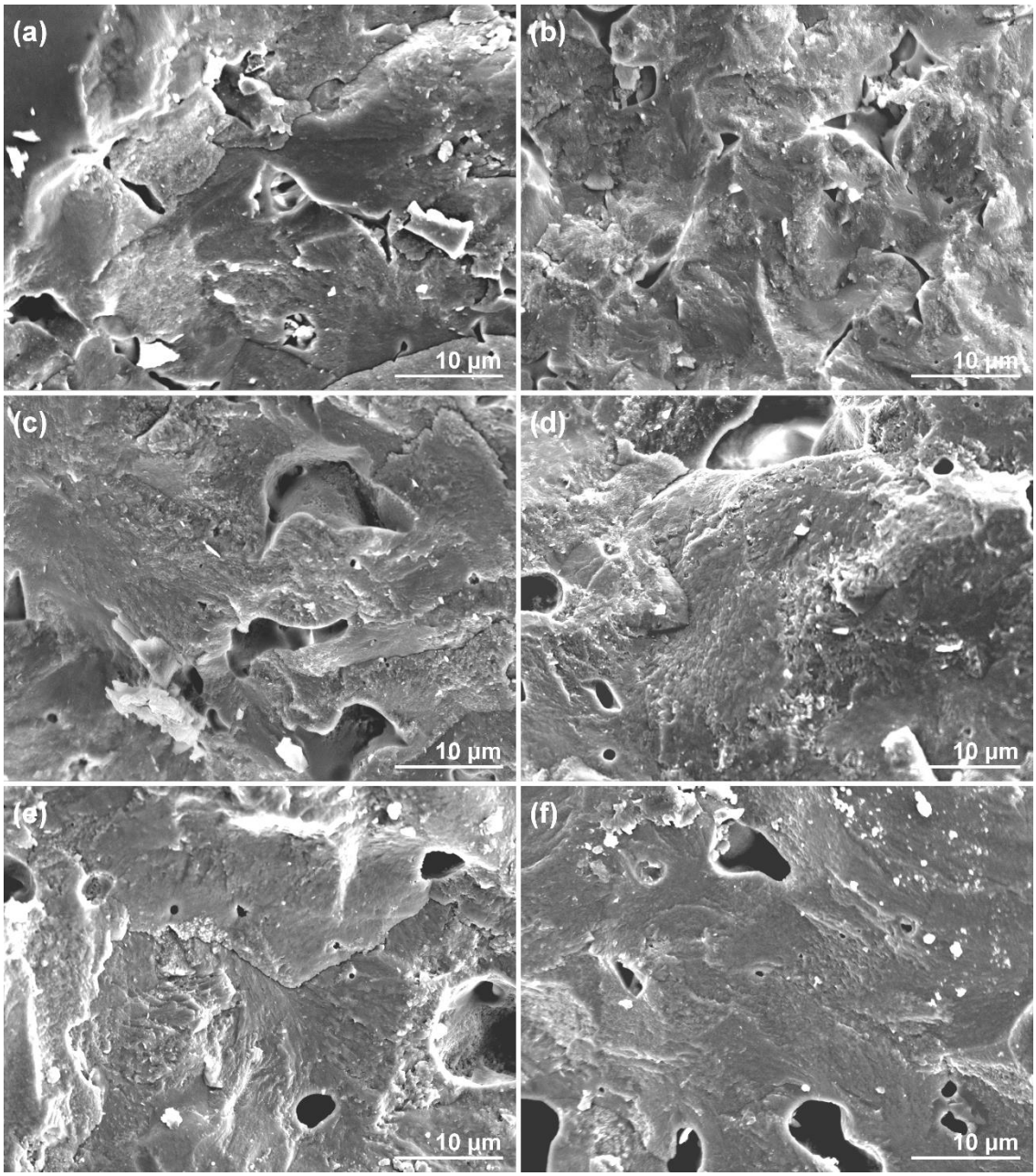

Figure 3.34: SEM micrographs showing details, at higher magnification, of the fracture surfaces of the samples displayed in Figure 3.33. Samples imaged from secondary electrons. (a) AW 0%, (b) AW 6.2%, (c) AW 12.5 %, (d) AW 18.7%, (e) AW 24.9%, (f) AW 37.4%. Scale bars represent 10 µm.

Fracture surfaces of samples tested for biaxial flexural strength appeared very similar to those observed for samples tested in compression (Figure 3.29 and Figure 3.30 in Section 3.3.6.1.1). The cracks propagated through particles, where visible, or through the dense material. Areas of different crystalline compositions could also be seen. The similarity in the aspect of fracture surfaces in compression and in flexure was due to the combination of the intrinsic brittle nature of the materials and their highly porous structure. In fact, because the struts of the porous samples had random orientations,

forces applied in compression to the samples were transmitted as tensile and flexural stresses to the struts, which actually caused failure.

3.3.7 Effect of strontium on the apatite-forming ability of strontium-containing AW glass-ceramic samples

The apatite-forming ability of the materials under study was first assessed on solid discs (Section 3.3.7.1) and then verified on porous scaffolds (Section 3.3.7.2).

3.3.7.1 Effect of strontium on the apatite forming ability of solid discs

3.3.7.1.1 Variation of SBF pH during soaking of discs

pH changes were monitored throughout the experiment and Figure 3.35 summarises the results for the six strontium compositions tested.

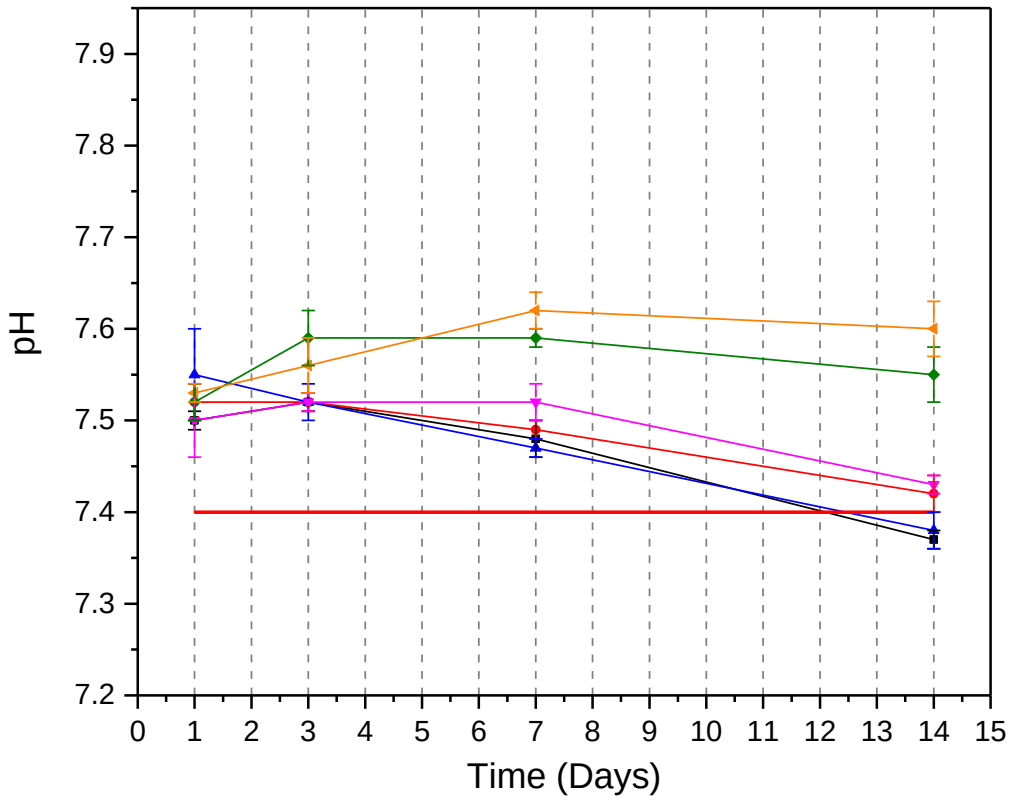

Figure 3.35: pH changes in SBF during soaking of solid discs. ■ AW 0%, ● AW 6.2%, ▲ AW 12.5%, ▼ AW 18.7%, ♦ AW 24.9%, ◄ AW 37.4%, – SBF solution. Error bars indicate the standard deviation (n=3).

After immersing the solid discs, the pH of the SBF solution changed due to ionic release and exchange. Compared to its initial value of 7.40, it first increased for all samples, becoming 7.50 to 7.55 for all compositions after 1 day. It then increased further for samples AW 24.9% and AW 37.4% to 7.60 within 7 days and did not change at the 14 day time-point. For samples AW 0% to AW 18.7%, it decreased after day 1 and reached values lower than the reference in the case of samples AW 0% and AW 12.5%, for which it was found 7.37 and 7.38, respectively. In general, variations of pH were small for all samples, with values remaining in the range 7.37 to 7.62. This could be due to the high volume of SBF used for each sample, chosen in order to avoid saturation of the solution and therefore spontaneous precipitation of apatite crystals instead of material-led bioactivity.

3.3.7.1.2 Surface morphology of discs during SBF soaking

Samples were tested for 1, 3, 7 and 14 days and their surface changes were monitored using SEM. Micrographs taken at the different time-points are shown in Figure 3.36 to Figure 3.41 for compositions AW 0% to AW 37.4%, looking for deposited apatite.

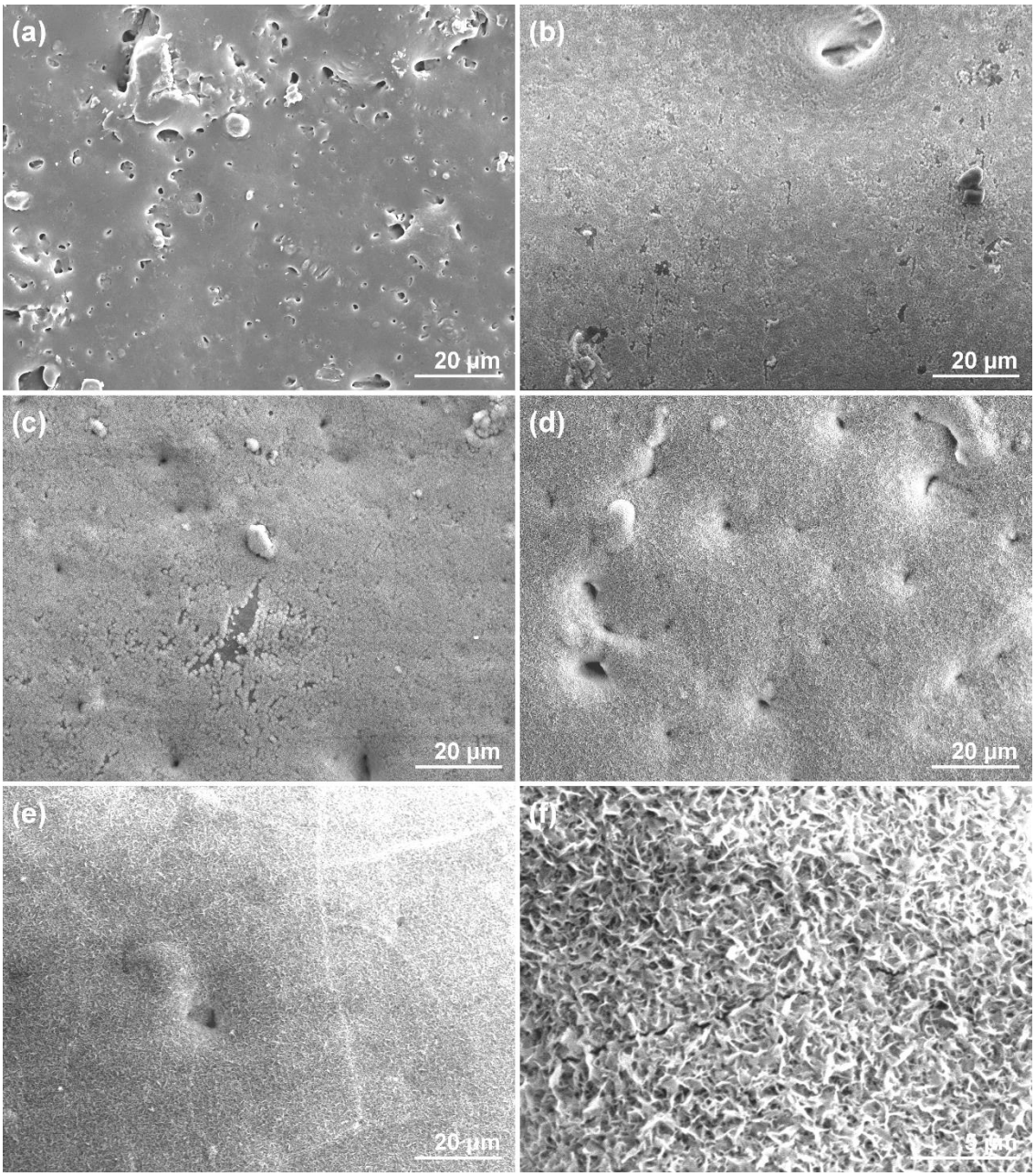

Figure 3.36: SEM micrographs, imaged from secondary electrons, of the surface of AW 0% solid discs upon soaking in SBF solution. (a) Disc as such, (b) 1 day soaking, (c) 3 days soaking, (d) 7 days soaking, (e) 14 days soaking, (f) higher magnification of the 14 day sample surface. Error bars in (a-e) represent 20 µm; the error bar in (f) represents 5 µm.

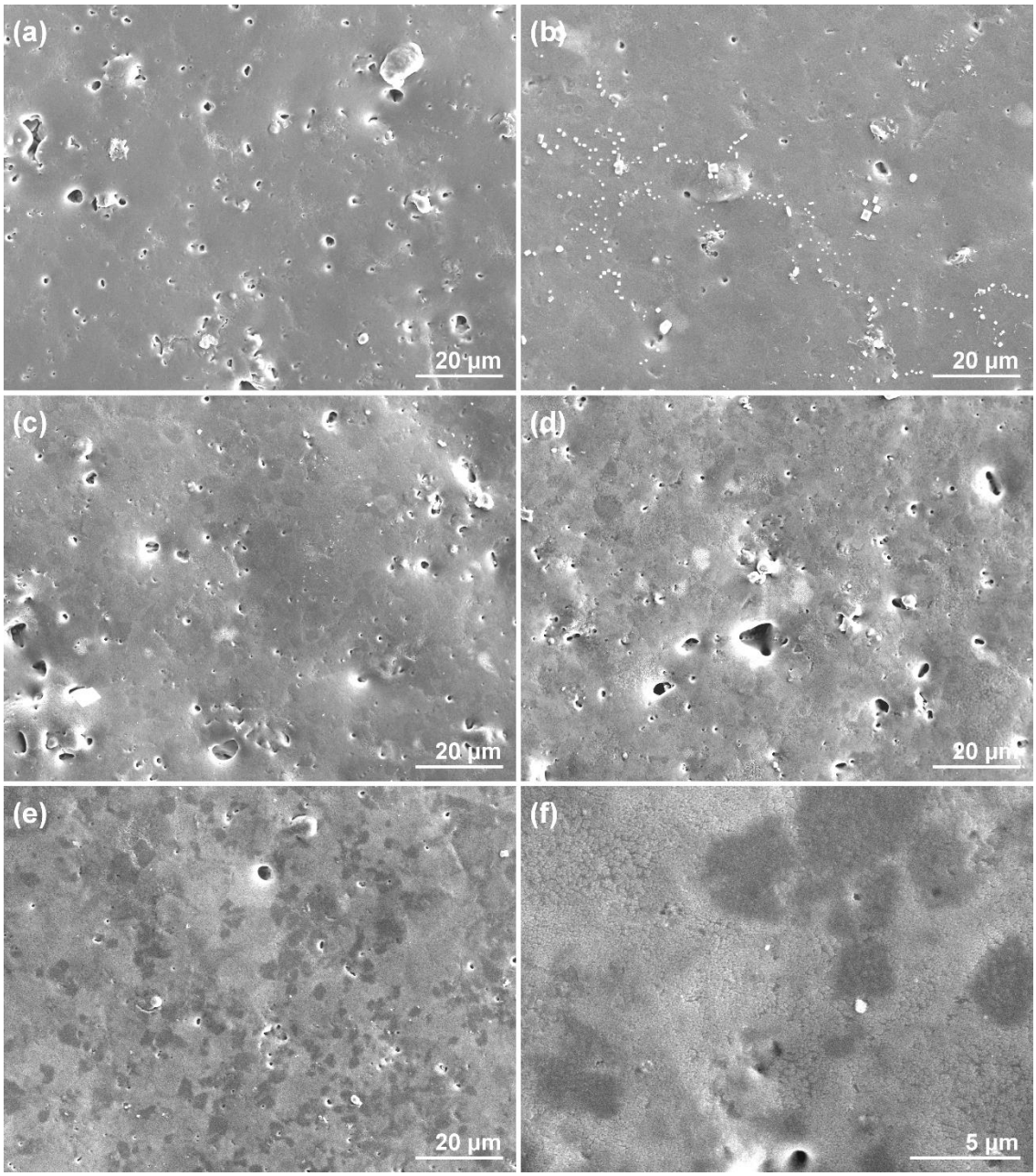

Figure 3.37: SEM micrographs, imaged from secondary electrons, of the surface of AW 6.2% solid discs upon soaking in SBF solution. (a) Disc as such, (b) 1 day soaking, (c) 3 days soaking, (d) 7 days soaking, (e) 14 days soaking, (f) higher magnification of the 14 day sample surface. Error bars in (a-e) represent 20 µm; the error bar in (f) represents 5 µm.

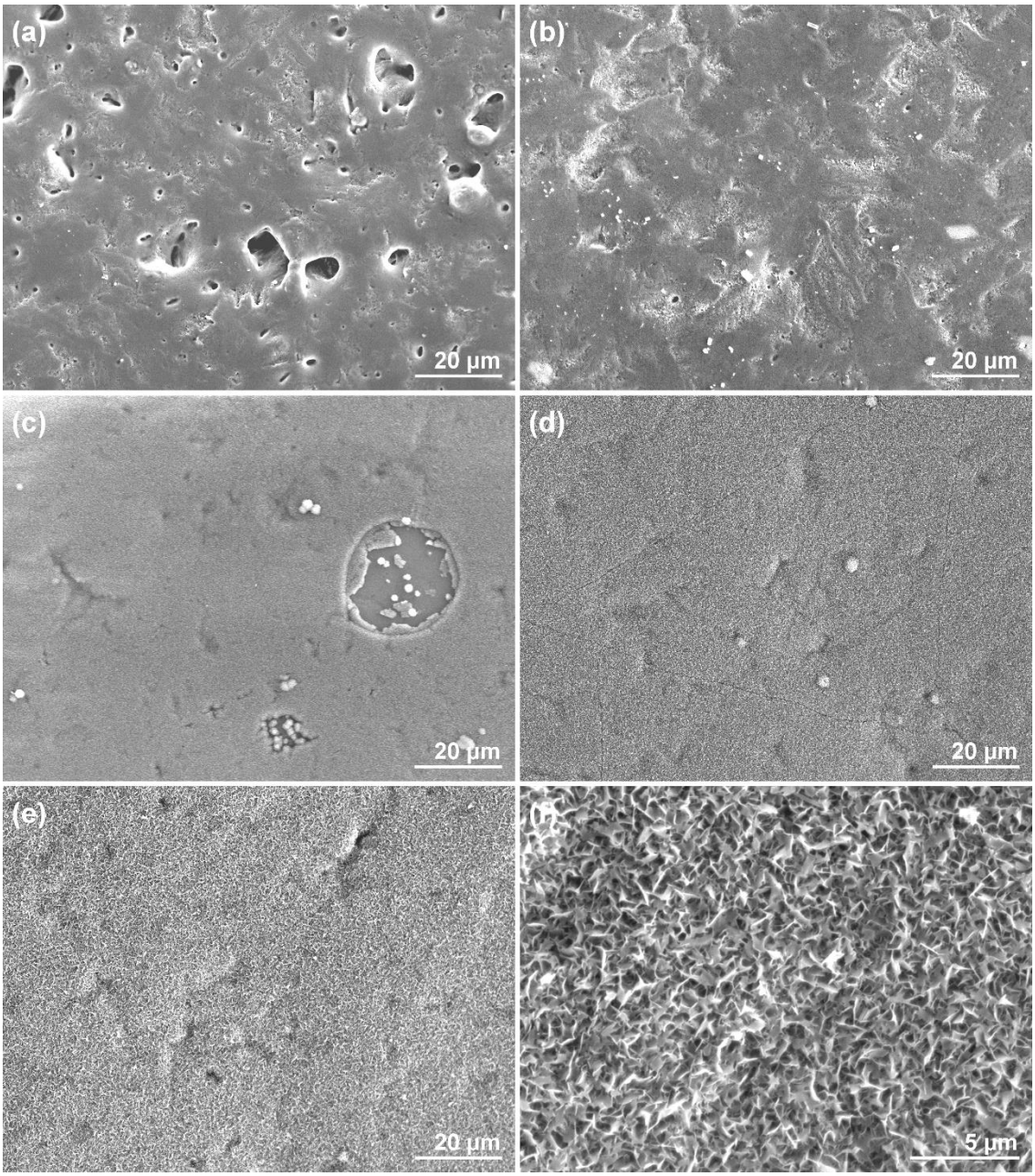

Figure 3.38: SEM micrographs, imaged from secondary electrons, of the surface of AW 12.5% solid discs upon soaking in SBF solution. (a) Disc as such, (b) 1 day soaking, (c) 3 days soaking, (d) 7 days soaking, (e) 14 days soaking, (f) higher magnification of the 14 day sample surface. Error bars in (a-e) represent 20 µm; the error bar in (f) represents 5 µm.

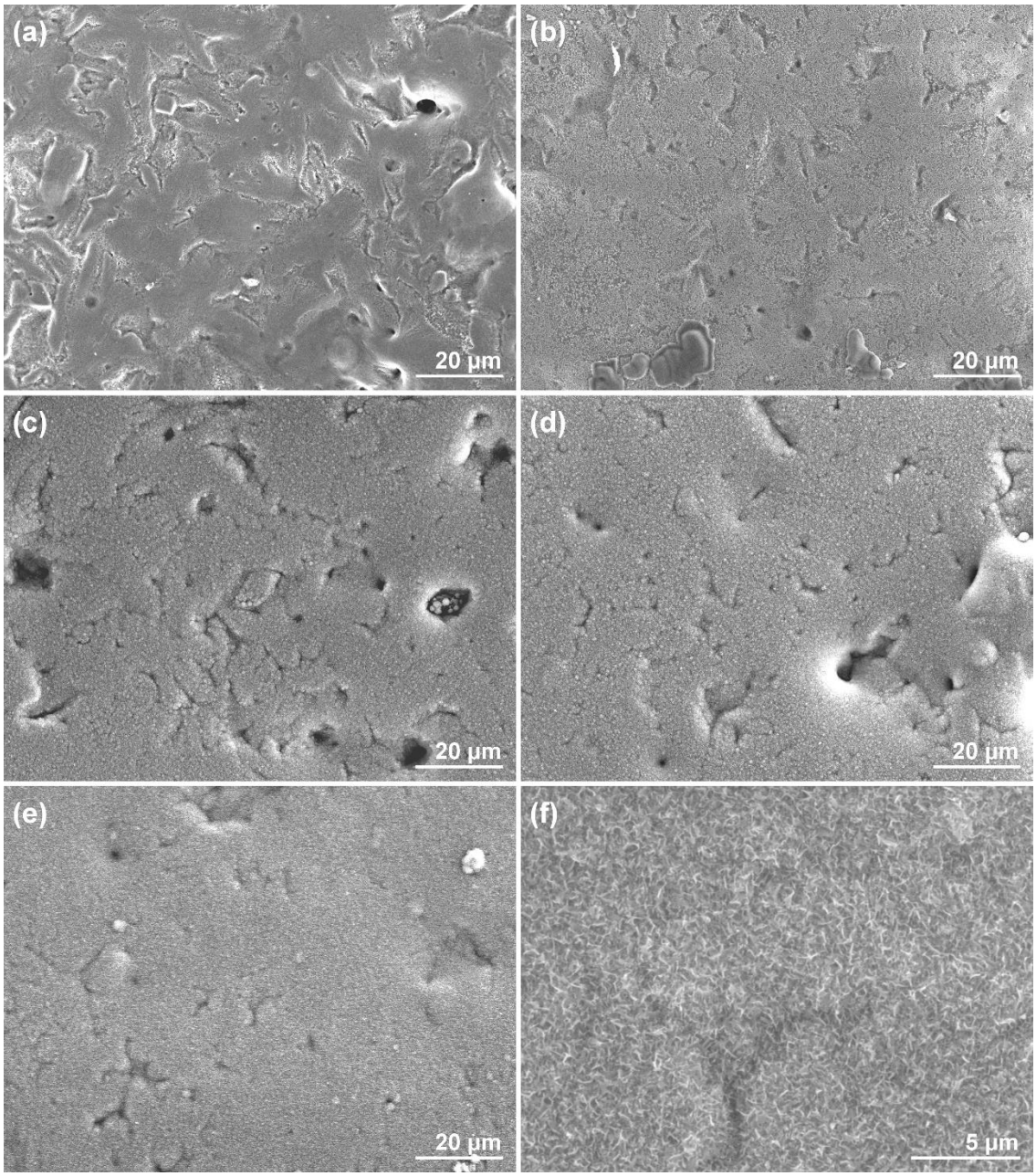

Figure 3.39: SEM micrographs, imaged from secondary electrons, of the surface of AW 18.7% solid discs upon soaking in SBF solution. (a) Disc as such, (b) 1 day soaking, (c) 3 days soaking, (d) 7 days soaking, (e) 14 days soaking, (f) higher magnification of the 14 day sample surface. Error bars in (a-e) represent 20 µm; the error bar in (f) represents 5 µm.

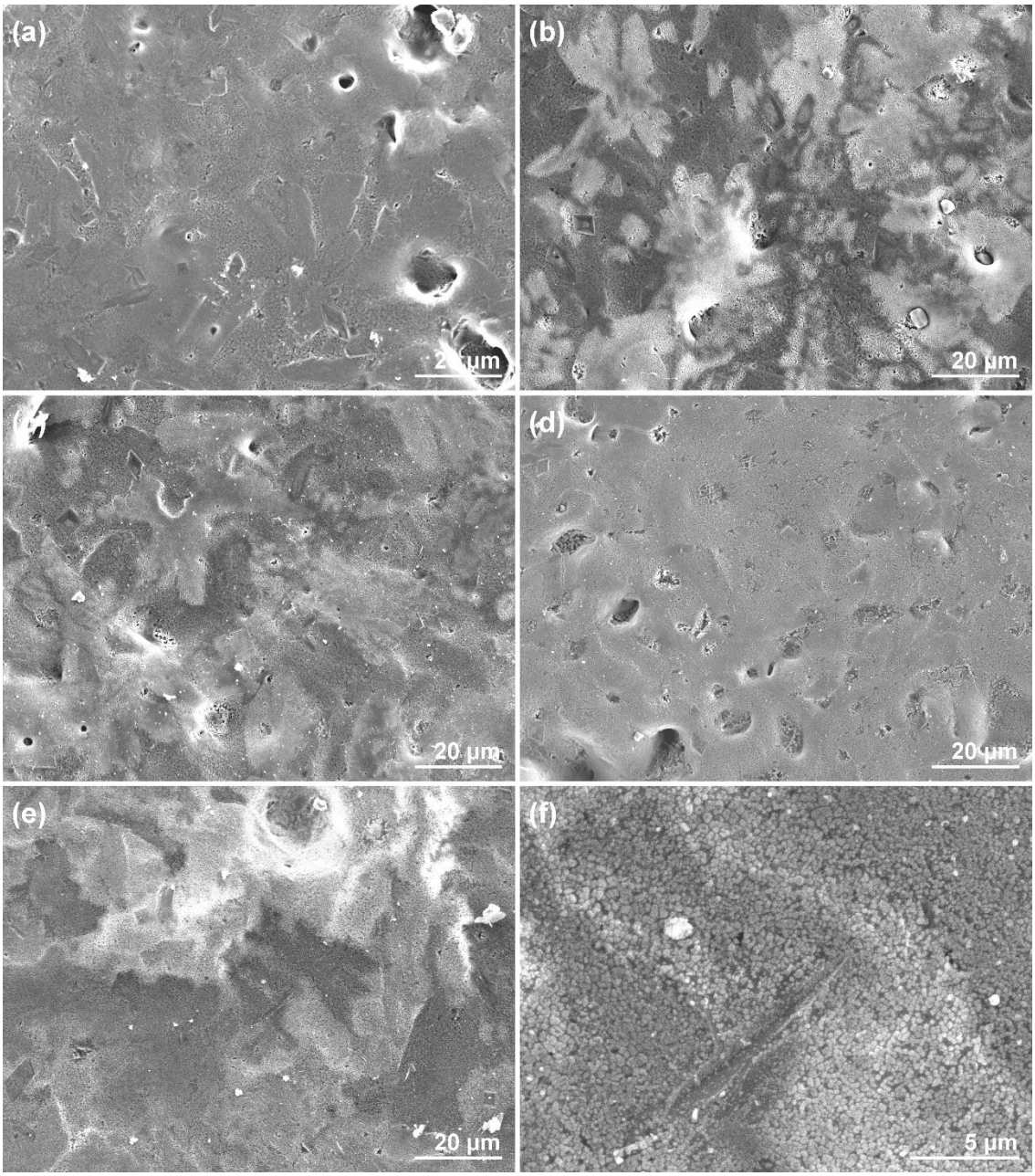

Figure 3.40: SEM micrographs, imaged from secondary electrons, of the surface of AW 24.9% solid discs upon soaking in SBF solution. (a) Disc as such, (b) 1 day soaking, (c) 3 days soaking, (d) 7 days soaking, (e) 14 days soaking, (f) higher magnification of the 14 day sample surface. Error bars in (a-e) represent 20 µm; the error bar in (f) represents 5 µm.

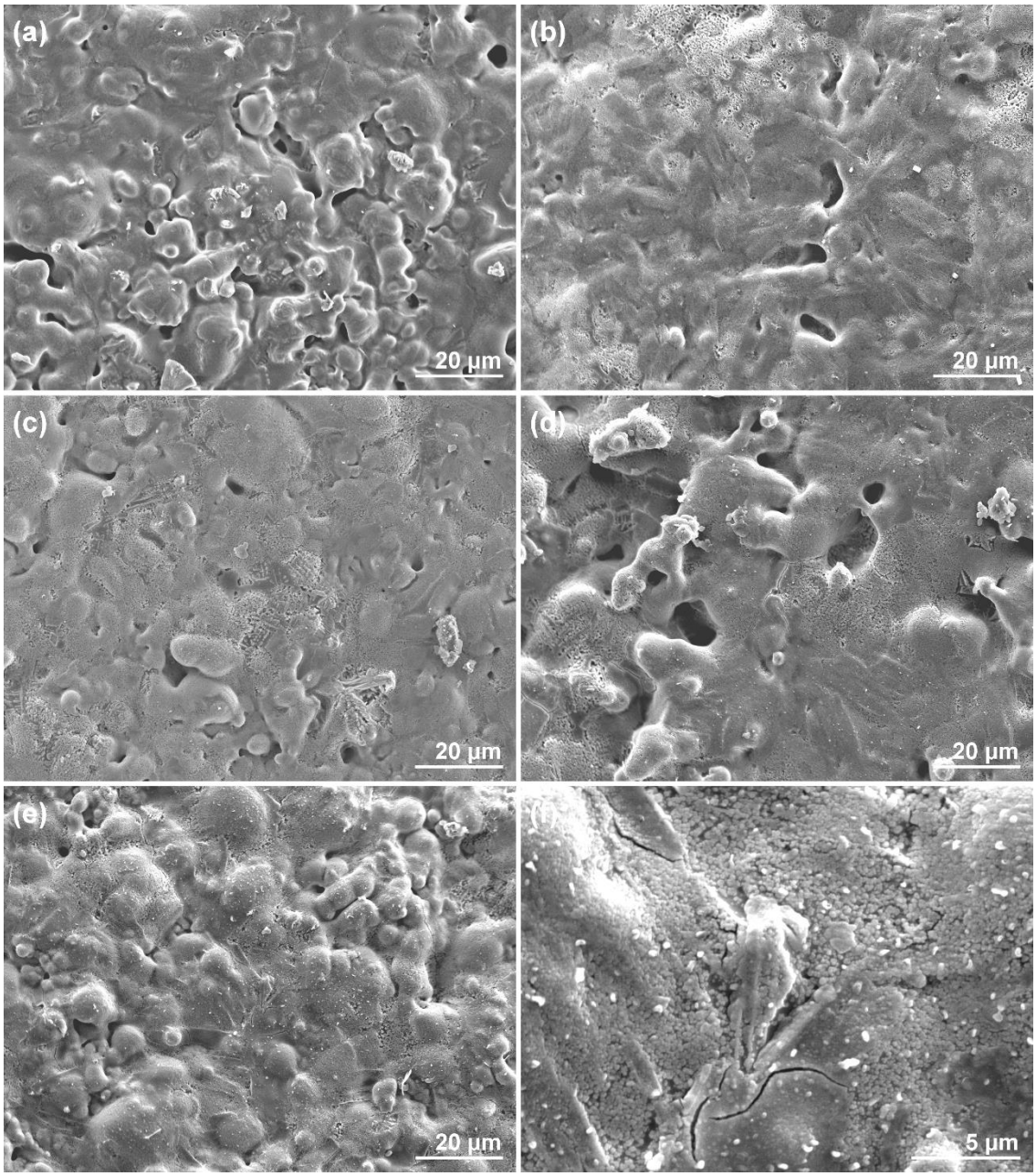

Figure 3.41: SEM micrographs, imaged from secondary electrons, of the surface of AW 37.4% solid discs upon soaking in SBF solution. (a) Disc as such, (b) 1 day soaking, (c) 3 days soaking, (d) 7 days soaking, (e) 14 days soaking, (f) higher magnification of the 14 day sample surface. Error bars in (a-e) represent 20 µm; the error bar in (f) represents 5 µm.

Changes of surface appearance suggested that only samples AW 0% and AW 18.7% underwent the deposition of apatite crystals after as early as 1 day of soaking in SBF solution. After 3 days of immersion, also composition AW 12.5% was covered in apatite. For these three compositions, the layer grew over the time-points becoming thicker. High magnification micrographs in panel (f) of Figure 3.36, Figure 3.38 and

Figure 3.39 showed the typical morphology of hydroxyapatite deposited on AW 0%, AW 12.5% and AW 18.7% discs from SBF solution, respectively, with needle and plate-like crystals as in the cauliflower structures often observed in apatite formation studies. However, crystals on samples AW 18.7% appeared smaller than those on samples AW 0% and AW 12.5%, suggesting that their growth could have been slower or, being samples AW 18.7% richer in strontium, that a different apatite was deposited. No deposition was observed on samples AW 6.2%, AW 24.9% and AW 37.4%, although a modification of their surface could be observed. In samples AW 6.2%, darker areas appeared with increasing soaking time, which could indicate that some zones with a different molecular composition were exposed over time. Changes in the surface appearance in samples AW 24.9% and AW 37.4% were stronger, with their ceramic phases becoming more evident. This could suggest that, in these samples, the residual glass phase was preferentially dissolved in the solution, leaving behind their ceramic phases. While the lack of apatite formation for samples AW 24.9% and AW 37.4% could be inferred from the pH readings (Figure 3.35), this was not expected for samples AW 6.2%, whose behaviour in SBF solution needs further investigation.

3.3.7.1.3 Surface composition of strontium AW discs after soaking in SBF

Data in Table 3.13 to Table 3.18 report the EDS atomic compositions (10 kV) of the surface of the same samples tested for apatite forming ability, which were shown in Figure 3.36 to Figure 3.41.

Table 3.13: EDS atomic composition (at%) of AW 0% solid discs soaked in SBF solution over time.

Atom	0 days	1 day	3 days	7 days	14 days
Si	31.34	24.01	9.52	0.40	0.55
Mg	4.28	4.10	2.95	2.04	2.25
F	2.29	2.50	1.84	2.07	1.87
Ca	46.34	48.40	54.20	55.92	55.94
P	15.75	20.99	31.49	39.57	39.29
Sr	0.00	0.00	0.00	0.00	0.10

Table 3.14: EDS atomic composition (at%) of AW 6.2% solid discs soaked in SBF solution over time.

Atom	0 days	1 day	3 days	7 days	14 days
Si	31.46	30.85	30.67	30.53	30.36
Mg	4.35	5.31	4.97	5.35	5.08
F	1.92	2.15	1.54	1.12	1.42
Ca	41.22	41.46	41.57	42.30	41.81
P	15.80	15.02	15.96	14.96	15.34
Sr	5.25	5.21	5.29	5.74	5.99

Table 3.15: EDS atomic composition (at%) of AW 12.5% solid discs soaked in SBF solution over time.

Atom	0 days	1 day	3 days	7 days	14 days
Si	30.78	26.29	16.84	0.41	0.81
Mg	5.19	4.31	2.85	1.94	1.97
F	2.63	2.97	3.54	2.03	1.65
Ca	35.85	37.93	42.12	56.55	54.69
P	14.83	13.07	23.12	39.05	40.67
Sr	10.72	15.43	11.53	0.02	0.21

Table 3.16: EDS atomic composition (at%) of AW 18.7% solid discs soaked in SBF solution over time.

Atom	0 days	1 day	3 days	7 days	14 days
Si	31.43	25.71	15.19	2.42	0.31
Mg	4.90	5.06	2.55	2.26	1.94
F	1.82	1.79	3.61	3.19	2.37
Ca	31.66	33.29	36.10	47.96	52.18
P	14.12	19.08	19.37	38.14	39.91
Sr	16.07	15.07	23.18	6.03	3.29

Table 3.17: EDS atomic composition (at%) of AW 24.9% solid discs soaked in SBF solution over time.

Atom	0 days	1 day	3 days	7 days	14 days
Si	33.18	23.98	20.95	25.38	18.55
Mg	5.64	4.35	3.33	5.14	3.55
F	1.84	3.51	3.98	1.62	4.10
Ca	23.71	26.12	27.20	26.01	27.30
P	14.04	14.55	16.04	22.28	18.09
Sr	21.59	27.49	28.50	19.57	28.41

Table 3.18: EDS atomic composition (at%) of AW 37.4% solid discs soaked in SBF solution over time.

Atom	0 days	1 day	3 days	7 days	14 days
Si	30.73	24.64	23.40	19.69	14.92
Mg	4.72	6.46	5.47	5.06	4.26
F	2.05	1.93	1.70	1.14	1.71
Ca	12.55	15.86	17.12	20.60	22.84
P	16.82	21.00	22.90	26.07	30.16
Sr	33.13	30.11	29.41	27.44	26.11

Variations in surface composition reflected what observed with SEM micrographs: samples AW 0%, AW 12.5% and AW 18.7% changed their composition as the apatite layer grew, increasing in calcium and phosphorus and reducing the amount of silicon, magnesium and strontium. No relevant changes could be seen for samples AW 6.2%, which maintained their composition throughout the two weeks of testing. An increase in calcium and phosphorus, along with a decrease in silicon, magnesium and strontium could also be observed for samples AW 24.9% and AW 37.4%, suggesting that a bioactive ionic exchange took place for these compositions as well, although it was slower and not strong enough to see the formation of the apatite layer during imaging (Figure 3.40 and Figure 3.41, respectively). The stoichiometric 1.67 calcium:phosphorus ratio of hydroxyapatite could not be found for any of the samples; however, samples AW 0% reached the value of 1.72, 1.41 and 1.42 after 3, 7 and 14 days respectively, while for samples AW 12.5% it was found 1.82, 1.45 and 1.34 after 3, 7 and 14 days respectively. It is therefore possible that the deposited apatite was actually a calcium-deficient hydroxyapatite, or that the variation from the expected value was due to instrumental error. In samples AW 18.7%, a small amount (3.29 at%) of strontium was still detected after 14 days of soaking, while it was 0.21 at% for AW

12.5%. This could mean that the deposited layer was a strontium-hydroxyapatite for composition AW 18.7%, which could also be the reason for the crystal morphology looking slightly different in Figure 3.39.

3.3.7.1.4 Ionic release from strontium AW discs during soaking in SBF

The ion release from solid discs was measured from the SBF solution, collected after soaking at each time-point, using ICP-OES and results are summarised in Figure 3.42.

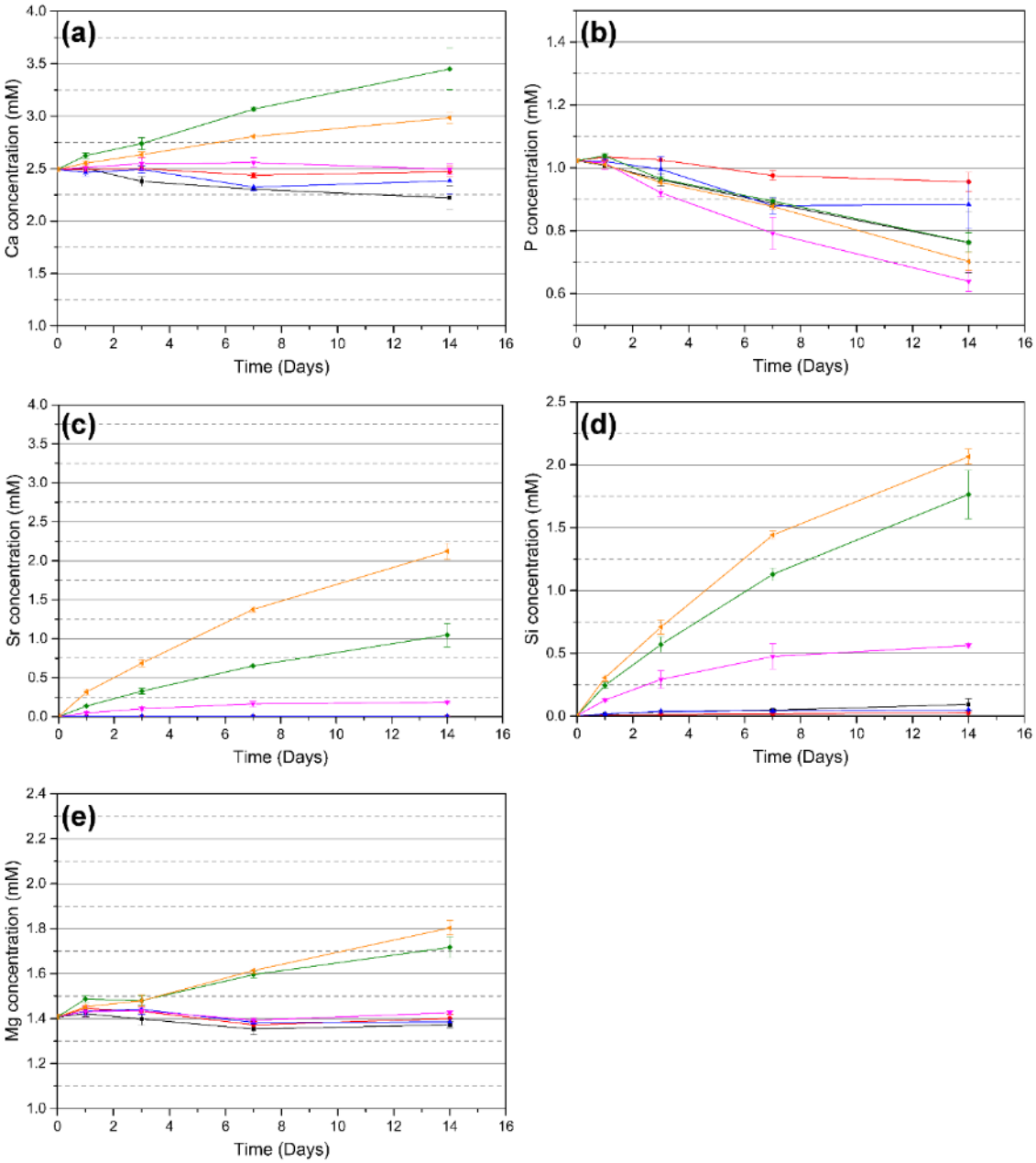

Figure 3.42: ICP-OES ion release measured from solid discs soaked in SBF solution for up to 2 weeks. (a) Calcium, (b) phosphorus, (c) strontium, (d) silicon, (e) magnesium. ■ AW 0%, ● AW 6.2%, ▲ AW 12.5%, ▼ AW 18.7%, ♦ AW 24.9%, ◄ AW 37.4%. Error bars indicate the standard deviation (n=3).

For all five ions tested (calcium, phosphorus, strontium, silicon and magnesium), little variations could be found in their concentration for compositions AW 0%, AW 6.2% and AW 12.5% compared to SBF as such (values at the 0 day time-point on the graphs). In particular, calcium and phosphorus slightly decreased from the baseline, no release of strontium could be detected and silicon and magnesium remained at similar concentrations compared to the initial SBF. For composition AW 18.7%,

calcium remained unvaried, phosphorus decreased the most, by 0.4 mM, strontium and silicon were progressively released with time up to 0.2 and 0.6 mM, respectively, while magnesium also remained unvaried. Samples AW 24.9% and AW 37.4% induced the highest release for all the tested ions: calcium, strontium, silicon and magnesium all increased, while phosphorus decreased by about 0.3 mM for both samples. In general, the concentration of strontium followed the expected trend, increasing with time and with the amount of strontium oxide in the samples. The fact that compositions AW 24.9% and AW 37.4% gave the highest release corresponded with the SEM and EDS results presented in Figure 3.40, Figure 3.41, Table 3.17 and Table 3.18, from which it was hypothesised a prolonged dissolution of the material allowed by the delayed formation of the apatite layer. The decrease in phosphorus concentration in the solution indicated that this ion was consumed by the soaked samples for their bioactivity process. The lack of detected release for samples AW 0% and AW 12.5% could be due to the formation of the apatite layer slowing down further ion release. Although samples AW 6.2% behaved similarly to AW 0% and AW 12.5% in terms of ion release, they did not show any sign of apatite forming during SEM imaging nor EDS compositional analysis, therefore further investigations would be required for this disc composition.

3.3.7.2 Effect of strontium on the apatite forming ability of porous scaffolds

3.3.7.2.1 Variation of SBF pH during soaking of porous scaffolds

Bioactivity was also tested on porous scaffolds, with soaking times of 1 day, 7 days and 14 days. Figure 3.43 shows the pH variation of the SBF solution during testing.

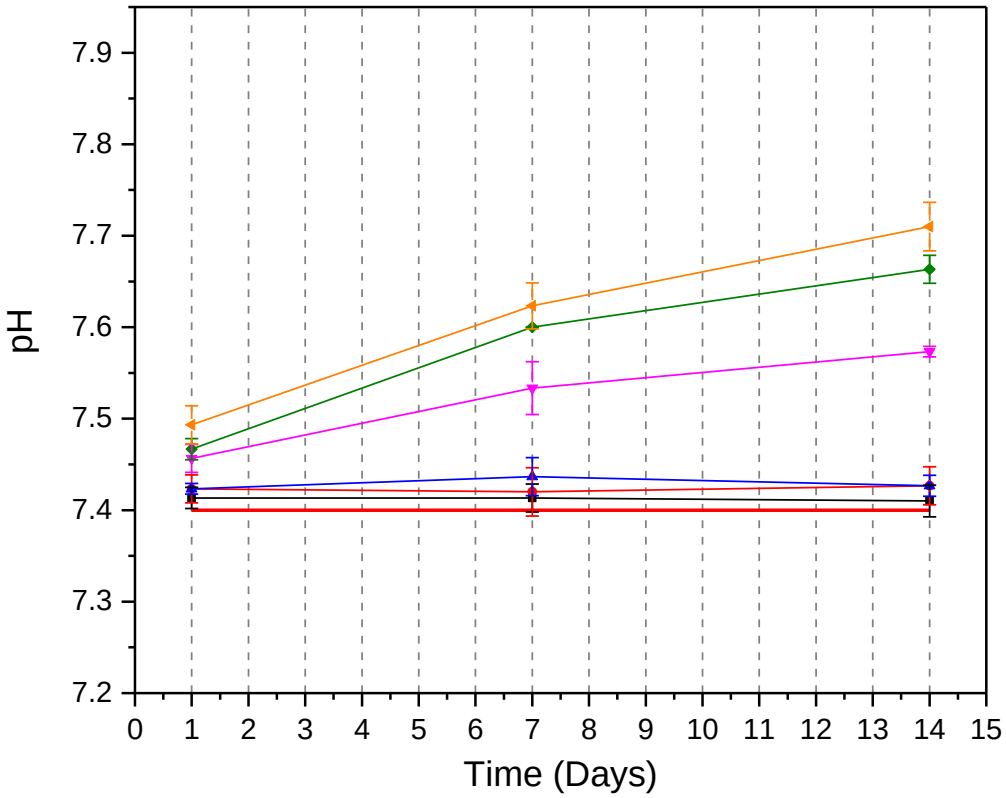

Figure 3.43: pH changes in SBF during soaking of porous scaffolds. ■ AW 0%, ● AW 6.2%, ▲ AW 12.5%, ▼ AW 18.7%, ♦ AW 24.9%, ◄ AW 37.4%, – SBF solution. Error bars indicate the standard deviation (n=3).

The pH did not vary significantly for compositions AW 0%, AW 6.2% and AW 12.5%, which maintained a physiological pH around 7.43 throughout the whole experiment. On the contrary, the pH of samples AW 18.7%, AW 24.9% and AW 37.4% increased with time, with compositions containing more strontium leading to a higher increase in pH. For samples AW 18.7%, the pH was 7.46 after 1 day of soaking, 7.53 after 7 days and 7.57 after 14 days; for samples AW 24.9% it was 7.47 after 1 day, 7.60 after 7 days and 7.66 after 14 days, while for samples AW 37.4% it was 7.49 after 1 day, 7.62 after 7 days and 7.71 after 14 days. This was different from what observed with flat solid discs (Figure 3.35), where pH either decreased or maintained the value reached at 7 days. These results for the porous scaffolds suggested that the three lower strontium compositions maintained an ionic equilibrium in the solution, while the three higher compositions kept dissolving and releasing ions over time. It must be noted that the pH measurements presented here described the general variations in the whole volume of SBF (30 mL), while bioactivity phenomena happen locally near the surface of the soaked sample. As it will be explained with the following pictures, in the case of porous scaffolds the growth of the apatite layer could only be observed for inner struts, suggesting that the conditions for the formation of apatite were reached only in a more

enclosed environment. In addition, as it was the case for the solid discs, the early formation of apatite in the samples could have prevented the further release of ions, keeping the pH of the SBF solution stable, while this did not happen for samples with a slower bioactivity behaviour, i.e. AW 18.7%, AW 24.9% and AW 37.4%.

3.3.7.2.2 Surface morphology of porous scaffold struts after soaking in SBF

Pictures in Figure 3.44 to Figure 3.49 are the SEM micrographs of scaffold struts at the different time-points of soaking in SBF solution. As mentioned before, the struts shown in the pictures are inner struts, as apatite could not be detected on outer struts for these samples. For this reason, the EDS signal could not be recorded, which would have provided compositional information about the deposited layer.

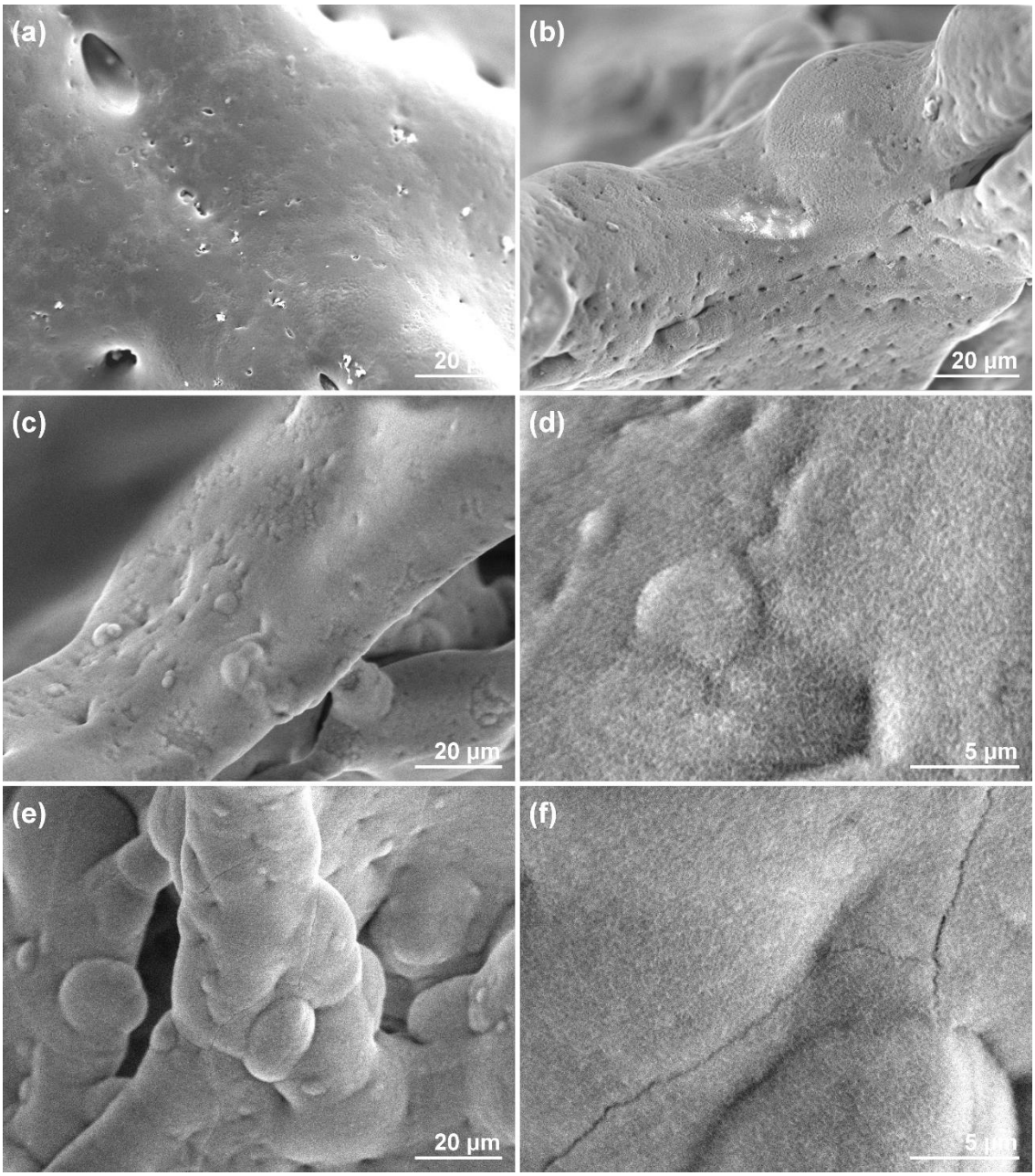

Figure 3.44: SEM micrographs, imaged from secondary electrons, of the surface of AW 0% porous scaffolds upon soaking in SBF solution. (a) Scaffold as such, (b) 1 day of soaking, (c) 7 days of soaking, (d) higher magnification of the 7 day sample surface, (e) 14 days of soaking, (f) higher magnification of the 14 day sample surface. Error bars in (a-c, e) represent 20 µm; error bars in (d, f) represent 5 µm.

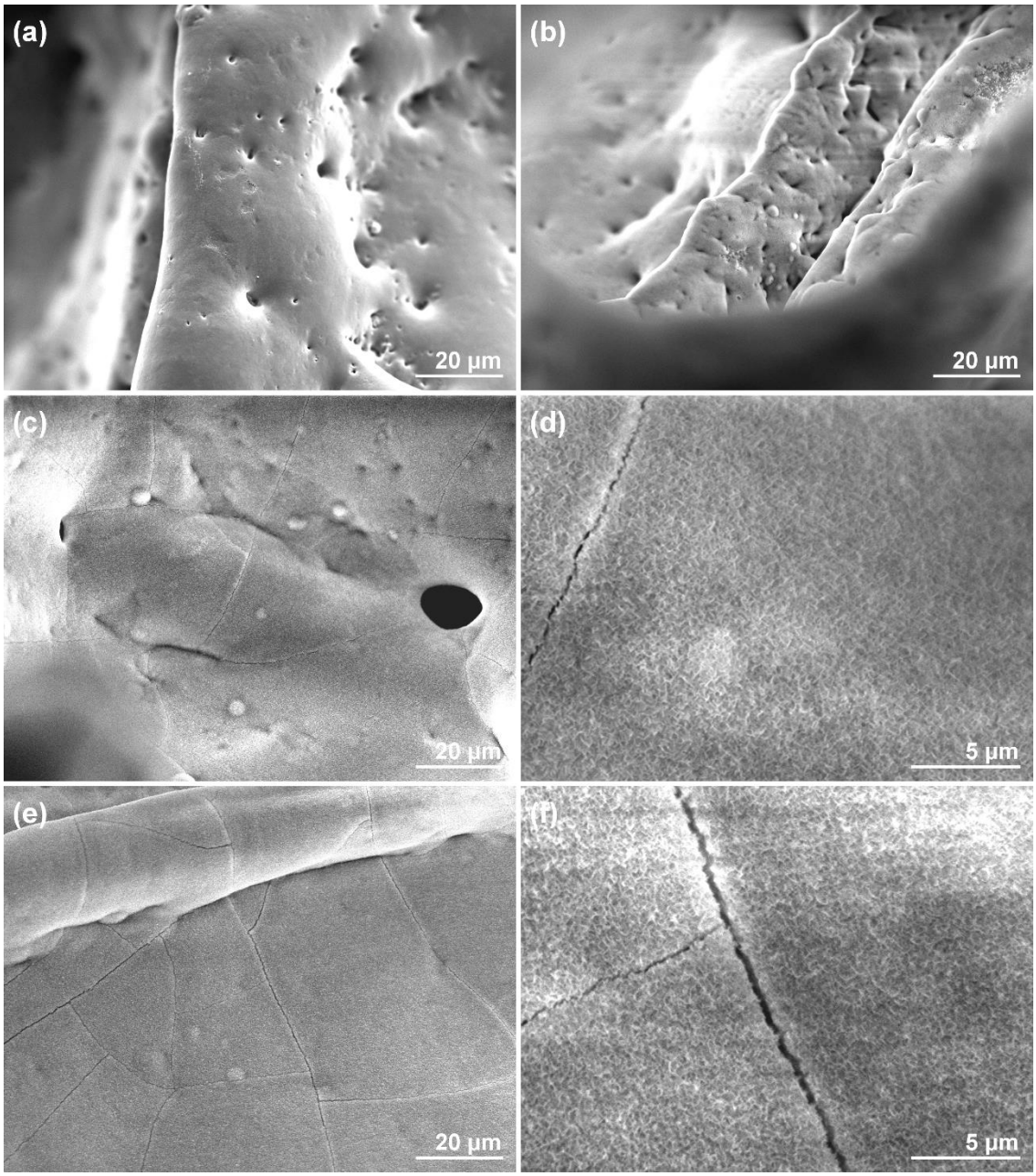

Figure 3.45: SEM micrographs, imaged from secondary electrons, of the surface of AW 6.2% porous scaffolds upon soaking in SBF solution. (a) Scaffold as such, (b) 1 day of soaking, (c) 7 days of soaking, (d) higher magnification of the 7 day sample surface, (e) 14 days of soaking, (f) higher magnification of the 14 day sample surface. Error bars in (a-c, e) represent 20 µm; error bars in (d, f) represent 5 µm.

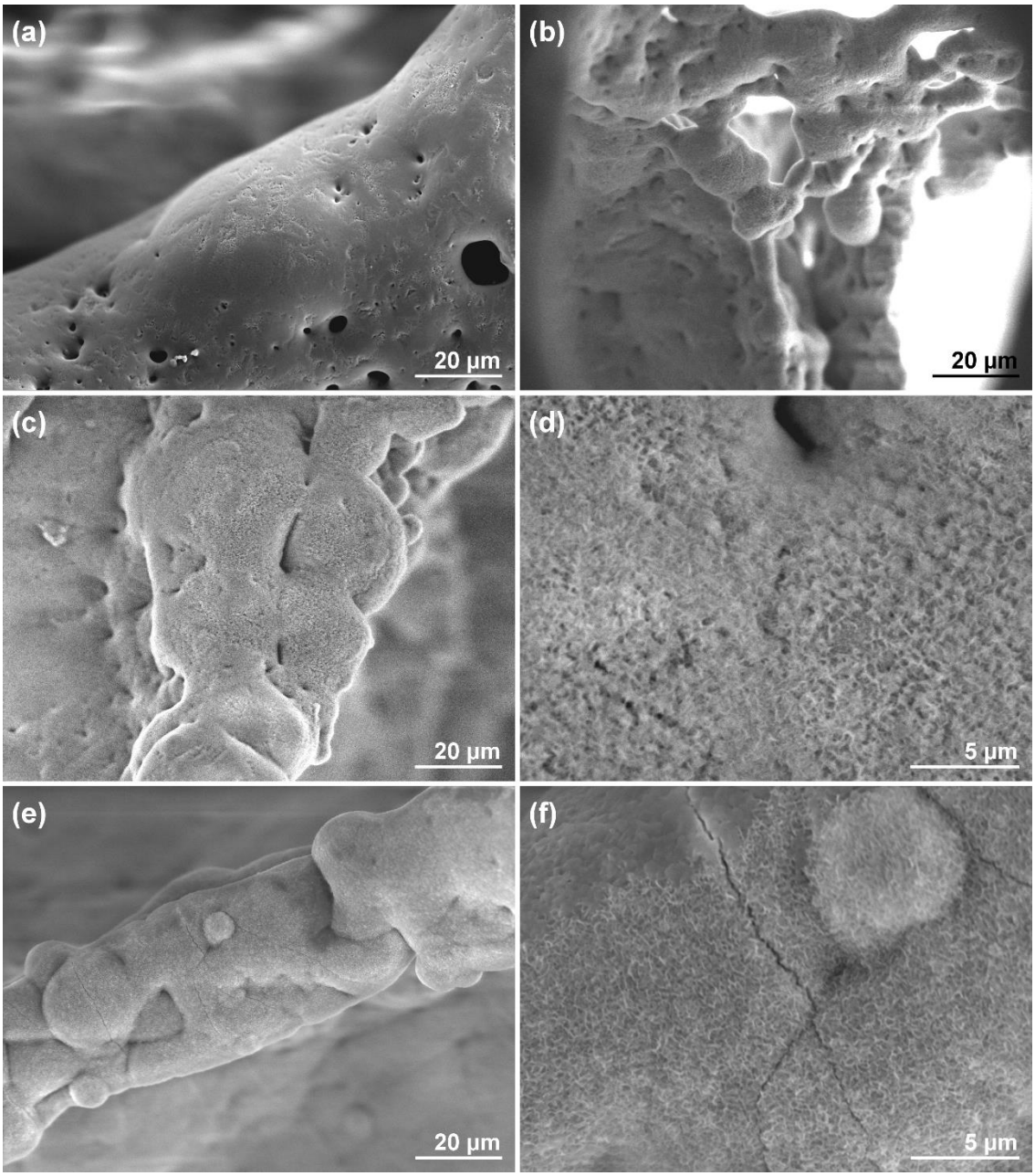

Figure 3.46: SEM micrographs, imaged from secondary electrons, of the surface of AW 12.5% porous scaffolds upon soaking in SBF solution. (a) Scaffold as such, (b) 1 day of soaking, (c) 7 days of soaking, (d) higher magnification of the 7 day sample surface, (e) 14 days of soaking, (f) higher magnification of the 14 day sample surface. Error bars in (a-c, e) represent 20 µm; error bars in (d, f) represent 5 µm.

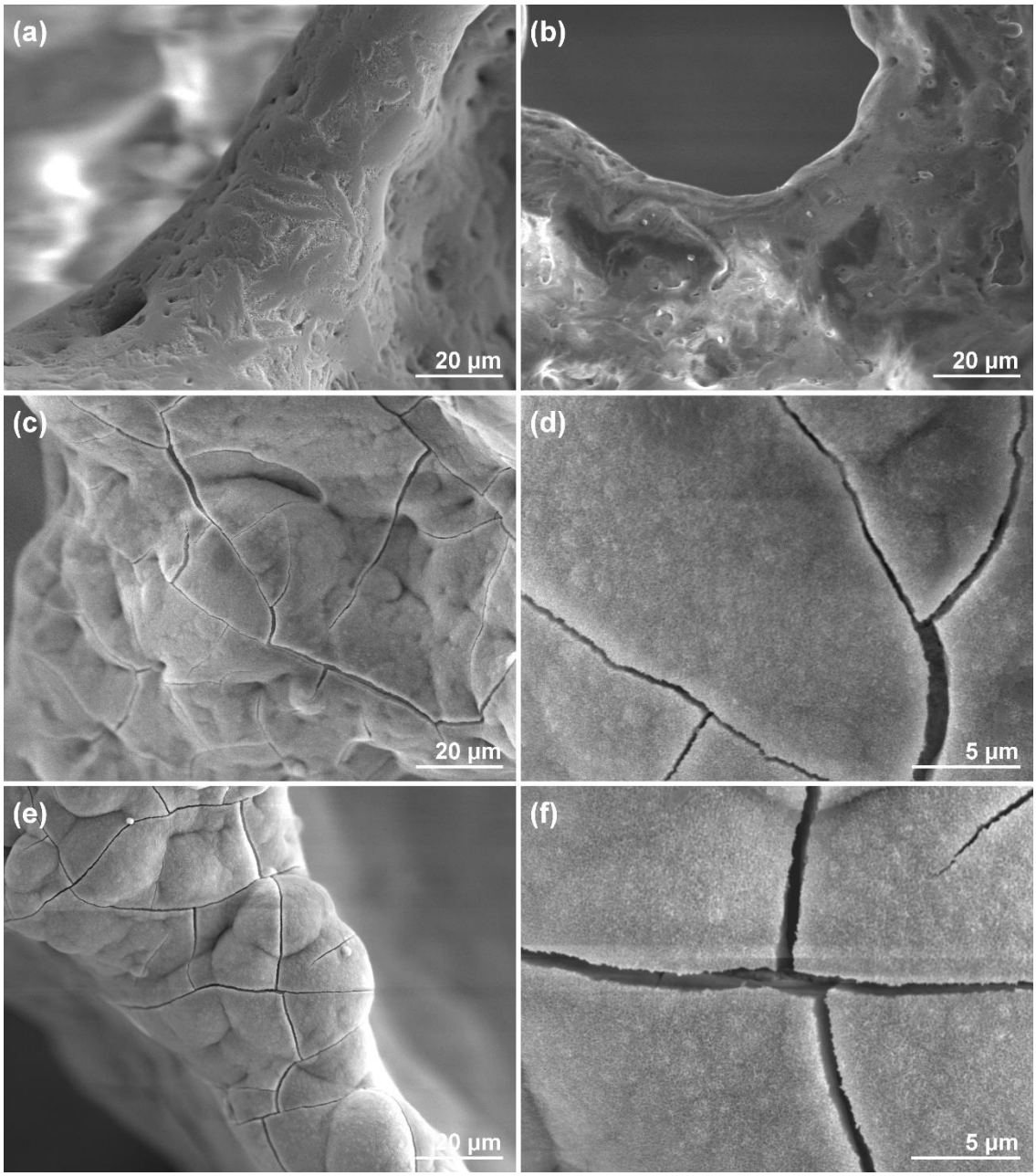

Figure 3.47: SEM micrographs, imaged from secondary electrons, of the surface of AW 18.7% porous scaffolds upon soaking in SBF solution. (a) Scaffold as such, (b) 1 day of soaking, (c) 7 days of soaking, (d) higher magnification of the 7 day sample surface, (e) 14 days of soaking, (f) higher magnification of the 14 day sample surface. Error bars in (a-c, e) represent 20 µm; error bars in (d, f) represent 5 µm.

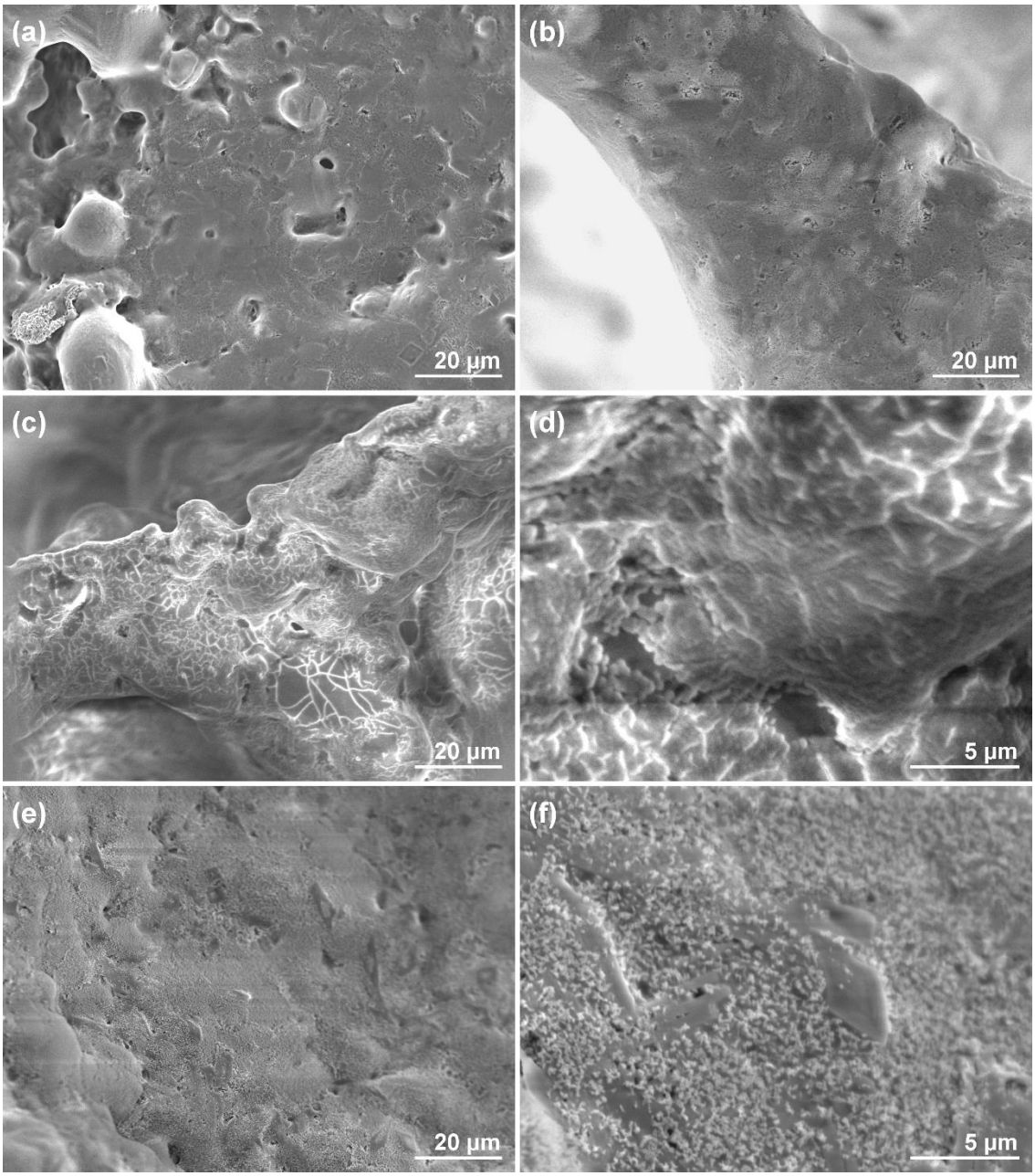

Figure 3.48: SEM micrographs, imaged from secondary electrons, of the surface of AW 24.9% porous scaffolds upon soaking in SBF solution. (a) Scaffold as such, (b) 1 day of soaking, (c) 7 days of soaking, (d) higher magnification of the 7 day sample surface, (e) 14 days of soaking, (f) higher magnification of the 14 day sample surface. Error bars in (a-c, e) represent 20 µm; error bars in (d, f) represent 5 µm.

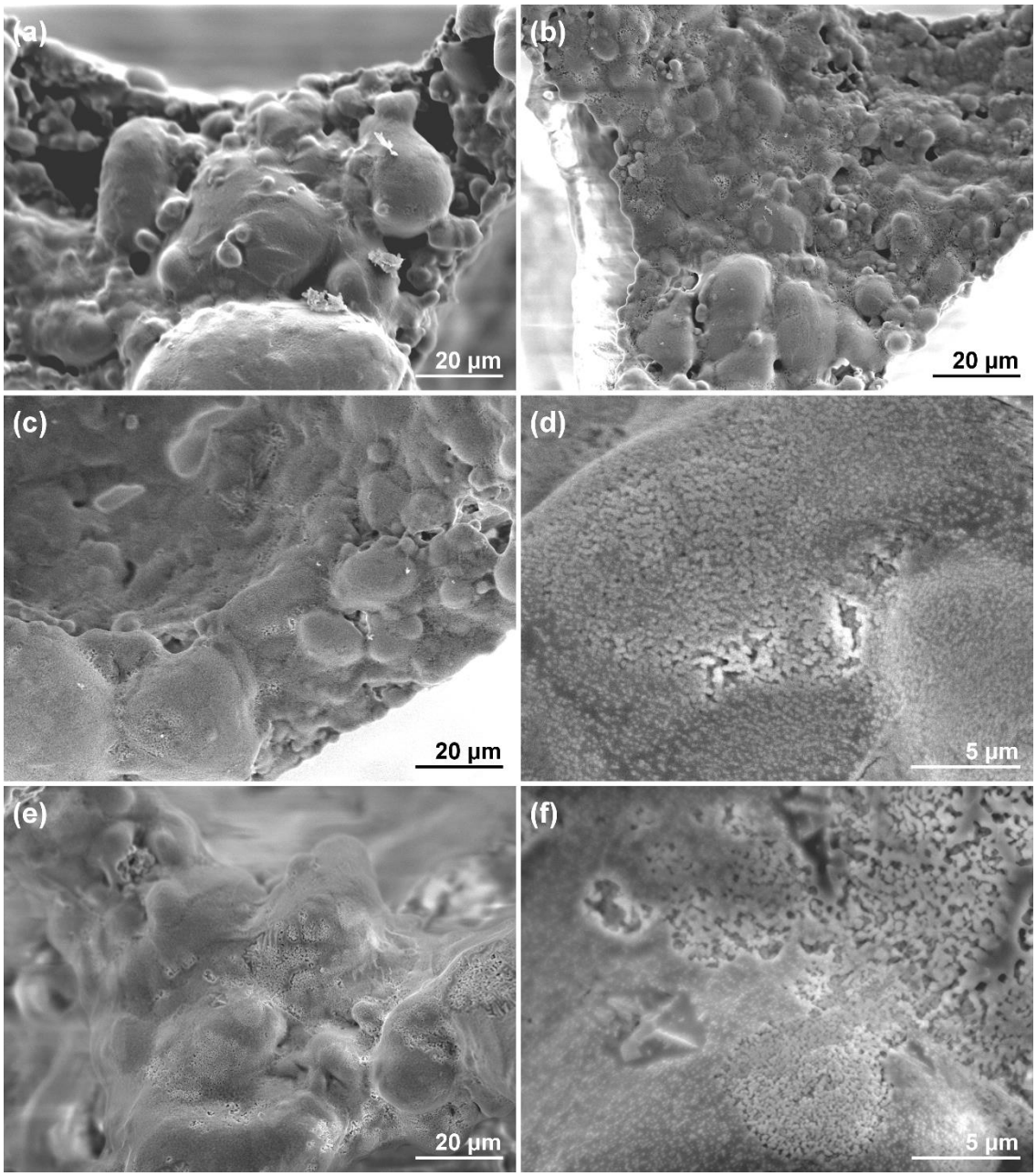

Figure 3.49: SEM micrographs, imaged from secondary electrons, of the surface of AW 37.4% porous scaffolds upon soaking in SBF solution. (a) Scaffold as such, (b) 1 day of soaking, (c) 7 days of soaking, (d) higher magnification of the 7 day sample surface, (e) 14 days of soaking, (f) higher magnification of the 14 day sample surface. Error bars in (a-c, e) represent 20 µm; error bars in (d, f) represent 5 µm.

All samples except AW 37.4% formed apatite on their struts within the two weeks of testing. As predicted from the pH results (Figure 3.43), samples AW 0%, AW 6.2% and AW 12.5% showed the formation of apatite after only 1 day of soaking in SBF solution. AW 18.7% was covered by a thick layer after 7 days, while AW 24.9% started to form

apatite between 7 and 14 days of soaking. As seen with the solid discs (Figure 3.41), in scaffolds AW 37.4% the sample surface changed over time so that crystals that were already present in the material became more evident, indicating that the remaining glass phase, being less stable compared to the crystal phases, dissolved preferentially. In addition, as previously observed for the flat discs as well, the morphology of the deposited apatite layer on samples AW 18.7% looked different than the morphology found on samples AW 0%, AW 6.2% and AW 12.5%: crystals looked thinner and smaller, giving a finer texture to the coating layer. As proposed basing on the results of Table 3.16, it is possible that in the case of samples AW 18.7% the deposited layer was actually a strontium-containing hydroxyapatite. In addition, observing the higher tendency to form cracks and the fact that the coating layer looked like it was almost detaching from the surface underneath, it could be that the addition of strontium in the samples caused the bioactivity process to follow a different mechanism, with the formation of a silica gel (more prone to cracking) that was not expected for the proposed original bioactivity mechanism reported for the AWGC material, which was described in Chapter 1.

3.3.8 Effect of strontium content on the radiopacity of AW porous samples

Radio density of samples was tested on 1.5 mm slices of scaffolds previously tested for biaxial flexural strength and on small cubic samples produced for tissue culture. Figure 3.50 shows the x-ray pictures used for calculating the radiopacity of the six compositions under study, while Table 3.19 and Table 3.20 report the average results for these two sets of samples, including the relative intensity compared to the no-strontium AW 0% sample, then summarised in Figure 3.51.

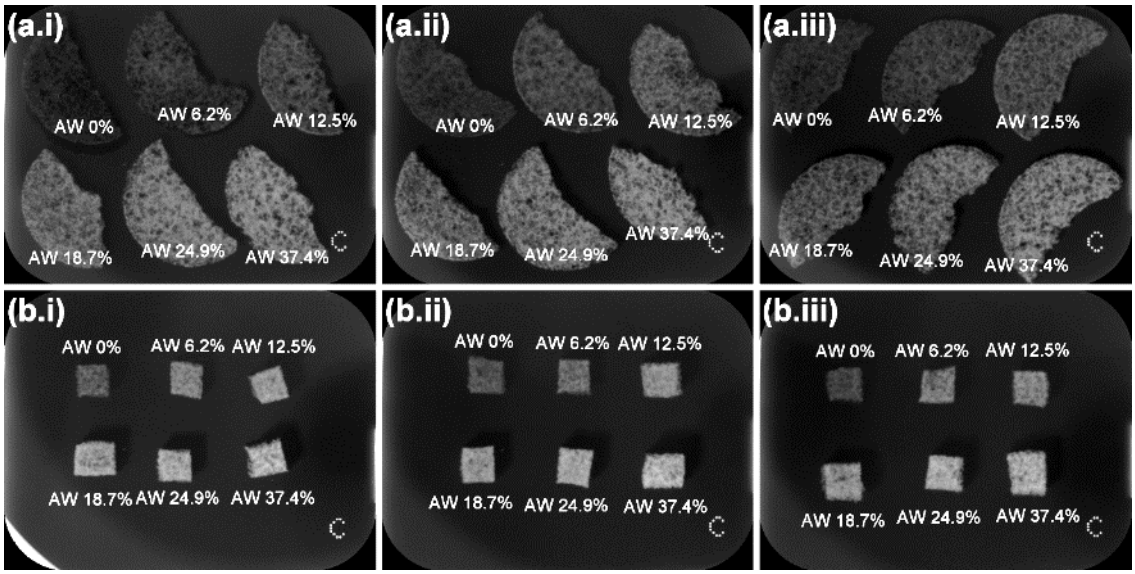

Figure 3.50: X-ray images of porous samples used to calculate their radiopacity, three repeats per set (i-iii). (a) Slices previously tested for biaxial flexural strength, (b) cubic scaffolds.

Table 3.19: Average pixel intensity (a.u.) of slices of porous scaffolds measured from the x-ray images in Figure 3.50a.i-iii, with relative intensity to AW 0% samples.

	Average	St. dev.	Relative intensity
AW 0%	15.76	2.09	1.00
AW 6.2%	24.21	3.23	1.54
AW 12.5%	31.10	3.03	1.97
AW 18.7%	37.06	4.95	2.35
AW 24.9%	44.09	4.17	2.80
AW 37.4%	50.07	2.77	3.18

Table 3.20: Average pixel intensity (a.u.) of cubic porous scaffolds measured from the x-ray images in Figure 3.50b.i-iii, with relative intensity to AW 0% samples.

	Average	St. dev.	Relative intensity
AW 0%	33.50	5.07	1.00
AW 6.2%	49.41	5.83	1.47
AW 12.5%	62.27	7.24	1.86
AW 18.7%	65.39	5.51	1.95
AW 24.9%	77.88	2.32	2.32
AW 37.4%	82.52	3.81	2.46

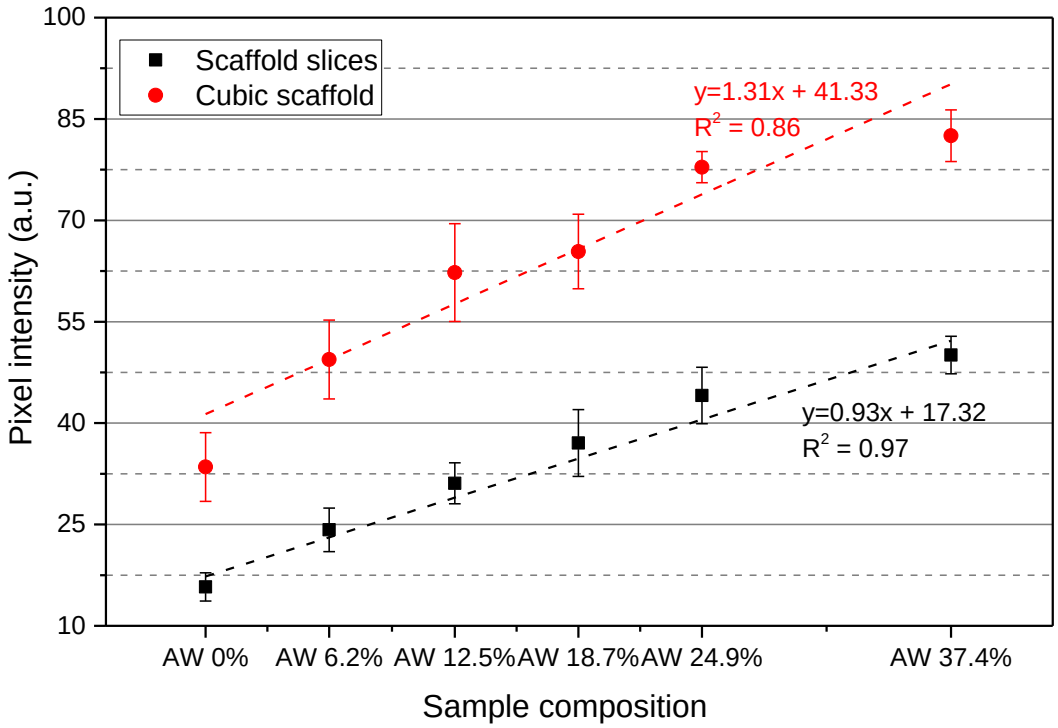

Figure 3.51: Radiopacity of porous scaffold slices and cubic porous scaffolds, as measured from the average pixel intensity of sample radiographs. Error bars indicate the standard deviation (n=3). Fitting trendlines are shown with corresponding equations and R-square values.

The increase in radiopacity with the increase in strontium in the samples was evident by eye from the pictures taken and then proven by the intensity measurements. Because the cubic samples pictured in Figure 3.50b.i-iii were thicker than the slices in Figure 3.50a.i-iii, their intensities reported in Table 3.20 and plotted in Figure 3.51 were higher than those of the thin slices of Table 3.19. However, the pixel intensity

relative to the no-strontium composition AW 0% was higher for the thin slices in all the strontium samples, meaning that the contrast between AW 0% and AW 37.4% was higher in the case of the thin slices than the cubic scaffolds. In the case of the cubic porous scaffolds, in some of the samples it was also possible to identify the presence of defects, visible as areas darker than the rest of the sample, indicating an imperfect coating of the original struts of the foam with the slurry during the foam replication process. The increase in radiopacity was found linear for both series of samples, with a better fitting of the trendline in the case of the scaffold slices (R^2=0.97) compared to the cubic scaffolds (R^2=0.86).

3.4 Discussion

This chapter described and presented the production and the characterisation of porous 3D scaffolds for bone regeneration, made using the AWGC material modified with strontium. The technique chosen for this work was the foam (or sponge) replication method, first used with hydroxyapatite by Tian and Tian in 2001 (79) and then transferred to glass-ceramics in 2006 (80, 81), but never applied to strontium-containing apatite-wollastonite before. The parent glasses used for producing the scaffolds were described in Chapter 2.

The foam replication method combines the use of a template that presents an interconnected porosity with the sintering and crystallisation of the glass particles used and it has been widely described in the literature since 2006. Different authors used Bioglass 45S5 in combination with the foam replication method, such as Boccaccini et al. (261), Bretcanu et al. (83), Baino et al. (258) and Li et al., who then coated the scaffolds with a vancomycin-containing polymer (262). Vitale-Brovarone et al. prepared foam-replicated scaffolds using a bioactive glass belonging to the SiO_2-P_2O_5-CaO-MgO-Na_2O-K_2O system named CEL2 (98), comparing CEL2 with ICEL2, which had inverted silica and phosphorus oxide molar amounts (257), or with SCNA (263), a glass-ceramic in the system SiO_2-CaO-Na_2O-Al_2O_3 used to create a porous coating on dense alumina. Fu et al. applied the foam replication method to the 13-93 glass of composition 53SiO_2-6Na_2O-12K_2O-5MgO-CaO-4P_2O_5 wt% (95), while Erol at al. and Fu et al. applied it to a boron-containing and a borate glass, respectively (264, 265). After the first sponge replication by Tian and Tian in 2001 (79), also Tripathi and Basu used hydroxyapatite for the preparation of porous bone-like scaffolds (82), while Vitale Brovarone et al. used a fluorapatite-containing glass-ceramic with nominal composition 50SiO_2-18CaO-9CaF_2-7Na_2O-7K_2O-6P_2O_5-3MgO mol%, then modified with silver to impart antibacterial properties to the constructs (266). Some authors proposed the use of marine natural sponges instead of the polyurethane foams generally utilised. For

example, Boccardi et al. used natural foams in combination with 45S5 Bioglass (267), while Wang et al. used natural sponges to create hierarchically porous scaffolds containing macro and mesopores through the combination of the foam replication method with the sol-gel production of glasses (268). Also other authors described scaffolds with a hierarchical porosity, either produced by coating foams with the early-stage solution of sol-gel glasses such as Li et al. (269), or using an electrophoretic deposition approach like Fiorilli et al., in order to deposit mesoporous glass particles on macroporous scaffolds (270). More related to the apatite-wollastonite material used in the present thesis, Jun et al. described the production of hydroxyapatite sponge-replicated scaffolds coated with apatite-wollastonite in a multi-step foam replication procedure (84), whereas Serna optimised the composition of the slurry for the production of apatite-wollastonite porous scaffolds (121). In addition, Ni et al. produced macroporous wollastonite scaffolds and compared them with β-TCP scaffolds using 25 PPI foams (271), while Kunjalukkal Padmanabhan et al. prepared hydroxyapatite/wollastonite composite porous scaffolds starting from ceramic powders of the two components mixed in the slurry, then using 25 PPI sponges as templates and sintering their samples at 1300 °C (272). However, no author described the use of strontium-containing apatite-wollastonite for 3D porous, foam-replicated scaffolds.

3.4.1 Strontium content in AW glass-ceramic scaffolds influences shrinkage and sintering

The addition of strontium to the starting apatite-wollastonite material caused its shrinkage to linearly decrease during thermal treatment with the increase of strontium, when all sample compositions were treated at 1050 °C for 2 h. This could be due to a reduction in the degree of sintering for the glass particles. In fact, as observed in the SEM micrographs in Section 3.3.4, the original particles constituting the material were still partially visible for compositions with higher strontium. Massera and Hupa (273) and Kapoor et al. (274) observed a reduction in the sintering temperature with increasing strontium or strontium and zinc substitution in silica-based glasses, respectively. The sintering temperature is usually obtained by testing the samples with hot stage microscopy (HSM) and it is defined as the temperature at which the height of the sample is reduced to 95% of its starting height during heating (273). Bellucci et al. did not observed any change in volume shrinkage of their CaO-rich silicate bioactive glass when substituting 10 mol% of CaO with SrO and/or MgO; however, they treated each sample at their specific sintering temperature found using HSM (275). In another study, the same research group doped a tricalcium phosphate (TCP) cement with strontium and/or magnesium: the authors did not find differences in the sintering

behaviour of samples depending on their composition, although they observed an increase in the residual porosity when samples were fired at a higher temperature (276). As explained also by other authors, this could happen because the onset of crystallisation could hinder further sintering, especially at low (below 700 °C) temperatures (277, 278). This observation corresponds with the results found for the materials under study in the present thesis during the DSC testing reported in Chapter 2. In fact, it was found that the onset of the first crystallisation, indicating the formation of the apatite phase, decreased with increasing strontium; therefore, the earlier onset of apatite could have hindered the sintering of the glass particles. This suggested that a composition-specific thermal treatment might be required for the materials under study, in order to adjust the volumetric shrinkage of samples and improve the sintering of glass particles. A sintering step could also be required, consisting of holding the temperature at a specific temperature determined through HSM, before further heating could be applied for a controlled crystallisation. As displayed in the SEM micrographs, in samples with a higher amount of strontium (AW 24.9% and AW 37.4%) the original glass particles were still visible, although smoothened and connected with wide sintering necks in both solid discs (Figure 3.14) and porous scaffolds (Figure 3.17). For the porous scaffolds, this also led to the formation of struts that looked incomplete or hollow, while this phenomenon was less important in lower strontium compositions. The formation of hollow struts during foam replication has been widely described in the literature, not only for Bioglass 45S5 (80, 258, 279), but also for other ceramic and glass-ceramic materials such as mullite (280), titania (281), a biphasic calcium phosphate (hydroxyapatite and β-TCP) (282) and a complex glass-ceramic derived from glass wastes (283). Although these defects are expected to cause a reduction in the mechanical properties of the constructs, this effect was not observed for the samples tested in this work, as it will be further discussed in Section 3.4.5. On the contrary, an effect on the different degree of shrinkage and sintering of samples could be observed on the porosity of scaffolds: as shown in Figure 3.26, the second peak in the pore size distributions calculated from micro CT data moved towards bigger diameters with the increase of strontium content, from 310 to 380 μm, as differences in volume were likely more easily detected on larger pores.

3.4.2 Strontium addition increases the density of AW glass-ceramics

The density of the ground glass ceramic scaffolds increased with increasing strontium, as it was already observed for the glass samples before the thermal treatment, reported in Chapter 2. A linear trend was found again, with densities after the

treatment being slightly higher than in the respective parent glasses for compositions AW 0% to AW 18.7%, while they were slightly lower for compositions AW 24.9% and AW 37.4%. This similarity could indicate that the atomic rearrangement due to heating was balanced by the formation of the crystal phases, which either had similar densities to the starting glass or balanced each other in the whole final glass-ceramic sample. In fact, a crystal phase might have a significantly higher or lower density than the starting glass, to the point that density could be used to measure the degree of crystallisation of a glass-ceramic (284), because the generated phase could move the density of the final glass-ceramic towards higher or lower values. In the case of the apatite-wollastonite material under study, Kokubo reported a density of 3.078 g/cm^3 for the AW 0% composition (103), which is slightly higher to what found in this study (3.002 g/cm^3) and could be due to the slower heating rate they used during crystallisation: 5 °C/min instead of the 10 °C/min applied to the samples in this thesis. The density of the individual phases, apatite and wollastonite, could be found in the literature: while the density of apatite is higher than the measured density of the final AW 0% sample, 3.156 g/cm^3 (285), the density of wollastonite is lower, 2.92 g/cm^3 (284). Hence, in the case of the AW 0% material under study, one crystal phase was denser than the starting glass and the other was less dense, thus balancing each other and giving, along with the remaining glass phase, only a little difference from the density of the starting glass. It can therefore be assumed that the same happened for the other compositions. For samples AW 24.9% and AW 37.4%, they contained higher strontium than the other compositions and their final densities were slightly lower than those found for their glasses. This could be due to the fact that strontium causes an enlargement of the atomic network, as seen with the parent glasses in Chapter 2; apatite preferentially picks up strontium, compared to the silicate phase, which likely reduces its density and hence the overall density also decreases.

3.4.3 The addition of strontium to AW affects the crystal phases formed during thermal treatment

XRD results of the AW 0% samples confirmed that they contained apatite and wollastonite. In particular, the matching phases that were found with X'Pert Highscore Plus were hydroxyapatite (ICDD 00-064-0738) and wollastonite 2M (ICDD 00-066-0271). This is in slight contrast with what Vickers found for the same composition, which was fluorapatite (ICDD 04-009-4021), instead of hydroxyapatite (186). However, it is in closer agreement with the description of the same material by Kokubo et al., who found that the precipitated phases were oxy- or fluorapatite ($Ca_{10}(PO_4)_6(O, F_2)$) and β-wollastonite ($CaSiO_3$) (85). In fact, because of the very small amount of CaF_2

contained in the parent glass (0.4 mol%), it is not possible that all the apatite phase that formed was fluorapatite, although the small amount that formed proved to be enough to be detected by x-ray diffraction. β-wollastonite is another name for wollastonite 2M and is the low temperature form of wollastonite. In fact, wollastonite undergoes a phase transformation, β to α (also called pseudowollastonite), when heated above 1200 °C (271, 286, 287). The two phases have different XRD patterns, as shown in Figure 3.52, and are both biodegradable. Ni et al. compared wollastonite to β-TCP and showed that wollastonite was bioactive, that α-wollastonite degraded more quickly than β-TCP, that bone-like cells attached better to β-wollastonite than α-wollastonite and better to α-wollastonite than β-TCP. Although the authors suggested that this could be due to the difference in surface roughness of the samples, they concluded that both types of wollastonite could be good candidates for bone implants, as long as the degradation rate would be kept under control (271, 287).

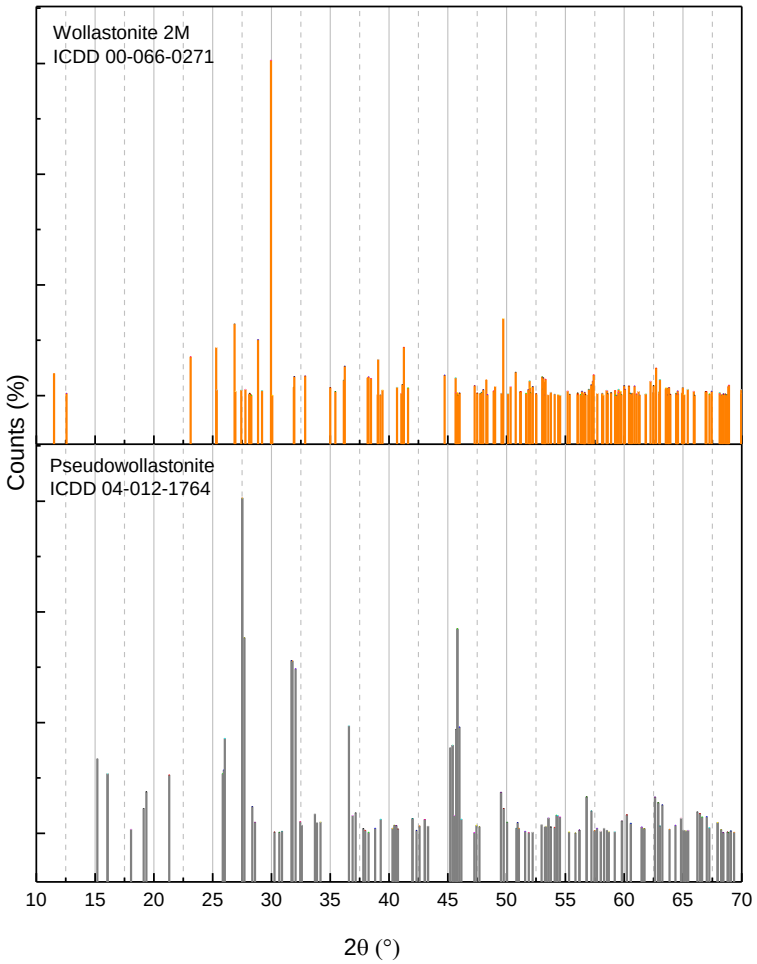

Figure 3.52: Comparison between the ICDD reference patterns for wollastonite 2M (β-wollastonite, top) and pseudowollastonite (α-wollastonite, bottom).

The modification of the initial AW 0% composition by the addition of strontium caused a progressive change in the XRD patterns recorded from the samples. In particular, it appeared that strontium interacted mainly with the apatite phase, starting from sample AW 6.2%, while a strontium-containing silicate could be found only for samples AW 24.9% and AW 37.4%. In fact, the wollastonite phase detected was wollastonite 2M (β-wollastonite, ICDD 00-066-0271) for samples AW 0% and AW 6.2%, it then shifted to diopside (calcium magnesium silicate, $CaMgSi_2O_6$, ICDD 04-011-6810) for sample AW 12.5%, it became pseudowollastonite (α-wollastonite, ICDD 04-012-1764) for sample AW 18.7% and eventually turned into calcium magnesium strontium silicate (ICDD 01-083-5061, $(CaSr)Mg(Si_2O_7)$) for samples AW 24.9% and AW 37.4%. On the other side, the apatite phase became a strontium apatite $(Ca_{7.7}Sr_{2.3})(PO_4)_6(OH)_2$ (ICDD 01-089-5632) with sample AW 6.2% and then moved to a strontium apatite with a higher content of strontium ($(Ca_{3.6}Sr_{6.4})(PO_4)_6(OH)_2$, ICDD 01-089-5633) from sample AW 12.5% and higher. A change in shape and height of peaks was also observed with the addition of strontium, in particular with the apatite peak becoming higher and narrower with the increasing strontium. This effect could be explained by the fact that strontium was more electron dense than calcium (186), thus giving a stronger signal, as also found by Lotfibakhshaiesh et al. (237). Because wollastonite did not acquire strontium as quickly as apatite, this altered the height ratio of peaks for the two phases and the apatite signal became predominant in the higher strontium compositions. These results can be related to the findings from the DSC analyses run on the glass powders. In fact, DSC results presented in Chapter 2 showed that, while the formation peak of apatite moved to lower temperatures with higher strontium, the formation of the silicate phase shifted towards higher temperatures. It is therefore likely that the first crystal phase that formed, apatite, started consuming the bivalent cations, calcium and strontium, thus depleting the remaining material and therefore delaying the formation of the silicate phase, making it shift to different phases and incorporate magnesium. In the literature, it has been widely shown that strontium substitution for calcium can cause changes in the XRD patterns detected from glass-ceramic samples. Hill et al. observed that a glass in the SiO_2-Al_2O_3-P_2O_5-CaO-CaF_2 system gave fluorapatite and mullite when no or 50 mol% of CaO was substituted with SrO, but when the substitution was 100 mol% then the XRD shifted towards lower 2θ, without corresponding to neither calcium or strontium fluorapatite; this was explained by suggesting that a solid solution of strontium/calcium apatite formed, with about 55 mol% of calcium apatite. Changes were attributed to the larger diameter of the strontium ion, also supposed to cause the shift from bulk to surface nucleation of the apatite phase (235). Lotfibakhshaiesh et al. reported that a SiO_2-P_2O_5-CaO-SrO-Na_2O-K_2O-MgO-ZnO glass, when treated at 900 °C, formed wollastonite if no strontium was

present and gave a strontium silicate ($SrSiO_3$) when all calcium was substituted with strontium. The intermediate composition, with 50 mol% of strontium substituted for calcium, gave an XRD pattern that did not match any known crystal phase; however, it looked similar to the strontium silicate pattern, but shifted to higher angles, thus suggesting the presence of a mixed calcium strontium silicate (237). Li_2O-CaO-SiO_2 glasses were studied by Salman et al. where strontium, magnesium and aluminium were added. They observed that the presence of strontium partially promoted the transition from wollastonite to pseudowollastonite (288), as also found in the present work in samples AW 18.7%. If magnesium was substituted for calcium, diopside was found, while if both strontium and magnesium were present then a strontium magnesium silicate and a calcium strontium silicate were detected (289). This is in agreement with what was found for the AW samples in the present work, having diopside detected for sample AW 12.5% and then a mixed silicate for scaffold compositions with higher strontium. The influence of strontium on the α-β transition was also confirmed by Wu et al.: they observed that when doping $CaSiO_3$ with increasing strontium, the detected crystal phase shifted from β for 0 or 1 mol% strontium, to a mixed composition of α and β calcium silicate for 2.5 mol% strontium, to only α pseudowollastonite for 5 and 10 mol% strontium calcium silicates. This was also proven by a decrease of the transformation temperature with increasing strontium during thermal analysis (290). Hesaraki et al. studied a sol-gel CaO-SrO-SiO_2-P_2O_5 glass, then treated at 1000 °C; they found that both Sr-free and Sr-containing glasses formed hydroxyapatite, thought to partially be Sr-hydroxyapatite for the Sr-containing sample. The second phase was classified as α-wollastonite for the Sr-free glass, then thought to become a mixture of Ca_2SiO_4 and various calcium strontium silicates, not precisely identified because of the similarity in the reference patterns (181). Bellucci and Cannillo modified the composition of Bioglass by adding strontium and magnesium, obtaining a glass with an ultra-high crystallisation temperature. This result was believed to be possible through the combination of the effects of magnesium, which can inhibit devitrification, and strontium, which favours the viscous flow and the sintering of the melting glass due to its larger ionic radius (291). Although these observations did not apply directly to the AW samples describe in the present thesis, as they formed two crystal phases, it is possible that they were valid for the wollastonite phase, which was the phase that acquired magnesium and that had its DSC peak moving towards higher temperatures with the increasing strontium (Chapter 2). Vickers studied the same AW compositions described in this thesis (except AW 37.4%) and also concluded that it was likely that, for the strontium-containing compositions (in particular those with a high content of strontium), more than one calcium silicate phase formed, thus giving a mixture of magnesium silicate,

pseudowollastonite and strontium silicate; because peaks of the reference patterns for all these phases highly overlap, it was not possible to discriminate which of these phases were effectively present in the samples and in which proportion (186). These observations appeared to be likely applicable to the materials studied in the present thesis.

3.4.4 Effect of strontium addition on the architecture of 3D porous scaffolds

Micro CT analysis of the porous scaffolds showed that all samples maintained their internal interconnected porosity. For all the compositions, most of the porosity was found to be open porosity, with closed porosity contributing for less than 0.5 % of the volume.

During the last decade, micro computed tomography (sometimes also referred to as microtomography) has become a powerful tool for assessing the microstructure of samples in a non-invasive way. In the field of biomaterials, it has been applied to all categories of materials: metals (292-294), polymers (295-297), composite cements (298-300) and ceramics (281, 301, 302), alongside bioactive glasses and glass-ceramics (121, 247, 267, 301, 303-312). For scaffolds belonging to this last category, micro CT imaging and analysis are particularly important for assessing their porosity and verifying the presence of open interconnected pores, with pore sizes that can allow colonisation and infiltration of cells. Different compositions of glass and glass-ceramic materials have been tested using micro CT porosity analysis. Jones et al. and Yue et al. tested 70S30C scaffolds prepared by sol-gel foaming: porosity was found between 85 and 92 % and the majority of pores were around 500 to 800 µm, depending on the sintering temperature (304); the analysis was then applied to *in vitro* SBF-soaked samples (247) and *ex vivo* samples (305) to assess their evolution over time. Liu et al. used micro CT analysis to compare unidirectional-frozen and foam-replicated samples *ex vivo* (306). Fu et al. used the glass 6P53B (51.9SiO_2-9.8 Na_2O-1.8K_2O-15.0MgO-19.0CaO-2.5P_2O_5) to prepare porous scaffolds with different porosities via direct ink assembly, then imaged with micro CT (307). Micro CT analysis has been applied also to foam replicated scaffolds: Renghini et al. prepared CEL2 scaffolds with 54 vol% porosity and 180 µm average pore size; they used micro CT to monitor sample evolution over soaking in SBF solution (308), also comparing them with Bioglass scaffolds (309). Baino et al. used CEL2 to prepare scaffolds from foams of 45, 30 and 20 pores per inch (PPI) in order to simulate healthy and osteoporotic bone, then they applied micro CT analysis to characterise all samples (310). Baino and Vitale-Brovarone found, with micro CT analysis, that foam replicated SCNA

scaffolds had a porosity of 56 vol% with mean pore size of 240 µm, also observing a bimodal pore size distribution on SEM micrographs, with macropores bigger than 100 µm and micropores below 10-20 µm (303). Boccardi et al. compared foam-replicated Bioglass scaffolds prepared using polyurethane foams and two types of marine sponges, using micro CT analysis for imaging their internal structure and assessing their porosity and pore size distribution (267). Shen et al. prepared foam replicated borosilcate and strontium-borosilicate scaffolds, using micro CT for imaging and measuring their porosity, which was about 73 vol% for both compositions (311). Oliveira et al. produced porous hydroxyapatite scaffolds using polyurethane foams and imaged them using micro CT (312), while Cunningham et al. followed the foam replication method with hydroxyapatite utilising different types of marine sponges, then comparing the scaffolds so obtained with micro CT quantitative analysis (301). Serna studied the fabrication of apatite-wollastonite foam-replicated scaffolds and found, through micro CT analysis, that the final porosity and pores size distribution depended on the liquid:glass ratio of the slurry, the heat treatment applied and the combination of the two, but all samples had the majority of their pores in the range of 40 to 450 µm, with porosities going from 40 to 56 vol% (121). The presence of two sets of pores observed by Baino and Vitale-Brovarone (303) was also observed for the strontium scaffolds under study in this work. In fact, all compositions had a small peak for pores in the range 25-45 µm and then macropores were mainly found, in a bimodal distribution, between 100 and 400 µm. As in the mentioned paper, pores in the smaller range could be attributed to the presence of residual porosity after the fusion of glass particles during sintering and crystallisation, while the bimodal distribution of pores bigger than 100 µm could be assigned to pores deriving from the template structure (peak around 200 µm) and pores created by incomplete struts (310 to 380 µm), originated during preparation by coating defects, as also suggested by Serna (121). It must be noted that, generally, micro CT-derived structural characteristics of sponge replicated scaffolds differ from those of natural human trabecular bone: while the porosity of synthetic scaffolds, as described above, ranges from 40 to 70 vol%, that of human trabecular bone spans between 50 and 90 vol% (30); this is reflected also on the average pore size found in the samples, as it usually ranges between 200 and 400 µm for the synthetic scaffolds, but it can be between 600 and 800 µm for natural bone (313-316). These differences are intrinsic to the foam replication method of producing scaffolds for bone applications and derive from the fact that the templates used do not exactly replicate the structure of bone. In fact, as explained in Chapter 1, the structure of trabecular bone is anisotropic and derives from the constant remodelling to which it is subjected *in vivo* (19, 317), depending on the mechanical stimuli and the physiological environment, and this condition cannot be simulated with an artificial

construct without bone cells. However, because the class of scaffolds under study is meant to dissolve and get remodelled once implanted, it has been demonstrated that bone regeneration can be achieved with implants that present more than 50 vol% porosity and pore size of at least 100 µm, better if bigger than 300 µm (30, 260). The micro CT analyses conducted on the strontium AW scaffolds showed that all compositions complied with these structural requirements. In addition, it must be taken into account that the majority of data for trabecular bone found in the literature derive from elderly patients who underwent surgery with osteoporosis or osteoarthritis, which affect the quality and structure of bone and, therefore, the results of porosity analyses. Osteoporosis in particular, causing bone resorption, can make the total porosity higher and the average pore size bigger (318), thus skewing the results towards higher values.

Another aspect that must be considered when discussing and comparing micro CT results is the computational model used for the calculation of pore sizes, which is not always specified in the literature. In the case of the CTAn Bruker software and the present work, a sphere-fitting model was used. Briefly, the algorithm automatically calculated the median axis for all the porous structures, then the diameter of a sphere was calculated for each voxel of this medial axis so that (i) the sphere contained the voxel and (ii) the sphere was completely enclosed within solid surfaces (319). This method allows for a reduction in the bias due to 3D orientation of pores; however, in the case of oval pores, the longer axis will not appear in the calculated diameters. Although this means that long pores in the scaffolds, such as those deriving from incomplete coverage of the foam struts with the slurry, will be considered smaller than their actual size in the pore size distribution, the diameter measured by the software will probably be the distance that cells will see when populating the sample, bridging pores across. Therefore, although very big pores might not appear in the final structural results for the samples, the general characterisation will still be valid for planning *in vitro* and *in vivo* studies.

3.4.5 Effect of strontium addition on the mechanical properties of porous AW glass-ceramic scaffolds

All strontium AW compositions were tested for their compressive strength and biaxial flexural strength, from which their elastic modulus and their Weibull distributions were obtained, respectively. For each composition, samples tested with the two methods belonged to the same batch for better comparison. It must be noted that no international standard exists for the optimal testing of porous ceramics (35). The American standard ASTM F2883-11 “Characterisation of ceramic and mineral based

scaffolds used for tissue-engineered medical products (TEMPs) and as device for surgical implant applications" (320) mentions only the compression test as the method for assessing the mechanical properties of scaffolds. However, this standard gives only generic indications for sample preparation and parameters for testing, without setting any criteria of acceptance for samples to pass the test. In addition, it must be considered that ceramic materials are not usually tested in compression because of their brittle nature. In fact, the ISO standard BS EN ISO 6872:2015 "Dentistry – Ceramic materials" (251) lists two different tests for the assessment of mechanical properties: a bending test and the biaxial flexural strength test used in this thesis. However, also this standard is only partially applicable to bone scaffolds, as it describes tests for solid, not porous, ceramics. In the literature, most authors tested their porous scaffolds only in compression (82, 95, 98, 238, 245, 258, 321); Chen et al. and Dong et al. combined compression strength tests with three-point bending tests (80, 322); three-point bending strength tests were also chosen by Kokubo et al. when testing solid apatite-wollastonite ceramics (12) and by Vickers when testing strontium-containing apatite-wollastonite samples (186), while Fan et al. tested sintered compacted hydroxyapatite samples with biaxial flexural testing (323). In the work presented in this thesis, it was chosen to perform two different tests for comparison: the most commonly used compressive strength test and the biaxial flexural strength test, following what was done by Serna (121).

In the present thesis, all strontium AW scaffolds showed an average compressive strength around 10 MPa, which is comparable to the upper value of the range reported in the literature for trabecular bone: 2-12 MPa (34, 35). No significant difference was found between samples ($p>0.05$). The high standard deviations found for all the compositions can be ascribed to the intrinsic variability of the production method, but also to the difficulty in preparing samples of exactly the shape required by the test: regular cylinders with two perfectly parallel surfaces. This value is well below the 1060 MPa reported by Kokubo et al. for apatite-wollastonite (85); however, that value was found for solid samples. On the contrary, Serna found a compressive strength between 2.3 and 3.6 MPa, depending on slurry composition and thermal treatment applied (121). Regarding foam-replicated scaffolds, different authors found different compressive strengths depending on the material used and their porosity. Muhamad Nor et al. produced foam-replicated porcelain (not bioactive) foams by varying the ceramic load of the initial slurry, thus obtaining compressive strengths between 3 and 23 MPa for porosities between 30 and 70 vol% (324). Fu et al. produced porous scaffolds using the 13-93 bioactive glass and modifying it with boron, obtaining 11 MPa compressive strength with 85 vol% porosity for the original composition (95) and 6.4 MPa with 72 vol% porosity for the boron-containing glass (265). Vitale-Brovarone

et al. used CEL2 glass-ceramic and tested different coating methods and thermal treatments; they obtained porosities that ranged from 53 to 72 vol% and compressive strengths comprised between 1.3 and 5.4 MPa (98). Baino et al. found that the compressive strength of Bioglass-based scaffolds varied between 0.2 and 2.5 MPa for porosities included between 70 and 83 vol%, depending on the particle size chosen for the slurry and the thermal treatment applied (258). Chen et al. also used Bioglass for the production of foam-replicated glass-ceramic scaffolds, reporting 90 vol% porosity for samples with 0.3-0.4 MPa compressive strength (80). Yin et al. found that the compressive strength of foam-replicated scaffolds made with the borate-based glass 13-93B2 slightly increased from 10 to 12 MPa, when the strontium content was increased from 0 to 9 mol% (214). Therefore, the results reported in the present thesis are comparable to the stronger samples described in the literature and, being closer to the upper limit of cancellous bone, are thus more promising for load-bearing applications.

Kokubo et al. showed how the precipitation of wollastonite in addition to apatite from the apatite-wollastonite parent glass caused an increase in bending strength and Young's modulus of the material, as the wollastonite crystals could deflect cracks, thus increasing the fracture surface energy and the toughness of the material (12, 106). The same effect was also observed for the compressive strength by Kunjalukkal Padmanabhan et al. in wollastonite/hydroxyapatite composite scaffolds, for compositions with up to 50 wt% wollastonite (272).

Conversely to compressive strength, the Young's modulus measured for the strontium AW scaffolds depended on the strontium content. In particular, it decreased with increasing strontium: it was found to be about 300 MPa for AW 0% and then it decreased to about 120 MPa for AW 37%, this being significantly lower than AW 0% ($p<0.005$) and AW 6.2% and AW 12.5% ($p<0.05$). Despite the variation, these values are all comparable with those found for cancellous bone, for which the reported elastic modulus is comprised between 50 and 500 MPa (32, 33), increasing linearly with increasing compression strength (22). The dependence of the Young's modulus on the strontium content for a glass-ceramic has not been reported in the literature before, where most porous scaffolds are described only in terms of compression strength. Barbieri et al. used Vickers indentation to measure the elastic modulus of strontium-containing feldspars and found that it depended on the porosity of samples, but not on their composition (325). Jallot studied the interface between an hydroxyapatite implant and bone *in vivo* and observed that, after implantation, an increase in strontium content corresponded with an increase of the Young's modulus measured with non-destructive, cyclic compression of explanted samples (326). Meixner and Cutler tested strontium-doped perovskites, where strontium was substituted for calcium, and found

that a high content of strontium corresponded with lower Young's modulus and lower fracture strength (327). Poh et al. produced composite scaffolds using Bioglass or strontium-doped Bioglass particles in polycaprolactone and observed that the Young's modulus increased with the presence of the dispersed glass, with the strontium Bioglass giving the highest elastic modulus (328). As suggested by Meixner and Cutler, the Young's modulus of a material depends on its atomic bonds (327), while the compressive strength depends more on the architecture of the tested samples. Therefore, the behaviour observed for the strontium AW scaffolds might be due to the distortion of the glass network caused by the bigger diameter of strontium compared to calcium.

As mentioned above, only few authors described the mechanical properties of their ceramic scaffolds also in terms of biaxial flexural strength. Despite it being a more suitable method for measuring the mechanical behaviour of ceramics, it requires sample machining and slicing, thus making the method more complicated when samples are highly porous and fragile (35). Meganck et al. tested solid samples of hydroxyapatite, biphasic calcium phosphate and β-TCP, finding that their biaxial flexural strengths were 130, 24 and 23 MPa, respectively, Weibull modulus 12, 13 and 9, respectively, and Weibull characteristic strength 135, 24 and 24 MPa, respectively (329). Fan et al. studied the behaviour of porous hydroxyapatite (porosity around 60 vol%) with the sintering temperature; the maximum mean fracture strength they found was 5 MPa for the highest sintering temperature, the Weibull characteristic strength increased from 1 to 5 MPa with increasing temperature, while the Weibull modulus varied between 6.6 and 15.5 independently from temperature (330). Zocca et al. 3D printed wollastonite, obtaining scaffolds with 64 vol% porosity, 6 MPa biaxial flexural strength, 6.6 Weibull modulus and 5.9 MPa Weibull characteristic strength (331). Vickers used the 3-point bending test for measuring the flexural strength of strontium AW scaffolds; he found that composition AW 24.9% had the highest flexural strength, 46 MPa, while composition AW 18.7% had the lowest, 23 MPa. He suggested that the different outcomes were due to the lack of liquid phase sintering for compositions AW 0%, AW 6.2% and AW 12.5%, along with the reduction in crystal volume percentage (186). Other authors compared the biaxial flexural strength with the bending strength of porous bioceramics or glass-ceramics. Chung et al. showed that there is a good correlations between 3-point bending strength and biaxial flexural strength for dental composite materials (332), while Xu et al. observed that, for dental Y-TZP (yttria-stabilised tetragonal zirconia polycrystal), the measured flexural strength was always higher for biaxial flexure than 3-point bending, which was higher than in 4-point bending (333).

It is evident from the literature reported above that the mechanical properties of scaffolds strongly depend on their porosity. Fu et al. showed in their review paper how compressive, flexural and tensile strengths all depend on the porosity of the scaffolds tested (35), with Liu (334) and Barralet et al. (335, 336) finding an exponential relation between compressive strength and porosity for hydroxyapatite and calcium phosphate cements, respectively. Similar trends were found also by Chen et al. when fitting experimental data of compressive and tensile strength from different scaffold materials to computational models (337). This could explain why, in the present study, no clear trend was found for the strontium AW scaffolds, despite them containing different crystal phases: it is possible that the effect of their porosity overcame that of their crystal composition. Fan et al. studied the relation between Weibull modulus of hydroxyapatite and its porosity and found that, for porosities between 10 and 55 vol%, the Weibull modulus remained in a narrow band from 4 to 11 (323). Scaffolds tested in the present study fell around the upper limit of this porosity and showed Weibull moduli between 4 and 5, thus agreeing with the authors' results. Therefore, despite the biaxial flexural strength being strongly dependent on porosity, the dispersion of its values was not influenced by it.

As already mentioned in this thesis, it is important that the mechanical properties of scaffolds match those of bone, in order to guarantee a full integration with the surrounding tissue, trabecular bone in this case, after implantation. Fu et al. reported a range of 2-12 MPa compressive strength, 10-20 MPa for flexural/bending strength and 1-5 MPa for tensile strength of cancellous bone (35). Therefore, values found in the present work are within the trabecular bone range and close to its upper limit. Currey compared the Young's modulus of human cancellous bone reported by different authors in the literature, measured following different methods in dry and wet conditions. Values ranged from 4 to 20 GPa (22), thus one or two orders of magnitude higher than what found for the samples tested here. It must be noted that bone is an anisotropic material, so its mechanical properties highly depend on the direction of the applied force during the test, as well as the method and conditions of testing, the harvesting of samples and their preservation before testing. In addition, bone tissue can be considered a composite material, with collagen imparting elastic and toughness characteristics that cannot be replicated with an only-ceramic (or glass-ceramic) material. Therefore, it would be advisable that scaffolds for bone regeneration would be also checked for toughness and fatigue resistance, along with static compressive, flexural and tensile strength. Furthermore, Liu et al. showed how 13-93 porous scaffolds moved from a brittle mechanical response before implantation to an elasto-plastic response *in vivo* after 12 and 24 weeks of implantation (96, 306). Therefore, it

is important that all mechanical properties are also monitored *in vivo*, especially for samples that degrade once implanted.

3.4.6 Strontium content affects the *in vitro* apatite forming ability of AW glass-ceramics

Both solid discs and porous scaffolds were tested for their ability to form apatite once immersed in SBF solution. This test was optimised by Kokubo et al. (255) and is described in the ISO standard 23317-2014 (254). For the solid discs, apatite was found on samples AW 0% and AW 18.7% after 1 day and on samples AW 12.5% after 3 days of soaking. For the porous scaffolds, compositions AW 0%, AW 6.2% and AW 12.5% formed apatite within 1 day, AW 18.7% within 7 days (3-day time-point was not tested) and AW 24.9% had some small deposited crystals at the 14 day time-point. Since bioactivity is a surface-driven mechanism, it is possible that these differences derived from the much higher exposed surface area of porous scaffolds compared to solid discs.

It has been shown in the literature that also the atomic structure of a bioactive glass has a strong influence on its bioactivity (62, 65). The network connectivity (NC), as explained in Chapter 1, is a parameter that describes the average number of bridging oxygens per [SiO_4] tetrahedron and, consequently, the solubility of a glass in solution. Its formula depends on the number of network formers and, for the glasses under study in the present thesis, on the atomic concentration of oxygen, phosphorus and silicon as the network former (62-64). For all the strontium AW compositions under study, NC was calculated as 1.98 (Hollings, personal communication). This is in line with the network connectivity of most bioactive glasses, being it below or close to 2.00, according to Hill (65) and Watts et al. (66). Fredholm et al. studied strontium substitution in a different bioactive glass and they also observed, through ^{29}Si Nuclear Magnetic Resonance (NMR), that it did not impact the NC of the glass (63). In a following publication, the same authors studied the bioactivity behaviour of the same glasses and observed that strontium was released linearly according to its initial amount, when the glass powder was soaked in SBF. They also concluded that strontium substitution enhanced bioactivity; however, XRD and FTIR (Fourier-Transform Infrared spectroscopy) showed the presence of calcium and strontium carbonates after soaking in SBF and only traces of apatite (230). Conversely, other authors observed that strontium could slow down the bioactivity of glasses. Hesaraki et al. observed a delay in the formation of apatite, after 7 days in SBF, when strontium was added to a calcium silicophosphate glass, concluding that strontium limited the growth of the apatite layer by preventing the formation of the intermediate phase

octacalcium phosphate (181, 338). Wu et al. prepared mesoporous 3D scaffolds with different mol% of strontium substitution and observed that the highest Sr composition (10 mol%) formed apatite after 3 days of soaking, while lower and no Sr compositions had an apatite layer after only 1 day (191). Kargozar et al. modified a multi-component bioactive glass by adding strontium and/or cobalt (6 mol% Sr, 0.5 mol% Co) and they showed that the formation of the apatite layer was delayed in compositions that contained the doping ions (216). They also observed that the formed apatite did not contain strontium in its lattice, while Pan et al. found that the calcium-deficient apatite layer that formed on strontium borate glasses in DMEM (Dulbecco's Modified Eagle's Medium) incorporated strontium and magnesium (339). Various authors observed an increase in dissolution for the strontium-containing compositions (177, 189, 191, 214), explained by the expansion of the glass network caused by strontium and discussed in Chapter 2. This is in contrast with what was found by Lao et al., who observed a reduction in dissolution for strontium glasses soaked in DMEM (215), and Wu et al., who studied strontium-$CaSiO_3$ ceramics and also observed a reduced dissolution rate in SBF for the doped compositions (290). Vickers, who studied the same glass-ceramic compositions presented in this thesis (except AW 37.4%), found that only AW 0% and W 6.2% formed an apatite layer after 1 day of soaking, giving a confluent layer after 7 days; AW 12.5% did not change its surface morphology, while AW 18.7% and AW 24.9% presented an increased size of their original apatite domains over the test period (186). This is partially in contrast with what was found in this work. However, samples were prepared in a different way: Vickers compacted 45-90 μm powders in carbon moulds, subsequently sintered, while in this thesis discs and porous scaffolds were made from a slurry, dried and then heat-treated. This caused differences in the resulting surface morphology, which has also been shown to have a strong influence on glass reactivity. This is particularly evident with mesoporous bioactive glasses, which can have NC close to 4 and still be bioactive, as shown by Arcos et al. (340). In this class of glasses, bioactivity highly depends on porosity (341), to the point that even porous silica can induce apatite precipitation in SBF (342).

The mechanism of bioactivity for AWGC was described by Kokubo and was presented in Chapter 1. Briefly, ion dissolution leads to the formation of silanol groups (Si-O-H) on the surface, which provide nucleation sites for the precipitation of apatite without the formation of the silica gel characteristic of 45S5 Bioglass (105, 109). The apatite that forms is a carbonated hydroxyapatite (Ca/P ratio 1.46), which contains small amounts of magnesium and silicon and is composed of needle-like nano-crystals, randomly oriented (105, 106). Here, differences between strontium AW compositions and between discs and porous scaffolds could have been caused by a combination of factors: the much higher exposed surface area for porous scaffolds could explain the

formation of HAp on sample AW 24.9% only for its porous form and not the disc form; the different morphology observed for the apatite found on samples AW 18.7%, with smaller crystals and big cracks in the layer, could suggest the formation of a silica gel for this composition, which could have delayed the re-precipitation of ionic species and was more prone to cracking when drying; the rapid formation of the HAp layer within 24 hours for some of the strontium AW compositions could have masked the pH changes and prevented further ionic release, to the point that the absence of pH variations could be used as a predictor for the formation of the bioactive apatite layer; the fact that HAp was found only on inner struts of the porous scaffolds highlighted how bioactivity is a local phenomenon; the change in surface morphology, with the apatite phase of the material becoming more prominent as described by Kokubo (109), could also be observed for samples AW 24.9% (discs) and 37.4% (discs and scaffolds); the absence of HAp for the AW 6.2% discs could be due to a substantial difference in surface morphology, for instance a much lower residual microporosity, or, if a silica gel formed, it caused the bond between the deposited layer and the sample to became too weak and the newly formed HAp was washed away during rinsing of the sample at collection.

O'Donnell and Hill and Maçon et al. illustrated how the SBF bioactivity test actually presents many flaws: it can be difficult to calculate the required amount of solution when samples are porous or in powder form; the solution contains no organic molecule, so it is not a true representation of biological fluids; it can give false positives or false negatives; the test is static and does not reproduce the movement of fluids *in vivo* (343, 344). Therefore, although bioactivity in SBF solution is a powerful tool for the initial evaluation of a new biomaterial, it does not always reproduce how a material will actually behave once *in vivo* and so care must be taken when interpreting the results.

3.4.7 The addition of strontium determines an increase in radiopacity of porous AW scaffolds

Section 3.3.8 showed x-ray pictures of the porous strontium AW samples, presenting a clear linear increase in radiopacity for increasing strontium content. The fact that strontium can impart radiopacity to a material is a known effect, often utilised in dental materials for their radiological assessment after implantation. For example, Watts showed that dental composites can achieve a higher radiopacity than enamel when the glass filler contains about 40 wt% of SrO, with a linear relationship between strontium content and equivalent mm of aluminium (345), as it has been observed in the present study. A linear correlation between radiopacity and strontium content was

also found by Shahid et al., who compared different strontium-containing glass compositions of glass ionomer cements (259). Lachowski et al. compared 28 commercial dental cements and resins and observed an enhancement in radiopacity for those containing strontium, compared to the respective standard compositions; the authors noticed that the radiopacity of the final material depended on the atomic number of the doping element, but also on the concentration of the radiopaque agent in the material (346).

The use of radiopaque cements is of great importance also in other orthopaedic specialisations. For instance, Romieu et al. investigated a strontium-containing calcium phosphate cement for spinal applications and found that its radiopacity was about three times higher than that of cortical bone and twice as higher as that of the no-strontium cement (347). A study closer to the final application of the strontium AW scaffolds studied in the present thesis was presented by Mohan et al., who prepared strontium calcium phosphate porous scaffolds through gel casting and monitored their radiopacity *in vivo* in a rabbit bone defect model; they found that the strontium-containing samples displayed a higher radiopacity compared to the hydroxyapatite controls, facilitating the follow-up assessment of the surgical site, of the callus formation and of the osseointegration of the implant (348). This showed how this intrinsic feature of strontium, when used for bone-repairing materials, could provide additional value to the design of a new material. In the case of the compositions studied in this thesis, radiopacity increased with the increase in strontium, however comparison with trabecular and cortical bone, as well as an *in vivo* assessment, would be necessary for the selection of the optimal composition.

Chapter 4
Microbiological testing of strontium and strontium glasses

4.1 Introduction

As described in Chapter 1, strontium has been a chemical element of interest for many years thanks to its therapeutic properties for bone regeneration (15, 150, 152). More recently, attention in the literature has increased on whether strontium could also present antibacterial properties for preventing and treating infections, either in combination with fluoride in glass ionomer cements (17, 195), or as a doping element in bioactive glass compositions (18, 197, 198). The incidence of infections in orthopaedics varies in the literature from 1 % to 20 % for primary joint replacements (129, 349-353), going up to 30 % in the case of traumatic fractures (131), with a huge economic burden for hospitals and health systems. In addition, resistance of bacteria to standard antibiotics is constantly increasing, therefore finding alternative treatments for post-operative infections is becoming of primary importance. Modifying the composition of bioactive glasses and glass-ceramics so that they can elute active ions once implanted is one of the explored solutions. The relevant bacterial species for *in vitro* tests depend on the applications of the material, for example oral bacteria are considered for materials designed for dental applications (17, 18), or species commonly found in peri-prosthetic infections are used when studying a new implant material (198, 201, 202), such as the scaffolds described in the present thesis.
The scope of this chapter is therefore to explore the potential antimicrobial features of the strontium AW glasses described in Chapter 2, with the ultimate aim of finding, if possible, a composition that could prevent or treat infections while enhancing new bone tissue formation at the same time. While the bone regenerative potential will be explored in Chapter 5, the present Chapter will focus on the antimicrobial testing of the base materials. Four bacterial species were chosen to study the effects of strontium, which are the four species most frequently detected in post-operative infections, including orthopaedic infections (130, 141, 354). Bacteria were first characterised for their growth profiles and antibiotic resistance. Strontium salts were then used to assess their susceptibility to this element, before the AW glass powders described in Chapter 2 were tested.

4.2 Materials and methods

4.2.1 Bacterial strain characterisation

Four species were chosen for the antimicrobial testing of strontium and the strontium AW glasses, which correspond to the four species most commonly found in nosocomial and post-operative infections (130, 141, 354): *Staphylococcus aureus*, *Staphylococcus epidermidis*, *Escherichia coli* and *Pseudomonas aeruginosa*. Their NCTC (National Collection of Type Cultures) strain and Gram-staining characteristic are summarised in Table 4.1.

Table 4.1: Summary of the four bacterial species used in this work.

Species	NCTC number	Gram
Staphylococcus aureus	8532	Positive
Staphylococcus epidermidis	11047	Positive
Escherichia coli	11954	Negative
Pseudomonas aeruginosa	10332	Negative

During every test, Gram-staining was systematically used to confirm the species in culture and the absence of contaminations, along with colony morphology on agar plates. Examples of Gram-stain appearance of the four species are shown in Figure 4.1. First, a small amount of bacterial cells was spread on a microscope glass slide with a droplet of water that was fixed using a Bunsen flame. The glass slide was then covered with crystal violet solution (Pro-Lab Diagnostics) for 1 min, rinsed with tap water, and the stain fixed using iodine solution (Pro-Lab Diagnostics). The slide was rinsed again under tap water, washed with ethanol and then covered in safranin solution (Pro-Lab Diagnostics) for counter-stain for 1 min. The slide was rinsed again under tap water, blotted, let dry and then observed under optical microscope (Motic B1-220A) using immersion oil and a 100x magnifying lens.

Each species was characterised for its growth curve, optical density standard curve and antibiotic susceptibility to gentamicin, as described in the following Sections.

All culture media was from Oxoid and prepared following the manufacturer instructions, culture plates were from Corning and Petri dishes from Scientific Laboratory Supplies Ltd. Brain Heart Infusion (BHI) was used for broth cultures of *S. aureus*, *S. epidermidis* and *E. coli*, while LB (Lysogeny Broth) was used for *P. aeruginosa*. Mueller-Hinton (MH) agar was used for culturing all the four species. Living cultures were maintained by streaking new plates at least once a week.

Incubation was performed in a Thermo Scientific Forma Direct Heat CO_2 Incubator, kept at 37 °C and 10 % CO_2. Because of its tendency to aggregate, planktonic cultures of *P. aeruginosa* were always incubated in a shaking incubator (MaxQ Mini 4450, Thermo Scientific) and aliquots withdrawn using cut-end pipette tips, as described in Schleheck et al. (355). 10-fold dilutions in 900 µL of phosphate buffered saline (PBS, Lonza) were carried out for CFU enumeration.
Statistical analysis was carried out using one-way ANOVA.

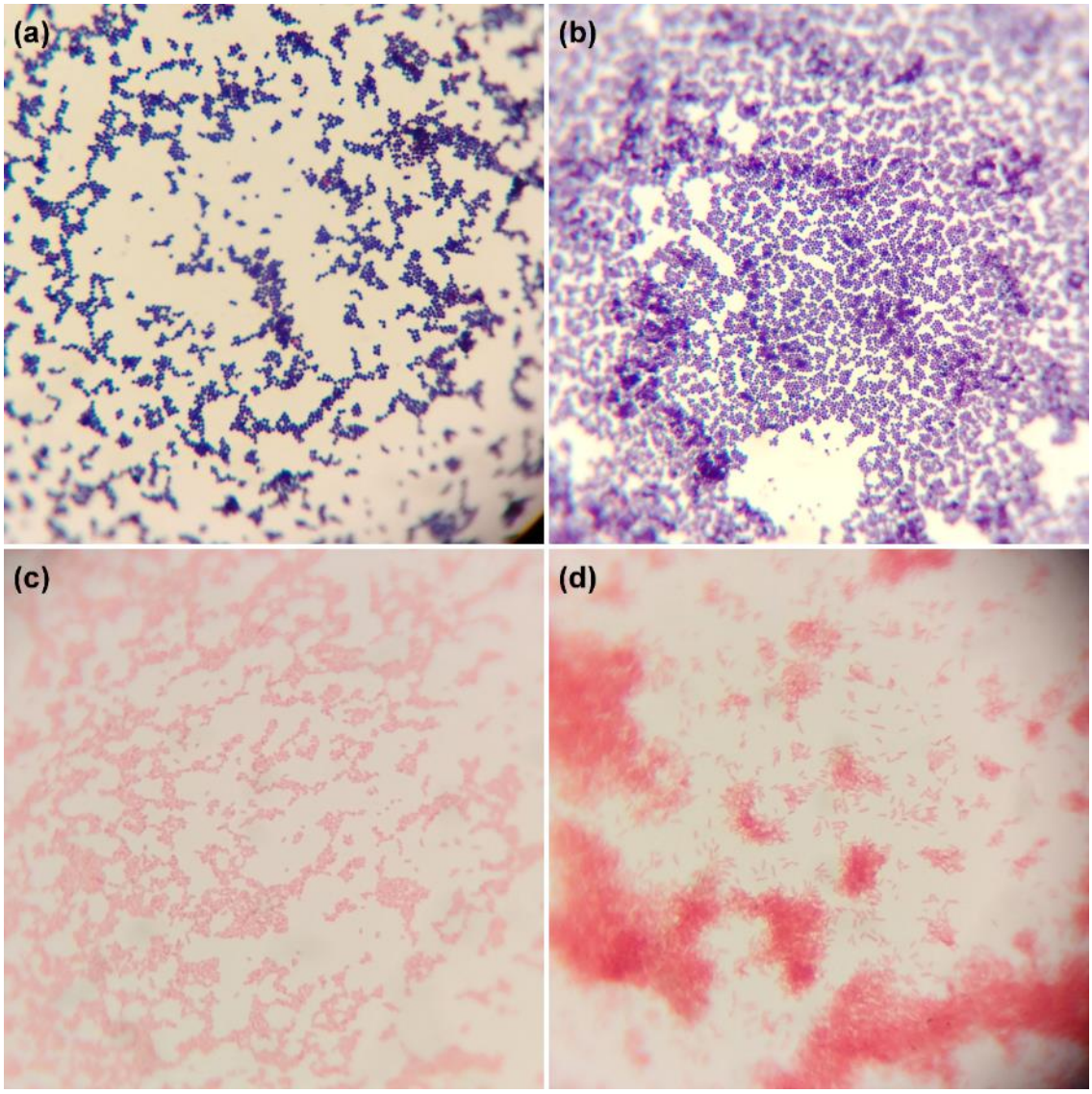

Figure 4.1: Microscope pictures of the four bacteria studied after Gram-staining, 100x lens, 4x camera. (a) *S. aureus*, Gram-positive, (b) *S. epidermidis*, Gram-positive, (c) *E. coli*, Gram-negative, (d) *P. aeruginosa*, Gram-negative.

4.2.1.1 Determination of the growth curves of bacterial cultures

The growth characteristics for the four bacterial species were investigated, in order to determine the time required to get a log-phase culture from inoculation of the broth. A schematic of the experimental procedure is displayed in Figure 4.2.

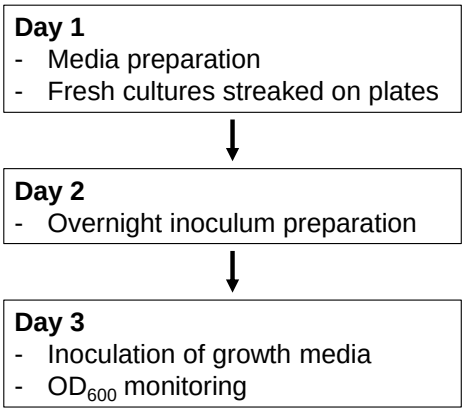

Figure 4.2: Diagram representing the experimental procedure for the determination of growth curves.

On the first day, 250 mL of BHI media was prepared in a 500 mL bottle and autoclaved for *S. aureus*, *S. epidermidis* and *E. coli* and LB for *P. aeruginosa*. Fresh agar cultures were started by streaking MH agar plates and incubating them overnight.
On the second day, 60 mL of stock media were inoculated with a small bacterial colony, taken from the fresh culture prepared the day before. This was also incubated overnight to reach a steady culture.
On day 3, the monitored growth was initiated: 25 mL of the overnight broth were poured into the 250 mL of pre-warmed media prepared on day 1, shaken and then 2 mL were taken for the 0 time-point optical density (OD) measurements at 600 nm using a Jenway 6305 spectrophotometer. The bottles were kept in the incubator between time points, *P. aeruginosa* cultures were kept in the shaking incubator set at 37 °C and 200 rpm (revolutions per minute). At each time-point, two samples of 1 mL were taken from the cultures, their OD_{600} measured and the two measures averaged. Measures were taken regularly until the steady phase was reached. OD_{600} measurements were zeroed using plain media saved before inoculation.
For each species, the test was repeated three times and average and standard deviation of results calculated.

4.2.1.2 Determination of the standard curves for calculating the bacterial cell concentration from optical density measurements

Standard curves were prepared in order to combine the optical density of a broth culture with its concentration of viable bacterial cells. The procedure is summarised in Figure 4.3.

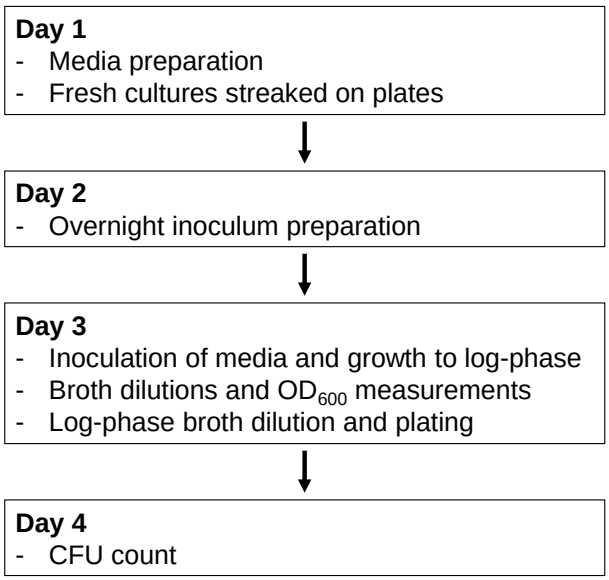

Figure 4.3: Diagram representing the experimental procedure for the determination of optical density (OD) standard curves.

First, new media was prepared and an agar plate streaked for fresh cells, incubated overnight. 10 mL of warm media were inoculated with a small colony from the streaked plate and the planktonic culture was also incubated overnight. 1 mL of this overnight culture was then transferred into 9 mL of warm new media and a timer started according to the results of the growth curve (Section 4.3.1.1) in order to get a late log-phase culture. The sample was then 2-fold diluted down to 1/64 of the initial log-phase, the OD_{600} of each dilution measured twice, the log-phase sample diluted down to 10^{-8} and plated on MH agar in duplicate. Plates were incubated overnight and the morning after colonies were counted from the dilutions that held 20-200 colony-forming units (CFUs). This was repeated three times for each species. Data from the three repeats were pooled together and linearly interpolated to obtain a simple equation that related measured ODs to CFU concentrations.

4.2.1.3 Determination of antibiotic concentrations to use as test positive controls

The antibiotic gentamicin sulphate (Sigma, potency ≥ 590 µg/mg) was chosen as the positive control for all the strontium tests presented in this Chapter. Sections 4.2.1.3.1 to 4.2.1.3.3 describe how the concentration of gentamicin required for each test and for each species was obtained. The EUCAST protocol (by Matuschek et al. (356)) was used as a reference for the disc diffusion tests described in Sections 4.2.1.3.1 and 4.2.1.3.2.

4.2.1.3.1 Determination of the concentration of gentamicin required for positive controls in zone of inhibition assays with paper discs

Paper discs were used for the testing of strontium salts, as described in Section 4.2.2. This test was carried out to find the gentamicin concentration needed for the positive controls. Three plates were prepared for each species. The procedure is schematically represented in Figure 4.4.

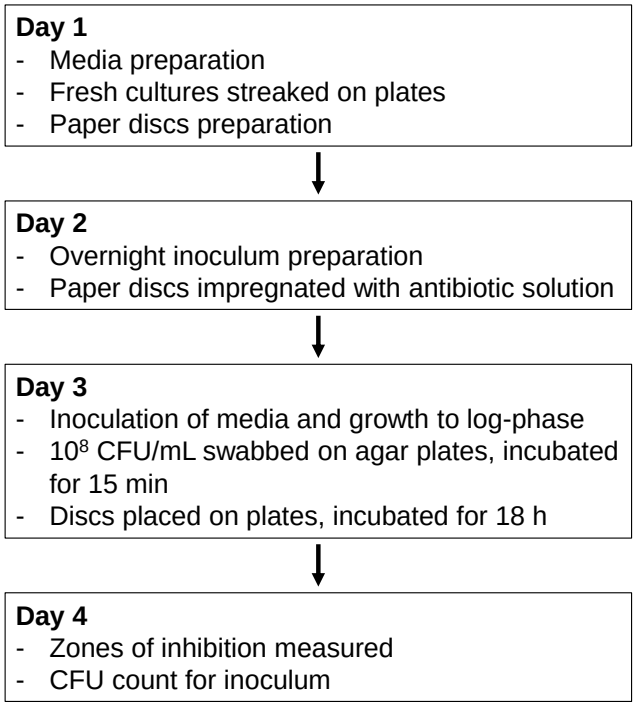

Figure 4.4: Diagram representing the experimental procedure for the determination of the effective concentrations of gentamicin in paper discs, to be used as positive controls in tests with strontium salts.

Before starting the test, new cultures were streaked on MH agar plates and cultured overnight, fresh media was prepared and paper discs (diameter 6.5 mm) were cut from Whatman Qualitative 1 filter paper, labelled and autoclaved.

40 mL of pre-warmed media were then inoculated with a small colony taken from the agar culture and also incubated overnight. Sterile gentamicin sulphate dilutions were prepared in distilled water in three concentrations: 35, 70 and 140 µg/mL. The filter paper discs were then placed in empty sterile Petri dishes and 20 µL of the corresponding antibiotic concentration dropped on each disc, as described by Walter et al. (357). PBS was used as the negative control. Discs were let dry at 37 °C before using them.

On the third day, log-phase cultures were started by inoculating 1 mL of the overnight broth into 9 mL of warm new media and cultured according to the results of the growth curves (Section 4.3.1.1). Cultures were then checked for their OD_{600} to ensure they had reached their log-phase of growth, their CFU concentration was calculated according to the standard curve reported in Section 4.3.1.2 and consequently diluted in new media to reach a concentration of 10^8 CFU/mL. This suspension was used to swab pre-labelled MH agar plates, which were then incubated for 15 minutes before the dried paper discs were placed on them using sterile tweezers. Each plate was divided in quarters as shown in Figure 4.5. The 10^8 suspension was then diluted and plated to verify the exact CFU concentration used. All plates were cultured for 18 h before inhibition zones were measured and the required gentamicin concentration found.

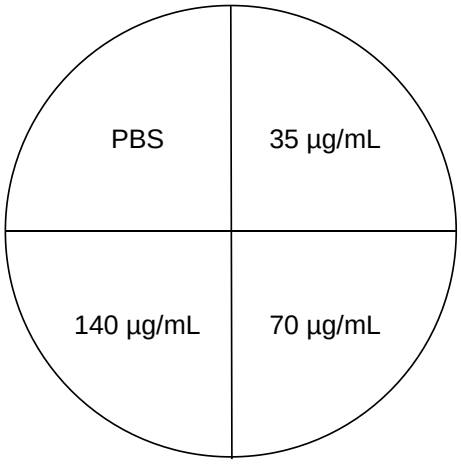

Figure 4.5: Partition of agar plates used for testing the required concentration of gentamicin sulphate in paper discs for disc diffusion assays.

4.2.1.3.2 Determination of the concentration of gentamicin required for positive controls in zone of inhibition assays with glass agar discs

This test was carried out to find the gentamicin concentration needed for the agar disc diffusion, described in Section 4.2.3 and adapted from the work published by Fernandes et al. (198). Three plates were tested for each species; a diagram for the test is represented in Figure 4.6.

Before starting the test, fresh media was prepared and MH agar plates were streaked for fresh colonies and incubated overnight.

For each species, a volume of 40 mL of media was then inoculated with a small bacterial colony and also incubated overnight. 2.4 % w/v technical agar was prepared using distilled water. Five gentamicin concentrations in agar were prepared: 17.5, 35, 70, 140 and 280 µg/mL; pure agar was used as the negative control. Gentamicin was dissolved in water and stock dilutions prepared so that the desired concentrations could be obtained by adding 1 mL of the stock solution to 100 mL of agar. For each gentamicin concentration, four plates were prepared by pouring 15 mL of the antibiotic agar in 90 mm Petri dishes.

Log-phase cultures were then started by inoculating 1 mL of the overnight culture into 9 mL of warm fresh media and incubating them according to their growth curve (Section 4.3.1.1). Three concentrations of gentamicin were tested for each species, depending on the results of the paper disc diffusion presented in Section 4.3.1.3.1, and are reported in Table 4.2.

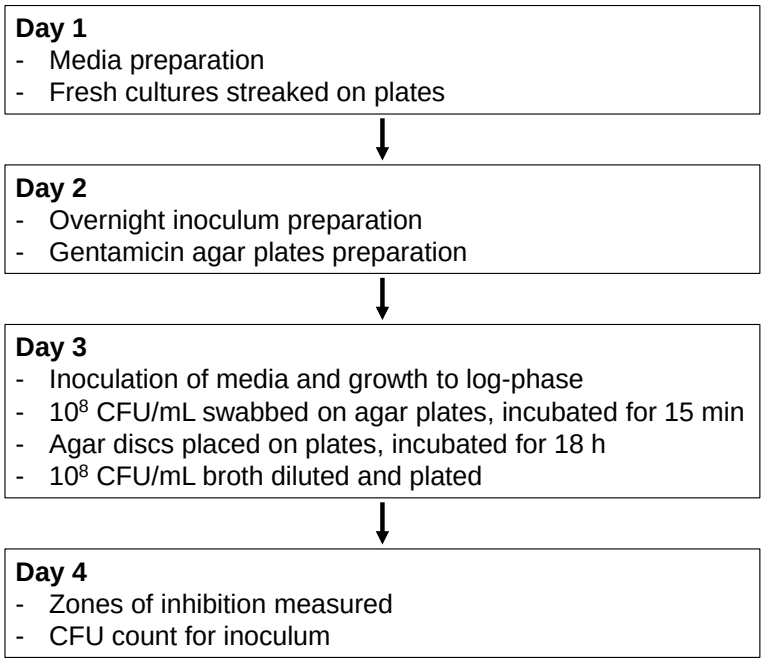

Figure 4.6: Diagram representing the experimental procedure for the determination of the effective concentrations of gentamicin in agar, to be used as positive controls in tests with glass agar discs.

Table 4.2: Concentrations of gentamicin sulphate tested in technical agar.

Species	Concentrations tested (µg/mL)
S. aureus	17.5, 35, 70
S. epidermidis	17.5, 35, 70
E. coli	35, 70, 140
P. aeruginosa	70, 140, 280

Once cultures had reached their log-phase, their CFU concentration was calculated according to their standard curve reported in Section 4.3.1.2 and dilutions were made to obtain 10^8 CFU/mL suspensions. For each species, three MH agar plates were swabbed and then incubated for 15 min. Small gentamicin agar discs were prepared by punching them off the plates prepared as described above, using a sterile size 4 puncher (disc diameter 7.5 mm, 3 mm thickness). These discs were then positioned using sterile tweezers on the swabbed plates, which were incubated for 18 h before measuring the zones of inhibition. Test plates were partitioned in quarters again, similarly to what shown in Figure 4.5 for the paper disc test. The 10^8 CFU/mL suspension was diluted and plated for verifying the actual amount of cells used.

4.2.1.3.3 Determination of the concentration of gentamicin required for positive controls in planktonic cultures

Positive controls for planktonic cultures were required for the broth dilution tests presented in Section 4.2.4. Gentamicin sulphate was selected as the antimicrobial agent for all the four bacteria under testing, consistently with the other tests presented in this Chapter. The minimum inhibitory concentration (MIC) and the minimum bactericidal concentration (MBC) were determined, where the MIC was defined as the minimum concentration of the antimicrobial agent that prevented further growth of the initial inoculum, while the MBC was the minimum concentration that could kill the initial inoculum.

The procedure for the testing is schematically shown in Figure 4.7.

First, new media and fresh cultures on agar plates were prepared, then overnight cultures were started.

Log-phase stage was reached by 10-fold diluting the overnight broth and incubating it accordingly to the growth curves shown in Section 4.3.1.1. In the meantime, well-plates were prepared: 48-well plates and a stock solution of 17.9 mg/mL of gentamicin sulphate in media were used, carrying out 2-fold dilutions in 1 mL of the stock and thus leaving 500 µL of gentamicin solution in each well. Once the bacterial suspension had reached its log-phase, its OD_{600} was measured and an inoculum prepared with a bacterial concentration of $2x10^6$ CFU/mL, basing on the standard curves displayed in Section 4.3.1.2. A volume of 500 µL of this inoculum was then added to the well-plate, thus bringing the final volume of each well to 1 mL. The final concentrations tested ranged from 8.95 mg/mL to 0.5 µg/mL, as shown in Figure 4.8. The used $2x10^6$ inoculum was diluted and plated to ensure that the correct CFU/mL concentration was prepared.

The inoculated well-plates were incubated for 24 h, after which they were collected and the MIC chosen as the lowest antibiotic concentration that did not show any growth in the corresponding well, i.e. that left clear media in the well. 10 µL of this concentration and of the three concentrations above were then plated: the MBC was chosen as the concentration that did not bring any growth on MH agar after 24 h incubation.

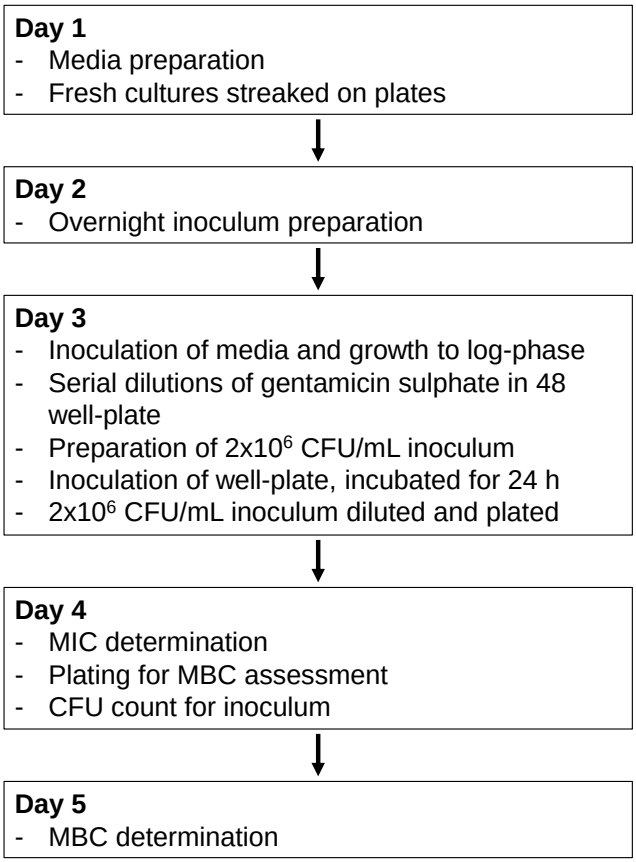

Figure 4.7: Diagram representing the experimental procedure for the determination of gentamicin MIC and MBC, to be used as positive controls in broth dilution tests.

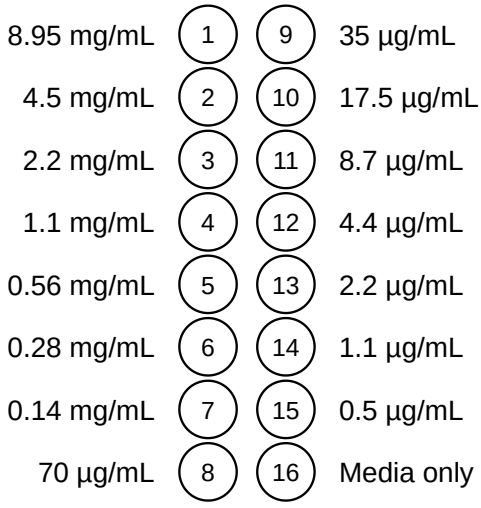

Figure 4.8: Gentamicin sulphate dilutions tested for MIC/MBC of the four bacteria under study.

4.2.2 Zone of inhibition tests using strontium salt solutions on paper discs

In order to test the potential antimicrobial effect of strontium ions, without the presence of the glass material, strontium chloride anhydrous (Fisher Scientific Ltd) and strontium nitrate (Sigma) were chosen to run the zone of inhibition tests described in Sections 4.2.2.1 and 4.2.2.2. Sodium chloride (Sigma) was used as a control for the effect of chlorine, PBS was used as the negative control. The procedure described in the EUCAST protocol (356) was followed.

4.2.2.1 Testing of the antibacterial effect of strontium using two strontium salts in zone of inhibition assays

A diagram describing the testing procedure is shown in Figure 4.9.
New MH agar plates were streaked and incubated overnight and fresh media was prepared. Paper discs were cut from Whatman Qualitative 1 filter paper, diameter 6.5 mm, labelled and autoclaved.

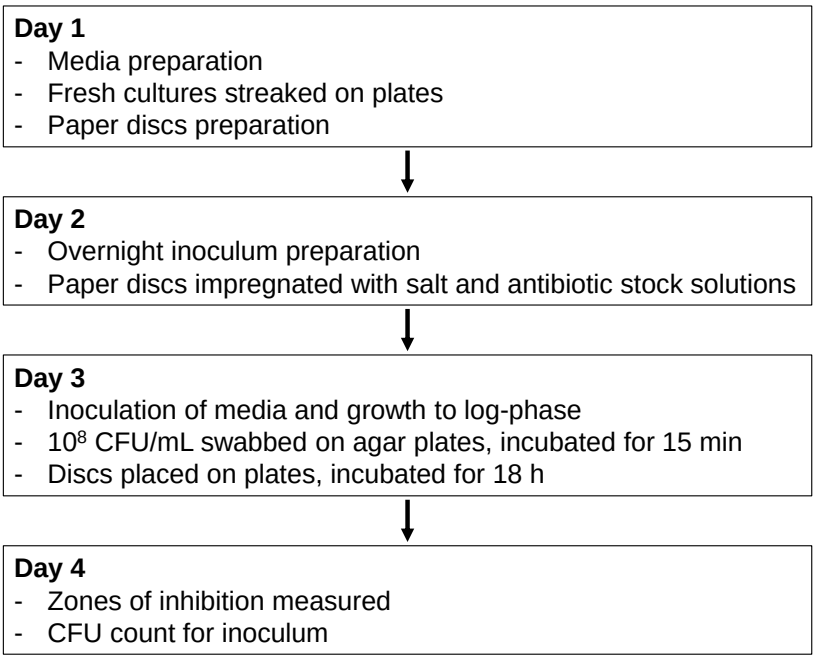

Figure 4.9: Diagram representing the zone of inhibition testing of strontium salts using paper discs.

The antibiotic stock was prepared according to the concentration found in Section 4.2.1.3.1. The stock solutions for strontium chloride and strontium nitrate were prepared at 4 mM concentration, while the sodium chloride solution was 8 mM to

match the chlorine concentration. Following the procedure described by Walter et al. (357), 20 µL of each solution were dropped on the corresponding paper disc, three repeats per bacterial species, and left in the incubator for drying. 40 mL of media were inoculated with a small colony from the fresh culture and incubated overnight.
On the following day, the CFU concentration was calculated at log-phase and a bacterial suspension of 10^8 CFU/mL was prepared. This was swabbed on MH agar plates, which were incubated for 15 minutes before the paper discs were placed on them using sterile tweezers. Plates were organised as shown in Figure 4.10. The 10^8 CFU/mL inoculum was diluted and plated to verify that the correct concentration was used. Zone of inhibitions were checked and measured after 18 h incubation.

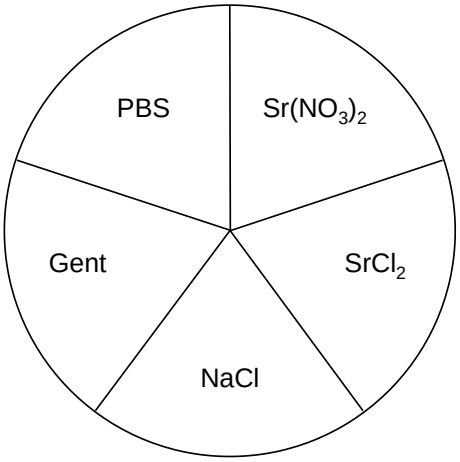

Figure 4.10: Partition of agar plates for the zone of inhibition assay using strontium salts. Gent: gentamicin positive control.

4.2.2.2 Comparison of strontium salts with silver and zinc salts in a zone of inhibition assay

The salts used in the test described in the previous Section 4.2.2.1 were compared also with zinc chloride and silver nitrate (both from Sigma), as zinc and silver are known for their antimicrobial activity (200, 358, 359). This test was done as a proof-of-concept experiment, using other elements that are established antimicrobial agents in the case it will be decided, in future work, that the composition of the glasses under study should be modified to strengthen their antibacterial properties.
The test was repeated as described in Section 4.2.2.1, preparing additional 4 mM zinc chloride and silver nitrate solutions for the discs. MH agar plates were divided as shown in Figure 4.11.

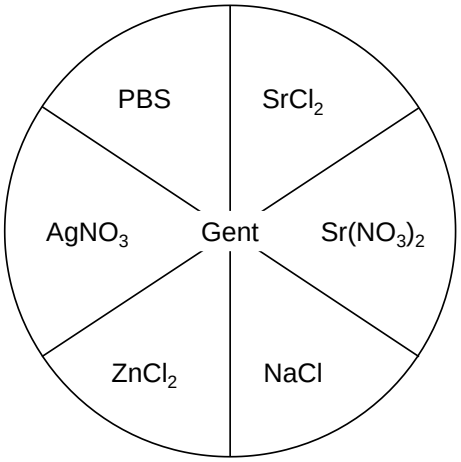

Figure 4.11: Partition of agar plates for the zone of inhibition assay, run to compare strontium salts with silver and zinc salts. Gent: gentamicin positive control.

4.2.3 Zone of inhibition tests using strontium glass powders embedded in agar

It has been described in the literature that some bioactive glass compositions can exert antimicrobial properties (17, 18, 197), even some that do not contain any antimicrobial agent (94, 204, 210). Therefore, after testing strontium alone, another zone of inhibition test that could include glass particles was carried out, so that the effect of the six strontium AW glasses could be assessed. This test was adapted from the work published by Fernandes et al. (198). Small agar discs containing 72 mg/mL of glass powder were produced and used on MH agar plates as samples for the zone of inhibition tests. The diagram for the test is shown in Figure 4.12.

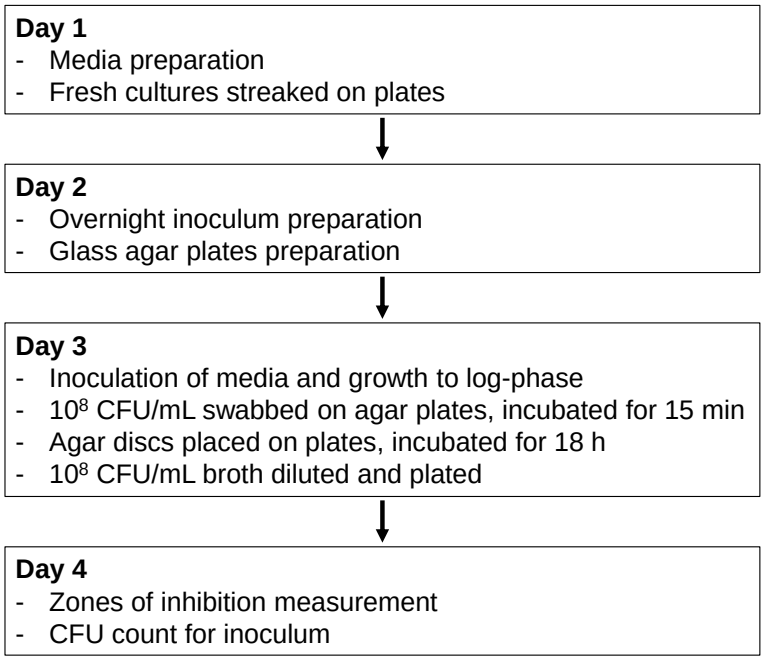

Figure 4.12: Diagram representing the zone of inhibition testing of agar discs containing strontium glasses.

New cultures were streaked on MH agar plates and cultured overnight, while fresh media was prepared.

40 mL of warm media were inoculated with a small fresh colony and incubated overnight. Glass-containing agar discs were prepared using 2.4 % w/v technical agar in distilled water. To obtain the glass concentration of 72 mg/mL, the main bottle of technical agar was kept at 50 °C, 1.44 g of autoclaved glass powder were poured in a sterile vial and 20 mL of agar added. The vial was vortexed in order to ensure a homogenous suspension of the glass particles, 15 mL were transferred into a sterile Petri dish and allowed to solidify at room temperature. This was repeated for all the strontium AW compositions and an agar-only plate was prepared as the negative control. Positive controls containing gentamicin were produced as described in Section 4.2.1.3.2. Small discs were obtained using a sterile size 4 puncher, 7.5 mm diameter. The morning after, log-phase cultures were prepared as already described above, their CFU concentration was calculated measuring their OD_{600} according to their standard curves (Section 4.3.1.2) and a 10^8 CFU/mL concentration was prepared. This was swabbed on MH agar plates, then incubated for 15 min before the small agar discs were placed on their surface using sterile tweezers. Plates were organised as shown in Figure 4.13 and incubated for 18 h. The 10^8 CFU/mL bacterial suspensions were diluted and plated so that the actual bacterial concentration utilised could be verified. The following day, zones of inhibition were checked and measured.

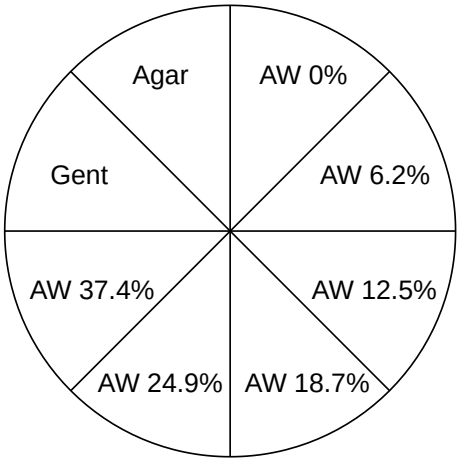

Figure 4.13: Partition of agar plates used for the zone of inhibition assay with glass agar discs. Gent: gentamicin positive control.

4.2.4 Broth dilution testing of strontium glass powders suspended in culture media

A different experiment was set up, so that previous results (presented in Sections 4.3.2 and 4.3.3) could be verified and the strontium glasses could be tested with a different approach. The test was based on the broth dilution method described by Fernandes et al. (198), where bacteria were tested in direct contact with the glass particles, rather than with ions leached from salts on paper or from glass powders embedded in agar. In this test, glass powders were suspended in media for either 24 h or 7 days, then a bacterial inoculum was added and incubated for 24 h before the concentration of CFUs was measured using serial dilutions and viable counts.
All four species were tested after the glass powders were soaked in media for 24 h (Section 4.2.4.1), *Pseudomonas aeruginosa* was tested also with glass powders soaked for a week (Section 4.2.4.2).

4.2.4.1 Determination of the antibacterial effect of strontium glass powders suspended in media for 24 hours

The method is visually summarised in Figure 4.14.

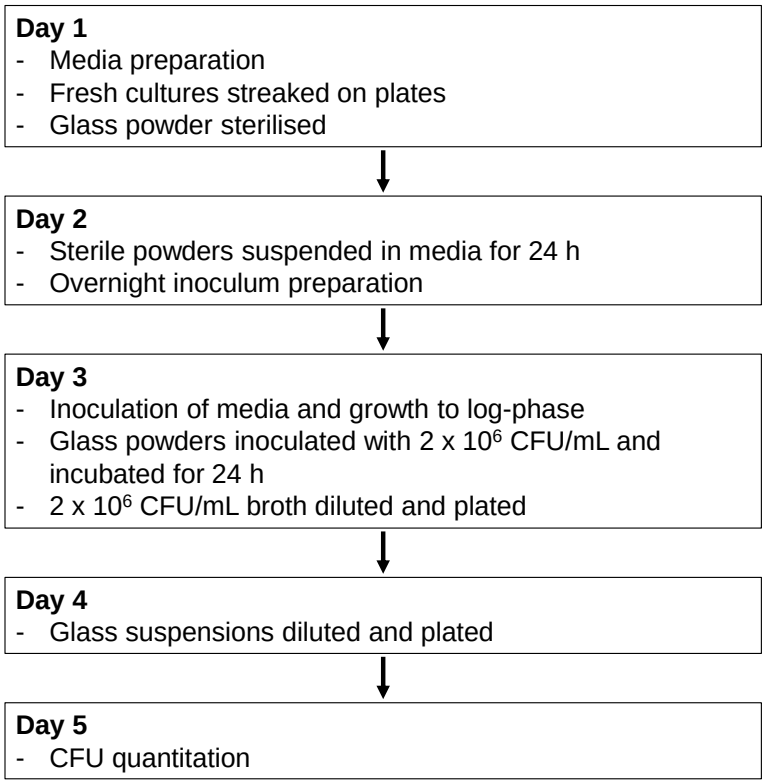

Figure 4.14: Diagram representing the broth dilution testing of strontium glass powders, suspended for 24 h.

432 mg of each composition of strontium glass powder <45 µm were weighed and autoclaved. Fresh media and new cultures on MH agar were prepared. The antibiotic stock was prepared in culture media (BHI for *S. aureus*, *S. epidermidis* and *E. coli*, LB for *P. aeruginosa*), so that the final concentration after the addition of the inoculum was the one found with the MIC/MBC test described in Section 4.2.1.3.3.
On the following day, the sterile glass powders were suspended in 3 mL of media, then 0.5 mL were transferred in 3 bijou vials as repeats. Three 0.5 mL vials were prepared with media only as the negative controls. Three 0.5 mL of the antibiotic dilutions were prepared as the positive controls. Vials were left in the shaking incubator set at 37 °C and 200 rpm for 24 h. 40 mL of warm media were inoculated with a small colony and cultured overnight.
Log-phase cultures were prepared and then diluted to 2 x 10^6 CFU/mL according to their standard curves. 0.5 mL of this bacterial dilution were added to all the vials, making their final volume 1 mL, and left in the shaking incubator for another 24 h. The inoculum used was diluted and plated to verify its actual bacterial concentration.
After 24 h incubation, all suspensions were diluted, plated on MH agar and incubated so that colonies could be counted.

Because *P. aeruginosa* showed some susceptibility for the strontium AW glasses (results shown in Section 4.3.4.1), this test was repeated three times for this species and also tested with a longer soaking time of the glass powders, as detailed in the next Section 4.2.4.2.

4.2.4.2 Determination of the antibacterial effect of strontium glass powders suspended in media for 7 days

The same test described in the previous Section 4.2.4.1 was repeated again for *Pseudomonas aeruginosa*, soaking the strontium AW glass powders for 7 days instead of 24 h (Day 2 in Figure 4.14) before the vials were inoculated, cultured for a further 24 h and then diluted and plated for measuring their CFU concentration.

4.3 Results

4.3.1 Growth characteristics and gentamicin susceptibility of *Staphylococcus aureus*, *Staphylococcus epidermidis*, *Escherichia coli* and *Pseudomonas aeruginosa*

4.3.1.1 Bacterial growth characteristics

Growth curve measurements were prepared for the four species under study, so that information on the time required to reach log-phase cultures could be obtained. Figure 4.15 shows the traces of the growth curves found for *S. aureus*, *S. epidermidis*, *E. coli* and *P. aeruginosa*.

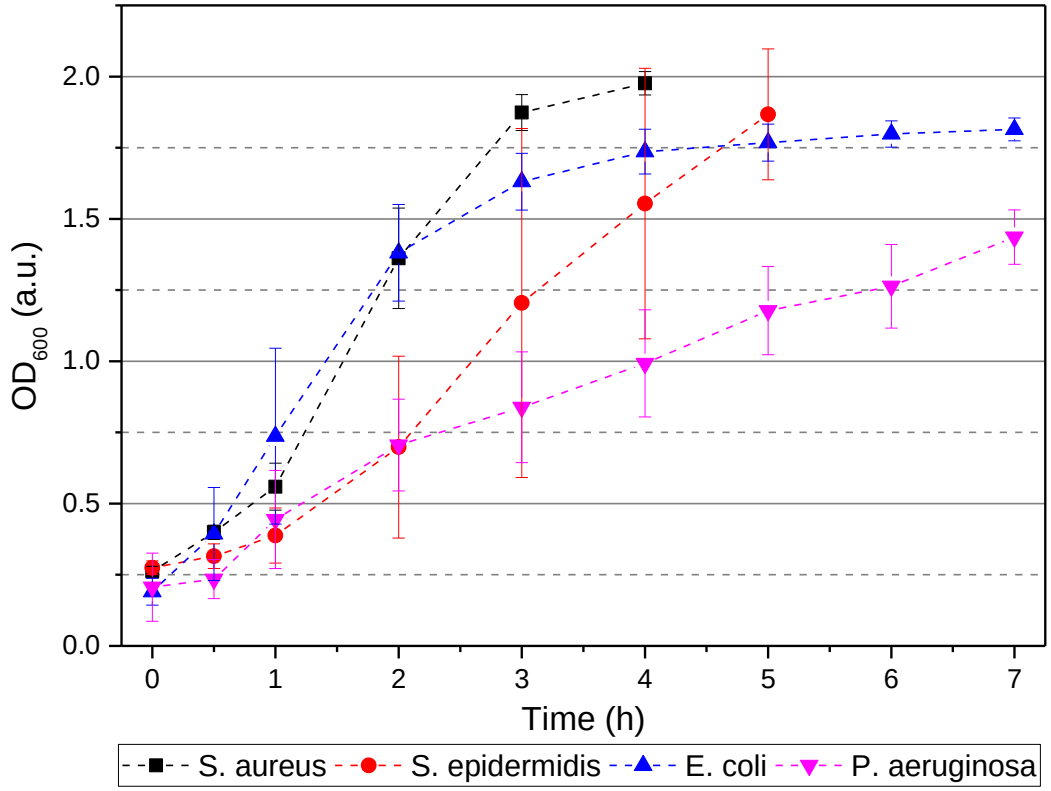

Figure 4.15: Growth curves for the four selected bacterial species. Error bars indicate the standard deviation (n=3).

The four bacteria reached their log-phase, the phase of fast growth characterised by a steep increase in optical density, at different times. *E. coli* was the fastest growing species, reaching the mid log-phase in about 1 h. *S. aureus* took about 2 h, while *S. epidermidis* took 3 h. *P. aeruginosa* took the longest, about 5 h; its optical densities were lower because of its high tendency to form agglomerates, which prevented accurate spectrophotometric measurements and caused the different trend of its growth curve, more similar to a line than a sigmoid curve. However, this test was used to have an indication of the time required by a culture to reach its log-phase for the next experiments described in this Chapter, therefore the information provided was considered acceptable.

Some degree of variability, represented by the standard deviation bars in the graphs of Figure 4.15, was probably due to differences in the concentration of alive bacterial cells present in the inoculum used to initiate the growth study.

The results of this test were used every time a planktonic culture was to be brought to its log-phase, as specified in the tests and assays previously described in Section 4.2.

4.3.1.2 Relation between bacterial cell concentration and optical density of cultures: Standard curves

Standard curves were obtained from optical density measurements and CFU counting and are shown in Figure 4.16. For each species tested, the equation for calculating the CFU concentration in a broth culture sample from its OD_{600} was derived and is reported in Equation 4.1 to Equation 4.4.

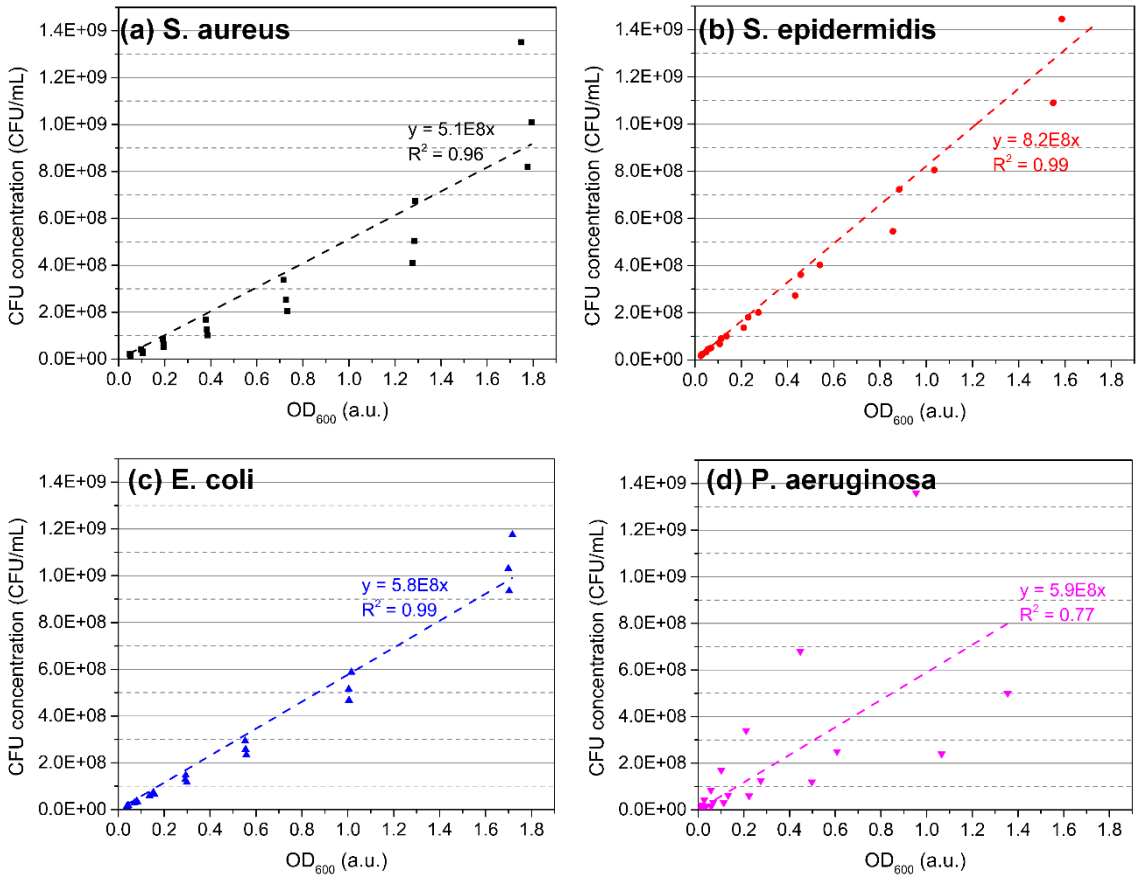

Figure 4.16: Standard curves, obtained from trendlines, that relate the measured optical density to the corresponding CFU concentration. (a) *S. aureus*, (b) *S. epidermidis*, (c) *E. coli*, (d) *P. aeruginosa*.

A linear relationship was chosen for interpolating all the data obtained from three repeats. *P. aeruginosa* showed the highest variability, leading to the lowest R^2 value of 0.77. The R^2 value found for the other fitting lines was 0.96 for *S. aureus* and 0.99 for *S. epidermidis* and *E. coli*. The formulas derived from the data are specified in Equation 4.1 for *S. aureus*, Equation 4.2 for *S. epidermidis*, Equation 4.3 for *E. coli* and Equation 4.4 for *P. aeruginosa*. These results were used every time an inoculum of a known CFU concentration was needed from a log-phase culture, as specified in the methods presented in Section 4.2.

$$CFU_{S.a.} = 5.1 \cdot 10^8 x\ OD_{600}$$

Equation 4.1: Formula for the calculation of *S. aureus* CFU concentration from the measured optical density OD_{600}.

$$CFU_{S.e.} = 8.2 \cdot 10^8 x\ OD_{600}$$

Equation 4.2: Formula for the calculation of *S. epidermidis* CFU concentration from the measured optical density OD_{600}.

$$CFU_{E.c.} = 5.8 \cdot 10^8 x\ OD_{600}$$

Equation 4.3: Formula for the calculation of *E. coli* CFU concentration from the measured optical density OD_{600}.

$$CFU_{P.a.} = 5.9 \cdot 10^8 x\ OD_{600}$$

Equation 4.4: Formula for the calculation of *P. aeruginosa* CFU concentration from the measured optical density OD_{600}.

4.3.1.3 Gentamicin susceptibility of *Staphylococcus aureus*, *Staphylococcus epidermidis*, *Escherichia coli* and *Pseudomonas aeruginosa*

Results reported in this section summarise the gentamicin sulphate concentrations needed as positive controls in the tests run with strontium salts and strontium AW glass powders, with glass agar discs and with loose glass powders in planktonic cultures.

4.3.1.3.1 Concentration of gentamicin required for positive controls in zone of inhibition assays with paper discs

Different gentamicin sulphate concentrations were tested to find the one required for the assays that used paper discs with strontium salts (Section 4.2.2.1) and with strontium, silver and zinc salts (Section 4.2.2.2). Three plates were tested for each species; Figure 4.17 shows one representative plate each. The required concentrations were chosen as the lowest concentrations that gave visible zones of inhibition on the plates.

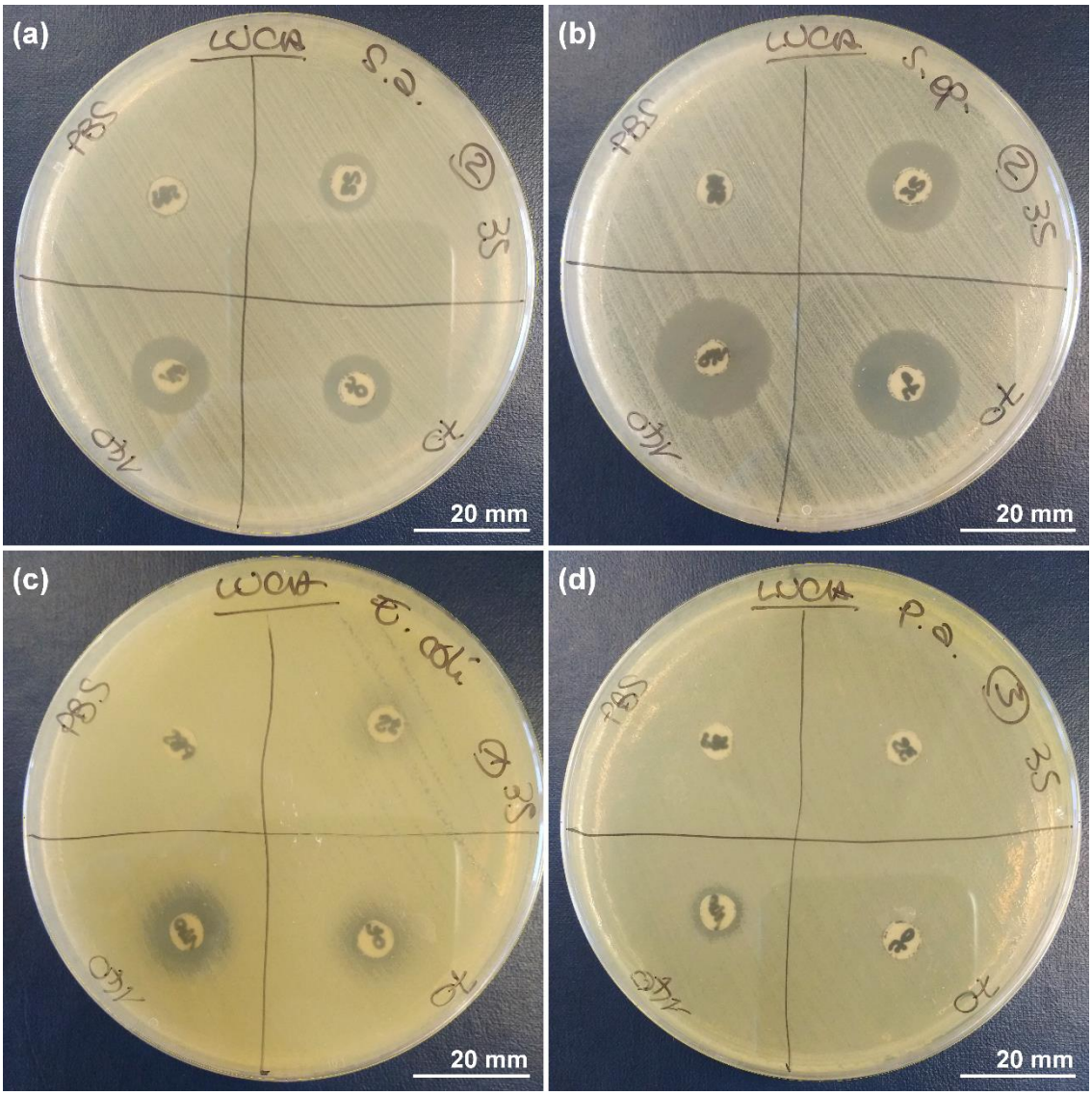

Figure 4.17: Gentamicin sulphate concentration testing from paper discs. (a) *S. aureus*, (b) *S. epidermidis*, (c) *E. coli*, (d) *P. aeruginosa*. Concentrations tested from top right and clockwise on each plate: 35 µg/mL, 70 µg/mL, 140 µg/mL of gentamicin sulphate, PBS (negative control). Scale bars represent 20 mm.

The four species tested led to different concentrations of gentamicin sulphate required for giving inhibition of growth. 35 µg/mL was enough to prevent the growth of *S. aureus* around the sample. For *S. epidermidis,* since the zone of inhibition observed for the lowest concentration tested, 35 µg/mL, gave a large area of growth prevention, half this concentration was chosen as the required concentration for positive controls with this species. On *E. coli* plates, both reduction and inhibition of growth were observed, so the lowest concentration that gave both was chosen. *P. aeruginosa* showed inhibition only with the highest concentration of gentamicin sulphate.
The required gentamicin sulphate concentrations found are summarised in Table 4.3.

Table 4.3: Gentamicin sulphate concentration required for the positive controls in the zone of inhibition assays run with paper discs and strontium salts.

Species	Gentamicin concentration (µg/mL)
S. aureus	35.0
S. epidermidis	17.5
E. coli	70.0
P. aeruginosa	140.0

4.3.1.3.2 Concentration of gentamicin required for positive controls in zone of inhibition assays with glass agar discs

As the agar disc diffusion assay required the use of small agar discs loaded with the strontium glass powder, equivalent agar discs were prepared containing different amounts of gentamicin sulphate. For each species, the lowest concentration that gave inhibition was chosen as the one to be used in positive controls for the test. Figure 4.18 shows a representative plate out of the three tested for each species.

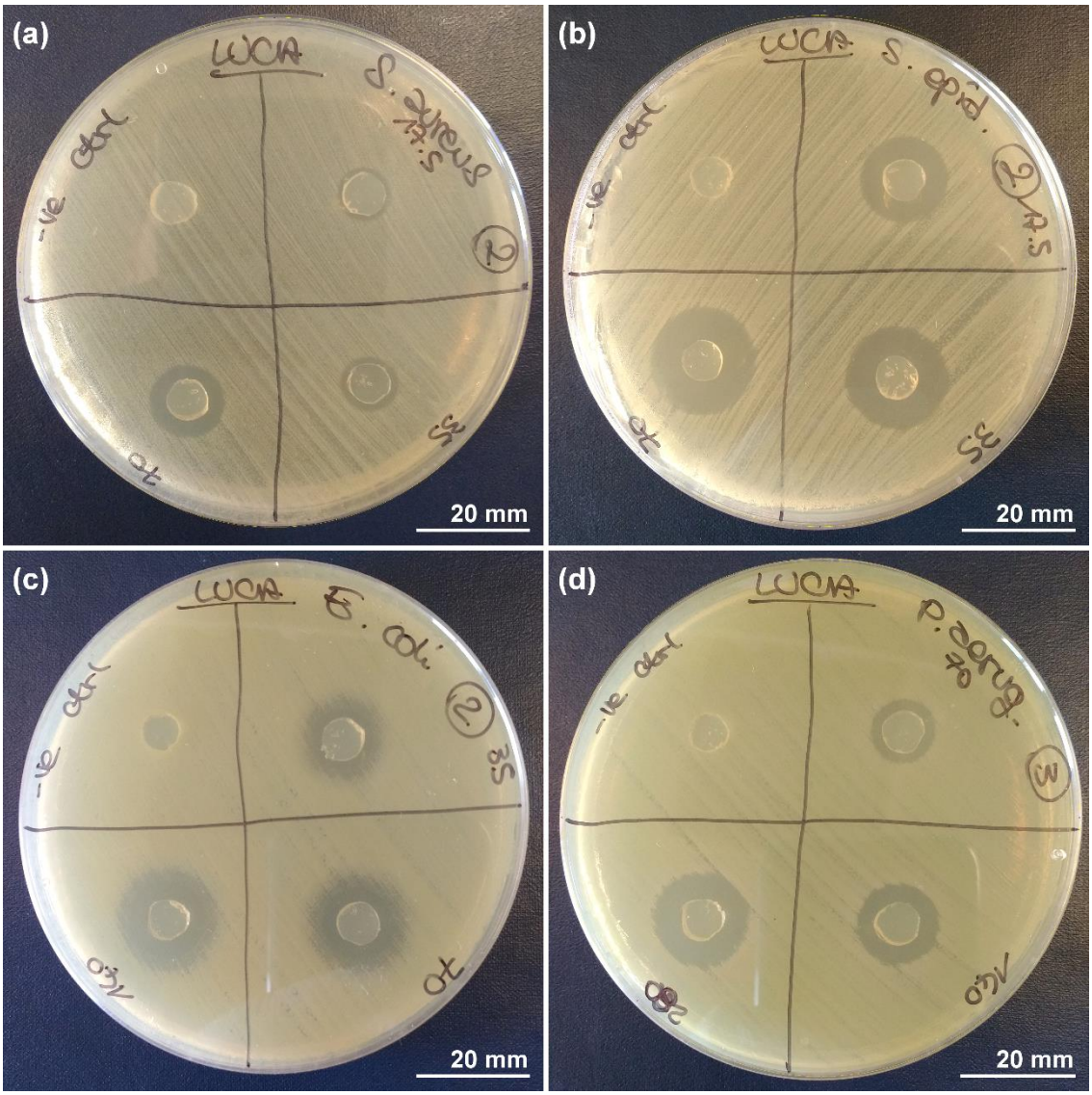

Figure 4.18: Gentamicin sulphate concentration testing from agar discs. (a) *S. aureus*, (b) *S. epidermidis*, (c) *E. coli*, (d) *P. aeruginosa*. Gentamicin concentrations increasing from top right and clockwise on each plate, amounts reported in Table 4.4. Top left sector of each plate: negative control (technical agar only). Scale bars represent 20 mm.

Like in the previous test with paper discs in Section 4.3.1.3.1, the required concentrations were different for each bacterial species and are summarised in Table 4.4.

Table 4.4: Gentamicin sulphate concentration required for the positive controls in the zone of inhibition assay using glass agar discs.

Species	Gentamicin concentration (µg/mL)
S. aureus	70.0
S. epidermidis	17.5
E. coli	35.0
P. aeruginosa	70.0

The same or lower concentrations were found compared to the paper discs test (Table 4.3), with the exception of *S. aureus* that in this case gave inhibition for a higher concentration (70 µg/mL).

4.3.1.3.3 Concentration of gentamicin required for positive controls in planktonic cultures for broth dilution tests

MIC and MBC were tested for the positive controls of the broth dilution tests described in Section 4.2.4, when planktonic cultures were grown in the presence of strontium AW glass particles.

As shown in Table 4.5, MIC for gentamicin sulphate against *S. aureus* was the same concentration found in the agar discs. MICs for the other three species were lower than those found in agar discs. *S. aureus* and *E. coli* had their MBC remaining at the same value of their MIC, while MBC for *S. epidermidis* and *P. aeruginosa* were higher than their MIC, but still lower than their agar disc concentrations.

Table 4.5: MIC and MBC values for gentamicin sulphate, to be used as the positive controls in the broth dilution tests.

Species	MIC (µg/mL)	MBC (µg/mL)
S. aureus	70.0	70.0
S. epidermidis	4.4	8.7
E. coli	17.5	17.5
P. aeruginosa	8.7	17.5

4.3.2 Susceptibility of selected bacteria to strontium salts in zone of inhibition assays

Salts were used as a simplified model of the strontium-containing glasses under study: since it was hypothesised in this work that the chemical element strontium could impart antimicrobial properties to the glasses, salts were used in zone of inhibition

tests to assess the effect of strontium ions alone on the selected bacterial strains. First, strontium chloride and strontium nitrate were utilised (Section 4.3.2.1). Then, silver nitrate and zinc chloride were also tested for a comparison with known antimicrobial elements (Section 4.3.2.2).

4.3.2.1 Susceptibility of selected bacteria to strontium salts: Strontium chloride and strontium nitrate

The effect of strontium, the doping agent chosen for the AW glasses described in this work, was studied by using two different strontium salts: strontium chloride and strontium nitrate. Sodium chloride was used as a control to take into account the potential effect of chlorine in strontium chloride, while PBS was used as the negative control. Figure 4.19 shows the results of the test, one representative plate per bacterial species (three were tested).

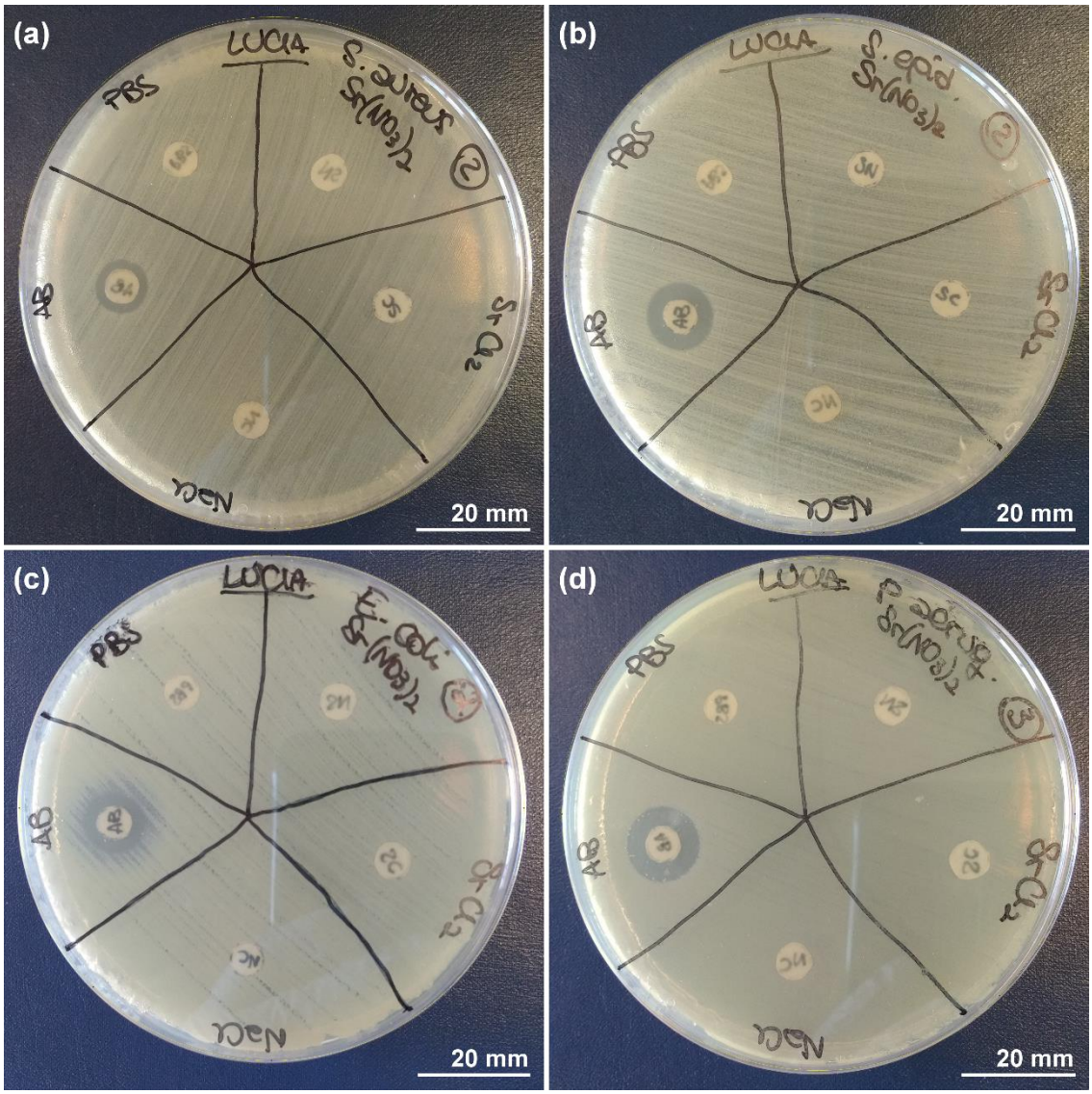

Figure 4.19: Plates showing the results of the zone of inhibition testing of strontium salts from paper discs. (a) *S. aureus*, (b) *S. epidermidis*, (c) *E. coli*, (d) *P. aeruginosa*. Samples from top right and clockwise on each plate: strontium nitrate, strontium chloride, sodium chloride, positive control (gentamicin), negative control (PBS). Scale bars represent 20 mm.

None of the tested salts induced inhibition of the growth of the four bacterial species. It was not possible to determine if this was due to a lack of antimicrobial action of the salts or if the concentration used was not high enough to highlight it. 4 mM was the highest concentration that could be tested before the stock solution precipitated, as strontium can react with sulphate, carbonate and phosphate ions contained in media (360). Although higher concentrations have been used in the literature (195), this highly depends on the media chosen; however, 4 mM is usually the concentration used in both bacterial (18) and cell studies (361).

4.3.2.2 Susceptibility of selected bacteria to strontium salts: Comparison with silver and zinc salts

Since the strontium salts showed no antibacterial effect in the test in Section 4.3.2.1, with no induced inhibition of growth, a silver and a zinc salt were also tested to check the response of the four chosen species to the same concentration of these known antibacterial elements. Three plates were produced for each bacterial species; one representative plate for each species is shown in Figure 4.20.

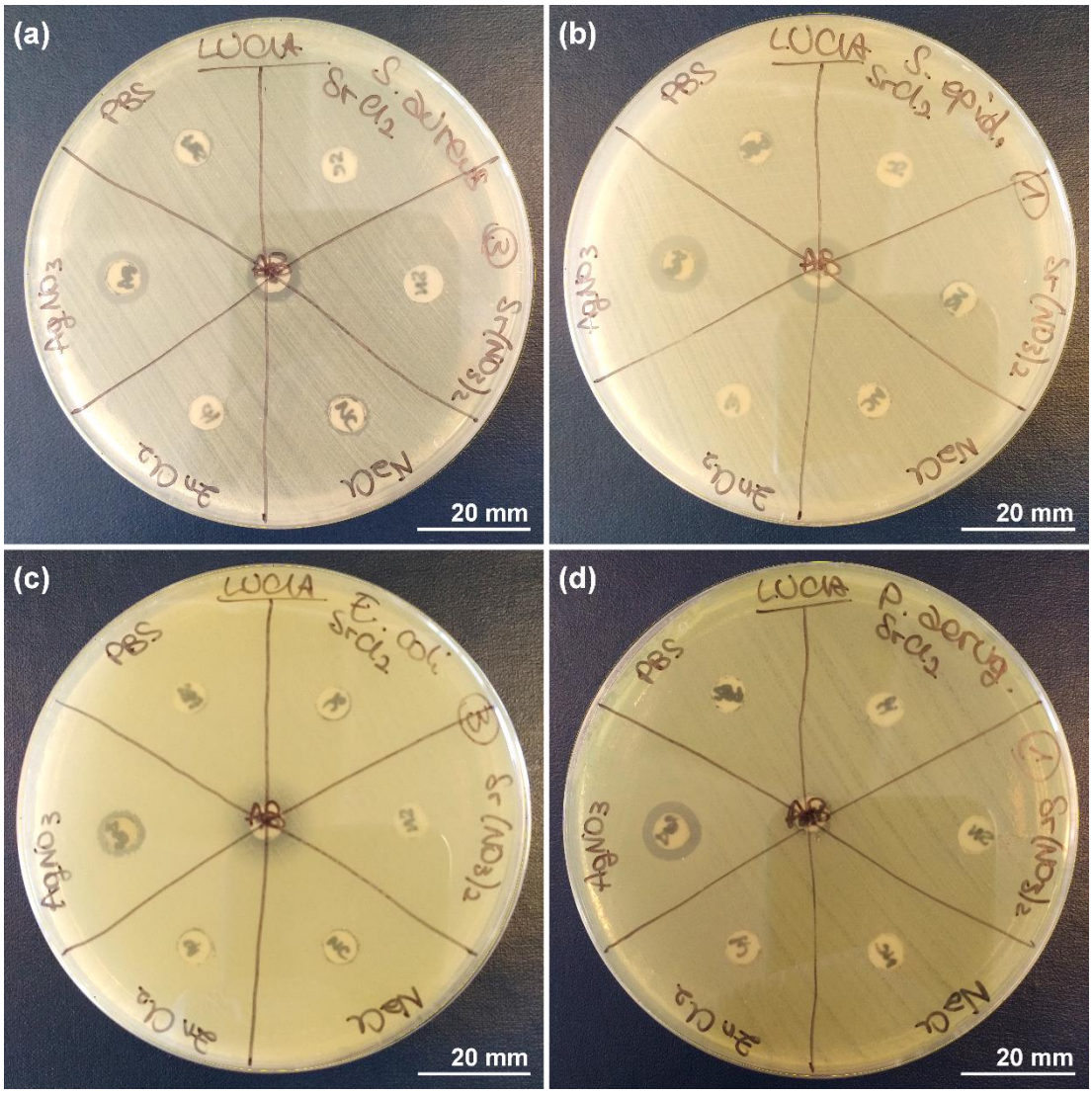

Figure 4.20: Plates showing the results of zone of inhibition testing using paper discs, comparing strontium salts with zinc chloride, silver nitrate and controls. (a) *S. aureus*, (b) *S. epidermidis*, (c) *E. coli*, (d) *P. aeruginosa*. Samples from top right and clockwise on each plate: strontium chloride, strontium nitrate, sodium chloride, zinc chloride, silver nitrate, negative control (PBS); centre sample: positive control (gentamicin). Scale bars represent 20 mm.

The strontium salts and sodium chloride did not induce any inhibition, as seen with the previous test, thus confirming results shown in Section 4.3.2.1. Zinc chloride also had no inhibitory effect on bacterial growth, suggesting that the 4 mM concentration used might be perhaps not high enough. However, a clear zone of inhibition was found around the silver disc for all the four species tested, average diameters of the halo are reported in Table 4.6. These results proved the much stronger antimicrobial action of silver, suggesting that this element could be taken into consideration as a second doping element for the strontium AW glasses under study, if stronger antibacterial properties were required. For *S. aureus* and *S. epidermidis*, the zone of inhibition produced by silver was comparable to the one induced by the antibiotic positive control. For *E. coli* and *P. aeruginosa*, the effect of silver was stronger than the antibiotic; for *P. aeruginosa*, the halo produced by the positive control was small, probably due to variations in the gentamicin sulphate stock solution prepared.

Table 4.6: Average diameter of the inhibition halo induced by silver nitrate, compared to the zone measured for the gentamicin sulphate positive controls. For *E. coli*, both diameter of inhibition and diameter of reduction of growth (in brackets) are reported.

Species	Silver Diameter (mm)	Gentamicin Diameter (mm)
S. aureus	9.17	9.07
S. epidermidis	10.57	11.73
E. coli	8.07	7.57 (11.77)
P. aeruginosa	9.90	7.13

4.3.3 Susceptibility of selected bacteria to strontium glass powders embedded in agar

The antimicrobial effect of the six strontium AW glasses was also investigated, so that the properties of the material for the final porous scaffolds could be characterised. In this Section, technical agar containing glass powder was used to produce cylindrical samples that were tested in a zone of inhibition type of assay. Figure 4.21 shows the results of this test with a representative plate for each species tested (three plates were made for each species).

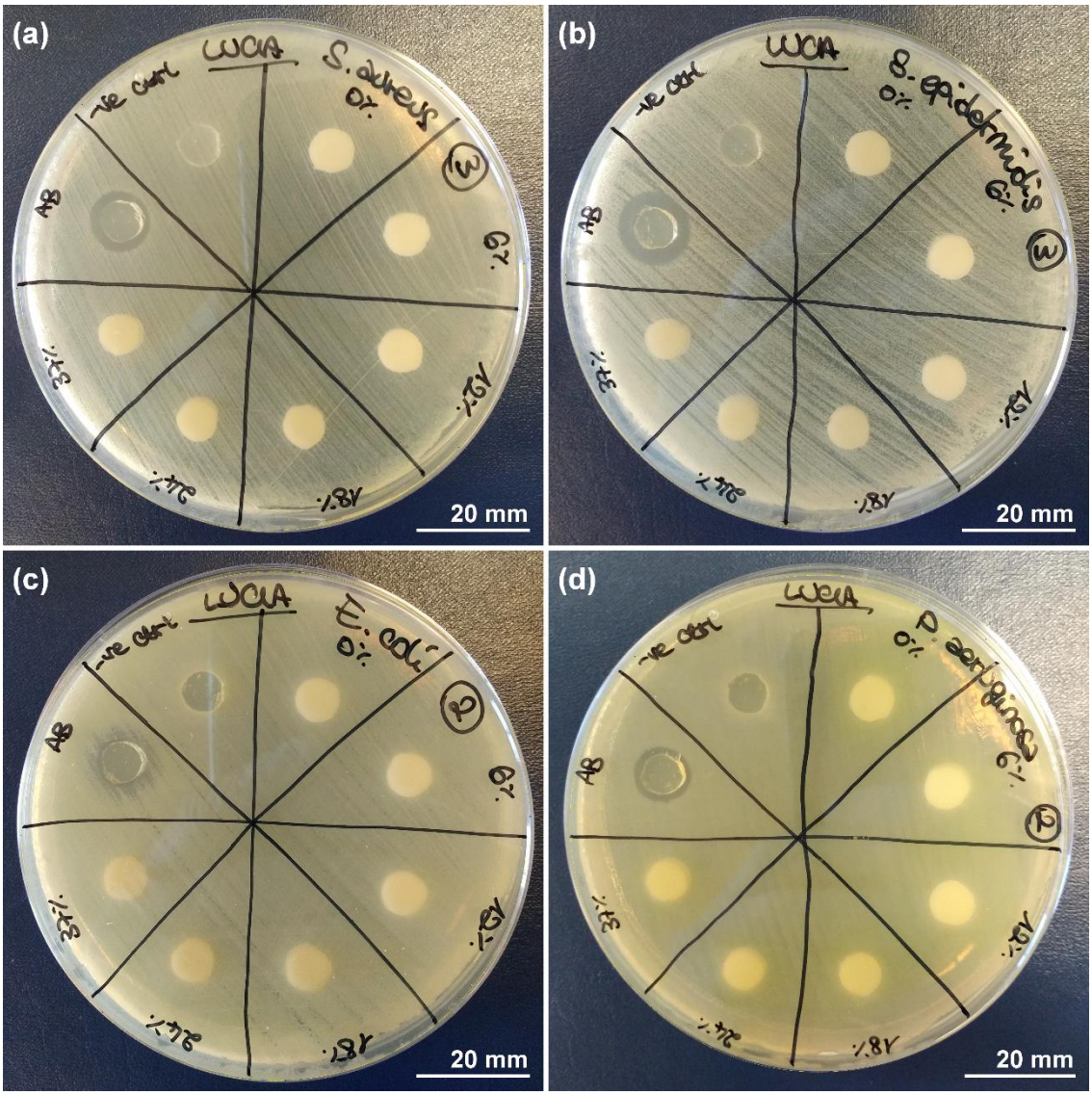

Figure 4.21: Plates showing the results of zone of inhibition testing using strontium AW glass powders mixed in agar discs. (a) *S. aureus*, (b) *S. epidermidis*, (c) *E. coli*, (d) *P. aeruginosa*. Samples from top right and clockwise on each plate: AW 0%, AW 6.2%, AW 12.5%, AW 18.7%, AW 24.9%, AW 37.4%, positive control (gentamicin) and negative control (PBS). Scale bars represent 20 mm.

None of the glass compositions produced a zone of inhibition for any of the four bacterial species tested, while halos were visible only for the positive controls. It is possible that the six strontium AW glasses did not allow enough ions to leak and diffuse through the agar, or that the concentration of glass powder used in the agar was not high enough; higher concentrations and ion release should be assessed in future work for better tuning of this experiment.

Because of the inconclusive results of this and the previous tests, it was chosen to investigate the antimicrobial properties of the six glasses under study with a different test rather than testing different concentrations for the glass agar discs; results are reported in the following Section 4.3.4.

4.3.4 Susceptibility of selected bacteria to strontium glass powders in broth dilution tests

Strontium AW glass powders were tested after soaking for 24 h against all the four bacterial species (Section 4.3.4.1), or after soaking for 7 days against *P. aeruginosa* (Section 4.3.4.2).

4.3.4.1 Susceptibility to strontium glass powders suspended in culture media for 24 hours

Figure 4.22 shows the results of the broth dilution test against the four bacterial species chosen in this work. The positive control was gentamicin sulphate at the four concentrations found in Section 4.3.1.3.3, negative control was culture media without any glass powder. In this case, the strontium AW glass powders were soaked and mixed in a shaking incubator for 24 h before inoculation. The test with *P. aeruginosa* was repeated three times with comparable results; the graph in Figure 4.22d shows the results of one of the three repeats.

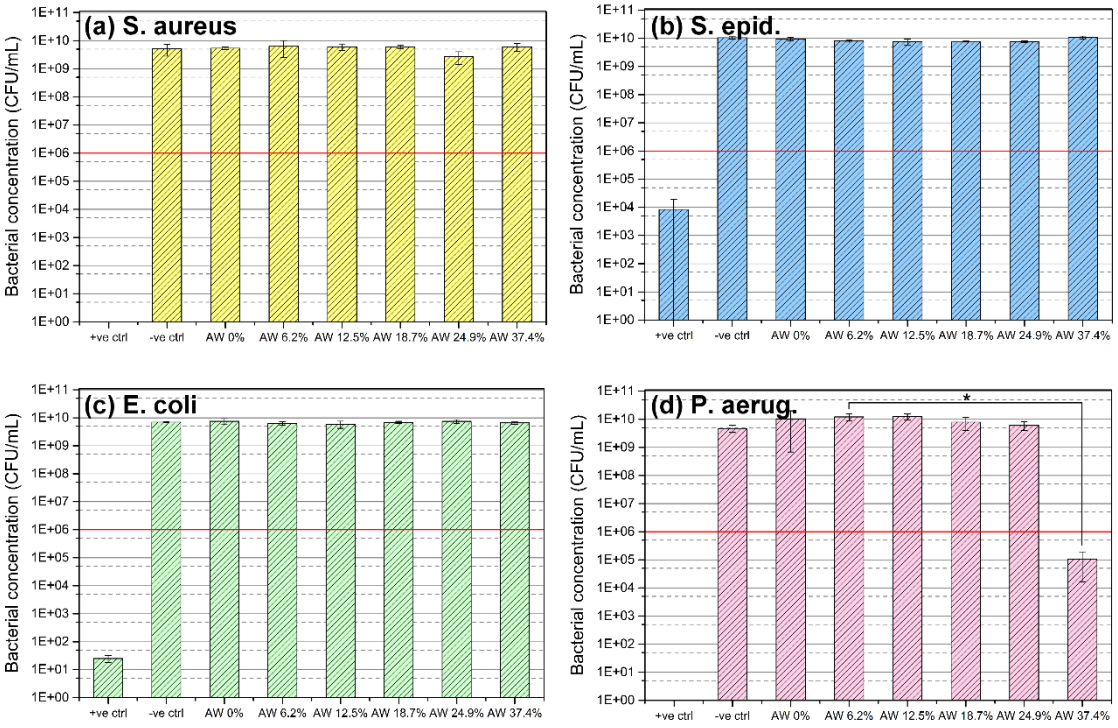

Figure 4.22: CFU count after 24 h incubation with the strontium AW glass powders pre-soaked for 24 h. The red line represents the bacterial concentration of the initial inoculum, positive control is gentamicin sulphate, negative control is culture media with no glass powder. (a) *S. aureus*, (b) *S. epidermidis*, (c) *E. coli*, (d) *P. aeruginosa*. Error bars indicate the standard deviation (n=3); * indicates significant difference with p≤0.05.

None of the strontium AW glass powders induced any reduction in bacterial growth for *S. aureus*, *S. epidermidis* and *E. coli* compared to the negative control. The positive control killed all the CFUs in the *S. aureus* and *P. aeruginosa* samples, while some live cells could still be detected for the positive controls of *S. epidermidis* and *E. coli*, possibly due to variations in the actual concentration of the diluted gentamicin stock. The large error bar of the positive control for *S. epidermidis* was due to the fact that the three plates gave very different CFU counts.

For *P. aeruginosa*, AW 37.4 % induced a reduction in CFU count compared to the other samples and the negative control, with a statistically significant difference to sample AW 6.2 % ($p<0.05$). The CFU concentration in sample AW 37.4 % was found lower than the 10^6 CFU/mL inoculum used, indicating that the sample was at least bacteriostatic, but also potentially had an antibacterial effect on this species.

4.3.4.2 Susceptibility to strontium glass powders suspended in culture media for 7 days

Since, with *P. aeruginosa,* sample AW 37.4 % showed some growth inhibition (Section 4.3.4.1), which indicated some possible susceptibility of this species to strontium-containing glasses, the test was repeated by soaking all the six AW glass powders for 7 days before inoculation. Only one repeat of the experiment was performed, with triplicates for each sample. Results are shown in the graph in Figure 4.23.

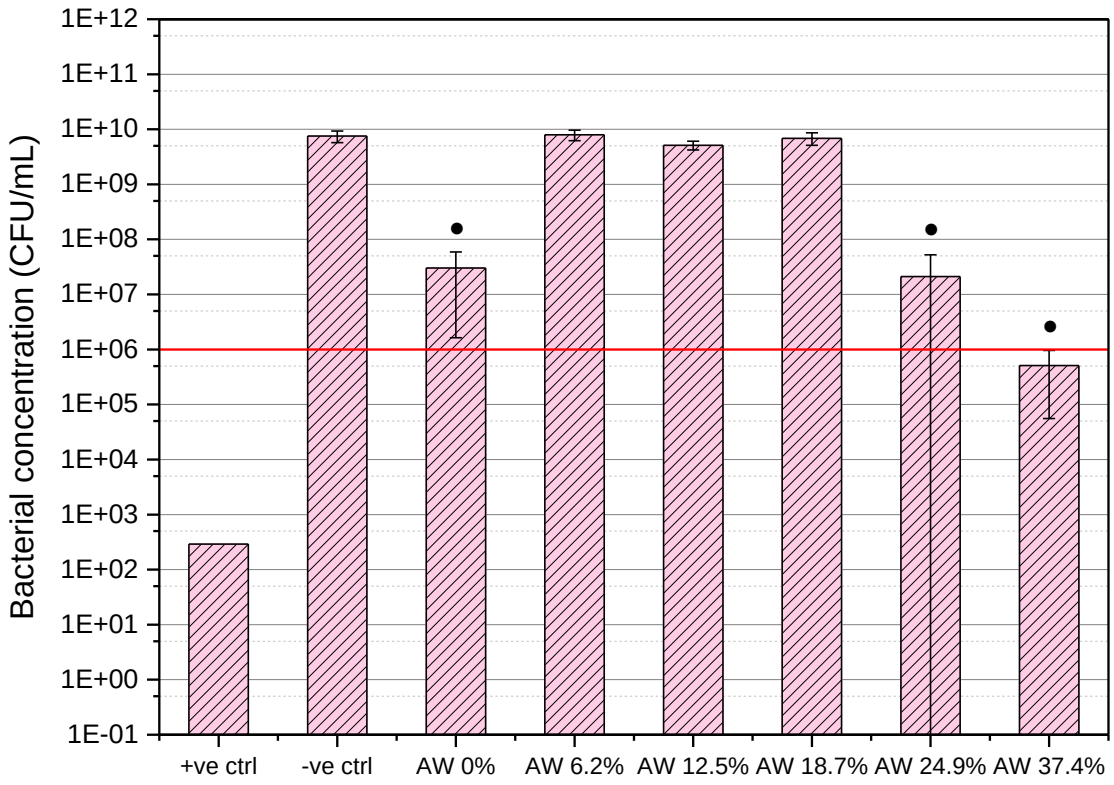

Figure 4.23: CFU count after 24 h incubation with the strontium AW glass powders, pre-soaked for 7 days. The red line represents the initial inoculum, positive control is gentamicin sulphate, negative control is culture media with no glass powder. Error bars indicate the standard deviation (n=3); no standard deviation could be calculated for the positive control. • indicates compositions that showed significant difference from the other compositions, but not from one another. P values are displayed in Table 4.7.

When the glass powders were soaked and mixed for 7 days before inoculation, three compositions showed reduction in the final CFU count of *P. aeruginosa* compared to the negative control (broth with no glass): AW 0%, AW 24.9 % and AW 37.4 %. These

were significantly different from the other samples, but not from one another, and the p-values are reported in Table 4.7. The positive control had no error bar because only one plate could be counted. Sample AW 24.9 % had a large error bar because of the difference in CFU count found for the three plates. Only AW 37.4 % gave a CFU count lower than the initial inoculum, confirming its bacteriostatic or bactericidal action seen in the previous Section 4.3.4.1.

Table 4.7: One way ANOVA p-value results with Bonferroni test for the compositions that showed significant differences when the strontium AW glass powders were soaked for 7 days and then incubated in the presence of *P. aeruginosa* for 24 h.

Compared compositions	Mean difference (CFU/mL)	p-value
AW 0% AW 6.2%	-7.90×10^{9}	5×10^{-5}
AW 0% AW 12.5%	-5.10×10^{9}	5×10^{-3}
AW 0% AW 18.7%	-6.84×10^{9}	5×10^{-4}
AW 0% Negative control	-7.50×10^{9}	5×10^{-5}
AW 24.9% AW 6.2%	-7.91×10^{9}	5×10^{-5}
AW 24.9% AW 12.5%	-5.11×10^{9}	5×10^{-3}
AW 24.9% AW 18.7%	-6.85×10^{9}	5×10^{-4}
AW 24.9% Negative control	-7.51×10^{9}	5×10^{-5}
AW 37.4% AW 6.2%	-7.93×10^{9}	5×10^{-5}
AW 37.4% AW 12.5%	-5.13×10^{9}	5×10^{-3}
AW 37.4% AW 18.7%	-6.87×10^{9}	5×10^{-4}
AW 37.4% Negative control	-7.53×10^{9}	5×10^{-5}

The reduction in CFUs found for the three compositions was strongly significantly different compared to the other samples. The p-values found with the Bonferroni test were 0.005 when glasses were compared to sample AW 12.5 % and lower for the other compositions, being 5×10^{-4} when the three glasses were tested against composition AW 18.7% and 5×10^{-5} when compared to glass AW 6.2% and to the negative control (absence of glass powder in the sample)

4.4 Discussion

As presented in Chapter 1, there is evidence in the literature that strontium-containing bioactive glasses can exert some antibacterial properties (17, 18). Therefore, this Chapter investigated strontium as a possible antimicrobial agent, both as a free

element through the use of strontium salts and as a dopant in bioactive glass powders intended for bone scaffolds. In the work described in this thesis, antibacterial characterisation only for the material used for the scaffolds was described, while testing of the final scaffolds will be part of the future work (Chapter 8) for a full assessment of the constructs.

4.4.1 Selection of bacterial strains

Four species were chosen for this work as the most representative of post-operative infections (130, 141), two Gram-positive and two Gram-negative: *Staphylococcus aureus*, *Staphylococcus epidermidis*, *Escherichia coli* and *Pseudomonas aeruginosa*. These were characterised for their growth profiles and antibiotic resistance to gentamicin sulphate. Gentamicin sulphate was chosen as the antibiotic control because all the four species under testing proved to have some degree of susceptibility to it, also confirmed by the literature (362-365). Although it might not be the antibiotic of choice for each of the four species, and in fact some live cells were found in the broth dilution tests (Section 4.3.4.1 and 4.3.4.2), it was not the scope of this work to find a specific antibiotic for each of them, but simply to have a positive control that proved that the strain responded to known antimicrobial agents.

4.4.2 Investigation of strontium antibacterial effect using salt solutions

First, strontium salts were tested for an initial investigation of the antibacterial properties of strontium. Two salts were chosen for comparison, strontium nitrate and strontium chloride, so that the possible effect of chlorine, a known antimicrobial agent (366), in strontium chloride could be ruled out. 4 mM was the highest concentration of strontium tested, as it is the highest concentration usually found in the literature for both antibacterial testing (18) and cell culture testing (361). In addition, 4 mM was found to be the maximum concentration that could be prepared in culture media without the formation of precipitates. It has been observed in fact that, although highly soluble in deionised water, strontium can easily react with sulphate, carbonate and phosphate ions present in a solution to give precipitates (360).
None of the two strontium salts nor sodium chloride induced growth inhibition in the four species tested. 20 µL of each solution were used, according to literature (357), on each paper disc, corresponding to about 7 µg/disc of strontium. Because no such test has been described in the literature using strontium salts, there is no comparison that could indicate if the concentration used was high enough and strontium had no effect,

or if the concentration was not high enough to see any effect. Looking at the literature, it is still uncertain whether strontium could impart antimicrobial properties to bioactive glasses. Guida et al. tested strontium-containing glass ionomer cements with the agar disc diffusion test against two species involved in dental caries: *Streptococcus mutans* and *Actinomyces viscosus*; they observed that the cement samples showed stronger antibacterial properties for strontium-containing compositions, with *S. mutans* being more susceptible than *A. viscosus,* and suggested a synergistic effect of fluorine and strontium (17). Liu et al. studied the effect of strontium-containing bioactive glasses against *Aggregatibacter actinomycetemcomitans* and *Porphyromonas gingivalis* using the AlamarBlue viability assay; they found that the presence of strontium enhanced the antibacterial activity of the material, although the no-strontium glass also showed antimicrobial properties. The authors also used strontium chloride to assess the effect of strontium itself, and they found a dose-dependent effect on the inhibition of bacterial growth with strontium, which was stronger against *P. gingivalis* than *A. actinomycetemcomitans* (18). Brauer et al. tested composite cements for spinal applications that contained strontium glasses; they found that the cell count of *Streptococcus faecalis* and *Staphylococcus aureus* was reduced in the presence of strontium, although the reduction was not enhanced for increasing strontium and also the composite cement containing the strontium-free glass induced a decrease in cell count after 6 days of culture (197). Dabsie et al. tested different strains implicated in carious or periodontal pathologies by exposing them to culture broth containing strontium chloride for 5 min, maximum concentration 1.11 M; they observed about 1 log reduction in cell count only for the highest strontium concentration (195). Fielding et al. produced silver and strontium containing plasma-sprayed hydroxyapatite coatings and tested their antimicrobial properties against *P. aeruginosa*; they found that the presence of strontium could offset the cytotoxic effect of silver, but only compositions containing silver showed antimicrobial properties (200). Geng et al. tested hydroxyapatite coatings, produced via hydrothermal treatment and doped with silver and strontium, against *E. coli* and *S. aureus*; all the silver-containing samples showed antimicrobial properties and the addition of strontium reduced the cytotoxicity of strontium in MG63 cells, but strontium-only samples did not show any antibacterial activity (201, 202). These last publications are in agreement with what was found in this work in the test that included silver and zinc: only silver proved to be a strong bactericidal agent, giving zones of inhibition for all the four species tested. Zinc is also a known antibacterial element, however, its effect is less strong than that of silver (358, 359) and in fact it did not show any inhibition in the test carried out here. This test with silver and zinc was carried out as a proof-of-concept, comparing the element under investigation, strontium, to other known antibacterial elements. Results

suggested that, for an AW-based scaffold material with enhanced antimicrobial properties against pathogens commonly found in orthopaedic peri-prosthetic infections, silver could be the element of choice, while strontium could be added for improving the cytocompatibility.

4.4.3 Effect of strontium on the antibacterial activity of AW glass powders

Testing of strontium AW glass powders was based on the work of Fernandes et al., who tested the same four bacterial species chosen for this work (198). Two types of test were performed: disc diffusion, using glass-loaded agar samples, and broth dilution, suspending the glass powders in media before inoculation.
For the agar disc diffusion, Fernandes et al. loaded agar discs (diameter 9.5 mm) with 72 mg of glass powder, while here, for simplicity reasons, technical agar was loaded with 72 mg/mL of glass powder and then small discs (diameter 7.5 mm) were cut out. The authors observed inhibition only for *P. aeruginosa*, which they therefore selected for the broth dilution testing. However, no inhibition could be observed from the strontium AW samples for any of the four species tested in this work. This difference in the results could be due mainly to three factors: differences in preparation of the test samples, the difference in the bacterial strains used (American Type Culture Collection (ATCC) or Coleccíon Española de Cultivos Tipo (CECT), for Fernandes et al. (198), NCTC in the present work) and the difference in the composition of the tested glasses. Differences in preparation of the test samples could have determined a difference in the final glass concentration, or a difference in the amount of glass powder in direct contact with the bacterial surface. Different bacterial strains could have generated different responses to antimicrobial agents. Different glass compositions could have induced different effects in bacteria. It is likely that the absence of response observed with the strontium AW glasses was caused by a combination of these three factors.
In the present work, broth dilution was carried out for all the four chosen species, using the highest concentration of glass powder in media that was used in the reference paper: 72 mg/mL. In this case, results agreed with the findings of Fernandes et al., as only *P. aeruginosa* appeared to be susceptible to the strontium glass powder of sample AW 37.4%. However, Fernandes et al. used different concentrations of the same glass to assess the dependence of *P. aeruginosa* susceptibility to strontium and they found that, with 1 day of glass incubation, 9 mg/mL of glass powder gave a bacteriostatic effect, while 18, 36 and 72 mg/mL eradicated the bacteria. The composition of their glass was $5Na_2O$-35SrO-$20B_2O_3$-$40SiO_2$ mol% (198), so close to AW 37.4% in terms of strontium content. In the present work, in order to reduce the

number of samples tested, only one concentration of glass in media was used and dependence to strontium was assessed through the six strontium AW compositions; with 1 day of glass dissolution and 1 day of incubation after inoculation, only AW 37.4% showed a bacteriostatic effect against *P. aeruginosa*, with about 1 log reduction of CFU from the inoculum. Because of these results, the strontium AW glass powders were tested again only against *P. aeruginosa* with 7 days of powder dissolution at 37 °C before inoculation. AW 37.4% confirmed its bacteriostatic nature, while AW 0% and AW 24.9% showed a reduction in CFUs compared to the negative control, but the final count was still higher than the inoculum, indicating that the growth was slowed down, but not prevented. While the effect of AW 24.9% could be expected as the second highest strontium-containing composition, the response to AW 0% was not predicted. However, other bioactive glass compositions have been described in the literature that showed antimicrobial properties without containing any specific antimicrobial agent. The best example, in this sense, is the case of the S53P4 glass, composition $53SiO_2$-$23Na_2O$-$20CaO$-$4P_2O_5$, commercially available under the brand BonAlive® as antibacterial granules indicated in the treatment of chronic osteomyelitis. For this glass, it is thought that its antibacterial properties derive from the increase in pH and osmolarity induced by the release of alkaline ions into the surrounding environment, which causes bacterial cell shrinkage and damage to the bacterial cell membrane (94, 205-208). In addition, Brauer et al. observed that their no-strontium composition of cement showed some antimicrobial properties, which were ascribed to a combined effect of fluorine (11.04 mol% CaF_2) and of the cement matrix (197). Moya et al. observed that soda-lime glass compositions containing more than 15 wt% CaO reduced the CFU count by more than 4 log for *E. coli*, *Micrococcus luteus* and *Candida krusei* (a yeast). They concluded that the antibacterial properties of this class of glasses were due to the depolarisation of the bacterial cell membrane caused by the very high concentration of Ca^{2+} at the glass-membrane interface, enhanced by the local low pH (< 2) induced by the proton pumping activity of bacteria (211). Cabal et al. showed that the same high-calcium compositions preserved their antibacterial properties when the material was turned into a glass-ceramic, proving its efficacy against five biofilm-forming bacterial species (210). Allan et al. (203) and Hu et al. (204) studied the behaviour of Bioglass 45S5 against different species and both publications found that the particulates or powders of this glass could induce a strong bactericidal effect, explained by the increase in pH that was induced by the material interacting with the culture media, along with the formation of needle-like debris that caused damage to the cell walls. On the contrary, Gorriti et al. tested Bioglass and boron-containing Bioglass glass-ceramic scaffolds against different strains of *S. aureus*, but did not observe any inhibition of bacterial growth (367). Two publications

compared the effect of different bioactive glass compositions on 29 aerobic species (208) and 17 anaerobic species (209); both found that all compositions induced moderate to strong antimicrobial effects, which were ascribed to the increase in pH and osmolarity induced by the glasses in solution, as well as the high concentration of Ca^{2+} perturbing the bacterial membrane potential.

In conclusion, many factors can influence the outcome of bacterial tests for bioactive glasses and methods can vary considerably between publications. Many species have been tested in the literature, using many different strains for each species. Outcome of testing of bioactive glasses and glass-ceramics can depend strongly on glass composition, form of the material (particles, paste, solid, porous solid, coating), particle size, crystallinity, concentration and reactivity of the glass. Different tests have been described depending on the proposed research question. When the antibacterial properties of a new glass are investigated, simple tests are typically carried out that can assess whether the material presents any antimicrobial feature, usually disc diffusion tests (also called agar diffusion test, or zone of inhibition test, or Kirby-Bauer test) (17, 198, 201, 202) or broth dilution tests (94, 197, 198, 203, 204, 206-211, 367). Only Liu et al. described the use of the AlamarBlue viability assay for assessing the antibacterial properties of strontium-containing glasses (18). Only once a glass had shown antimicrobial properties, additional tests can be carried out to investigate, for example, its effect on biofilms (200, 202, 205, 207, 210), the effect on cell morphology through imaging (201, 202, 204-206, 208, 211) or the mechanisms of action of the specific composition under study (203, 211). In the case of the glass compositions described in this thesis, only the first level of testing was carried out and results suggested that composition AW 37.4%, tested as <45 µm glass powder, 72 mg/mL in LB, exhibited bacteriostatic action against *P. aeruginosa*, strain NCTC 10332. A mild bacteriostatic effect was also observed for compositions AW 0% and AW 24.9% under the same testing conditions, but with a longer dissolution time. Therefore strontium AW glasses could induce only minor antimicrobial effects and thus did not indicate to be promising antibacterial materials for the prevention and treatment of post-operative bone infections.

Chapter 5
Effect of strontium AW scaffolds on the growth and osteogenesis of bone-forming cells

Although the mechanism of action of strontium on bone-forming cells is still unclear, its positive effect on bone formation and regeneration has long been studied. In fact, as described in Chapter 1, this element is known for its dual ability of inducing osteogenic differentiation in bone marrow mesenchymal stromal cells (MSCs) and bone extracellular matrix deposition in osteoblasts, as well as reducing bone resorption by osteoclasts (15, 150). In clinical applications, a strontium salt, strontium ranelate, is currently used for treating severe osteoporosis (16, 163, 165). However, as potential systemic side effects have been associated with this drug (173, 176), localised delivery of small doses of strontium would be preferable. Various compositions of bioactive glasses have been proposed for the fabrication of strontium-containing bone scaffolds in the literature (151, 156, 177, 181, 368). However, this is the first time that this element has been added to the AW glass-ceramic material for the production of foam-replicated scaffolds. This chapter will explore the effects of the strontium AW porous scaffolds, produced as described in Chapter 3, on bone-forming cells *in vitro*. Tests were initially carried out using G292 cells, an osteosarcoma cell line commonly used as a model for MSCs (369-371), before samples were tested on human bone marrow-derived MSCs (hBM-MSCs).

5.1 Materials and methods

The six compositions of strontium AW porous scaffolds were prepared as described in Chapter 3. Samples were first tested using the G292 cell line to screen for any osteogenic or proliferative effect. Some of the strontium AW compositions were then further tested using primary human bone marrow-derived mesenchymal stromal cells (hBM-MSCs). General cell culture methods, seeding and analysis techniques are described in Sections 5.1.1, 5.1.2 and 5.1.3, respectively. Details on the tests conducted on the G292 cell line are reported in Section 5.1.4 and tests carried out on the hBM-MSCs are described in Section 5.1.5.

5.1.1 General cell culture

5.1.1.1 General cell culture materials

Alpha-modified minimum essential media (α-MEM) and 1x phosphate buffered saline (PBS) were purchased from Lonza; foetal bovine serum (FBS), penicillin-streptomycin (PS), L-glutamine, trypsin-ethylenediaminetetraacetic acid (trypsin-EDTA) solution and dimethyl sulphoxyde (DMSO) were from Sigma; all plasticware was from Corning, unless otherwise stated.

5.1.1.2 *In vitro* cell culture and expansion

20 mL of media were used for T75 culture flasks, 30 mL for T175 flasks. Plain media was prepared as α-MEM with 1 % PS (resulting in 100 units/mL of penicillin and 0.1 mg/mL of streptomycin in the final media) and 2 mM L-glutamine. G292 culture media was prepared by adding 10 % FBS to plain media, while culture media for hBM-MSCs was prepared by adding 15 % FBS to plain media. Cells were harvested by rinsing the flask twice with PBS and then incubating them with trypsin-EDTA for 5-10 min. Detachment was confirmed under a microscope and the cell suspension was diluted with FBS-containing media and collected in a Falcon tube; the centrifugation protocol will be specified, depending on the cell type, in the relevant Section 5.1.4 for G292 and 5.1.5 for hBM-MSCs. The cell pellet was then re-suspended in different media according to the experimental design and the cell number was counted using a haemocytometer.

5.1.1.3 Cryopreservation of cells

Cells were detached, counted and pelleted down as described previously. Freezing media was prepared by adding 30 % FBS and 10 % DMSO to α-MEM. Each cell pellet was re-suspended with 1 mL of freezing media, transferred to a cryogenic storage vial and placed in a Mr. Frosty (Thermo Scientific) box containing isopropanol, which was placed in a -80 °C freezer overnight. The day after the vials were moved to a storage box and kept at -80 °C until use.

5.1.2 Seeding of cells on 3D porous scaffolds

100 mm^3 porous scaffolds, prepared from 5 mm-side foams as described in Chapter 3, were sterilised by autoclaving and handled using sterile tweezers.

Scaffolds were pre-treated with plain media containing 20 % FBS overnight at 4 °C, in order to modify their surface chemistry and facilitate cell attachment. Treated scaffolds were then rinsed in plain media before cells were seeded. The effect of performing this treatment was verified with G292 cells against samples treated with plain (no FBS) media, as described in Section 5.1.4.1.

Cells were counted as described in Section 5.1.1.2 and suspensions were prepared in plain media so that 1 x 10^5 cells were seeded on each scaffold in a 50 µL drop. Cells were allowed to attach for 3 h in incubator at 37 °C, then scaffolds were rinsed in plain media to remove all the non-attached cells and cultured in 48 well-plates using the designated culture media (500 µL per well).

Media was changed twice a week, with a rinsing step with plain media, until the required time-point.

5.1.3 General characterisation of seeded scaffold

5.1.3.1 Fluorescent labelling for visualising cell attachment

The staining solution was prepared by adding 5 µL of calcein AM (from the Invitrogen live/dead kit: 4 mM calcein AM) to 10 mL of plain media and the solution well mixed before use.

Samples were incubated in 500 µL of the staining solution, covered in foil, for 30 min at 37 °C, then rinsed in plain media; the calcein AM signal (495/515 excitation/emission) was observed under inverted fluorescence microscope (Zeiss Axio Vert A1). Images were taken using the Zeiss imaging software, with live cells represented in green.

5.1.3.2 Live/dead staining and confocal imaging

Confocal microscopy was used to observe the 3D distribution of cells in the porous scaffolds.

The staining solution was prepared using the Invitrogen live/dead kit, following the manufacturer's instructions: 20 µL of 2 mM ethidium homodimer-1 (dead cell stain) and 5 µL of 4 mM calcein AM (live dead stain) were added to 10 mL of plain media. Scaffolds were rinsed in plain media before they were incubated in 500 µL of staining solution, covered in foil, for 30 min at 37 °C. Samples were then rinsed again in plain media and kept in 500 µL of plain media if observed immediately with the confocal microscope, or preserved in 500 µL of 10 % formalin (Sigma) at 4 °C overnight and observed the day after.

During imaging, samples were moved to PBS and observed using immersion lenses under a Leica SP8 confocal microscope. 488 nm and 552 nm lasers were activated and filters adjusted to minimise cross-talking of the channels. Stacks of planar images were taken, 5 µm apart, then combined for a 3D projection of maximum signal. Live cells were represented as green, dead cells as red, scaffolds in greyscale.
After confocal imaging, samples were kept in 10 % formalin at 4 °C until SEM imaging was carried out.

5.1.3.3 Cell morphology with cold-stage scanning electron microscopy

Samples kept in 10 % formalin were first rinsed in distilled water. A Daben cold-stage, connected to the Hitachi S-3400N scanning electron microscope (SEM), was pre-cooled to 0 °C, then samples were placed on the stage and moisture removed with absorbent paper. Temperature was gradually brought to -20 °C while pressure in the SEM chamber was reduced to 70 Pa. Pictures were acquired in backscattered electrons (BSE) mode for better contrast between cells and scaffold.

5.1.3.4 Alkaline phosphatase staining

Alkaline phosphatase (ALP) is an early marker of osteogenic differentiation in MSCs, which indicates the commitment of the stromal cell to the osteoblast lineage (372).
To qualitatively assess the presence and the amount of this enzyme, samples were rinsed in PBS and fixed using 98 % ethanol at 4 °C for 20 min. Then samples were rinsed again in PBS and let air dry.
10 mL of ALP staining solution were prepared by mixing 9.6 mL distilled water with 0.4 mL Naphthol AS-MX phosphate (Sigma) and 4.2 mg Fast Violet B salt (Sigma). 500 µL of this staining solution were added to the samples, then covered in foil and incubated at 37 °C for up to 60 min, until stain was visible. The staining solution was then removed, samples air dried and pictured using a Leica M205C stereomicroscope, coupled with Leica KL1500 LCD illumination and Schott KL1500 light system.

5.1.3.5 PrestoBlue metabolic activity quantification

PrestoBlue is a resazurin-based reagent that can measure the viability of cells. It contains a blue, non-fluorescent, cell-permeant compound (resazurin) that gets reduced within the cell cytoplasm by cell respiration; when reduced, it turns into red, fluorescent resorufin. The conversion is proportional to the number of metabolically active cells and it can be measured as fluorescence or absorbance. The compound

does not interfere with cell metabolism, so the same cells can be monitored over time or collected for DNA and ALP activity quantification (373, 374), as done in the present thesis (Sections 5.1.3.6 and 5.1.3.7).
In the case of cells cultured on the strontium AW scaffolds, samples were rinsed and then placed in 500 µL of plain media in a 48 well-plate. Negative controls consisted of plain media only. 50 µL of Invitrogen PrestoBlue Cell Viability Reagent were added to each well as per manufacturer's instructions. The plate was covered in foil and incubated at 37 °C until a significant change in colour could be observed. 100 µL aliquots were then taken from each well and transferred to a 96-well plate. The fluorescence signal was measured using a Thermo Fisher Varioskan Flash plate reader, set at 560 nm for excitation and 590 nm for emission. The average signal from the negative controls was subtracted from the measured signals.
Samples were then transferred back to plain media for 1 h, in preparation for DNA and ALP quantification (Section 5.1.3.6 and 5.1.3.7, respectively).

5.1.3.6 PicoGreen DNA quantification

The lysing solution of 0.1 % Triton-X in carbonate buffer was prepared by dissolving 4.2 g of sodium carbonate (Na_2CO_3, Thermo Fisher) in 200 mL of distilled water and 1.7 g of sodium hydrogencarbonate ($NaHCO_3$, Thermo Fisher) in 100 mL of distilled water. The two solutions were then mixed together and the pH adjusted to 10.2 using 1 M hydrochloric acid. Triton-X (Fisons) was then diluted to 0.1 vol% in the so-prepared carbonate buffer.
The DNA standard and the testing solution were prepared using the Invitrogen Quant-iT PicoGreen dsDNA assay kit. First, the provided 20x TE buffer was diluted to 1x in distilled water. The standard sample was prepared by adding 10 µL of the dsDNA to 490 µL 1x TE buffer. The PicoGreen testing solution was prepared by adding 10 µL of the PicoGreen stock to 1990 µL of 1x TE buffer.
Scaffolds were rinsed in PBS, moved to new wells and 500 µL of lysing solution were added. Well-plates were sealed with Parafilm, then frozen at -80 °C and thawed 3 times, before samples and solution were transferred to 1.5 mL Eppendorf vials and sonicated for 5 min in an ultrasonic water bath (Advantage-Lab AL04-01).
The calibration curve was set up by serially diluting the DNA standard in 1x TE buffer. 5 µL of sample lysing solution were added to 95 µL of 1x TE buffer in a 96 well-plate. 100 µL of the PicoGreen solution were added to each well, then the plate was incubated, covered in foil, at room temperature for 5 min and fluorescence measurements were taken with the Thermo Fisher Varioskan Flash plate reader set at

480 nm excitation and 520 nm emission. Linear interpolation of data from the standard curve was used to calculate the DNA concentration in the samples.
Results were used to normalise cell viability (PrestoBlue assay, Section 5.1.3.5) and ALP activity (Section 5.1.3.7) measurements.

5.1.3.7 Alkaline phosphatase activity quantification

The ALP standard and the testing solution were prepared using the Alkaline Phosphatase Diethanolamine Activity kit (Sigma-Aldrich). The ALP standard was diluted to 1 U/mL in the provided reaction buffer, while a 0.67 M dilution of the p-nitrophenyl phosphate (pNPP) substrate was prepared in ultrapure water.
10 to 50 µL of each sample, depending on how strong the signal was expected, were diluted in the reaction buffer in a 96 well-plate, so that the total volume in each well was 98 µL. The standard curve was set up by serially diluting the ALP standard, obtaining a final volume of 98 µL in each well. 2 µL of the pNPP substrate solution were added to each well and the plate incubated at 37 °C, covered in foil, for up to 60 min until a change in colour was clearly visible. The reaction was then stopped by adding 100 µL of 1 M sodium hydroxide to each well, before the absorbance was read at 405 nm with the Thermo Fisher Varioskan Flash plate reader.

5.1.3.8 Picroserius Red staining of extracellular deposited collagen

The Picroserius Red Stain kit (Polysciences, Inc.) was used to qualitatively investigate the presence of deposited collagen on seeded scaffolds. It contains:

- Solution A: Phosphomolybdic Acid;
- Solution B: Picrosirius Red F3BA Stain;
- Solution C: 0.1 N Hydrochloric Acid.

After fixing in 10 % formalin, the seeded scaffolds were first rinsed in distilled water and then moved to a new 48 well-plate. 500 µL of solution A were added to each sample and incubated at room temperature for 2 min. Samples were then rinsed in distilled water, before 500 µL of solution B were added and scaffolds incubated at room temperature for 1 h, after which they were moved to solution C for 2 minutes. Scaffolds were then thoroughly rinsed in distilled water and let dry, before being imaged under the Leica M205C stereomicroscope.

5.1.3.9 Statistical analysis

In the quantitative assays, statistical differences in the average results between compositions at each time-point were confirmed with one-way analysis of variance (ANOVA) tests. Results were displayed as mean ± standard deviation. P values over 0.05 were considered as not significant.

5.1.4 Culture of G292 cells on strontium AW porous scaffolds

G292 cells, clone A141B1, were purchased from Sigma. G292 cultures were started from frozen stocks of previously expanded cells. Cryovials were first quickly thawed at 37 °C in a water bath, the content transferred to a Falcon tube, re-suspended in plain media and centrifuged at 1100 rpm (Eppendorf 5804 R centrifuge) for 5 min. The supernatant was discarded, the pellet re-suspended again in plain media, cells counted and a known amount seeded in culture flasks containing culture media with 10 % FBS. Media was changed twice a week. Cells were passaged when at least 70 % confluency was reached.

5.1.4.1 Effect of serum pre-treatment on G292 cell attachment on scaffolds

Only AW 0% scaffolds were used to verify whether the pre-treatment of scaffolds in FBS-rich media was necessary to guarantee good cell attachment. Two scaffolds were pre-treated overnight with FBS-rich media (20 % FBS), while two were treated in plain media. For this test, cells (monolayer) were labelled directly in the flask using calcein AM, before being harvested. After moving the scaffolds to new sterile vials, 1 mL of the prepared cell suspension (3×10^5 cells/mL) was added onto the scaffolds; after 3 h of incubation, the seeded scaffolds were rinsed in plain media to remove the unattached cells before being observed under the fluorescence microscope. Pictures were taken while scaffolds were kept in plain media.

5.1.4.2 G292 cell growth in basal vs osteogenic media

This study compared the use of basal culture media, prepared as described in Section 5.1.1, with osteogenic media (StemMACS OsteoDiff Media).
Only compositions AW 0%, AW 12.5% and AW 24.9% were tested. All scaffolds were pre-treated in 20 % FBS media overnight, then 25 samples per composition were seeded as described in Section 5.1.2, but left in plain media for 24 h before being

moved to basal or osteogenic media. As shown in the diagram in Figure 5.1, three samples per composition were stained for live cells and imaged under fluorescence microscope at 3 h and 24 h after seeding, for monitoring the cell attachment and spreading on the scaffolds. 5 samples per composition were then collected for the 1 day time-point testing, so the 1 day samples included only the plain media condition. The remaining cell-scaffold constructs were moved to either basal or osteogenic media and cultured for 7 and 14 days.

At each time-point, 5 samples per condition were tested as follows:

- 1 scaffold per composition was stained for live/dead cells and imaged under confocal microscope, before being fixed in 10 % formalin and then imaged with SEM;
- 1 sample per composition was fixed in 98 % ethanol for ALP staining;
- 3 scaffolds per composition were tested for metabolic activity, before being collected and frozen for DNA and ALP activity quantitative assays.

For this experiment, the confocal microscope used for live/dead imaging was a Leica TCS SP2.

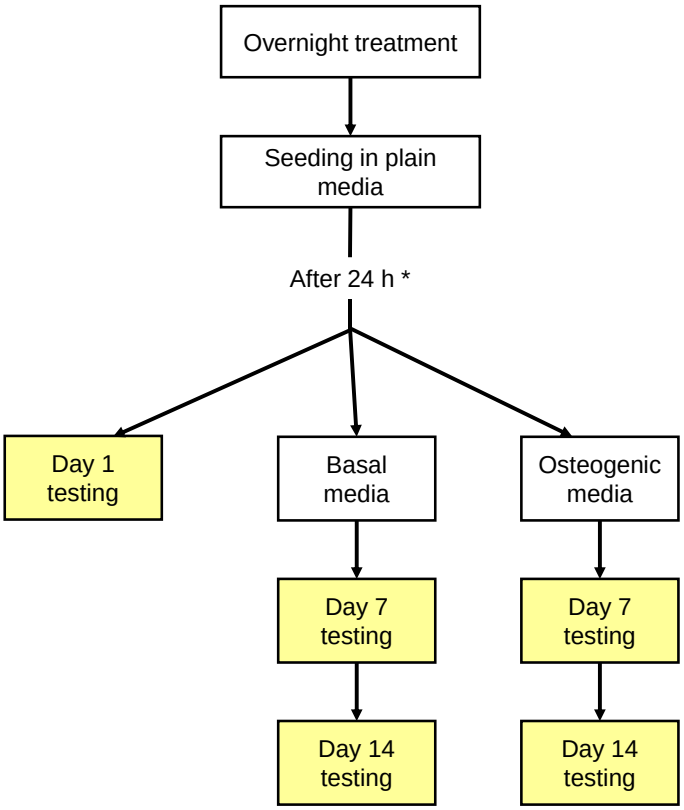

Figure 5.1: Schematic representation of the test carried out to compare the culture of G292 cells in basal and osteogenic media. Compositions AW 0%, AW 12.5% and AW 24.9% were tested. For each yellow box, 5 samples per composition were tested. *Cell attachment was checked with fluorescence microscopy at 3 h and 24 h.

5.1.4.3 Assessment of the effect of strontium content in AW porous scaffolds on the growth and osteogenesis of G292 cells

All the six strontium AW porous scaffold compositions were tested. Scaffolds were seeded as described in Section 5.1.2 and then cultured in basal media for 3 h, 1 day, 3 days and 7 days after seeding.

At each time-point, 10 scaffolds per composition were collected and tested as follows:

- 1 scaffold per composition was stained for live/dead cells and checked under the fluorescence microscope, before being fixed in 10 % formalin for confocal microscopy and SEM imaging;
- 3 scaffolds per composition were stained for ALP;
- 6 scaffolds per composition were tested for metabolic activity, then cells were lysed and frozen before DNA and ALP activity quantitative assays were run.

5.1.5 Culture of human mesenchymal stromal cells on strontium AW porous scaffolds

Human mesenchymal stromal cells were obtained from bone marrow mononuclear cells (hBM-MSCs), purchased from Lonza. The Certificate of Analysis provided informed that cells were cryopreserved on 12th November 2007 and that the donor was a 41 year-old African-American man.
Cell cultures were started following the manufacturer's instructions. The as-bought cryovial was quickly thawed at 37 °C, its content transferred to a 50 mL Falcon tube, the cryovial rinsed with 1 mL of plain media containing 10 % FBS and 20 U/mL of DNase I (Sigma) and then the rinse was slowly added to the Falcon tube. The volume of the cell suspension was slowly brought to 50 mL by adding the same DNase-containing media dropwise and then centrifuged at 200 G for 15 min (Eppendorf 5804 R centrifuge). The supernatant was then gently removed, leaving 2 mL of media in which the pellet was re-suspended. Cells were then transferred to a 15 mL Falcon tube, rinsing the 50 mL tube with plain media containing 10 % FBS and transferring the wash to the second tube. The volume was slowly brought to 15 mL, the tube centrifuged again at 200 G for 15 min, the supernatant removed and the pellet re-suspended in 2 mL of media. Cells were counted, then rested in incubator for 1 h before being counted again and transferred to culture flasks with plain media containing 15 % FBS. From the mononuclear population, it is expected that only MSCs would attach to the culture flasks (375-377); cells were cultured for 3 days before the first media change was carried out, thus eliminating all the non-adherent cells.
Cells were cultured in the 15 % FBS media described in Section 5.1.1 and media was changed twice a week. Cultures were passaged when at least 70 % confluent. When harvested, cell suspensions were centrifuged at 200 G for 15 min, as per manufacturer's instructions. Cells were used after passage 3, to ensure that the population contained only stromal cells.

5.1.5.1 Assessment of the effect of basal and osteogenic media on the osteogenic differentiation of hBM-MSCs

Only compositions AW 0%, AW 6.2%, AW 18.7% and AW 37.4% were tested to assess the effect of the culture media on the osteogenic differentiation of hBM-MSCs. After pre-treating in 20 % FBS, 6 scaffolds per composition were seeded with cells at passage 4 as described in Section 5.1.2 and cultured for 2 weeks. 3 samples per composition were cultured in basal media, while 3 samples per composition were cultured in osteogenic media (StemMACS OsteoDiff Media).

At 3 h, one scaffold per composition was labelled with the live cell marker and cell attachment was verified under fluorescence microscope, as described in Section 5.1.3.1. After 2 weeks of culture, all samples were stained for ALP as described in Section 5.1.3.4.

5.1.5.2 hBM-MSCs proliferation and differentiation on AW 0%, AW 6.2% and AW 12.5% porous scaffolds

16 scaffolds for each of the three compositions AW 0%, AW 6.2% and AW 12.5% were seeded with hBM-MSCs, as described in Section 5.1.2, and cultured in osteogenic media. All cells were at passage 5.
At both time-points of 7 and 14 days, 8 samples per composition were collected for the following tests:

- 1 scaffold per composition was stained for live/dead cells and checked under the fluorescence microscope, before being fixed in 10 % formalin for confocal microscopy and SEM imaging;
- 3 scaffolds per composition were stained for ALP;
- 4 scaffolds per composition were tested for metabolic activity, before being collected and frozen for DNA and ALP activity quantitative assays.

5.1.5.3 hBM-MSCs collagen deposition on strontium AW scaffolds

hBM-MSCs s at passage 5 were seeded on strontium AW scaffolds of composition AW 0%, AW 6.2% and AW 12.5%, as described in Section 5.1.2, and cultured in osteogenic media for 4 weeks. For each of the 3 compositions, 3 scaffolds were seeded, while one scaffold per composition was kept in culture media without cells (as control for the staining).
On the day of collection, scaffolds were rinsed in PBS and fixed in 10 % formalin. They were then rinsed in distilled water before being stained with Picroserius Red as described in Section 5.1.3.8. After staining, each sample was pictured under the stereomicroscope; bare scaffolds stained as pink, while the deposited collagen stained as orange.

5.2 Results

5.2.1 Effect of strontium AW porous scaffolds on G292 cells

G292 cells were initially chosen as a model for bone MSCs, in the preliminary study of strontium-doped AW scaffolds. After assessing the effect of the scaffold pre-treatment

in FBS-rich media in Section 5.2.1.1, a pilot study was carried out to compare the use of basal and osteogenic media, shown in Section 5.2.1.2. Then all six strontium AW compositions were tested in basal media for cell proliferation and ALP activity (Section 5.1.4.3).

5.2.1.1 Effect of serum pre-treatment of strontium AW porous scaffolds on G292 cell attachment

This experiment was carried out using AW 0% scaffolds to investigate whether a pre-treatment step in FBS-rich media was necessary to ensure effective cell attachment. Fluorescence microscope pictures were taken for two samples per condition and are shown in Figure 5.2, with cells represented in green when positively stained with calcein-AM.

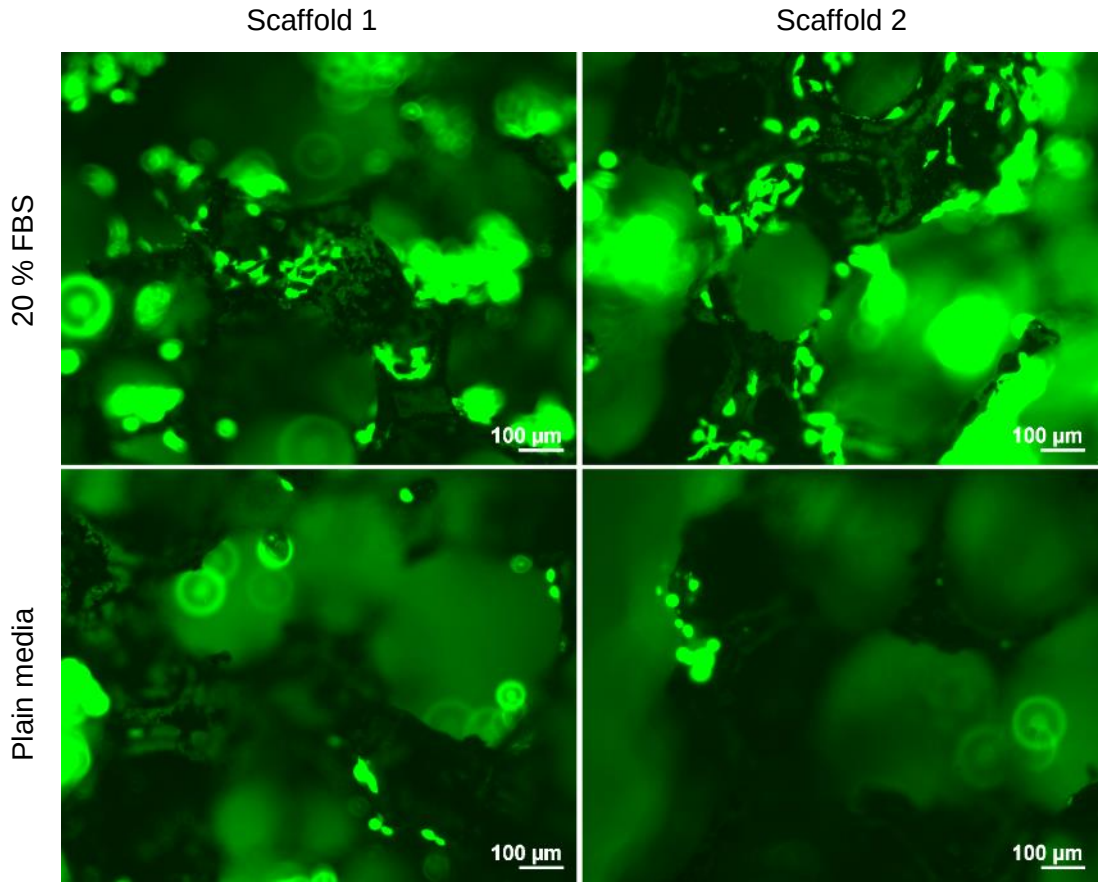

Figure 5.2: Fluorescence micrographs of G292 cells 3 h after seeding on AW 0% scaffolds, comparing overnight pre-treatment in 20 % FBS media with treatment in plain media. Live cells display in green. Scale bars represent 100 µm.

Scaffolds pre-treated with 20 % FBS media showed a higher number of attached cells, which were starting to spread after 3 h of incubation. On the contrary, scaffolds pre-treated in plain media had fewer and still round cells.
It was concluded that a pre-treatment step in 20 % FBS media was required to guarantee effective cell attachment and it was therefore applied to all the following tests, with both G292 cells and hBM-MSCs.

5.2.1.2 Effect of basal and osteogenic media on G292 cells cultured on strontium AW porous scaffolds

Before the effect of basal and osteogenic media was assessed, the attachment and spreading of cells to scaffolds was verified. Figure 5.3 shows the attachment and spreading of G292 cells on the strontium AW scaffolds 3 h and 24 h after seeding, where the green colour indicates staining with the fluorescent dye calcein-AM.

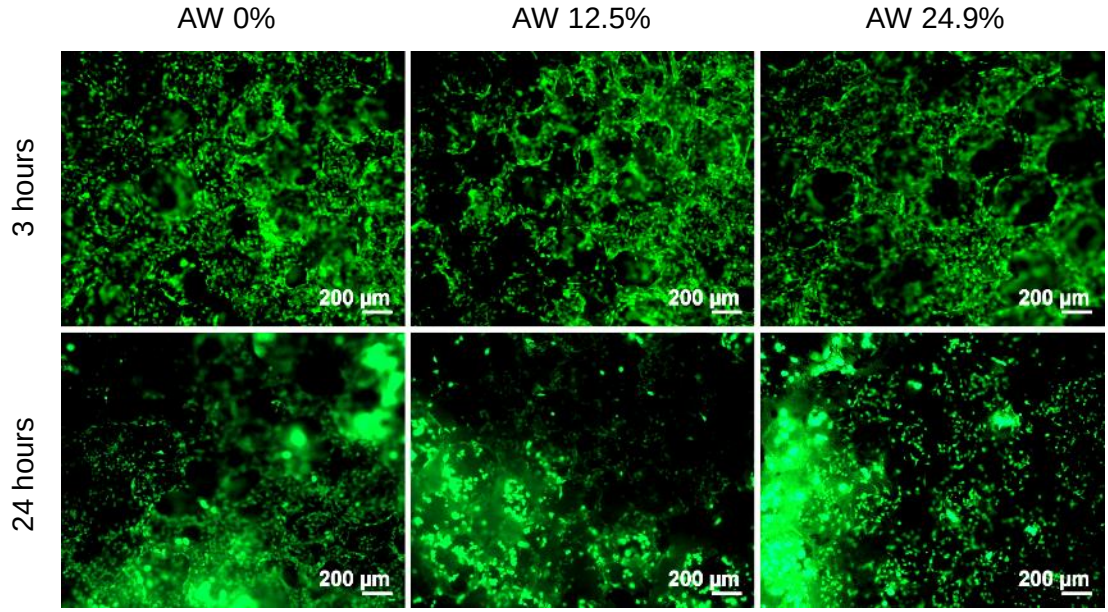

Figure 5.3: Staining of live G292 cells on scaffolds AW 0%, AW 12.5% and AW 24.9%, observed under fluorescence microscope. Cells were kept in plain media and observed 3 h and 24 h after seeding. Live cells display in green. Scale bars represent 200 µm.

All three compositions of scaffolds were highly populated 3 h after seeding on preconditioned scaffolds, with cells that had already started to spread. After 24 h, fewer round cells were visible and most cells were well spread on the scaffold struts. Fewer cells appeared visible on the scaffolds at 24 h than at 3 h incubation and

therefore a 3 h incubation step was considered sufficient to ensure cell attachment. No clear difference could be observed between scaffold compositions.

5.2.1.2.1 Effect of culture media on G292 cell proliferation

After 24 h in plain media, the seeded scaffolds were moved to either basal media or osteogenic media and cultured for up to 14 days. At each time-point (1, 7 and 14 days, where day 1 represents the scaffolds as-seeded), samples were stained with live/dead fluorescent markers and the cell viability was observed under the confocal microscope (Figure 5.4). Signal from the scaffolds could not be collected for technical reasons.

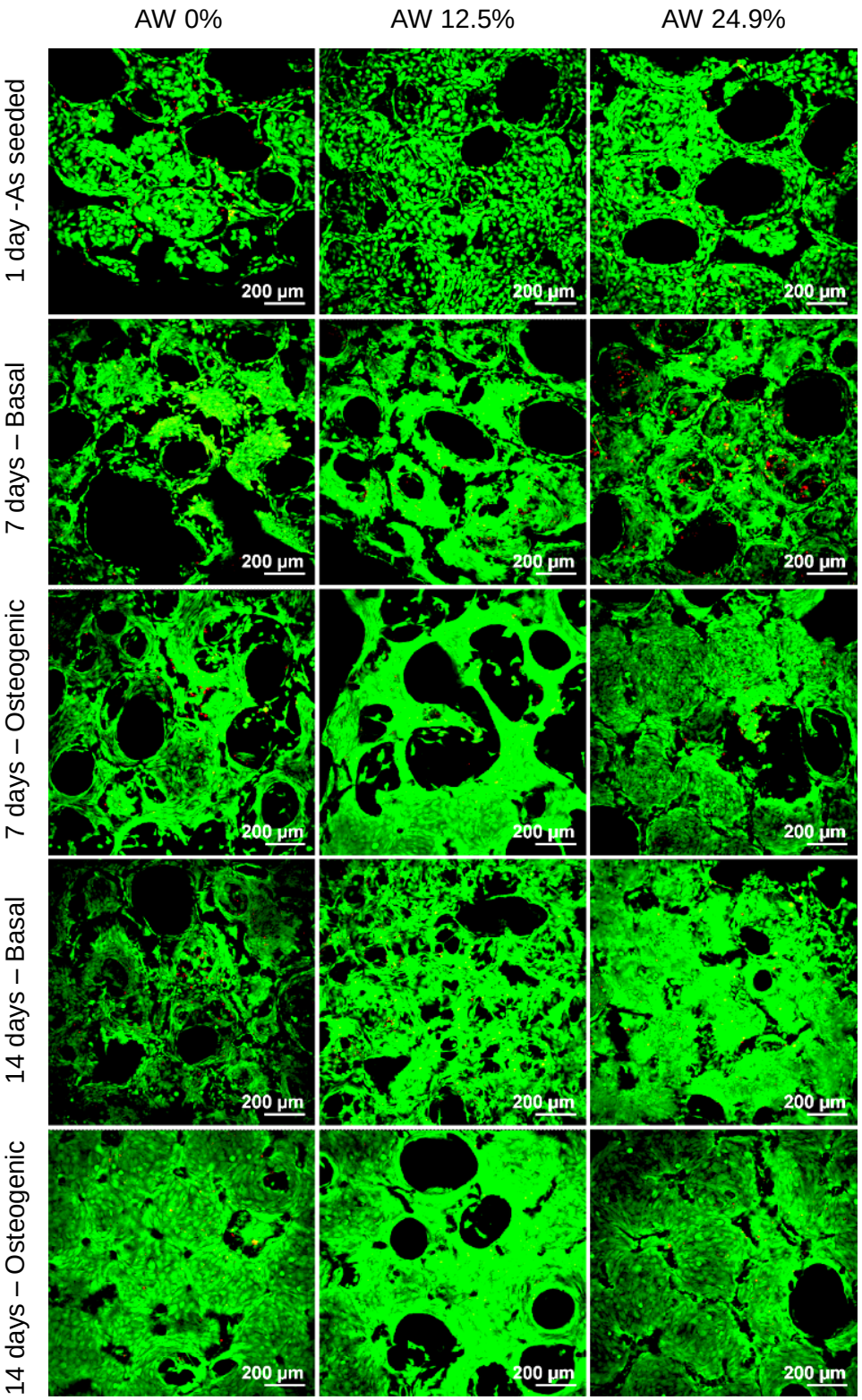

Figure 5.4: Confocal microscopy pictures of AW 0%, AW 12.5% and AW 24.9% scaffolds seeded with G292 cells and observed 1 day, 7 days and 14 days after seeding. 1 day samples were kept in plain media and are considered as-seeded. Samples collected 7 days and 14 days after seeding were cultured in either basal media or osteogenic media. Live cells are labelled as green, dead cells are labelled as red. Images taken with Leica TCS SP2. Scale bars represent 200 µm.

Individual cells could be observed on the as-seeded (1 day) samples, although already covering most of the scaffold struts of their top surface.
After 7 days of culture in basal media, cells had formed sheets that bridged across the borders of the pores of the scaffold structure. More pore coverage was found for compositions AW 12.5% and AW 24.9% than AW 0%. A higher number of red dots, indicating dead cells, could be observed for composition AW 24.9%. When scaffolds were cultured in osteogenic media, cell sheets appeared denser than on the corresponding compositions cultured in basal media. Sample AW 12.5% presented the strongest live signal from the 7 day samples and only few dead cells could be found on the compositions cultured in osteogenic media.
After 14 days of culture in basal media, more occluded or nearly occluded pores could be seen, which indicated that a higher number of cells were bridging across the scaffold struts. The cell number appeared to be increasing from AW 0% to AW 12.5% and then further to AW 24.9%. No dead cell signal could be detected. For samples cultured in osteogenic media, cells were organised in dense sheets for all the three scaffold compositions, while very few dead cells could be observed only on sample AW 0%.
In general, progressive proliferation could be observed for both culture media tested. However, the use of osteogenic media appeared to induce stronger proliferation of the G292 cells for all three strontium AW compositions. In basal media, a higher number of cells could be found on scaffolds AW 12.5% and AW 24.9% compared to AW 0% at both 7 and 14 days, with the densest cell sheet being on sample AW 24.9% at 14 days. Cells appeared to have reached confluency on all three compositions after 14 days in osteogenic media.

The same scaffolds were then pictured under SEM. Micrographs for all the compositions and conditions tested are summarised in Figure 5.5 and, at higher magnification, in Figure 5.6.

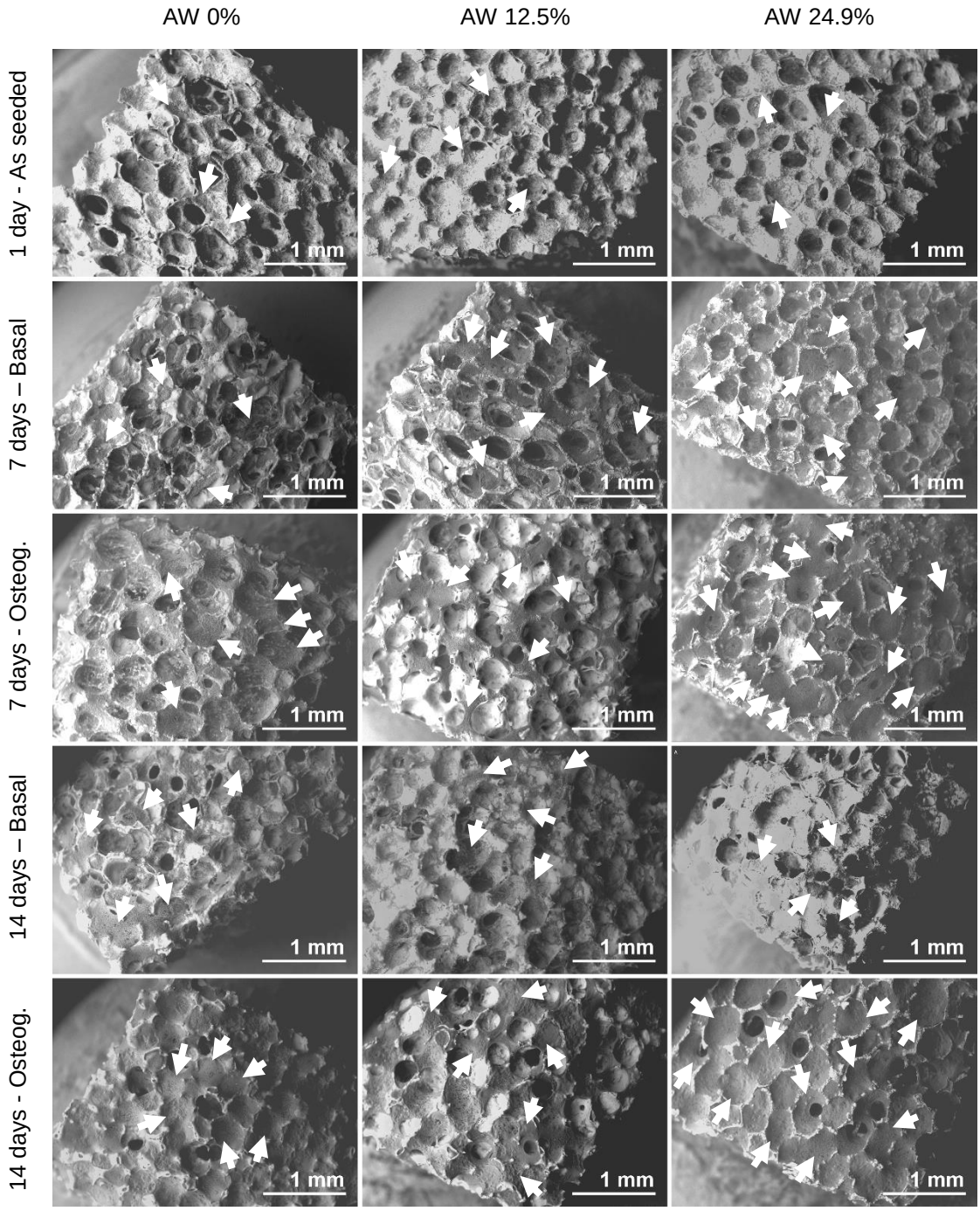

Figure 5.5: Scanning electron micrographs showing the overall coverage of AW 0%, AW 12.5% and AW 24.9% scaffolds with G292 cells, acquired in backscattered mode at 1 day, 7 days and 14 days after seeding. 1 day samples were kept in plain media and are considered as-seeded. Samples collected 7 days and 14 days after seeding were cultured in either basal media or osteogenic media. Cells appear as dark grey on lighter grey scaffolds; some agglomerates and sheets are pointed by white arrows. Scale bars represent 1 mm.

Results from the SEM imaging confirmed what observed with the confocal microscope. 24 h after seeding, individual cells could be observed on the surface of scaffolds, accumulating in concavities.

After 7 days of culture in basal media, the number of cells covering the surface of samples had significantly increased, with cell sheets being visible across some of the pores for composition AW 12.5% and covering most of the pores for composition AW 24.9%. Cell number was evidently higher on all the three samples cultured in osteogenic media for 7 days, with wider cell sheets covering sample AW 6.2% and thicker sheets on sample AW 24.9%.

After 14 days of culture in basal media, no clear further proliferation could be observed. On sample AW 12.5%, cell aggregates appeared sparse and sheets looked thin; on sample AW 24.9%, cells were visible only on a portion of the scaffold, in thick layers partially detached from the scaffold struts, which is in contrast with what observed for the same sample under the confocal microscope in Figure 5.4. It is possible that this sample was damaged between the confocal imaging and the SEM imaging, or while decreasing temperature and pressure in the SEM chamber. Samples cultured in osteogenic media for 14 days showed very dense cell layers on their surface, bridging pores for all the three compositions; most of the surface of sample AW 24.9% appeared covered with cells.

In general, cells appeared to populate mainly the upper surface of all samples, which could be a consequence of the seeding method (the upper surface was the seeded surface) and of the fact that nutrients and oxygen were more easily available on the outer surface of scaffolds when in static culture. Osteogenic media induced faster proliferation on all the three compositions tested, with scaffolds AW 24.% showing most of their pores bridged across by cell sheets at 7 and 14 days.

Details from the same samples are shown in Figure 5.6.

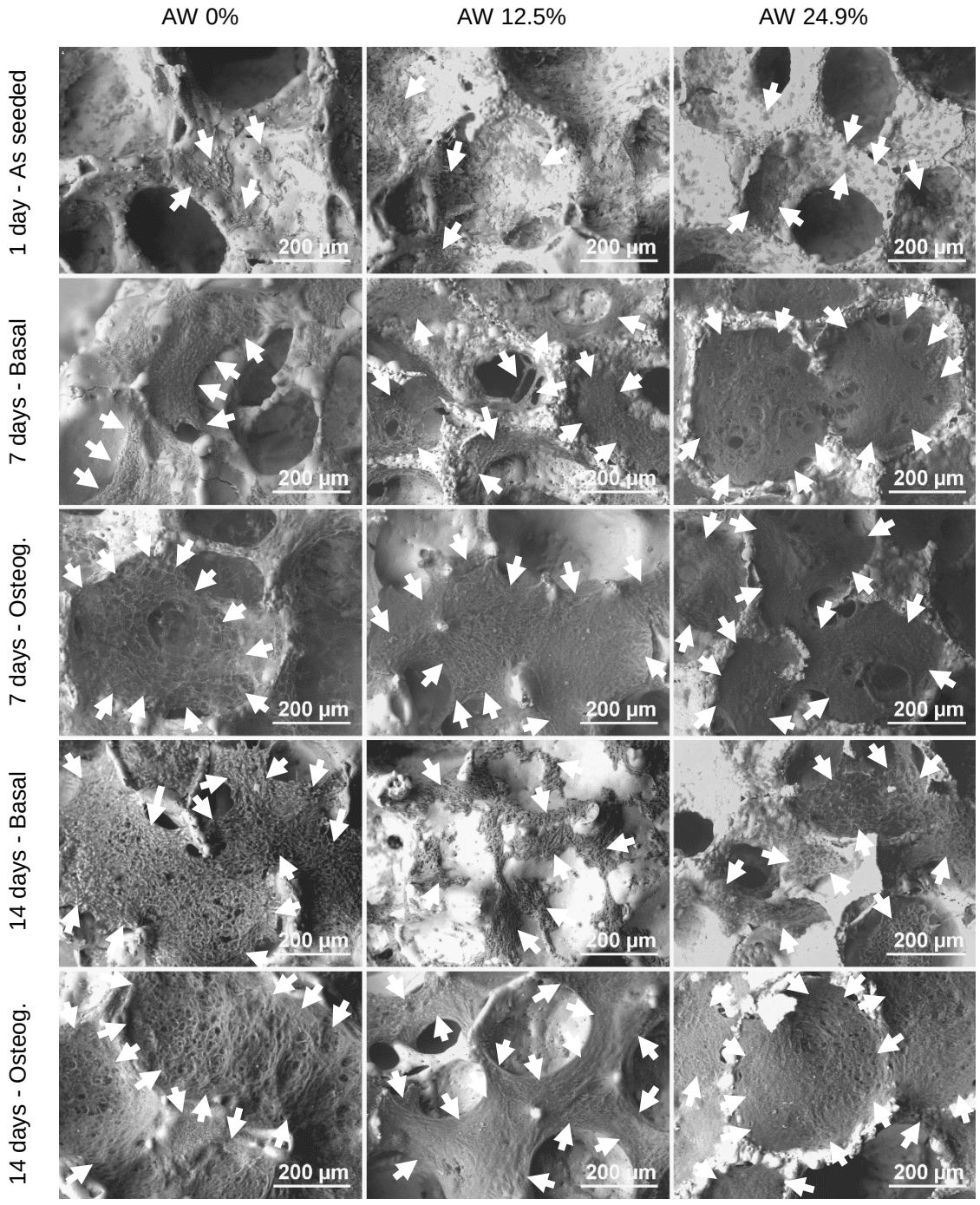

Figure 5.6: Scanning electron micrographs, at higher magnification, of the AW 0%, AW 12.5% and AW 24.9% scaffolds seeded with G292 cells shown in Figure 5.5, acquired in backscattered mode 1 day, 7 days and 14 days after seeding. 1 day samples were kept in plain media and are considered as-seeded. Samples collected 7 days and 14 days after seeding were cultured in either basal media or osteogenic media. Cells appear as dark grey on lighter grey scaffolds; agglomerates and sheets are pointed by white arrows. Scale bars represent 1 mm.

When samples were observed at a higher magnification, it was possible to better discern the morphology of cells and cell constructs.
Individual cells were clearly visible on the as seeded samples, which were kept in plain media for 24 h before the two culture media were used. Cells appeared elongated on sample AW 0% and more rounded on sample AW 24.9%. On sample AW 12.5%, cells had already formed small aggregates, which extended across small pores.
Cell sheets starting to bridge the scaffold pores could be found on scaffolds AW 0% and AW 12.5% cultured in basal media for 7 days, where cells grew circularly around the pores and progressively extending towards the centre. Fully bridged pores were observed on the corresponding sample AW 24.9%, with thin cell sheets still presenting small gaps. When cultured in osteogenic media for 7 days, all samples presented covered pores, with cells extending from the borders of pores or from asperities in the struts, with the thickness of the cell sheet increasing from AW 0% to AW 12.5% and then further to AW 24.9%.
After 14 days in basal media, pores of sample AW 0% looked mainly covered by sheets where individual cells could still be identified. Small aggregates could be observed on the surface of the struts of scaffold AW 12.5% with more elongated cells, while partial thin cell sheets could be found on sample AW 24.9%, which again could indicate that the two samples were damaged prior to or during the SEM analysis.
Thicker cell sheets could be observed on samples cultured in osteogenic media for 14 days. Pores were covered by a layer of cells on sample AW 0% and, by a denser layer, on sample AW 24.9%. Cell structures appeared to stretch from the pore borders and strut asperities across larger gaps on sample AW 12.5%.
In general, it was confirmed that osteogenic media induced a more rapid formation of denser cell layers compared to samples cultured in basal media. Enhanced proliferation, signified by thicker cell sheets, was observed for strontium-containing samples.

5.2.1.2.2 Effect of culture media on ALP staining of G292 cells

One scaffold per composition and per condition, at each time-point, was stained for ALP activity. Pictures of the samples are shown in Figure 5.7.

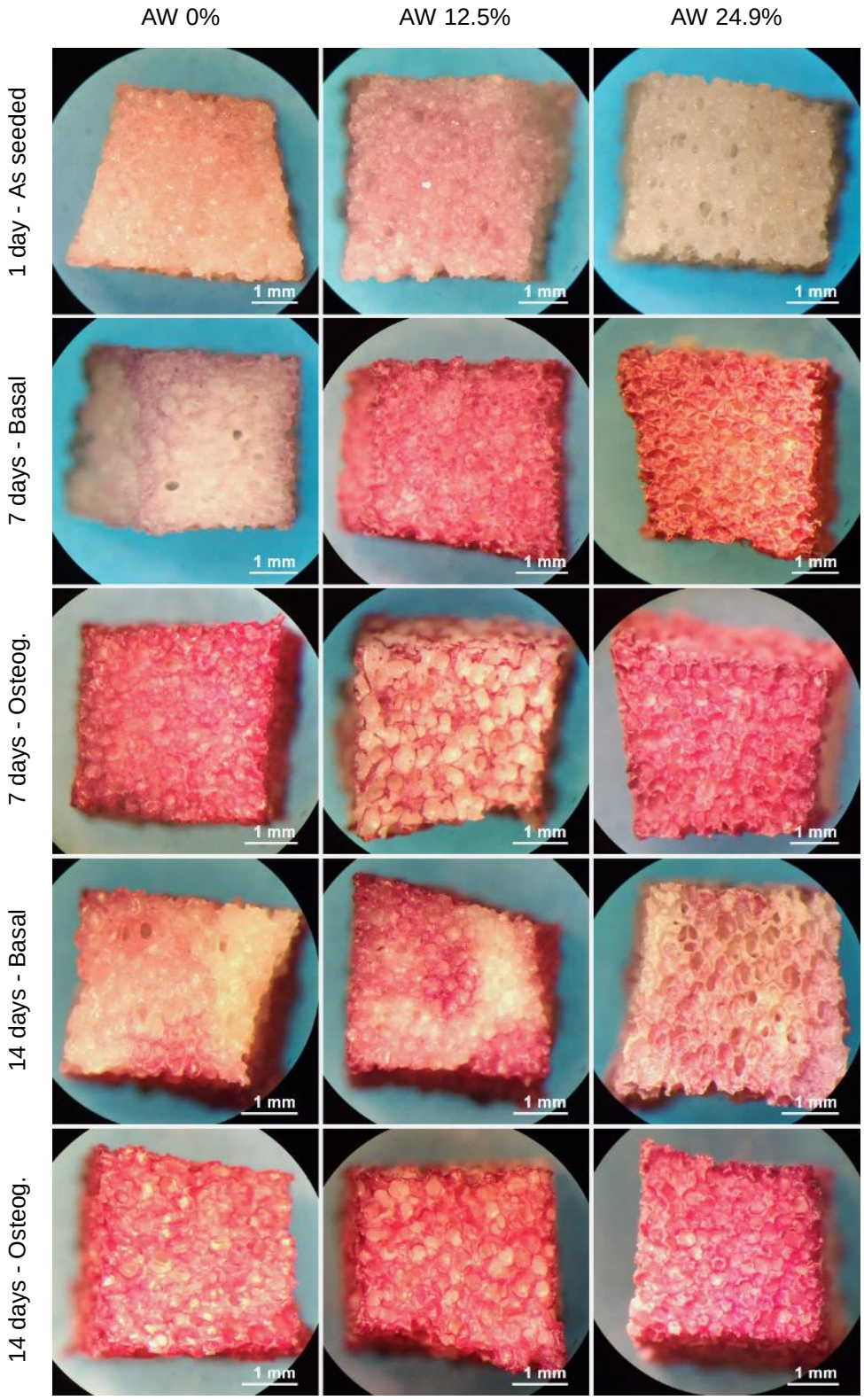

Figure 5.7: Stereomicroscopic pictures of AW 0%, AW 12.5% and AW 24.9% scaffolds, seeded with G292 cells and stained for ALP activity 1 day, 7 days and 14 days after seeding. 1 day samples were kept in plain media and are considered as-seeded. Samples collected 7 days and 14 days after seeding were cultured in either basal media or osteogenic media. ALP-positive areas appear as pink. Scale bars represent 1 mm.

While all three scaffolds that were collected 24 h after seeding appeared poorly stained, ALP staining became stronger after 7 and 14 days of culture.
Sample AW 0% cultured in basal media for 7 days showed very low staining, while the other two compositions showed a stronger staining, particularly sample AW 12.5%. When cultured in osteogenic media for 7 days, samples AW 0% and AW 24.9% gave a very strong staining, while sample AW 12.5% showed only clusters of stained cells. When cultured in basal media for 14 days, all three scaffolds presented areas with very poor staining, probably indicating that issues occurred during the staining process. However, sample AW 12.5% clearly showed the strongest staining compared to the other two compositions. When cultured in osteogenic media for 14 days, all three compositions gave a very strong staining, comparable across compositions.
In general, the use of osteogenic media during culture seemed to induced faster proliferation. It must be noted that G292 cells, being osteosarcoma-derived cells, normally express ALP. Therefore, for these samples, stronger stain corresponded also to the presence of more numerous cells and not only to a higher expression of markers related to osteogenic differentiation.

5.2.1.2.3 Effect of culture media on DNA concentration, ALP activity and metabolic activity of G292 cells

Results of quantitative assays for DNA concentration, ALP activity and metabolic activity are summarised in the graphs in Figure 5.8. In this case, 3 samples per composition and per condition were measured at each time-point and averaged. The same 1 day results are shown in the graphs for both basal and osteogenic media, as they correspond to the as-seeded samples collected before scaffolds were moved to their assigned culture media for the other time-points.

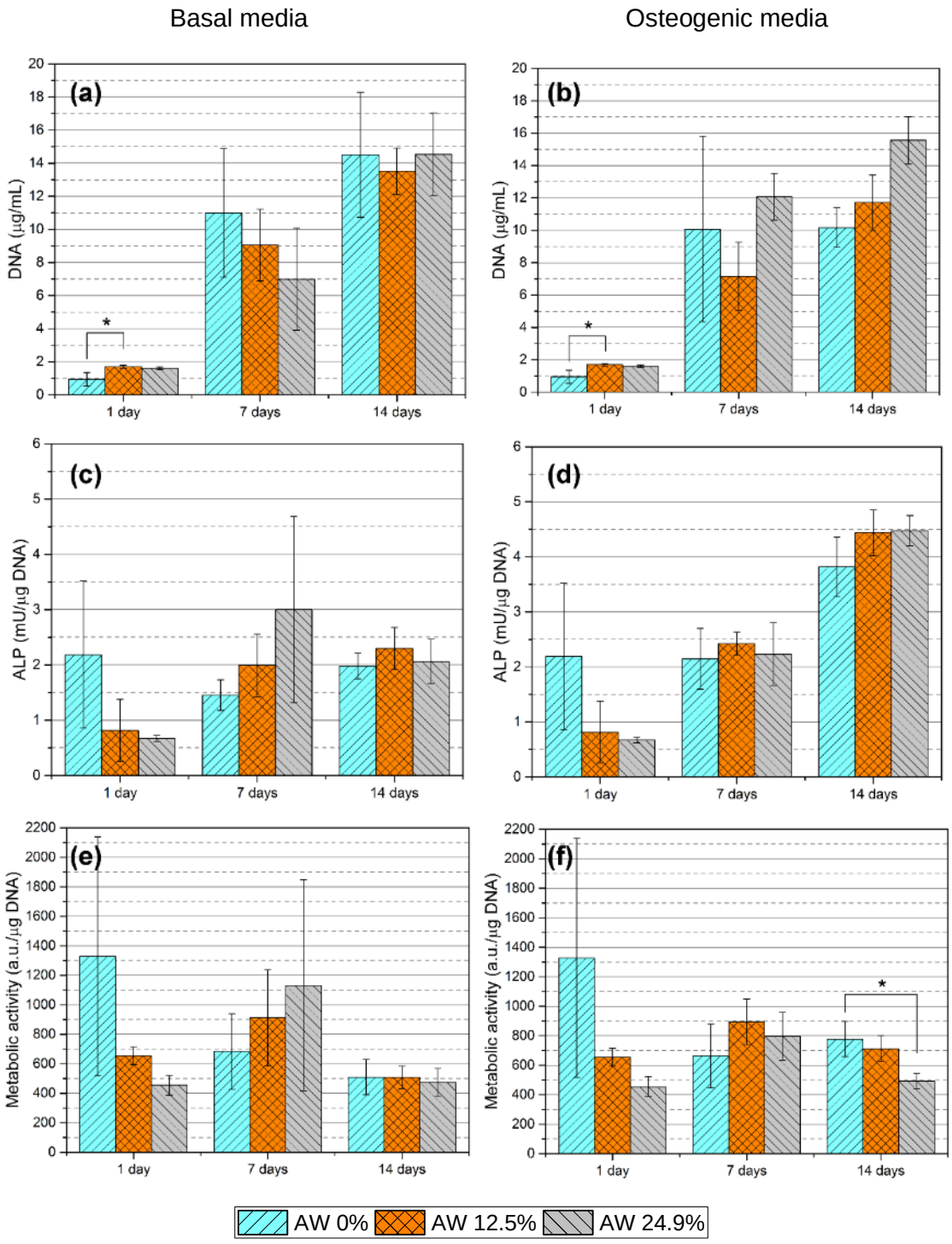

Figure 5.8: Quantification, for G292 cells cultured on AW 0%, AW 12.5% and AW 24.9% scaffolds in basal and in osteogenic media, of (a & b) DNA concentration, (c & d) ALP activity normalised to DNA and (e & f) metabolic activity normalised to DNA. 1 day data are the same for basal and osteogenic media graphs, as they represent samples as-seeded before they were moved to their assigned culture media. Error bars indicate the standard deviation of data (n=3), * indicates significant difference between compositions ($p \leq 0.05$).

As expected from the previous qualitative results, the amount of DNA increased with increasing incubation time for all the three compositions in both basal and osteogenic media. No significant difference could be found between the two culture media tested, apart from sample AW 24.9% that, at 7 days, had about twice the amount of DNA in osteogenic media than in basal media. Significant difference ($p<0.05$, Bonferroni test for mean comparison) was observed for samples AW 0% and AW 12.5% at 1 day (samples as seeded), though this could derive from uneven seeding.
ALP activity increased at 14 days for samples in osteogenic media, while it was comparable for basal and osteogenic media at 7 days. Although no significant difference could be found, the relative ALP activity appeared to progressively increase from sample AW 0% to AW 12.5% and further to AW 24.9% when cultured in basal media. Comparable ALP activity was found for the three compositions when cultured in osteogenic media for 7 days, while it was higher at 14 days.
Metabolic activity, normalised to DNA quantity, was similar between the two culturing conditions; only at 14 days and in samples cultured in osteogenic media, the metabolic activity of cells on AW 0% scaffolds was significantly higher than on AW 24.9% ($p<0.05$, Bonferroni test), with composition AW 12.5% falling in between.
Very high standard deviations were found for some of the samples, possibly due to variability in the seeding efficacy. No significant difference was found between compositions. However, proliferation appeared to be enhanced by composition AW 0% in basal media (7 days) and AW 24.9% in osteogenic media (7 and 14 days). ALP production was higher for composition AW 24.9% in basal media at 7 days and strongly enhanced at 14 days in osteogenic media for all three compositions.
Therefore it was concluded that the use of osteogenic media could mask the effect of strontium on G292 cells by strongly enhancing their ALP production, as observed at the 14 day time-point with both this quantification assay and the ALP stain (Figure 5.7). Hence, only basal media was used when testing all the six compositions of strontium AW scaffolds with G292 cells, results are reported in the next Section 5.2.1.3.

5.2.1.3 Effect of strontium content in AW porous scaffolds on G292 cells

The proliferation and ALP production of G292 cells were tested by culturing all the six strontium AW compositions of scaffolds in basal media for up to 7 days.

5.2.1.3.1 Effect of strontium content on G292 cell attachment and proliferation

For all compositions, cell attachment (3 h), spreading (1 day) and proliferation (3 and 7 days) were first checked under the fluorescence microscope; images are shown in Figure 5.9.

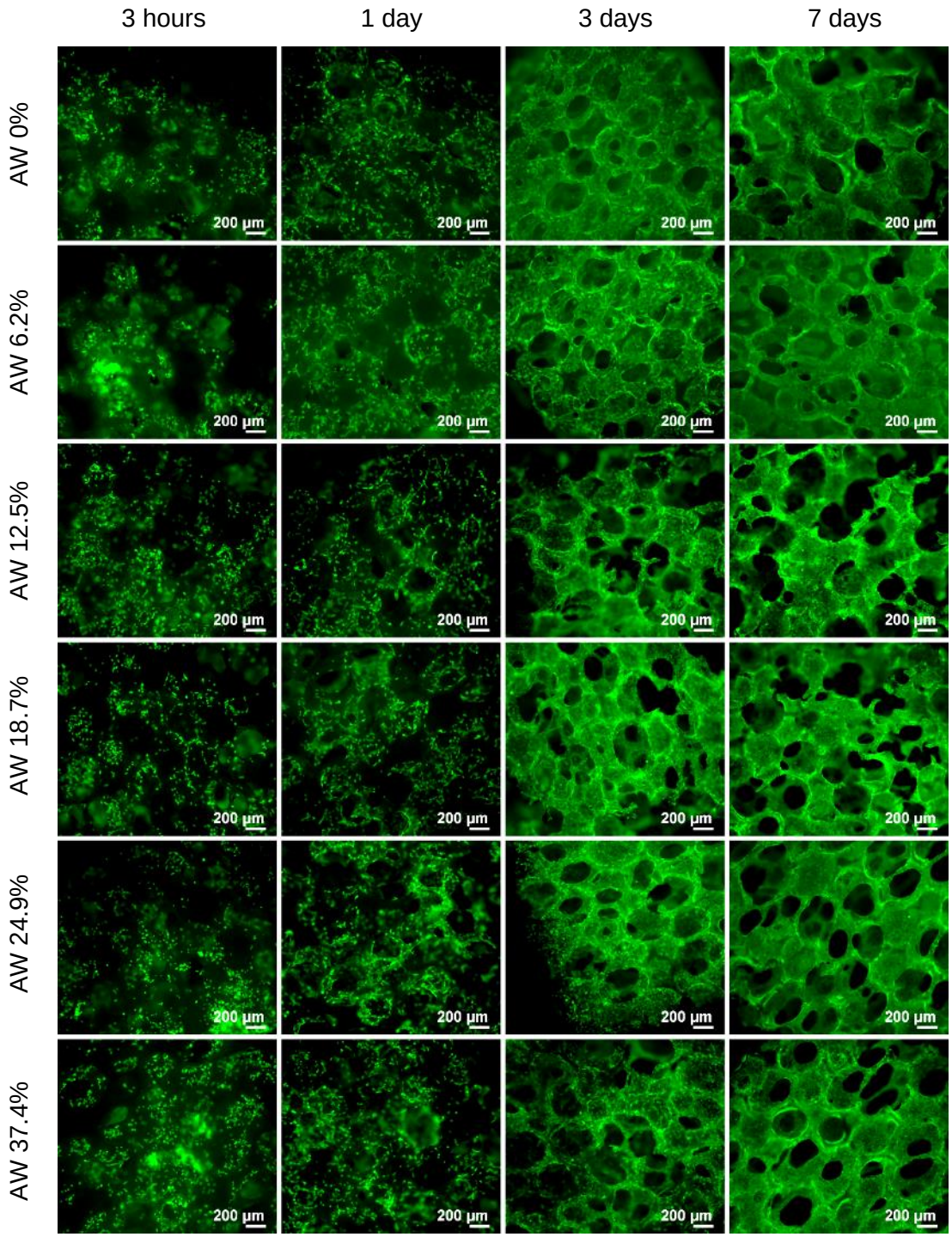

Figure 5.9: Live stain of G292 cells cultured in basal media on AW 0%, AW 6.2%, AW 12.5%, AW 18.7%, AW 24.9% and AW 37.4% porous scaffolds, viewed under fluorescence microscope. Samples were observed for cell attachment (3h in plain media after seeding) and proliferation at 1 day, 3 days and 7 days of culture in basal media after seeding. Live cells display as green. Scale bars represent 200 µm.

3 h after seeding, all six compositions of scaffolds appeared covered in a high number of cells that were already starting to spread on the scaffold struts. This confirmed the results of Section 5.2.1.1 that 3 h were enough to guarantee good cell attachment and to observe initial spreading of G292 cells.
At 24 h after seeding, cells were well spread on all the compositions and had already started to proliferate.
After 3 days of culture in basal media, scaffold struts were completely covered in what appeared to be a single layer of cells; single cells could still be identified within the layers.
At 7 days of culture, the cell layer covering the scaffold struts had become denser, with cells forming a continuous sheet on all the six strontium AW compositions.
Very similar results were found for all the compositions, with no evident difference between them.

The same samples, stained with fluorescent live/dead markers, were then observed under the confocal microscope. Results are summarised in Figure 5.10.

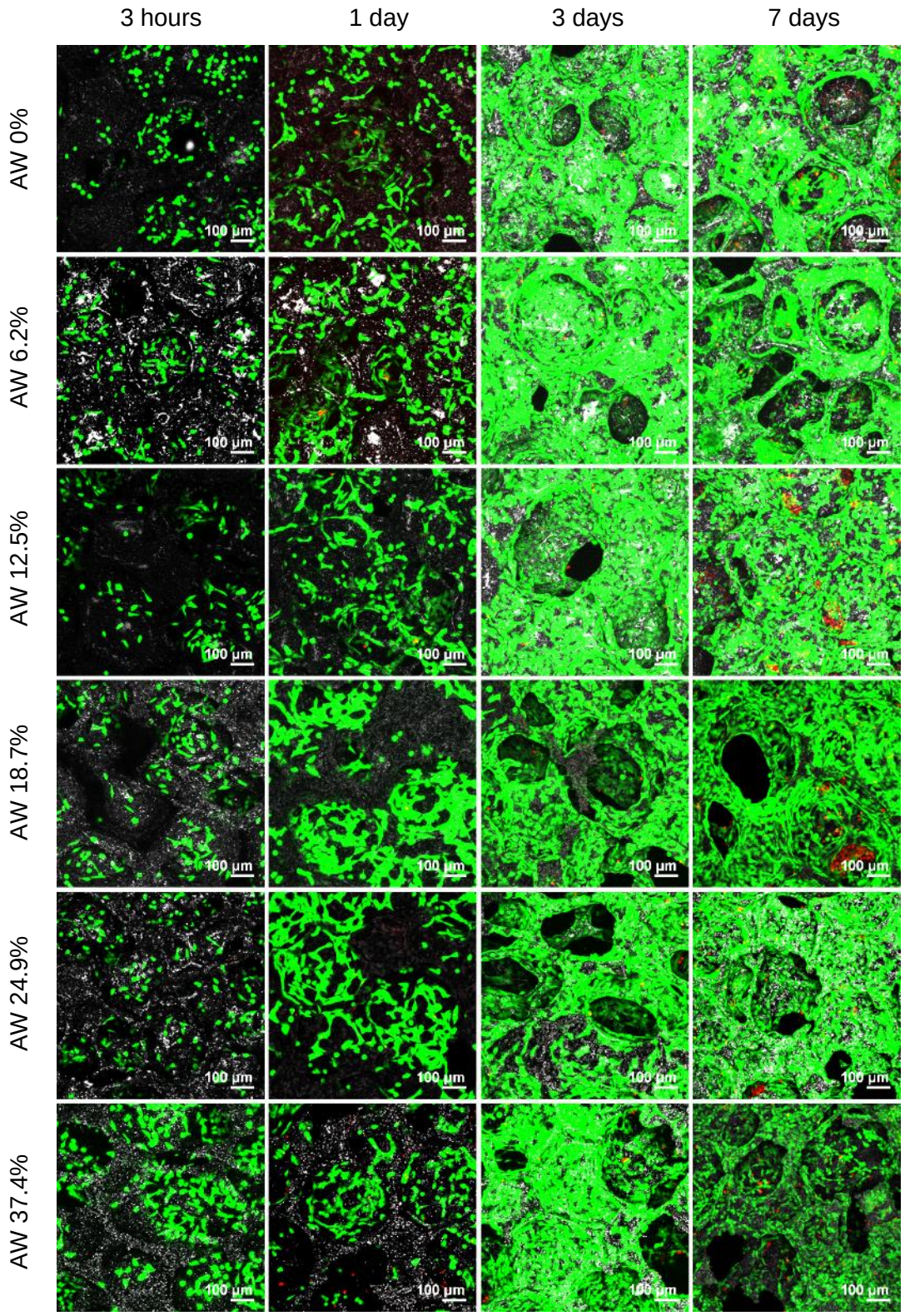

Figure 5.10: Confocal microscopy pictures of the AW 0%, AW 6.2%, AW 12.5%, AW 18.7%, AW 24.9% and AW 37.4% scaffolds seeded with G292 cells. Samples were observed for cell attachment (3h in plain media after seeding) and proliferation after 1 day, 3 days and 7 days of culture in basal media. Live cells are represented as green, dead cells are represented as red and scaffolds are shown in greyscale. Scale bars represent 100 µm.

3 h after seeding, it was confirmed that G292 cells had attached to all samples, with some cells appearing elongated, thus showing they had started to spread, especially on the five strontium-containing compositions.
At 24 h culture after seeding, well spread cells could be observed forming agglomerates in correspondence with scaffold concavities. These were denser for compositions AW 18.7% and AW 24.9%. Very few dead cells could be seen on all the compositions.
At 3 days, cells were covering most of the scaffold struts and had started to bridge pores around their borders. Again very few dead cells could be found on all the scaffolds.
After 7 days of culture, all scaffolds still appeared fully covered with live cells growing on the surface and ingrowing along pores. On compositions AW 0% and AW 6.2% they appeared to form dense elongated agglomerates that stretched across pores, while for the other compositions they were more uniformly distributed on the struts. Clusters of dead cells were found on compositions AW 12.5% to AW 24.9%, while sparse dead cells could be observed on sample AW 37.4% and, fewer, on AW 0% and AW 6.2%.
In general, no distinct differences could be found between compositions.

The same samples were then observed with SEM, in BSE mode; results are shown in Figure 5.11, and, at higher magnification, in Figure 5.12.

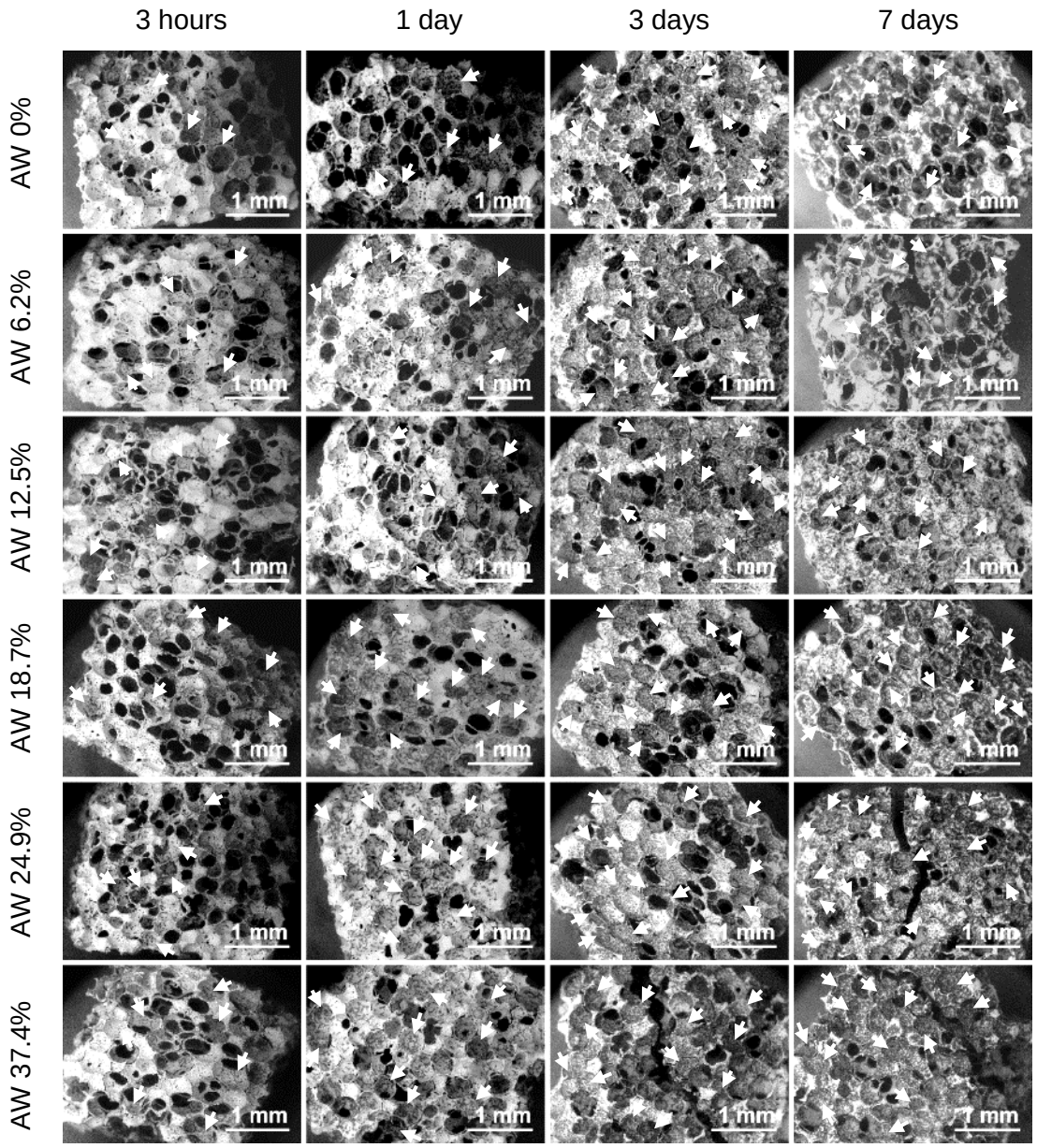

Figure 5.11: Scanning electron micrographs showing the overall coverage of AW 0%, AW 6.2%, AW 12.5%, AW 18.7%, AW 24.9% and AW 37.4% scaffolds seeded with G292 cells, acquired in backscattered mode. Samples were observed for cell attachment (3h in plain media after seeding) and proliferation at 1 day, 3 days and 7 days of culture in basal media after seeding. Cells appear as dark grey on lighter grey scaffolds; white arrows point to cell aggregates. Scale bars represent 1 mm.

SEM imaging allowed to observe the whole surface of scaffolds. Since images were taken in BSE mode, cells appeared as darker spots on the brighter background of the scaffold material.

3 h after seeding, small sparse individual cells could be seen on the surface of all strontium AW samples.
At 1 day culture after seeding, a significantly higher number of cells could be observed on all samples. Cells appeared more elongated on the strontium-containing samples than on sample AW 0%.
After 3 days of culture in basal media, most surface of the scaffolds was covered in cells for all the six compositions. No differences could be observed between compositions.
At 7 days, dense cell agglomerates could be found in concavities and around the pores of samples of composition AW 0% and AW 6.2%. For samples AW 12.5%, AW 18.7% and AW 24.9%, cells appeared elongated and more evenly distributed on the surface of the scaffolds, with smaller agglomerates found in concavities, while on sample AW 37.4% cells were uniformly scattered on the surface.
Clear proliferation could be observed for all the samples. At day 7, cells appeared to concentrate in concavities for compositions AW 0% and AW 6.2%. Some of the samples fractured during imaging, probably due to thermal shock while decreasing temperature and pressure in the SEM chamber.

Details, at higher magnification, of the same samples are shown in Figure 5.12.

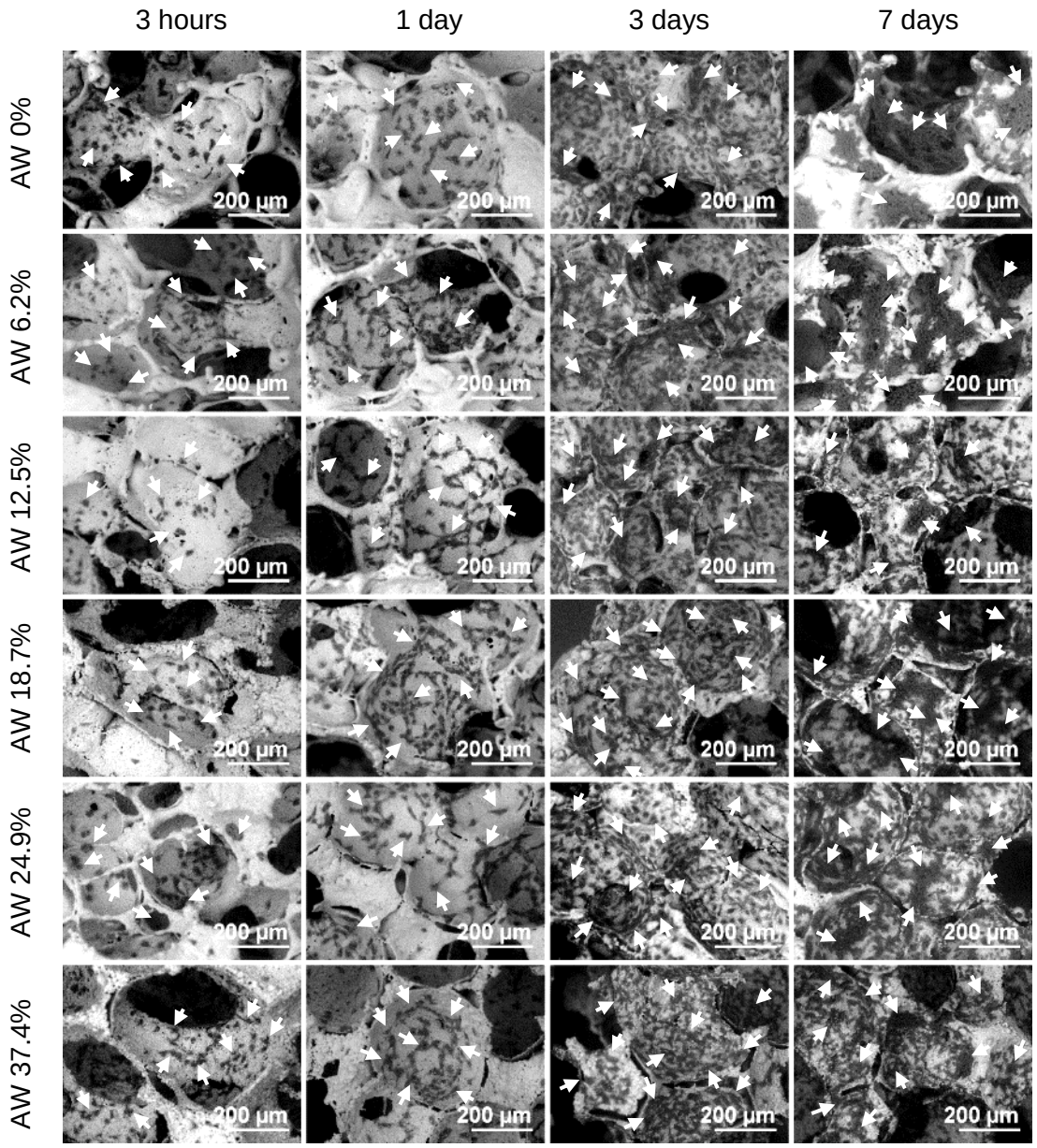

Figure 5.12: Scanning electron micrographs, at higher magnification, of the AW 0%, AW 6.2%, AW 12.5%, AW 18.7%, AW 24.9% and AW 37.4% scaffolds seeded with G292 cells shown in Figure 5.11, acquired in backscattered mode. Samples were observed for cell attachment (3h in plain media after seeding) and proliferation at 1 day, 3 days and 7 days of culture in basal media after seeding. Cells appear as dark grey on lighter grey scaffolds; white arrows point to cells and agglomerates. Scale bars represent 200 µm.

Individual cells could be seen on the strut surface of all samples after 3 h and 1 day of culture in basal media, with an increased number of cells and some initial cell-to-cell contact at 1 day. Cells also appeared more elongated after 1 day than after 3 h, indicating further spreading after the initial attachment.

By day 3, all scaffolds were covered by cells, with individual cells still clearly visible, but forming small aggregates where few cells were in contact. Aggregates stretching along the scaffold struts could be seen on scaffolds AW 6.2%, AW 12.5% and AW 18.7%.

At day 7, no individual cells could be distinguished on samples AW 0% and AW 6.2%, where cells appeared to have moved to concavities and formed agglomerates that stretched across pores. Cell agglomerates forming in the scaffold concavities could also be observed on scaffolds AW 12.5%, AW 18.7% and AW 24.9%, although single cells could still be seen. Mainly individual cells covered the struts of scaffold AW 37.4%.

In general, proliferation from 3 h to 7 days of culture was confirmed. Only compositions AW 0% and AW 6.2% appeared to induce the early formation of cell structures that partially covered the scaffold pores at 7 days after seeding.

5.2.1.3.2 Effect of strontium content on G292 cell ALP staining

Three samples per composition per time-point were stained for ALP and pictured using a stereomicroscope. One sample per composition per time-point was chosen as representative of the group and they are shown in Figure 5.13.

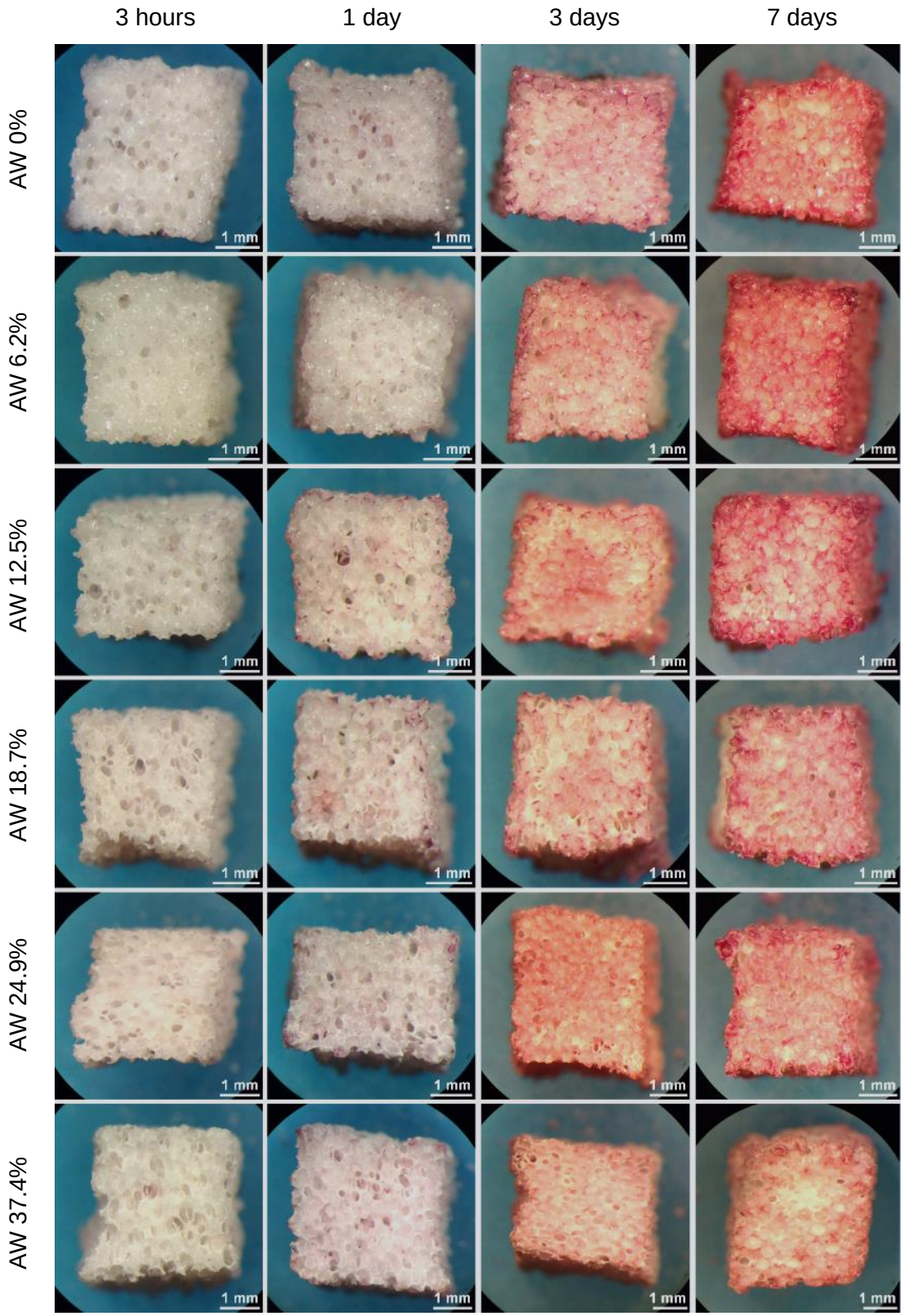

Figure 5.13: Stereomicroscopic images of the AW 0%, AW 6.2%, AW 12.5%, AW 18.7%, AW 24.9% and AW 37.4% scaffolds seeded with G292 cells and stained for ALP activity. Samples were collected after 3h in plain media (as seeded) and at 1 day, 3 days and 7 days of culture in basal media after seeding. ALP-positive areas appear as pink. Scale bars represent 1 mm.

As expected, no staining could be observed for samples collected 3 h after seeding, as cells had only just adhered to their surface and no significant proliferation could have taken place.

A pale staining could be observed for samples cultured for 24 h, indicating mild proliferation of cells. The staining appeared mildly stronger for scaffolds AW 12.5% and AW 18.7%.

By day 3, all compositions produced clear staining of their surface, which appeared slightly stronger for samples AW 0%, AW 6.2%, AW 12.5% and, only on certain areas of the surface, sample AW 18.7%. Sample AW 24.9% appeared uniformly stained, but did not present areas of more intense staining as seen for lower strontium-containing compositions, while the staining for sample AW 37.4% appeared clearly less intense.

Very strong staining was found for samples AW 0%, AW 6.2% and AW 12.5% after 7 days of culture in basal media. Scaffolds AW 18.7% and AW 24.9% also presented uniform, but less strong staining, while sample AW 37.4% showed again a less intense staining compared to the other compositions.

In general, ALP activity followed the observed proliferation: as G292 cells naturally express ALP, an increase in their cell number also generates a stronger staining on the sample. Compositions AW 6.2% and AW 12.5%, along with the starting composition AW 0%, induced a mildly stronger total expression of the enzyme.

5.2.1.3.3 Effect of strontium content on DNA concentration, ALP activity and metabolic activity in G292 cells

In order to quantify these results, the ALP activity was measured, along with metabolic activity, and normalised to the DNA concentration from 6 samples per composition and per time-point. Results are shown in Figure 5.14.

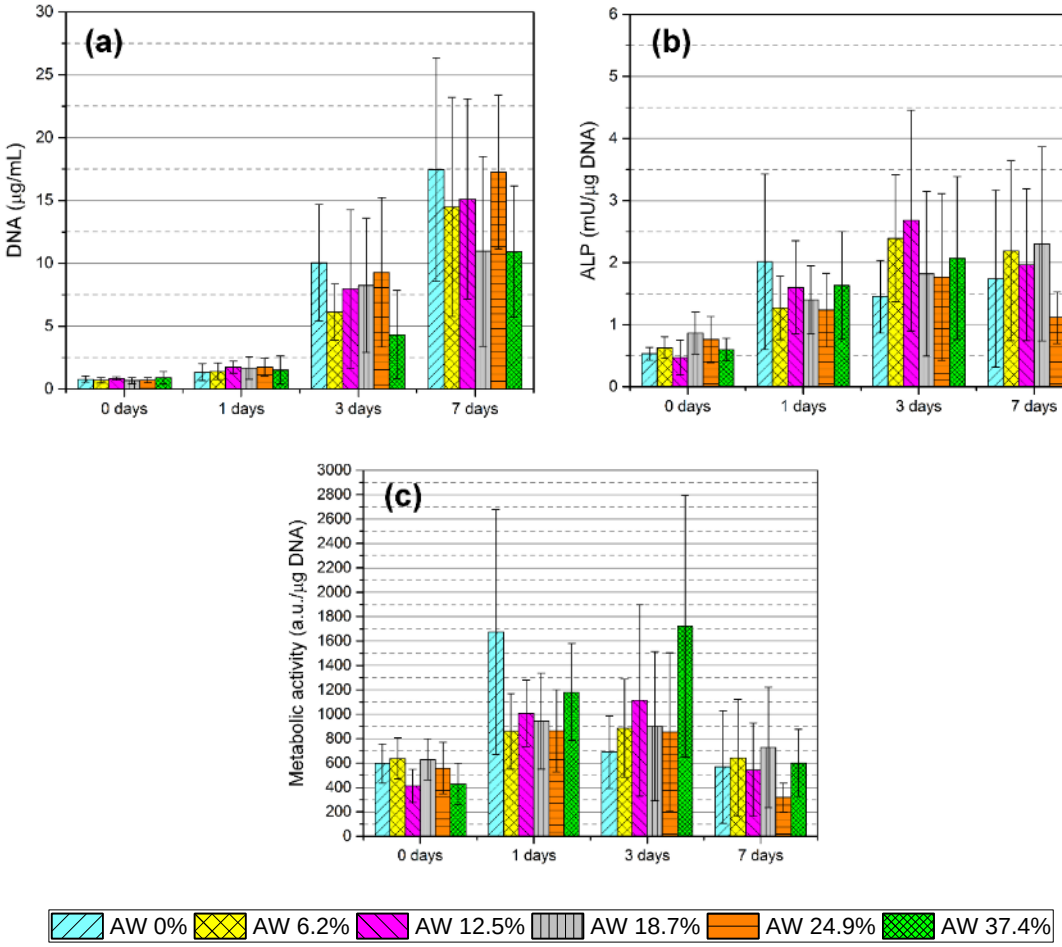

Figure 5.14: Quantification for G292 cells cultured in basal media on AW 0%, AW 6.2%, AW 12.5, AW 18.7%, AW 24.9% and AW 37.4% scaffolds of (a) DNA concentration, (b) ALP specific activity, normalised to DNA content and (c) metabolic activity, normalised to DNA content. Error bars indicate the standard deviation of data (n=6).

The DNA quantification showed that G292 cells proliferated on all the six compositions of scaffold tested, as already observed with the imaging techniques. Only composition AW 37.4% appeared to cause a reduced proliferation compared to the other samples, although the difference was found not statistically significant ($p>0.05$).

The ALP activity increased from the as-seeded samples to the 3-day time-point, then it maintained the same level at 7 days. Compositions AW 6.2% and AW 12.5% had a higher average normalised ALP activity at 3 days compared to the other samples, while the ALP activity for sample AW 0% was higher at 24 h than 3 days. At 7 days, samples AW 24.9% and AW 37.4% had lower ALP activity than the other compositions at the same time-point and compared to their previous time-points.

Normalised metabolic activity was higher at day 1 and day 3, while it decreased at day 7 for all the six compositions under study. The decrease in metabolic activity at day 7

could be due to the rapid proliferation of cells on the samples, which could have caused a faster consumption of nutrients from the media. Further tests would be needed to confirm this. No significant difference was found between compositions at any time-point.
In conclusion, the high variability of results meant that no significant difference ($p>0.05$) could be observed between compositions for any of the three parameters measured at any time-point. However, results suggested that compositions AW 6.2% and AW 12.5% could have supported a mild increase in ALP activity.

5.2.2 Effect of strontium AW porous scaffolds on human bone marrow-derived mesenchymal stromal cells

Since the aim of this chapter was to assess whether strontium-doped AW scaffolds could better stimulate bone regeneration than no-strontium AW, further tests were carried out to study the osteogenic differentiation of human bone marrow-derived mesenchymal stromal cells (hBM-MSCs). First, the use of osteogenic culture media was tested against basal media (Section 5.2.2.1). Then three of the compositions were studied for cell proliferation and ALP activity (Sections 5.2.2.2.1 to 5.2.2.2.3) and for extracellular matrix production through collagen staining (Section 5.2.2.2.4).

5.2.2.1 Effect of basal and osteogenic media on ALP staining of hBM-MSCs cultured on strontium AW porous scaffolds

Three strontium compositions (AW 6.2%, AW 18.7% and AW 37.4%) were compared to the no-strontium composition AW 0% in both basal and osteogenic media, in order to evaluate whether osteogenic media was required to induce osteogenic differentiation in the chosen hBM-MSC population. hBM-MSCs were at passage 4 for this test.

First, before samples were divided between basal and osteogenic media, cell attachment was verified by fluorescence microscopy 3h after seeding. Pictures at different magnifications are shown in Figure 5.15.

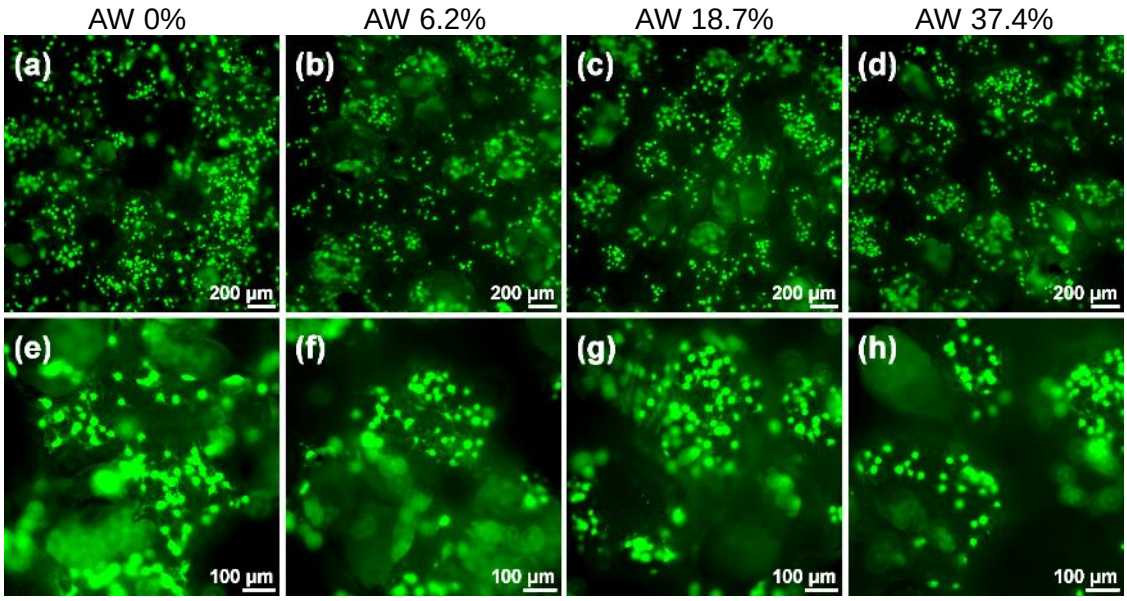

Figure 5.15: Live stain of primary hBM-MSCs (passage 4) on AW 0%, AW 6.2%, AW 18.7% and AW 37.4% porous scaffolds, observed under fluorescence microscope 3 h after seeding and before being moved to culture media. (a-d) cell attachment on scaffolds observed at lower magnification, (e-h) initial spreading of cells observed at higher magnification. Live cells are labelled as green. Scale bars in images (a-d) represent 200 µm, in images (e-h) represent 100 µm.

3 h after seeding, all the tested scaffold compositions were well populated with attached cells. As shown in detail in the higher magnification micrographs (Figure 5.15e-h), round cells were observed on compositions AW 18.7% and 37.4%, while some cells had already started to spread on the scaffold struts of compositions AW 0% and AW 6.2%.

After being observed under the fluorescent microscope, scaffolds were put back into culture in the assigned culture media and collected after two weeks. Three samples per condition and per composition were cultured and only ALP activity staining was carried out. Results are shown in Figure 5.16.

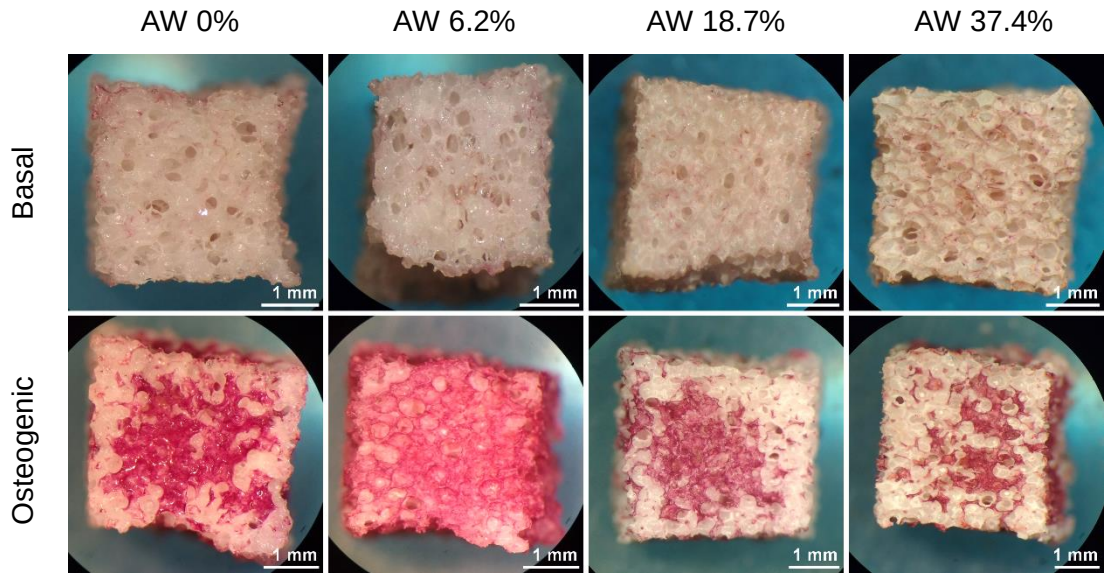

Figure 5.16: Stereomicroscopic images of AW 0%, AW 6.2%, AW 18.7% and AW 37.4% scaffolds seeded with hBM-MSCs at passage 4, cultured in either basal or osteogenic media and stained for ALP activity. ALP-positive areas appear as pink. Scale bars represent 1 mm.

All samples cultured in basal media presented very little staining after 2 weeks of culture, with no difference between compositions.

When cultured in osteogenic media, all scaffold compositions showed some clear staining. Sample AW 6.2% was covered in cells expressing a high amount of ALP, as all its surface was stained. Scaffolds AW 0% and AW 18.7% presented a large patch of stained cells approximately in the centre of their upper surface, while scaffold AW 37.4% had smaller stained areas.

From this pilot study, it was evident that osteogenic media was necessary to induce any osteogenic differentiation in the chosen hBM-MSC population. Amongst the four compositions tested, AW 6.2% appeared to be the sample that could better enhance osteogenic differentiation. Therefore, basing on these results, scaffolds AW 6.2% were compared, in the following study, only with AW 0% as the no-strontium control and AW 12.5% as the next-higher strontium composition.

5.2.2.2 Effect of strontium content in AW porous scaffolds on hBM-MSCs

Three strontium AW compositions were tested: AW 0% as the no-strontium control, AW 6.2% and AW 12.5%. Only 2 time-points were considered, culturing in osteogenic media: 7 days and 14 days. Proliferation and ALP activity were tested and results are presented in Sections 5.2.2.2.1 to 5.2.2.2.3; samples cultured for 4 weeks were tested for extracellular collagen deposition and results are shown in Section 5.2.2.2.4.

5.2.2.2.1 Effect of strontium content on hBM-MSCs proliferation

At first, the presence of cells and their distribution on the scaffold surface was verified under fluorescence microscope; images are displayed in Figure 5.17.

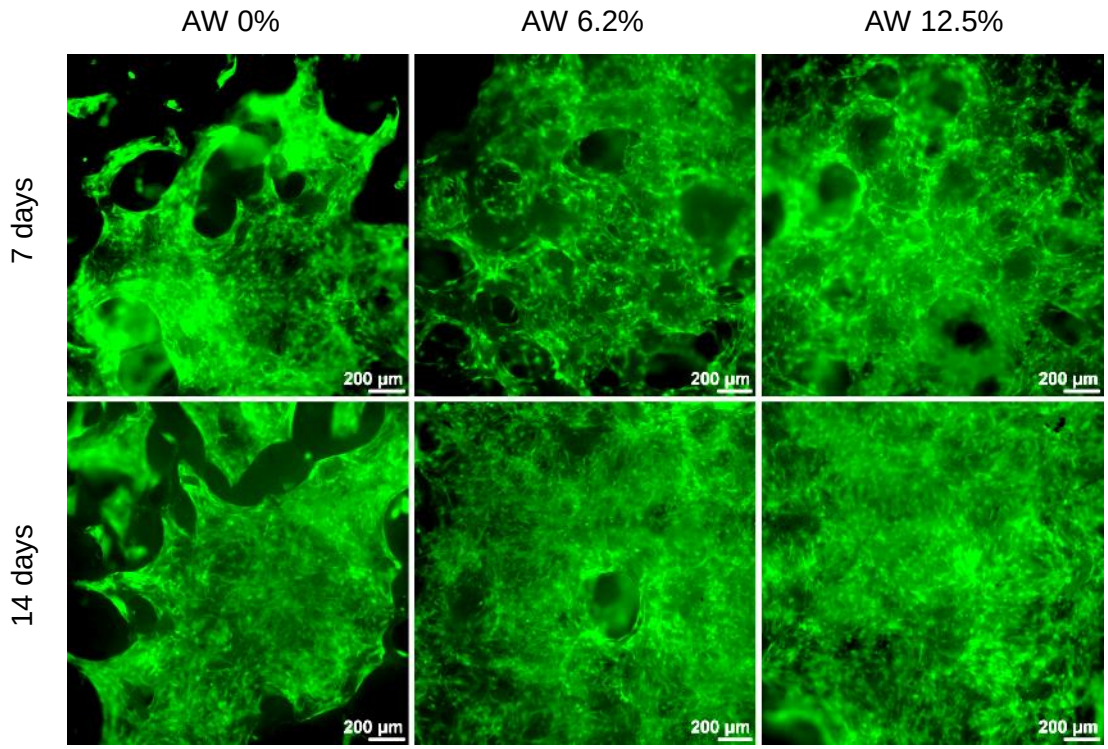

Figure 5.17: Live stain of hBM-MSCs (passage 5) grown on AW 0%, AW 6.2% and AW 12.5% porous scaffolds, observed under fluorescence microscope. Samples were cultured in osteogenic media for 7 and 14 days. Live cells are labelled as green. Scale bars represent 200 µm.

After 7 days of culture in osteogenic media, all three compositions presented a high number of live cells distributed on their surface. On scaffold AW 0% cells appeared to grow in patches, stretching across pores.
At 14 days, scaffolds AW 6.2% and AW 12.5% appeared covered by a dense layer of cells, while sample AW 0% still presented cells growing in separate patches.

The same samples were then observed under confocal microscope, to assess the distribution of live and dead cells within the scaffolds, and under SEM, to observe the overall cell distribution and morphology on the sample surface. Pictures are shown in Figure 5.18 to Figure 5.20.

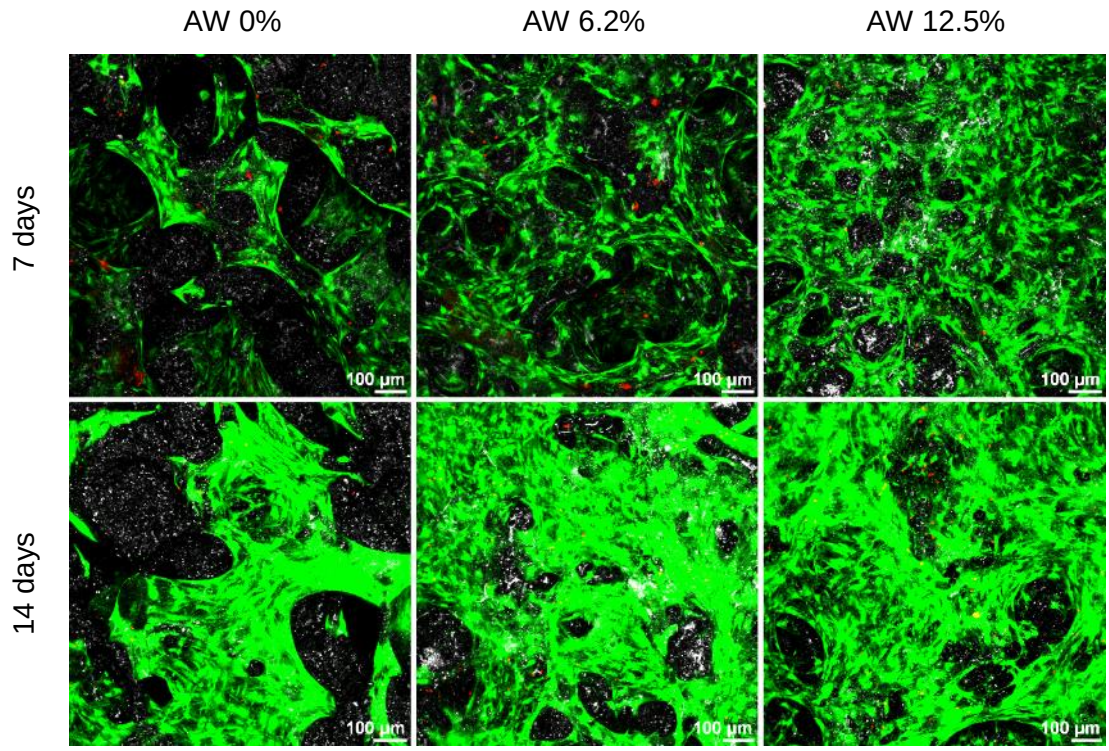

Figure 5.18: Confocal microscopy pictures of the AW 0%, AW 6.2% and AW 12.5% scaffolds seeded with hBM-MSCs at passage 5. Samples were cultured in osteogenic media for 7 and 14 days. Live cells are represented as green, dead cells are represented as red and scaffolds are shown in greyscale. Scale bars represent 100 µm.

After 7 days of culture in osteogenic media, hBM-MSCs grown on samples AW 6.2% and AW 12.5% appeared to form a layer that uniformly covered the struts of the scaffolds. On scaffold AW 0%, the presence of patches of cells scattered on the surface of the scaffold was confirmed. A few red dots, indicating the presence of dead cells, were observed on all the three scaffolds.

At 14 days, the layer of cells on samples AW 6.2% and AW 12.5% had become denser, with cells growing around pores and bridging them, showing evidence of cell proliferation. Patches on sample AW 0% appeared denser and larger, indicating that cell proliferation occurred also for this composition. Very few dead cells could be seen on the three samples.

No obvious difference could be found between composition AW 6.2% and AW 12.5% at any of the two time-points.

The same samples were observed under cold-stage SEM, and micrographs at lower and higher magnification are shown in Figure 5.19 and Figure 5.20, respectively.

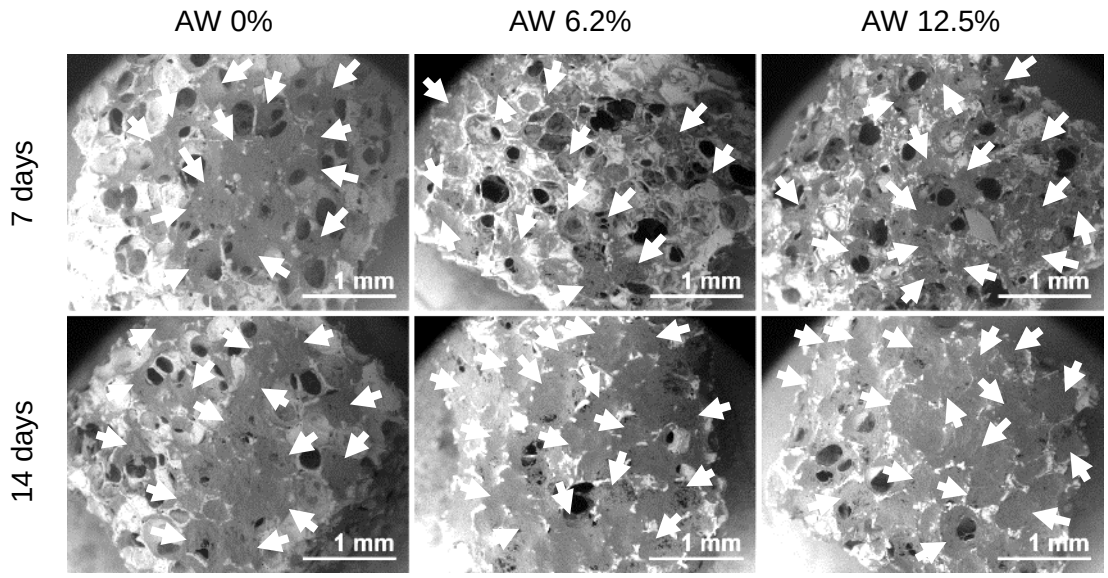

Figure 5.19: Scanning electron micrographs showing the overall coverage of AW 0%, AW 6.2% and AW 12.5% scaffolds seeded with hBM-MSCs (passage 5), acquired in backscattered mode. Samples were observed for cell proliferation after 7 days and 14 days of culture in osteogenic media. Cells appear as dark grey on lighter grey scaffolds; white arrows point to cell sheets. Scale bars represent 1 mm.

SEM micrographs allowed for the visualisation of the whole scaffold surface.
At 7 days of culture in osteogenic media, it was confirmed that, on sample AW 0%, hBM-MSCs tended to grow in patches that appeared to bridge over pores of the scaffold structure. Cells were more scattered and evenly distributed on the surface of scaffolds AW 6.2% and AW 12.5%, covering some of the pores or bridging across them.
At 14 days, proliferation was evident for samples AW 6.2% and AW 12.5%, where most of the surface was covered by a dense layer of cells that occluded the scaffold pores and bridged over to form a continuous sheet. For scaffold AW 0%, part of its bare surface was still visible as cells did not cover all of it, but remained in separate patches as observed at the earlier time-point and in Figure 5.17 and Figure 5.18.
In general, proliferation and cell distribution across the scaffold surface were higher for scaffolds AW 6.2% and AW 12.5% than scaffolds AW 0%, but no definite difference could be found between the two strontium compositions.

Details of the same samples are represented, at higher magnification, in Figure 5.20.

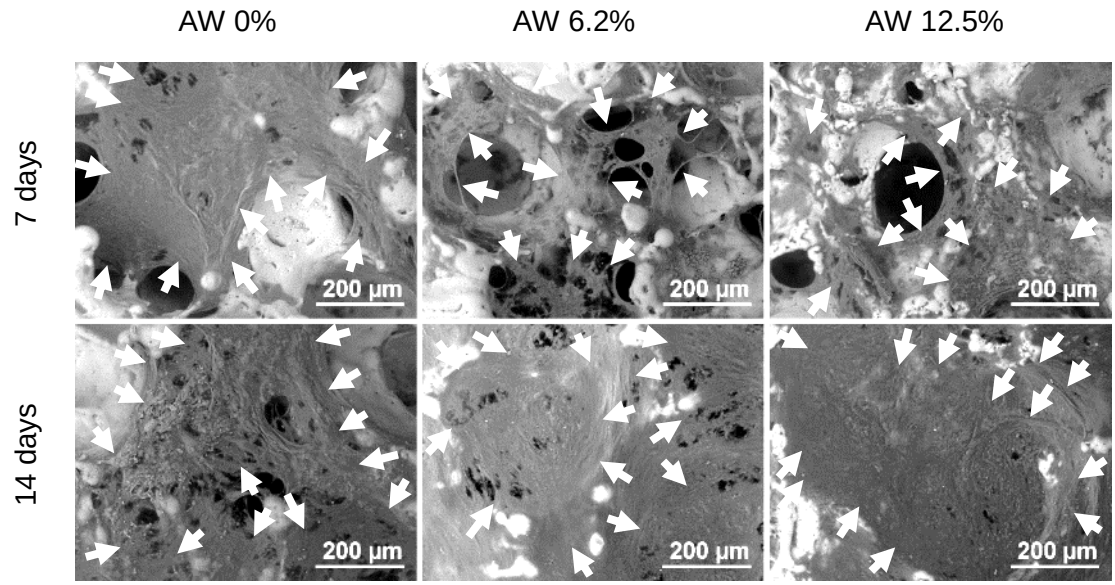

Figure 5.20: Scanning electron micrographs of the AW 0%, AW 6.2% and AW 12.5% scaffolds seeded with hBM-MSCs (passage 5) shown in Figure 5.19, acquired in backscattered mode at higher magnification. Samples were observed for cell proliferation after 7 days and 14 days of culture in osteogenic media. Cells appear as dark grey on lighter grey scaffolds; white arrows point to cell sheets. Scale bars represent 200 µm.

Cell sheets bridging across the samples could be observed on all scaffolds and at both time-points.

At 7 days, the cell sheet on sample AW 0% appeared denser than those on samples AW 6.2% and AW 12.5%, which still presented large gaps over the scaffold pores.

At 14 days, scaffold AW 12.5% presented very thick layers of cells occluding the scaffold pores and bridging over struts. The cell layer covering samples AW 0% and AW 6.2% still presented small gaps, with cells growing directionally around the border of pores and along struts.

5.2.2.2.2 Effect of strontium content on ALP staining of hBM-MSCs

Differences in ALP activity at the two time-points for the three compositions tested were qualitatively assessed by staining 3 samples per composition and per time-point, pictured under the stereomicroscope. One representative sample for each composition and condition is shown in Figure 5.21.

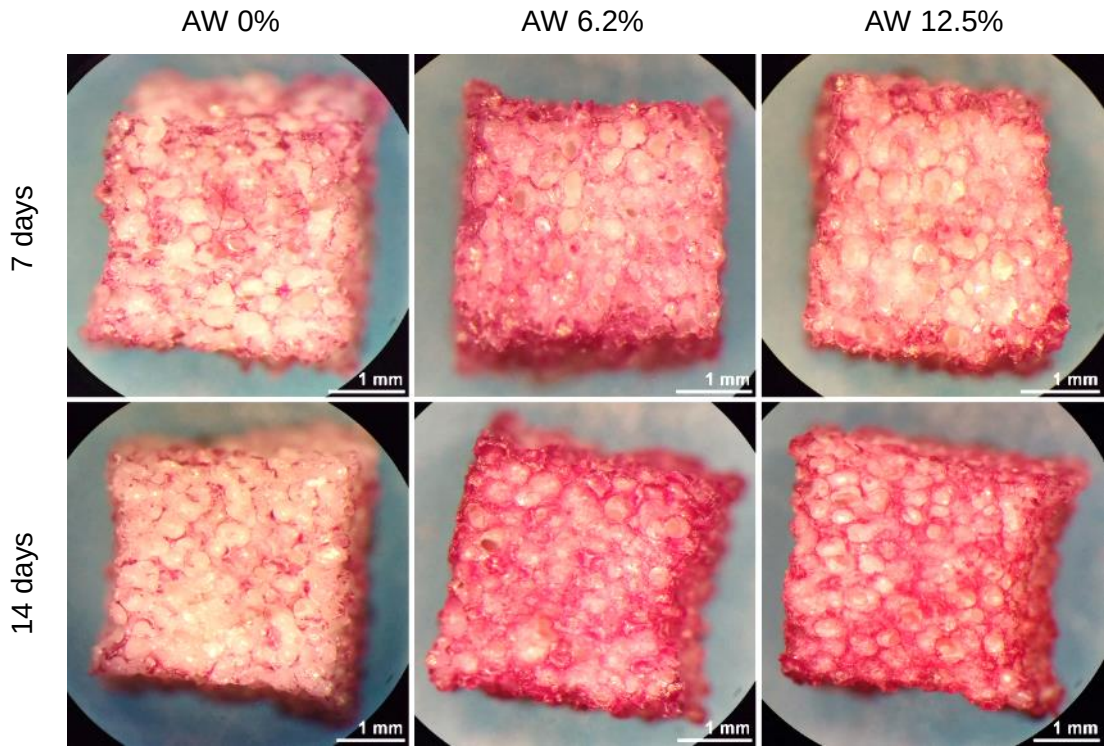

Figure 5.21: Stereomicroscopic images of ALP staining of AW 0%, AW 6.2% and AW 12.5% scaffolds, seeded with hBM-MSCs at passage 5 and cultured in osteogenic media for 7 and 14 days. ALP-positive areas appear as pink. Scale bars represent 1 mm.

The ALP staining of hBM-MSCs at 7 days of culture in osteogenic media showed stronger staining for composition AW 6.2%, followed by AW 12.5%; a less strong staining was observed for the no-strontium control AW 0%.
The difference between sample AW 6.2% and AW 12.5% was less evident at 14 days of culture, when both compositions gave very strong staining, thus indicating enhanced osteogenic differentiation of cells grown on these scaffolds. A lighter staining was found again for scaffold AW 0%, thus qualitatively confirming that an increase in ALP activity was induced when cells were cultured on strontium-containing porous scaffolds.

5.2.2.2.3 Effect of strontium content on DNA concentration, ALP activity and metabolic activity in hBM-MSCs

In order to confirm the qualitative results, quantitative measurements of DNA concentration, ALP activity and metabolic activity were carried out and are summarised in the graphs in Figure 5.22. Four samples per composition and per time-point were measured and averaged.

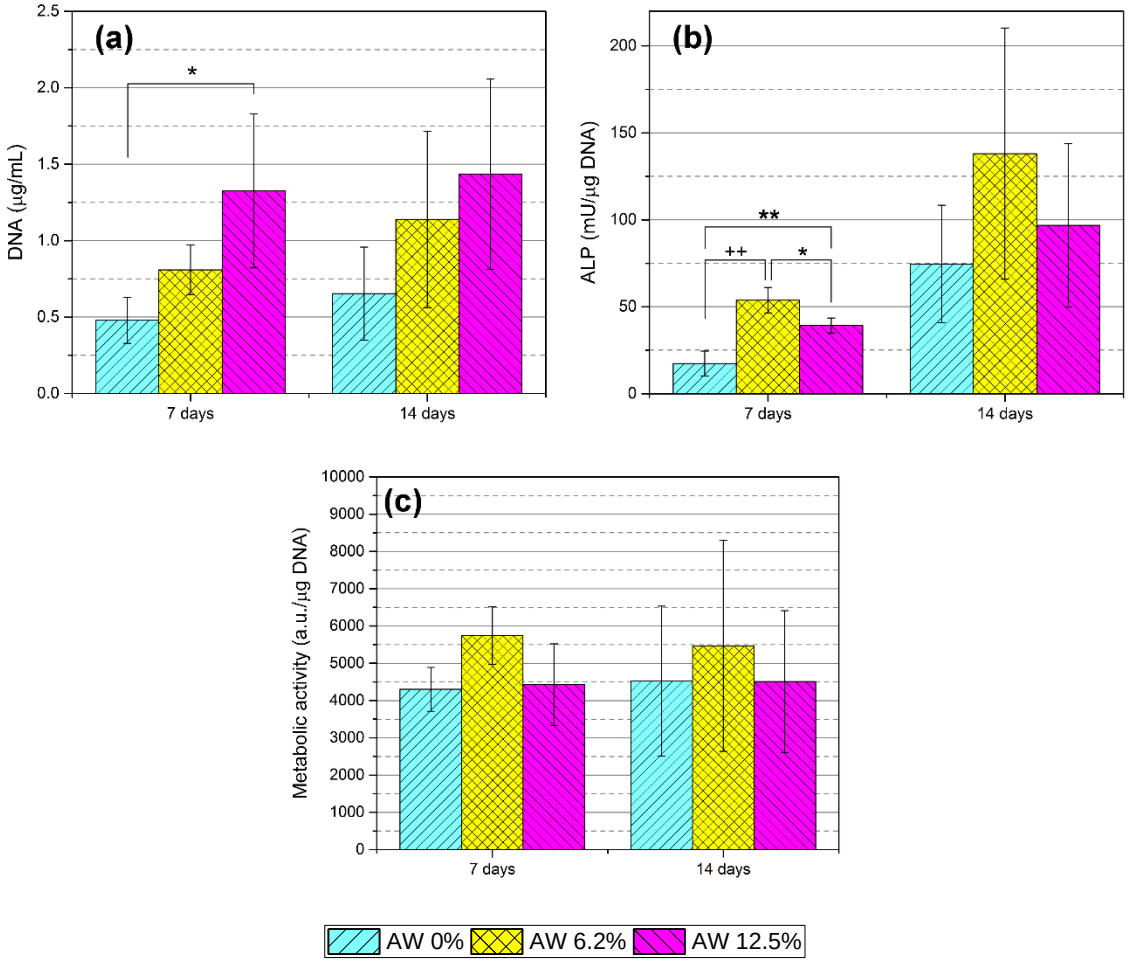

Figure 5.22: Quantification of total DNA concentration (a), ALP specific activity normalised to DNA content (b) and metabolic activity normalised to DNA content (c) for hBM-MSCs grown on AW 0%, AW 6.2% and AW 12.5% scaffolds. Cells were seeded at passage 5 and cultured in osteogenic media for 7 and 14 days. Error bars indicate the standard deviation of data (n=4); significant difference was represented as *p≤0.05, **p≤0.005, ++p≤0.0001.

The DNA quantification of hBM-MSCs seeded at passage 5 and cultured in osteogenic media confirmed the increase in cell number with time, from 7 days to 14 days of culture, for all the three compositions tested. At 7 days, the amount of DNA measured from scaffolds AW 0% was found to be significantly lower ($p \leq 0.05$) than that of scaffolds AW 12.5%.

ALP activity, normalised to DNA content, of samples AW 6.2% was found the highest at both time-points, thus agreeing with what observed with the qualitative staining in Figure 5.21. At 7 days, it differed significantly from both AW 0% ($p \leq 0.0001$) and AW 12.5% ($p \leq 0.05$); the ALP activity of samples AW 12.5% was also found significantly

higher ($p \leq 0.005$) than that of AW 0% at 7 days. Although significance was not found at 14 days due to the high variability of results, the same trend could be observed for the average values. An increase in ALP activity from day 7 to day 14 was observed for all the three compositions.

Trends similar to those of the ALP activity were also observed for the metabolic activity, normalised to DNA, of cells grown on the scaffolds, but no significant difference was found. Comparable levels of metabolic activity were observed between 7 and 14 days for all three compositions.

Overall, quantitative results suggested that the presence of strontium in the scaffolds enhanced hBM-MSCs proliferation and they seemed to point to scaffolds AW 6.2% as the composition inducing the strongest ALP activity, hence the best for enhancing stromal cell osteogenic differentiation in constructs designed for bone repair. However, due to the high variability in results, further tests are needed to confirm this.

5.2.2.2.4 Effect of strontium content on extracellular collagen deposition

In order to assess the deposition of extracellular matrix on the cultured scaffolds, collagen deposition was checked using Picroserius Red staining after 4 weeks of culture in osteogenic media. Three samples were tested for each composition (AW 0%, AW 6.2% and AW 12.5%) and unseeded scaffolds were used as the negative controls. Pictures of the stained samples are shown in Figure 5.23.

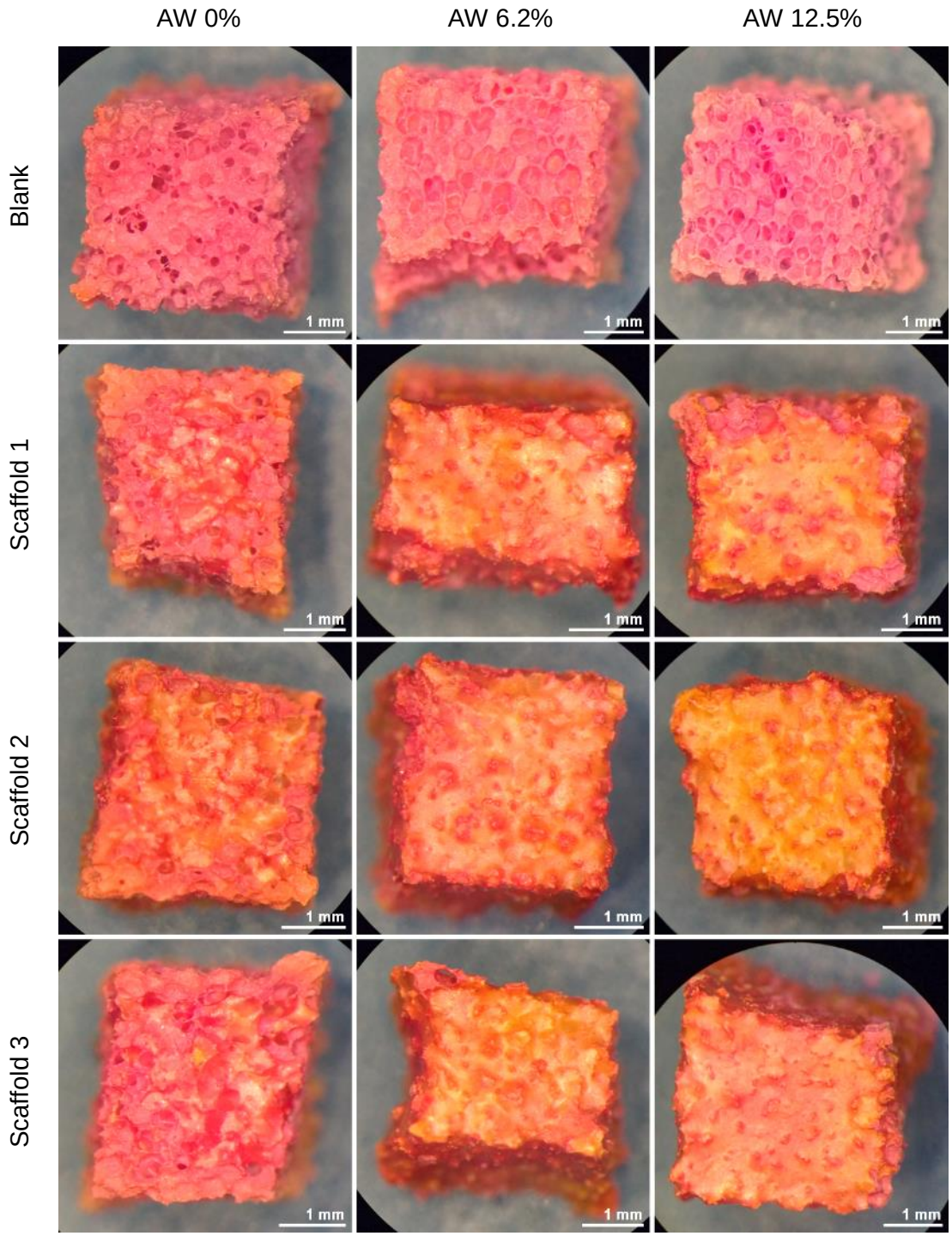

Figure 5.23: Picroserius red staining of extracellular collagen deposited by primary hBM-MSCs at passage 5 on AW 0%, AW 6.2% and AW 12.5% scaffolds, cultured for 4 weeks in osteogenic media. Three repeats per composition were compared to unseeded (blank) scaffolds. Bare scaffolds stained as pink, collagen stained as orange. Scale bars represent 1 mm.

During staining, the glass-ceramic scaffolds stained as pink, while the deposited collagen stained as orange.

Samples AW 0% had the weakest stain for collagen, confirming the qualitative and quantitative results reported in the previous Sections, which showed the two strontium-containing compositions better enhanced proliferation and differentiation of hBM-MSCs.
For both compositions AW 6.2% and AW 12.5%, most of their surface appeared covered in a thick layer of cells that stained orange, thus indicating a high deposition of extracellular matrix. No clear difference could be seen between these two compositions, suggesting that both induced similar proliferation in the long term, along with the formation of new bone tissue.

5.3 Discussion

As described in Chapter 1, strontium is a chemical element well-known for its ability to enhance bone formation and regeneration, capable of stimulating osteogenic differentiation and bone deposition and simultaneously inhibiting bone resorption (15, 150). The drug strontium ranelate, an organic salt containing strontium, is currently used in clinic, administered orally, to treat severe osteoporosis (163, 165). Because vascular and cardiac side effects have been recently associated with its use (173, 176), a local delivery of small amounts of strontium would be ideal for a targeted treatment of certain bone diseases such as osteoporosis and osteoarthritis or repair of bone loss.
Numerous alternative materials that contain strontium, in particular bioactive glasses and glass-ceramics, have been described in the literature for the use in bone substitutes (151, 177, 182, 185). However, the optimal amount of strontium necessary for improving bone regeneration is still not known and highly depends on the initial composition and final form of the material. This chapter explored the effects of strontium-containing apatite-wollastonite glass-ceramic (AWGC) porous scaffolds on the proliferation and differentiation of bone-forming cells. Preliminary studies were carried out by Vickers on the substitution of strontium in AWGC scaffolds obtained from compressed powders (186). Here porous samples were first tested using the osteosarcoma cell line G292 and then with human bone marrow-derived MSCs (hBM-MSCs), in order to identify the composition that would represent the best option for bone implants.

5.3.1 Effect of strontium content on G292 cells

Osteosarcoma-derived cell lines are often used as models for osteoblasts, due to their reproducibility and ability to proliferate continuously without losing their characteristics.

Examples of bone-forming cell lines used in the literature include mouse-derived MC3T3-E1 (190), rat-derived ROS17/2.8 (183) or human-derived SaOS-2 (186, 378) or MG-63 (370).
For the work presented in this thesis, the human osteoblast-like G292 cell line was used. This is a well established line that has been used in the literature for preliminary testing of different materials for bone tissue engineering, from ceramics (379, 380), metals (381) and silk (382) to composites (383) and nanocomposites (384-386). It is widely available, responds consistently and is robust, as it is routinely used for cytotoxicity studies (385-387); it is also responsive to osteogenic stimuli, usually measured in terms of increase in ALP activity (381, 384, 385, 387). In addition, examples in the literature exist on the use of G292 cells for bioactive materials that contain strontium (369, 370, 388).

In the present thesis, as a preliminary step to all the subsequent tests, the need for scaffold preconditioning in serum-rich media was evaluated. Pre-treating scaffolds in media before seeding them is a step that has been described in the literature for polymeric (389), composite (390-392) and glass-ceramic (151, 186, 393-395) scaffolds. It has been shown, in fact, that pre-treating scaffolds prevents the initial burst of ionic release from causing an increase in pH that could induce cytotoxicity (390, 396), while, at the same time, does not affect dissolution and apatite formation kinetics (397). In the present work, porous scaffolds were preconditioned in 20 % FBS media overnight, before seeding; qualitative results informed that the pre-treatment enhanced the initial attachment of G292 cells. As these cells were used as a model for MSCs, the same preconditioning was also applied to scaffolds to be seeded with hBM-MSCs. Methods for performing this treatment vary across the literature, as some authors use serum-free culture media (151, 390, 392-394), while others described the use of 10 % FBS media (186, 395) or 20 % FBS media (389, 391); some authors treat their scaffolds for 2 or 3 h (389, 391), others for 24 h (390, 395) and others for 3 days (151, 392-394).
Culture conditions were also tested to verify whether basal (10 % FBS) or osteogenic media was best for culturing G292 cells, once seeded on the strontium AW scaffolds. Because G292 cells normally express ALP (398), its activity can always be detected in the presence of viable cells and only variations in its production can be assessed. In the present work, samples cultured in osteogenic media showed increased cell proliferation and, in particular, stronger ALP activity with no difference between material compositions. It is possible that the osteogenic media was masking the effects of strontium, hence, in order to avoid this, it was concluded that basal media would have been a better choice for testing G292 cells with the strontium AW

scaffolds. In addition, this was in line with the methods described in the literature, where strontium-containing materials, when tested with the same G292 cell line, are usually cultured in basal media containing either 10 % (369, 388) or 5 % FBS (370).

The effect of strontium content on the G292 cells was therefore tested in basal media for all the six compositions. Although differences were not significant, composition AW 37.4% appeared to support a lower rate of cell proliferation, while compositions AW 6.2% and AW 12.5% showed a mild increase in ALP activity, compared to the no-strontium control and the other strontium compositions. This corresponds well with the literature more generally, which has found that strontium doped glasses support G292 growth and can raise ALP activity. Pouria et al. used G292 cells to study strontium-doped gypsum and observed that low-strontium compositions induced significantly higher proliferation at 7 days and higher ALP activity at 3 days, compared to the no-strontium control (369). Sharifianjazi et al. showed that glasses containing different amounts of silver and a fixed 5 mol% of strontium oxide could sustain G292 cell proliferation and ALP activity, even when the content of silver oxide increased to 5 mol%, suggesting that Sr may also aid cell survival (388). Taherkhani and Moztarzadeh tested SiO_2-CaO-SrO-P_2O_5 sol-gel derived glasses with 0-100 mol% strontium substituted for calcium: they used glass-conditioned media (culture media in which the glass powder had been soaked for 4 h, then filtered out and the resulting media used for growing cells) and they found that all compositions were biocompatible with G292 cells (370).

Similar results were also reported in publications that made use of other osteoblast-like and osteosarcoma cell lines for the study of strontium-modified materials. Taherkhani and Moztarzadeh tested the same sol-gel glasses described above for ALP activity with MG-63 cells and found that it increased for up to 25 mol% Sr substitution (corresponding to 9 mol% SrO in the glass), while it then decreased for higher strontium amounts (370). Qiu et al. tested porous strontium-calcium-polyphosphate scaffolds with rat osteosarcoma cells ROS17/2.8 and they observed an increase in cell viability for compositions up to 10 mol% strontium substitution, while ALP activity and proliferation at 7 days were the highest for the composition with 1 % strontium substitution (183). The MG-63 human osteosarcoma cell line was also utilised by Thakur et al. to assess the cytotoxicity of strontium-substituted sol-gel glasses, showing that low concentrations of strontium improved the viability of cells exposed to high amounts of glass powder (399). Bellucci et al. used mouse pre-osteoblast cells MC3T3-E1 to show that ALP activity could be enhanced by adding strontium to bioactive glass-TCP composites, although they also found that proliferation and collagen production were similar for all the scaffolds tested (276).

More recently, the same group used an osteocyte-like cell line, MLO-Y4, to test strontium and magnesium-modified glasses, proving the biocompatibility of the materials and showing enhanced proliferation and metabolic activity in comparison with the original glass and Bioglass 45S5 (275). Human osteosarcoma cells SaOS-2 were chosen by O'Donnell et al. (177), Kargozar et al. (368) and Gentleman et al. (151). O'Donnell et al. observed higher viability and spreading of cells when cultured in 10 mol%-substituted glass conditioned media (177). Kargozar et al. substituted 6 mol% of strontium oxide and 0.5 mol% of cobalt oxide for calcium oxide in a multicomponent glass and observed that culture in glass-conditioned media increased the expression of osteogenesis-related genes, with the higher expression found for Co and Co-Sr containing samples (368). These studies have generally found that a relatively low substitution of Sr into the materials prompted the optimum response from the cells. However, only Gentleman et al. found that high-strontium compositions of solid discs (50 and 100 mol% substitution for CaO in their SiO_2-P_2O_5-Na_2O-CaO bioactive glass) gave the best proliferation and ALP activity compared to the no-strontium control samples (151). These were close, in terms of mol% of contained strontium oxide, to compositions AW 12.5% and AW 24.9% described in the present thesis, respectively. It is important to note that the composition of a glass, in particular its ratio between network formers and modifiers described by the network connectivity (discussed in Chapter 3), can strongly influence its solubility, therefore the ionic concentrations encountered by cells cultured either in direct contact with the glass or in its conditioned media. Consequently, comparison between different glasses might not be straight-forward, even if their strontium oxide content is the same.

Since osteoblasts are not the only cell type that can be affected by strontium and strontium-containing glasses and glass-ceramics, some authors explored its effects on cell lines of different cell types. For example, Farag et al. verified that the proliferation of primate kidney-derived Vero fibroblast cells was not affected by a gamma irradiation treatment of a strontium-containing glass (400). More interestingly, as strontium is known for also inhibiting osteoclast activity (15), the rat-derived macrophage cell line RAW264.7 has been utilised as a model for osteoclasts: Gentleman et al. observed a correlation between strontium content in the glass and reduced osteoclast activity (151), while Weng et al. studied copper and strontium co-doped glasses and observed that only strontium-containing samples inhibited osteoclast activity (401). Although this aspect was not investigated in the present work, it is certainly of interest for future work.

5.3.2 Effect of strontium content on human bone marrow-derived mesenchymal stromal cells

It is important to consider that immortalised cells can represent normally functioning cells only in preliminary studies, where mainly cytotoxicity and trends in proliferation are investigated. For example, Maleki-Ghaleh et al. worked with both G292 cells (the same used in part of this work and discussed above) and rat bone marrow MSCs while studying a ceramic coating for titanium alloy samples; they used G292 cells for assessing the biocompatibility of the coating, but primary MSCs for studying the morphology and distribution of cells grown on the samples (371). As shown by Pautke et al. when comparing three cell lines with normal human osteoblasts, each cell line exhibited a different immunocytochemical profile, all of which differed significantly from osteoblasts and lacked both contact inhibition and dependence of morphology on cell density (402). Clover and Gowen compared human osteosarcoma cells MG-63 and HOS TE85 with cells harvested from human trabecular bone and concluded that these cell lines were not suitable for modelling proliferation and ALP activity of osteoblasts (403). Lauvrak et al. compared 22 cell lines as osteosarcoma models and found that G292 cells presented medium-high colony forming ability and had low migratory potential and proliferation capacity when compared to the other cell lines tested (404); however, comparison with normal osteoblasts was not presented in this publication.

In the literature, different sources of mesenchymal stromal cells (MSCs) are described: animal-derived cells (usually mouse or rat), or human-derived cells harvested from different possible tissues, from bone marrow or adipose tissue to the umbilical cord. In the study presented in this thesis, human bone marrow-derived MSCs (hBM-MSCs) were used that were obtained from bone marrow-derived mononuclear cells; hBM-MSCs were isolated following the standard procedure of sub-culturing only cells that adhered to tissue culture plastic, expanded to at least passage 3 to ensure that the majority of cells consisted of hBM-MSCs (375-377).
Initial tests were carried out to verify whether osteogenic media was necessary to induce osteogenic differentiation or if basal media could have been enough in the presence of strontium. No ALP staining was found after two weeks in basal media, while clear staining could be observed on samples cultured in osteogenic media. This corresponds with what observed by Schumacher et al., who tested strontium-doped calcium phosphate cements and did not find any osteogenic response when hBM-MSCs were cultured in basal media, while ALP activity and expression of bone sialoprotein II (a late marker of osteogenic differentiation) increased for all strontium-containing compositions when cultured in osteogenic media, with best results found for

the composition containing 8.5 wt% SrO (405). Similarly, Yang et al. compared the osteogenic differentiation of MSCs isolated from human umbilical cord in basal media, osteogenic media and osteogenic media containing 2 mM Sr^{2+} and found very low ALP activity in the basal group, while the presence of strontium further enhanced the expression of ALP, collagen I, osteopontin and the formation of mineralised nodules, compared to the osteogenic media-only group (406). It is also in partial agreement with the findings of Birgani et al.: they tested hBM-MSCs from two donors on tissue culture plastic and modified calcium phosphate coatings in both basal and osteogenic media and found that strontium enhanced the ALP activity and bone sialoprotein expression in osteogenic media; however, the two donors presented opposite responses in basal and osteogenic media when cultured on the strontium-containing coatings (407). Santocildes-Romero et al. measured the metabolic activity of rat bone marrow MSCs cultured in the presence of strontium-substituted 45S5 Bioglass in basal media, but compared the expression of osteogenic genes in basal and osteogenic media; they found that cells cultured in indirect contact with the strontium glass powder showed increased metabolic activity, compared to the no-strontium glass, and the up-regulation of ALP, bone morphogenetic protein 2 (Bmp2) and Runt-related transcription factor 2 (Runx2) was stronger when cells were cultured in osteogenic media (156). Only Hesaraki et al. (181) and Lin et al. (408) carried out their cell culture tests exclusively in basal media. Findings from Hesaraki et al. were in line with the general literature and with the results reported here, as rat foetal calvaria osteoblastic cells grown on a sol-gel silicophosphate glass containing about 8 wt% SrO induced higher proliferation and increased ALP activity at 5 days, compared to the no-strontium composition and the control (181). Lin et al. studied the effects of strontium-calcium silicate scaffolds (10 mol% substitution) on MSCs harvested from osteoporotic rats and also observed enhanced viability, ALP activity and gene expression when compared to the no-strontium samples (408).

According to the conclusion that osteogenic media was required for observing osteogenic differentiation in the samples presented in this thesis, scaffold compositions AW 0%, AW 6.2% and AW 12.5% were compared for proliferation, ALP activity and extracellular collagen deposition. The two strontium-containing compositions induced higher proliferation, ALP activity and collagen deposition, compared to the no-strontium control, with AW 6.2% giving the highest ALP activity. The fact that low-strontium compositions of bioactive materials appeared to give the best osteogenic response was already observed in the preliminary study with G292 cells and has been discussed previously. Here results were therefore confirmed by the testing of hBM-MSCs, which represent a more accurate model for the *in vivo*

behaviour of the material. These results are also supported by numerous examples in the literature. Isaac et al. compared strontium-modified SiO_2-CaO sol-gel glasses with their parent glass using mouse calvaria osteoblastic cells and they found that the glass containing 5 wt% SrO showed higher ALP activity at day 6 of culture; at day 12, the expression of genes involved in osteoblast differentiation, as well as the production of osteocalcin, was significantly higher for samples SrO 5 wt% than for SrO 1 wt% and the control (180). Montesi et al. tested hydroxyapatite bone cements containing 2 or 5 mol% SrO: mouse MSCs showed higher expression of ALP and Runx2 when cultured on the 2 % SrO cement; in addition, the cell line MC3T3-E1 was used as a model for osteoblasts and presented increased viability with increasing strontium, while osteoclast gene expression decreased with time in RAW264.7 cells in the presence of the strontium samples, compared to the no-strontium control (409). Strobel et al., when culturing hBM-MSCs in the presence of strontium-containing bioactive glass nanoparticles, did not observe any difference in proliferation, but found a significant increase in the expression of osteocalcin, collagen type 1, VEGF (vascular endothelial growth factor) and Runx2 compared to the no-strontium nanoparticles (217). Sila-Asna added different amounts of strontium ranelate in osteogenic media, from 0.2107 to 210.7 µg/mL, and observed the effects on hBM-MSCs: no effect of strontium was observed on proliferation, but the ALP activity was significantly higher in the strontium groups, compared to the media as such; early detection of osteogenesis-related genes was found with Reverse transcriptase-Polymerase chain reaction (RT-PCR) in the strontium-treated samples, although bone sialoprotein inhibition was observed for the highest strontium concentration; therefore the culture media containing 21.07 µg/mL strontium ranelate appeared to be the most promising (410). Weng et al., with their Cu- and Sr-doped bioactive glass fibres, found that the conditioned media from strontium-containing fibres enhanced the proliferation, ALP activity and mineralisation of adipose-derived stem cells (ADSCs) compared to the no-strontium compositions (401).

Regarding the specific composition of scaffolds studied in the present thesis, tests of hBM-MSCs on AW (with no strontium) porous scaffolds have been described by Dyson et al., who observed increased osteogenic gene expression in cells cultured on AW scaffolds, compared to culture plastic, in both basal and osteogenic media, along with higher ALP activity compared to cells cultured on a commercial calcium phosphate control (120). Serna tested human ADSCs on foam replicated AW 0% scaffolds and confirmed that the samples could support cell attachment and proliferation (121). Vickers studied the effect of strontium addition to AW microporous samples with hBM-MSCs derived from three different donors and observed an increase in ALP activity for composition AW 6.2% compared to the other compositions

(186). Therefore, the finding that the porous AW scaffolds with low strontium content provide the optimum osteogenic response are in keeping with work done previously on this material.

In general, even though some variability in the conclusions can be observed in the literature, the majority of publications support the findings of the present work that a small amount of strontium added to bioactive glass and glass-ceramic materials can promote the osteogenic differentiation of stromal cells. As mentioned previously, differences in the observations drawn when using strontium to treat mesenchymal cells are highly dependent on the form and composition of the material tested. Another key point in the research around the use of strontium in bone regeneration is the fact that the mechanisms through which this ion acts *in vivo* are still not fully understood, despite the widespread use of strontium ranelate as an anti-osteoporosis drug and the number of publications on its use and delivery (15, 16, 161, 162, 164, 167). A recent article by Xie et al. showed how strontium could promote cell function in osteoblasts only in the presence of a calcium-rich environment (411). This is consistent with the findings of the present work and many published articles reported above, where strontium oxide is substituted for calcium oxide and only low-strontium (corresponding to high-calcium) compositions enhanced osteogenic differentiation in MSCs. This hypothesis would also explain the results of Wornham et al. that Sr salts inhibit mineralisation in *in vitro* osteoblast cultures (412) and the results of Aimaiti et al. that high doses of strontium induce ADSCs apoptosis in *in vitro* cultures (413), along with the results of Li et al. that new bone formation is improved *in vivo* when Sr and Ca are co-administered (414). Arepalli et al. found that substituting strontium oxide for silica instead of calcium oxide, thus preserving the quantity of calcium while reducing the network connectivity of the material, significantly improved the biological properties of their bioactive glass when tested on human osteosarcoma U2-OS cells (415). Wu et al. also substituted strontium oxide for silica in their mesoporous scaffolds and observed a significant increase in ALP activity and osteogenesis-related gene expression with increasing strontium, although their highest composition contained only 10 mol% SrO (191). Therefore, further research is required to understand the therapeutic mechanisms of strontium on bone and its potential interaction with calcium.

In addition, other factors can play a relevant role in cell response when new materials and constructs, such as the glass-ceramic scaffolds described in this work, are tested. For example, Dalby et al. showed how the nanotopography of a substrate can direct the differentiation of hBM-MSCs without the need of osteogenic supplements (416, 417). This was also found by Hu et al., who observed improved osteogenic

differentiation of bone marrow MSCs on nanostructured coatings, further enhanced by the addition of strontium that also inhibited osteoclastogenesis (418). Another important aspect is then represented by the elastic modulus of the material used for producing the scaffolds, as the Young's modulus of the substrate can dictate the phenotype to which MSCs commit for their differentiation, as shown by Engler et al. (419, 420).

Finally, numerous considerations are required when working with MSCs, as reviewed by Dawson et al. (421), and these should all be taken into account when designing experiments or comparing results with the literature. One of them is the level of expansion of the initial cell population, which is measured in terms of its passage number. In the present work, hBM-MSCs were tested at passages 4 and 5; Bonab et al. observed that the differentiation potential of hBM-MSCs dropped from passage 6 (422). Other aspects that need considering include cell selection and characterisation, choice of source for the primary population, concentration of MSCs in the initial sample and their expansion, how their differentiation is controlled and the choice of the substrate for a tissue engineered construct (421, 423). All these additional aspects will have to be considered in future work, including testing cells obtained from different donors, so that a deeper understanding of the effects of strontium AW scaffolds on bone cells can be achieved.

Chapter 6
General discussion

6.1 Rationale of the project

The repair of bone defects, in particular large bone defects and especially defects in load bearing bones, still represents a clinical challenge, with bone currently being the second most transplanted tissue after blood (6, 7). Autografts are the current gold standard as they allow for bone regeneration without causing any immune response. However, only a limited volume can be available for each patient, they cause donor site morbidity and prolong the duration of surgery, which increases the risk of infections (47-49). The use of synthetic alternatives would be the ideal solution, but it is strictly necessary that they comply with numerous requirements to be as effective as the autologous grafts. These include supporting and stimulating new bone formation, presenting mechanical properties comparable to those of the host tissue, being cost-effective to produce and being easy to use in the operating theatre (9, 34, 58).
Bone infections subsequent to trauma or surgical intervention represent another important clinical challenge to the life of patients at high risk and presents very high costs of treatment: it is estimated that 1-20 % of primary joint replacements (128, 129, 349-353) and up to 30 % of open traumatic fractures result in infections (131), with associated costs up to 4 times higher than those of the initial procedure (132).
The apatite wollastonite glass-ceramic (AWGC) material, first developed by Kokubo and co-workers (85), presents superior mechanical properties and excellent apatite-forming and bone-bonding ability compared to other bioactive glasses and glass-ceramics (12, 101, 102). Its commercial form, Cerabone®, was used as granules and porous and solid spacers to successfully treat more than 60,000 patients in Japan between 1990 and 2000 (115).
The chemical element strontium is known for its dual effect on bone cells; it can in fact stimulate bone deposition and, at the same time, decrease bone resorption (14, 15, 150, 151). Strontium ranelate was approved in Europe in 2004 as a treatment for severe osteoporosis, after numerous studies on its efficacy (162-167). However, concerns were raised from 2012 on its systemic cardiovascular side effects (169-171); as a result, stricter recommendations for its use are now in place, set by the European Medicines Agency (172-175). At the same time, studies are still ongoing to verify whether this element could present antimicrobial features, since a synergistic effect

has been observed in combination with fluoride in glass ionomer cements (17, 195) or when added as doping agent in bioactive glasses (18, 197, 198). Therefore, a local delivery of smaller doses of strontium would be preferable to stimulate bone regeneration and, potentially, prevent bone infections, while avoiding undesired side effects.

In the work presented in this thesis, the AWGC material was modified with different amounts of strontium; preliminary work by Vickers on the substitution of strontium in AWGC (186) was combined with Serna's investigations on the production of AWGC porous scaffolds following the foam replication method (121). Here, the effects of strontium substitutions on the physicochemical, antibacterial and biological properties of porous foam-replicated scaffolds were investigated.

6.2 Effect of strontium on the properties of the AW material

In order to investigate the effects of strontium substitution for calcium in AWGC, six compositions were designed with increasing strontium content, from AW 0% (the original AWGC described by Kokubo (85), which represents the no-strontium control) to AW 37.4%, which corresponds to 75 mol% of calcium oxide being substituted with strontium oxide. The changes in the parent glasses were studied, before the thermal treatment for the controlled crystallisation and sintering was applied.
The substitution of up to 75 mol% strontium oxide for calcium oxide (composition AW 37.4%) was proven feasible and the composition of the glass powders was confirmed with EDS analysis. Along with Vicker's results, who showed substitution of up to 50 mol% in the same AW system (186), similar modifications have been widely described in the literature for different systems of bioactive glasses. Strontium addition to Bioglass 45S5 has been described for up to 100 % of calcium substitution with strontium (177, 178); calcium oxide in sol-gel glasses was substituted for up to 5 wt% (215) and up to 9 mol% in the borate-based glass 13-93B2 (214). Successful substitutions in glass-ceramics have been described for calcium silicates (182), calcium phosphates (183) and hydroxyapatite (184, 185).

The thermal properties of the six systems produced in this thesis were investigated for glass powders <45 µm. It was found that the glass transition temperature and the formation of the first crystal phase (apatite) moved towards lower temperatures with increasing strontium, while the formation of the second crystal phase (calcium silicate) highly depended on the strontium content, moving to higher temperatures with the increase in strontium. A similar effect on the glass transition temperature has been

reported in the literature for other bioactive glass compositions upon addition of strontium (177, 214, 230), as well as in the presence of other modifying ions such as magnesium (66, 231) or zinc (232). O'Donnell developed a mathematical model (Equation 6.1), based on iterative least-square fitting of experimental data that could predict the glass transition temperature of some bioactive glasses starting from their molar composition (424):

$$T_g\ (°C) = A + B[SiO_2] + C[Na_2O] + D[CaO] + E[P_2O_5] + F[SrO] + G[MgO] + H[K_2O] + I[B_2O_3] + J[CaF_2]$$

Equation 6.1: Mathematical model proposed by O'Donnell for predicting the glass transition temperature of a bioactive glass from the molar concentration of its constituents (424).

However, the range of compositions included in O'Donnell's study did not cover the apatite-wollastonite parent glass. In fact, all the glasses used for the study were divided into two sets based on their composition, for which different parameters were calculated, but these did not include glasses with lower SiO_2, higher CaO or SrO and no Na_2O, as it would be the case for the glasses studied in this thesis. In addition, Hill and Brauer showed how this model failed in taking into consideration structural effects of compositional changes such as phase separation, local structural effects and the role of intermediate oxides within the glass network, along with the fact that the model is not applicable to glasses outside the considered compositions (425).

The formation of the crystal phases in AW 0%, at 887 °C for apatite and 944 °C for wollastonite, was close to what reported by Kokubo and co-workers when they first described the material: 870 °C for apatite and 900 °C for wollastonite (85, 104). The temperature for the nucleation and growth of the two crystal phases in the strontium-containing compositions varied with the amount of strontium, with trends that were observed also by Vickers when he tested compositions up to AW 24.9% (186). One possible reason for these variations is the expansion of the glass network caused by the presence of the larger ion. This was confirmed by the XRD measurements taken from the six parent glasses, which showed the amorphous hump characteristic of silicate-based glasses moving towards lower angles with the increase in strontium. This is an effect commonly observed in the literature for various glass compositions when modified with strontium (63, 236, 237) and further confirmed by Hollings (personal communication) for the six glasses under study here, through neutron diffraction and Raman spectroscopy analyses. In addition, it was shown that different

strontium AW compositions formed different crystal phases, each of which likely presented different activation energies for initiating their phase transformation. In fact, XRD analysis of ground porous scaffolds for the six glass-ceramic compositions revealed that early incorporation of strontium occurred in the apatite phase from composition AW 6.2%, while no strontium was detected in the silicate phase until composition AW 24.9%; this, in turn, was found to contain magnesium in compositions AW 12.5% and above. The earlier glass transition in strontium samples could have facilitated the migration of divalent cations towards the nucleation sites of apatite, thus allowing for an earlier formation of this phase; at the same time, the facilitated formation of apatite could have consumed most of the available calcium and strontium ions, thus delaying the formation of the silicate phase. A more in-depth study of the crystal phases formed, using for example a Rietveld refinement approach for the XRD patterns, would inform on the weight ratios of the crystal phases present in the final samples, thus confirming whether more apatite formed in higher strontium samples. Hill et al. also suggested that the substitution of strontium for calcium in fluorapatite glasses caused the apatite phase to turn from a bulk to a surface nucleation mechanism (235); however, this effect was not detected in the present study and further investigations would be required to confirm it in the case of strontium AW glasses. In fact, the amount and ratio of crystal phases, their composition and morphology, their distribution within the material and their formation temperatures can all influence the degree of sintering, mechanical properties, reactivity and bioactivity of 3D porous structures obtained upon the application of a thermal treatment. These factors all play a major role in the outcomes obtained from biological and microbiological tests of the final samples, as they can affect the substrate and the chemical environment encountered by cells and bacteria.

The presence of strontium caused the density of the parent glasses and of the glass-ceramic porous scaffolds to increase, as expected from the substitution of a heavier ion for a lighter ion. Similar trends were observed before and after the thermal treatment, with densities linearly increasing with the amount of strontium in both cases. Values presented in Chapter 2 and Chapter 3 for the glasses and the glass-ceramics, respectively, are here compared in Table 6.1.

Table 6.1: Comparison between the density measurements of the strontium glasses before the thermal treatment (full data presented and discussed in Chapter 2) and of the glass-ceramic samples, after the treatment (full data reported in Chapter 3).

	Density glass (g/cm^3)	Density glass-ceramic (g/cm^3)
AW 0%	2.9372	3.00157
AW 6.2%	3.0915	3.10460
AW 12.5%	3.1925	3.23409
AW 18.7%	3.2849	3.29850
AW 24.9%	3.3538	3.32916
AW 37.4%	3.5796	3.47934

In general, similar values were obtained before and after the thermal treatment, with densities after the treatment being slightly higher than before the treatment for compositions AW 0% to AW 18.7%, while they were slightly lower for compositions AW 24.9% and AW 37.4%. This similarity could indicate that the atomic rearrangement due to heating was balanced by the formation of the crystal phases, which either had similar densities to the starting glass or balanced each other in the whole final glass-ceramic sample. The second case was confirmed by the literature, where a density of 3.156 g/cm^3 was reported for apatite (103), thus higher than the average density of the AW 0% glass-ceramic sample, and 2.92 g/cm^3 was reported for wollastonite (283), so lower than the average and the starting glass. This effect of opposite contributions can be explained using Equation 6.2, which was adapted for the AW system from Shelby (60) and shows that the final density of a glass-ceramic derives from the weighted average of densities of the phases it contains:

$$\rho_{AW} = \rho_A V_A + \rho_W V_W + \rho_G V_G$$

Equation 6.2: Formula for the final density of the AW glass-ceramic, deriving from the contributions of apatite (A), wollastonite (W) and the remaining glass phase (G). Adapted from (60).

For compositions AW 24.9% and AW 37.4%, lower densities were obtained for the final glass-ceramics than for their parent glasses. This was likely due to the high amount of strontium substituting for calcium that induced an expansion not only in the glass network, but also in the atomic lattice of the formed crystal phases, in particular

apatite, which was the denser term in the equation for the other strontium AW compositions.

The increase in density was also observed when samples were pictured for radiopacity: a linear increase in the overall intensity of the sample image was measured from the radiographs of sliced and cubic scaffolds with the increase in strontium. This was an expected effect basing on what has been described in the literature (259, 345-347), where promising results have also been reported of porous scaffolds implanted in an animal model: strontium-containing samples resulted in more easily visible follow-up radiographs of the operated limb (348), thus showing that the use of strontium in glass-ceramic materials could facilitate the monitoring of the operated site over time.

6.3 Effect of strontium on the structure and architecture of porous AW scaffolds

All six of the strontium compositions under study were utilised in the production of 3D porous scaffolds following the foam replication method.

The same thermal treatment (1050 °C for 2 h, 10 °C/min) was applied to all samples and shrinkage of the cubic scaffolds was measured by comparing their volume before and after the treatment. It was observed that it linearly depended on the amount of strontium contained in the samples, with shrinkage decreasing with increasing strontium. From the SEM assessment of the topography of samples, it was deduced that different degrees of sintering were obtained for the different compositions. This was considered the main reason for the observed differences in volumetric shrinkage and it could be a consequence of the differences in thermal behaviour that were found for the six compositions: in fact, it has been reported in the literature that the earlier onset of a crystal phase can hinder further sintering of the glass particles, especially at temperatures below 700 °C (277, 278). As also shown in Table 6.2 where results from Chapter 2 are summarised, the sintering window, defined as the range of temperature between the glass transition temperature and the onset of the first crystallisation (237, 321), became wider from composition AW 0% to AW 12.5%, but then decreased for samples AW 18.7% to AW 37.4%.

Table 6.2: Width of the sintering window for the six strontium AW glasses, derived from the glass transition temperature T_g and the onset of the apatite formation T_{on1} obtained from the DSC measurements in Chapter 2. All data in °C.

	T_g	T_{on1}	Sint. window
AW 0%	754.8 ± 9.3	854.0 ± 3.8	99.2
AW 6.2%	748.9 ± 3.3	867.1 ± 4.2	118.2
AW 12.5%	743.7 ± 1.8	863.7± 3.7	120.0
AW 18.7%	747.5 ± 4.8	859.2 ± 0.9	111.7
AW 24.9%	741.3 ± 3.1	853.9 ± 5.8	112.6
AW 37.4%	744.7 ± 9.3	838.3 ± 2.7	93.6

As a consequence, composition-specific thermal treatments might be needed to achieve similar shrinkages across the six compositions of glasses, with a step at a specific temperature that could be selected using hot stage microscopy (HSM). In fact, this would allow for a more similar topography across compositions and, potentially, mechanical properties of the final scaffolds, thus eliminating one variability factor for the biological tests.

For all scaffold compositions, their porosity was found to be mostly open porosity, thus confirming the presence of interconnected pores that would allow for cell ingrowth. All compositions presented an average porosity around 55 vol%, which is comparable to values presented in the literature, for example by Baino and Vitale-Brovarone (303), Renghini et al. (308) and Cunningham et al. (301). All samples produced distributions with two main peaks, around 200 µm and between 310 and 380 µm. The second peak at larger pore sizes, from a qualitative assessment of the distributions, appeared to vary between compositions and moving from lower to larger values with the increase of strontium. It was assumed that these larger pores derived from structural defects such as incomplete struts, which were observed for all compositions through SEM and micro CT imaging. It was hypothesised that this increase of the larger pore sizes with strontium could be a consequence of the different degrees of shrinkage obtained for the different compositions described above, as the lower volume reduction for high-strontium samples would be more evident on larger pore diameters. However, despite these minor differences, the structural characteristics of all tested samples fell within the general requirements of at least 50 vol% open porosity and pore size larger than 100 µm, possibly 300 µm (30, 260). Strontium AW scaffolds were also found structurally comparable with many other foam-replicated bioactive scaffolds, as is summarised in Table 6.3. The same table includes examples of structural

characteristics of trabecular bone obtained from micro CT data; in general, bone presents higher porosity and larger pores than synthetic scaffolds produced via the foam replication method. These differences are intrinsic to this scaffold production method, which cannot replicate the structural anisotropy of bone tissue nor its response to mechanical stimuli. In addition, data on human bone usually derives from samples harvested from elderly subjects during surgery, therefore often presenting osteoporosis or osteoarthritis, which can alter the structure of bone (318).

Table 6.3: Comparison of average porosity, strut thickness (Tr.Th.) and pore size (Tr.Sp.) between the strontium scaffolds produced in this study, other bioactive glasses and bone, as measured by micro CT data analysis. Values are reported as average ± standard deviation, when available. N.D. indicates that the information was not provided in the referenced study.

Material	Foam/Site	Porosity (%)	Tr.Th. (μm)	Tr.Sp. (μm)	Ref.
AW 0%	PU 90 PPI	63.07 ± 3.50	96.29 ± 4.14	250.15 ± 11.77	Present work
	PU 90 PPI	41.4 ± 0.6	171 ± 2	118 ± 2	Serna (121)
AW 6.2%	PU 90 PPI	57.15 ± 2.13	123.02 ± 4.45	247.77 ± 12.92	Present work
AW 12.5%	PU 90 PPI	56.70 ± 3.82	103.45 ± 5.18	223.38 ± 28.44	Present work
AW 18.7%	PU 90 PPI	57.00 ± 4.56	138.09 ± 8.52	274.88 ± 26.55	Present work
AW 24.9%	PU 90 PPI	50.45 ± 3.05	130.10 ± 5.95	244.55 ± 13.97	Present work
AW 37.4%	PU 90 PPI	57.31 ± 2.30	126.08 ± 3.80	268.84 ± 5.15	Present work
CEL2	PU	54.0 ± 0.9	60.4 ± 2.4	183.6 ± 9.1	Renghini (308)
	PU	40.2	N.D.	N.D.	Renghini (309)
	PU 45 PPI	66.2	95	229	Baino (310)
	PU 30 PPI	75.8	96	433	Baino (310)
	PU 20 PPI	82.0	115	952	Baino (310)
SCNA	PU	56 ± 6	N.D.	240	Baino (303)
Bioglass	PU	63.1	N.D.	N.D.	Renghini (309)
	PU 45 PPI	93.00 ± 0.25	N.D.	670 ± 70	Boccardi (267)
	Spongia lamella	76 ± 2	N.D.	265 ± 20	Boccardi (267)
	Spongia agaricina	68.0 ± 0.2	N.D.	215 ± 2.7	Boccardi (267)

Table 6.3 (Continued).

Material	Foam/Site	Porosity (%)	Tr.Th. (μm)	Tr.Sp. (μm)	Ref.
TiO_2	PU 45 PPI	85.6 ± 0.6	33.8 ± 5.7	530.5 ± 30.9	Fostad (281)
HA	PU	67.8 ± 5.0	N.D.	N.D.	Oliveira (312)
	Spongia officinalis	65.6 ± 5.4	1132 ± 448	843 ± 316	Cunningham (301)
	Spongia zimocca	62.9 ± 2.2	508 ± 215	444 ± 269	Cunningham (301)
	Spongia agaricina	55.6 ± 3.1	257 ± 95	349 ± 82	Cunningham (301)
Borosilicate	PU 50 PPI	73.3 ± 2.8	N.D.	N.D.	Shen (311)
Sr borosilicate	PU 50 PPI	73.2 ± 3.5	N.D.	N.D.	Shen (311)
Trabecular	Iliac crest	84.4 ± 5.4	151 ± 27	747 ± 150	Hildebrand (313)
bone	2nd lumbar vertebra	91.7 ± 2.4	122 ± 19	792 ± 135	Hildebrand (313)
	Femoral head	73.9 ± 7.8	194 ± 33	638 ± 114	Hildebrand (313)
	Calcaneal core	88.0 ± 3.5	129 ± 18	679 ± 107	Hildebrand (313)
	Femoral head	69.71	192 ± 69	427 ± 193	Chen (314)
	Maxilla	85.41 ± 7.68	100 ± 20	630 ± 180	Kim (315)
	Mandible	72.72 ± 10.19	90 ± 20	420 ± 180	Kim (315)
	Proximal femur	72.129 ± 3.735	224 ± 31	746 ± 65	Hambli (316)

Scaffolds were mechanically tested for compression strength and biaxial flexural strength. No statistically significant differences ($p>0.05$) were found between compositions for their compressive strength, which was around 10 MPa for all samples. This value is within the range and near the upper limit of 2-12 MPa reported for trabecular bone (34, 35) and is also comparable to values reported in the literature for bioactive scaffolds (95, 214, 265). However, the elastic modulus was found to decrease with the increase in strontium, from about 300 MPa for composition AW 0% to 120 MPa for AW 37.4%. Although these values are all within the range of 50-500 MPa described in the literature for cancellous bone (32, 33), no other examples could be found on the dependence of the Young's modulus on the strontium content. As explained by Meixner and Cutler (327), while the elastic modulus of a material derives from the atomic bonds between its atoms, the compressive strength depends more on the overall architecture of the samples; since similar porosities were found for the samples tested, this could explain the similar compressive strengths measured.

The same samples were then tested for biaxial flexural strength, which is considered a more valid test for brittle materials, at least in their solid form (251). In this case, the strength of samples AW 12.5% was found significantly lower ($p<0.0005$) than that of scaffolds AW 0%, which were also significantly stronger than AW 37.4% ($p<0.005$). However, it must be noted that results derived from a single batch of samples and therefore inter-batch variability was not taken into account. The Weibull distributions showed a similar dispersion of data for the six compositions, with the modulus of the distribution ranging from 3.77 for samples AW 6.2% to 5.64 for scaffolds AW 12.5%. No comparison with trabecular bone is available in the literature in this case, but again results were comparable or superior to other glass-ceramic scaffolds described in published work (329-331).

Some authors compared test results for samples tested in both compression and flexure, which is represented in Figure 6.1 for the strontium AW scaffolds under study.

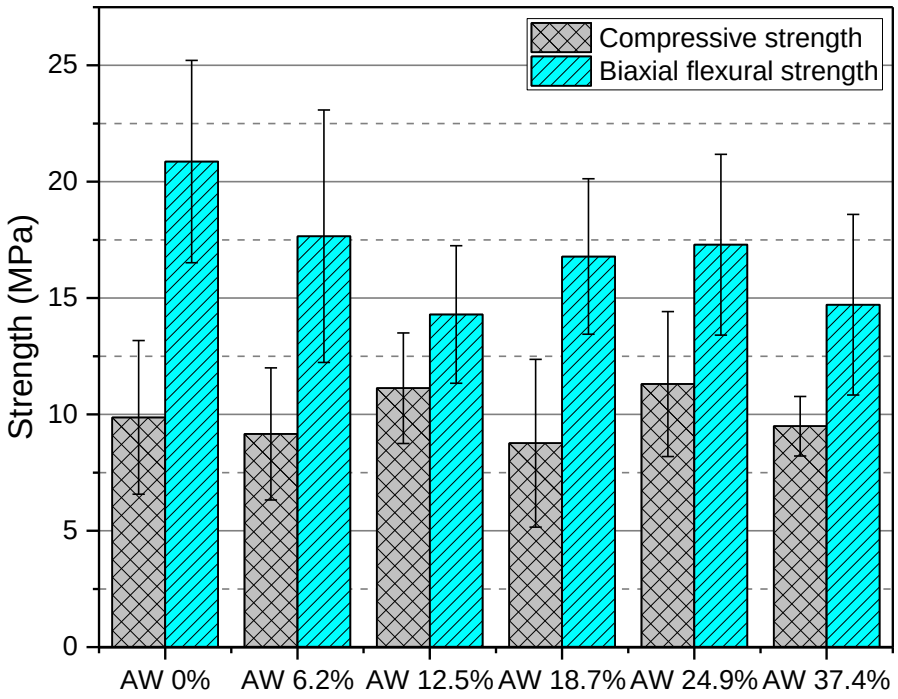

Figure 6.1: Comparison between compressive strength and biaxial flexural strength for the strontium AW porous scaffolds; data were reported individually in Chapter 3. Error bars indicate the standard deviation (n=8 for compressive strength, n=15 for biaxial flexural strength).

It can be observed that results from the two methods, presented and discussed individually in Chapter 3, generally followed the same trend, with flexural strength being always higher than the relative compressive strength for each composition. Chen et al. found that, for the same porosity, the 3-point bending strength was higher than the compressive strength and they concluded that the struts buckling led to the formation of shear stresses during the compression test, which caused an underestimation of both strength and elastic modulus (80). Magdeski also ascribed the high dispersion of results in the compression test to a damage accumulation process, observing a strong dependence on porosity when testing alumina samples with both methods (426). Sabree et al. produced porous wollastonite and pseudowollastonite scaffolds: they found that the 4-point bending strength of the bulk material was 6.2 MPa, while porous samples tested in compression showed a strength of 12 to 24 MPa, depending on porosity (427). Also Dong et al. observed a higher compressive strength (17.4 MPa) than 3-point bending strength (7.2 MPa) for porous hydroxyapatite scaffolds (322). However, Serna tested foam-replicated AW scaffolds prepared with different slurry compositions and sintering regimes and he found that the biaxial flexure test gave higher strength values (2 to 10 MPa) than the compression test for each scaffold type (2 to 4 MPa) (121).

In general, it could be concluded that strontium mainly influenced the elastic modulus of the samples tested, causing it to decrease with the increase of strontium in the scaffolds. Conversely, the general compressive strength did not show major variations between compositions and was likely dominated by the overall porosity deriving from the template, thus masking trends within the tested compositions. The biaxial flexural strength of scaffolds AW 12.5% and AW 37.4% was found significantly lower than that of scaffolds AW 0%, but this would need to be confirmed by testing other batches of samples.

The apatite-forming ability of the glass-ceramic samples under study was tested on the porous scaffolds, as well as solid discs as a simplified model for which ion release and elemental composition analysis of the deposited layer could be carried out. The bioactivity of samples was tested through soaking them in Simulated Body Fluid (SBF) solution, as described by Kokubo et al. (255) and in the ISO standard 23317-2014 (254). A decrease in apatite-forming ability was observed with the increase in strontium, with samples AW 0%, AW 6.2% and AW 12.5% forming apatite within 1 day, AW 18.7% within 7 days and AW 24.9% giving small deposits at the 14 day time-point, while AW 37.4% did not show any evidence of deposited crystals up to the latest time-point. These results were confirmed by monitoring the pH for both discs and scaffolds and by the ionic release and EDS elemental analysis from discs. For the pH measurements, it was observed that only samples that did not develop apatite, or that developed it at later time-points, increased the pH of the soaking solution, while it remained constant or it slightly decreased for samples with faster bioactivity. This demonstrated that sustained ionic dissolution continued only for less bioactive compositions. The ion release from discs also confirmed that only the higher strontium compositions, which formed apatite at later time-points or did not form it, presented a sustained ion release, with the concentration of calcium, silicon and magnesium increasing and with the concentration of phosphorus decreasing over time. The concentration of strontium in the soaking solution was also higher for increased strontium amounts in the soaked sample, but this was obviously due to the starting composition of the samples. The EDS elemental analysis showed a decrease in the percentage of detected strontium and silicon, along with an increase in phosphorus, for samples that formed an apatite layer within the tested time-points, with clear differences from the pre-soaking compositions already at the 3 day time-point. Scaffolds AW 18.7% showed a slower precipitation of apatite and this was reflected in their elemental analysis as well, with clear differences from the 7 day time-point and with a higher amount of detected strontium at the last time point. These measurements, along with the observation of the different morphology of the deposited

layer with smaller and thinner crystals, suggested that a different apatite might have been deposited on these samples. It is also possible that this layer evolved from the formation of a silica gel layer, as the SEM micrographs of the cracked surface suggested. However, these results will need confirming.

The reduction in bioactivity with the substitution of strontium has been reported in the literature (181, 191, 215, 216, 290, 339), although examples also exist of enhanced bioactivity with increasing strontium (230). It must be noted that different glass compositions can present different dissolution rates and reactivity, along with different bioactivity mechanisms, which would explain the differences in results reported in the literature. The network connectivity (NC) has been proposed as a parameter that can predict the bioactivity of a glass based on its atomic structure (62-64). For all the six strontium AW compositions under study, the NC was calculated as 1.98 (Hollings, personal communication); however, differences in their bioactivity were found that could be ascribed to limitations in the model, such as that it does not take into account which network modifiers are present in the glass nor the role of phosphate in the bioactivity mechanism (62, 66). In conclusion, the bioactivity of porous strontium AW scaffolds was found to decrease with the increase in strontium, with the layer formed on samples AW 18.7% potentially containing strontium and deriving from an initial silica gel layer. Further studies are therefore required to clarify the apatite-forming mechanisms for the six compositions under study and the nature of the deposited crystals.

6.4 Antimicrobial effect of strontium

The potential antimicrobial effect of strontium, as a free ion and when added to a bioactive glass, is still under discussion. On the one hand, observations were made that a synergistic antibacterial effect of strontium and fluoride was obtained when these two elements were combined in glass ionomer cements (17, 195), as well as in a bioactive glass for a composite cement (197), in silicate and borate bioactive glasses (18, 198) or in hydroxyapatite nanoparticles (199). On the other hand, it has been reported that no enhancement of the antibacterial properties was found in silver-containing glasses and ceramics when strontium was added, although cytotoxicity of the materials was reduced (200-202).

For this reason, antimicrobial investigations were divided in two parts in the present thesis. At first, the antibacterial effect of elemental strontium was tested using strontium salts in a zone of inhibition assay. Then, the effect of the six strontium AW glasses on bacteria was also tested using an adapted zone of inhibition assay and broth dilutions assays, basing on the methods described by Fernandes et al. (198).

Four bacterial species were tested: *Staphylococcus aureus*, *Staphylococcus epidermidis*, *Escherichia coli* and *Pseudomonas aeruginosa*, as representative of the most commonly detected species responsible for peri-prosthetic infections (133, 140, 141).

The investigation on the effect of elemental strontium was carried out using strontium nitrate and strontium chloride at 4 mM concentration in water, dispensed on paper discs for a zone of inhibition type of testing. All tests were run following the EUCAST indications of using a bacterial suspension of 10^8 colony forming units (CFU) per mL of media and incubating the plates for 18 h before assessing the zones of inhibition (356). No inhibition was found that could indicate an antibacterial effect from the salt solutions. The test was therefore repeated adding silver and zinc salt solutions at the same molar concentration, to compare the results with known antimicrobial elements. This was the first time that this test was carried out with strontium salts, therefore no means of comparison could be used to assess the results. It is possible that the concentration of 4 mM used for the salt solution was not strong enough to induce any growth inhibition. However, the concentration was chosen basing on literature concentrations of strontium chloride used for testing cell and bacterial cultures (18, 361); in addition, 4 mM was the highest concentration that could be obtained without observing the formation of precipitates, due to the fact that strontium is likely to react with sulphate, carbonate and phosphate ions in a solution (360).
The additional tests run using silver and zinc salts were carried out as a proof-of-concept, to validate the test against elements with known antibacterial properties. Only silver inhibited the growth of all four species tested, but no inhibition was observed from the zinc samples. While it is known that the microbial susceptibility to zinc is lower than that of silver (358, 359), these results suggested that, if definite antimicrobial properties will have to be imparted to strontium AW scaffolds in future work, silver would be the element of choice.

Further tests were carried out using the six strontium AW parent glasses, in powder form and in their <45 µm fraction. At first, small cylinders of agar containing a suspension of the glass powders were used in a zone of inhibition type of testing. No inhibition was observed, which could either indicate that the glass powders under study did not possess antibacterial properties, or that the agar was not the optimal medium for ensuring ionic diffusion from the glass particles to the inoculated surface of the culture plate. It was therefore decided to test the susceptibility of the chosen bacterial species when grown in direct contact with the glass powders in broth dilution tests. Initially, all powders were kept suspended in media for 24 h before being

inoculated with a known concentration of bacteria. Only the highest strontium composition AW 37.4% prevented bacterial proliferation with a final bacterial count that was about 1 log lower than the inoculum, but only against *P. aeruginosa*, indicating a possible mild antibacterial effect of strontium-containing AW glasses. The test was then repeated with only *P. aeruginosa* and maintaining the glass powders in suspension for a week, before inoculating the samples. In this case, composition AW 37.4% confirmed its bacteriostatic effect by producing a final CFU count lower than the initial inoculum; in addition, compositions AW 0% and AW 24.9% gave a lower count than the negative (no glass powder) control and the other compositions. While the effect of sample AW 24.9% could be predicted, as the second highest strontium composition dissolved for a longer time compared to the previous test, AW 0% results were not anticipated. A possible explanation could be the fact that different glass compositions might present different ion release profiles; these could influence the final concentration of ionic species and the final pH of the media used to culture the bacteria, which, in turn, affect the survival and proliferation of bacterial cells.
Therefore, further studies will be necessary in future work to better understand the antibacterial effects of these glasses and their relative glass-ceramic compositions, starting from an investigation on the ionic release in culture media.

6.5 Effect of strontium content in AW scaffolds on the proliferation and osteogenic differentiation of bone cells

Strontium can be sensed by bone cells through the calcium-sensing receptor (CaSR) and it is considered an uncoupling agent (14, 15). In osteoblast precursors, it stimulates proliferation and the production of osteoblastic markers, thus inducing bone deposition (153-156); in osteoclasts, it interferes with the actin network in their cytoplasm, it reduces differentiation and induces apoptosis (159, 160).
The drug strontium ranelate is used to treat severe osteoporosis and to prevent osteoporotic fractures (162-167). However, cardiovascular side effects have been recently associated with its use (168-176), therefore a local delivery of low doses of strontium would be preferable to locally induce bone regeneration. In the present thesis, the effect of the addition of strontium to AW glass-ceramic porous scaffolds was studied *in vitro* on bone-forming cells.

First, osteosarcoma-derived G292 cells were used to investigate proliferation and ALP activity when cultured on the six scaffold compositions in basal media (α-MEM containing 1 % penicillin-streptomycin, 2 mM L-glutamine and 10% serum). A high variability in the results was found, therefore no definite conclusion could be drawn.

However, results seemed to suggest that all compositions except AW 37.4% could support proliferation and that low-strontium compositions AW 6.2% and AW 12.5% could induce higher ALP activity, as observed in the literature for both G292 cells and other cell lines (183, 276, 369, 370, 388).

Scaffolds were then tested using primary human bone marrow-derived mesenchymal stromal cells (hBM-MSCs). No ALP activity was detected through staining when samples were cultured in basal media (α-MEM containing 1 % penicillin-streptomycin, 2 mM L-glutamine and 15% serum), while sample AW 6.2%, when cultured in osteogenic media, gave the strongest staining compared to compositions AW 0%, AW 18.7% and AW 37.4% (other compositions not tested). These results indicated that osteogenic media was necessary to induce osteogenic differentiation in the selected cell population and suggested that low strontium compositions could give the highest bone formation. Scaffolds AW 0%, AW 6.2% and AW 12.5% were therefore further tested in osteogenic media. Results confirmed that strontium-containing samples increased cell proliferation, as observed with the G292 cell line and the ALP staining tests, and also enhanced extracellular collagen deposition; in addition, results showed that cells cultured on AW 6.2% samples induced the highest ALP activity after 7 and 14 days of culture. Therefore, composition AW 6.2% appeared to be the most suitable for the fabrication of foam-replicated AW scaffolds modified with strontium. These results were comparable to most published work, where partial substitution of strontium oxide for calcium oxide in bioactive glasses or glass-ceramics is shown to induce the strongest osteogenic differentiation of MSCs towards an osteoblastic phenotype (180, 186, 409, 410). However, in the present work the role of topography induced by the different degrees of sintering observed in Chapter 3 was not taken into account; it would be preferable to optimise the thermal treatment for each composition and then repeat these tests. In addition, only one donor was considered in the present study; therefore, it would be preferable to confirm these results with cells harvested from other donors, so that the optimal composition could be selected for a bone substitute that could enhance bone regeneration.

In conclusion, sample compositions containing a low amount of strontium showed greater potential as scaffolds for bone repair than higher strontium compositions: they presented similar architecture, degree of sintering, topography, mechanical properties and apatite-forming ability to the original composition AW 0%, as well as improved radiopacity and promising sustained proliferation and osteogenic differentiation of hBM-MSCs. However, antimicrobial properties could only be observed in one of the four bacterial species tested, *P. aeruginosa*, and only for the highest strontium

composition AW 37.4%, thus suggesting that a high content of strontium would be required to impart antibacterial properties to the glass-ceramic scaffolds under study.

Chapter 7
Conclusions

The work presented in this thesis described the production and characterisation of strontium-doped apatite-wollastonite glass-ceramic (AWGC) porous scaffolds, intended as novel bone grafts for enhanced bone repair. Six compositions, containing from 0 to 37.4 mol% strontium oxide substituted for calcium oxide, were evaluated. Thermal behaviour, crystallisation, morphology, mechanical properties, apatite-forming ability, antimicrobial effect and osteogenic properties were taken into account. The aim of the present work was to investigate the effects of strontium substitution in the AWGC material when used for foam-replicated scaffolds. Results from this work would help identifying the composition that could ensure a good mechanical match and bonding ability to cancellous bone tissue, that could provide antimicrobial features for preventing post-operative infections and that could stimulate bone regeneration for improved tissue repair.

The findings of the present thesis can be summarised as follows:

- Six compositions of strontium-containing AWGC parent glasses could be successfully produced via the melt-quenching route. All compositions were amorphous and their density linearly increased with the molar amount of strontium. All glasses were ground and sieved <45 μm. The same bimodal particle size distribution was found for all six glass powders, with one peak around 250 nm indicating the presence of a significant fraction of small particles; the second peak was centred around 25 μm, with a hump at about 6 μm.
- Thermal analysis of < 45 μm glass powder fractions showed that all six compositions underwent two main exothermal events, corresponding to the nucleation and growth of two crystal phases. Characteristic temperatures depended on the strontium amount. Glass transition temperature and the temperature of the first exothermic peak linearly decreased with increasing strontium, with 10 °C and 30 °C difference between the no-strontium composition and the highest strontium composition, respectively. The temperature of the second exothermic peak linearly increased with increasing strontium content, with an 80 °C shift between the no-strontium sample and the highest strontium glass. The melting temperature followed a second order equation, with the composition containing 24.9 mol% strontium (50 % substitution) representing a possible eutectic composition.
- 3D porous scaffolds could be produced via foam replication method with all the six compositions tested. Shrinkage linearly decreased during sintering with increasing

content of strontium, being about 58 % for the no-strontium control composition and about 48 % for the 37.4 mol% strontium (75 mol% substitution) composition.

- After crystallisation and sintering, the density of the glass-ceramic material obtained from the six compositions of glass linearly increased with the amount of strontium.
- X-ray diffraction (XRD) analysis showed that strontium preferentially substituted in the apatite phase. Magnesium substitution was found for wollastonite in compositions containing 12.5 mol% strontium and above; pseudowollastonite was identified for the composition containing 18.7 mol% strontium (37.5 mol% substitution). A calcium-magnesium-strontium silicate phase was identified in compositions containing 24.9 mol% and 37.4 mol% strontium oxide, which correspond to 50 mol% and 75 mol% substitution, respectively.
- Scanning electron microscopy confirmed the formation of the porous network for all the six compositions investigated. The degree of sintering decreased with the increase in strontium, as the original glass particles, though rounded and fused, could still be identified in scaffolds containing 24.9 mol% and 37.4 mol% strontium oxide. Crystals presenting different morphologies could be observed in samples containing 12.5 mol% strontium oxide and above; large smooth crystals were identified as the calcium silicate phase, while small round crystals were identified as the apatite. Energy dispersive x-ray spectroscopy showed an even distribution of the crystal phases in the no-strontium control and the composition containing 6.2 mol% strontium oxide, while, for compositions containing 12.5 mol% of strontium and above, a magnesium-rich crystal phase could be detected, which was identified as magnesium-containing wollastonite, thus confirming the results of the XRD analysis.
- Micro computed tomography imaging and post-analysis showed that all six strontium compositions formed interconnected open pores. All compositions presented about 55 vol% porosity, with most pore sizes being between 100 and 400 µm. Pore sizes presented bimodal distributions for all six compositions, with the first peak being around 200 µm for all samples and the second peak moving from 310 µm to 380 µm with increasing strontium.
- The compressive strength of porous scaffolds was found around 10 MPa for all six compositions. However, their Young’s modulus decreased with increasing strontium content, going from about 300 MPa for the no-strontium controls to about 120 MPa for scaffolds containing AW 37.4 mol% strontium oxide.
- The biaxial flexural strength of samples varied between 14 MPa for the composition containing 12.5 mol% strontium oxide to 21 MPa for the no-strontium composition. Weibull analysis showed that the Weibull characteristic strength of samples was between 15 MPa for the composition containing 12.5 mol% strontium oxide and 23

MPa for the no-strontium composition. The Weibull modulus ranged from 3.7 for samples containing 6.2 mol% strontium to 5.6 for samples containing 12.5 mol% strontium, thus showing a quite high dispersion of the biaxial flexural strength values for all compositions.

- The apatite-forming ability was tested by soaking samples in simulated body fluid solution. Discs induced the fast formation of an apatite layer for the no-strontium control and for compositions containing 12.5 mol% and 18.7 mol% strontium oxide. Formation of apatite on the porous scaffolds could be observed only on the inner struts of samples and the presence of strontium induced a delay in apatite formation. Scaffolds containing no strontium, 6.2 mol% and 12.5 mol% strontium oxide induced the precipitation of apatite within 24 h of soaking; scaffolds containing 18.7 mol% strontium oxide showed apatite formation after 7 days of soaking, while small apatite crystals could be observed on scaffolds containing 24.9 mol% strontium when soaked for 14 days.
- The substitution of strontium oxide for calcium oxide caused a linear increase in radiopacity with increasing strontium.
- Testing of strontium-containing salts against *Staphylococcus aureus*, *Staphylococcus epidermidis*, *Escherichia coli* and *Pseudomonas aeruginosa* in a zone of inhibition test showed no antimicrobial action for the 4 mM strontium concentration chosen.
- 4 mM silver nitrate showed an antibacterial effect against *Staphylococcus aureus*, *Staphylococcus epidermidis*, *Escherichia coli* and *Pseudomonas aeruginosa* in the same zone of inhibition type of test. No inhibition was induced by a 4 mM zinc chloride solution.
- No inhibition of the growth of *Staphylococcus aureus*, *Staphylococcus epidermidis*, *Escherichia coli* and *Pseudomonas aeruginosa* could be observed when the strontium AW glass powders were mixed with technical agar to produce small discs that were used in a zone of inhibition assay.
- Strontium-containing <45 µm glass powders were tested in a broth dilution test against *Staphylococcus aureus*, *Staphylococcus epidermidis*, *Escherichia coli* and *Pseudomonas aeruginosa*. The glass containing 37.4 mol% strontium oxide induced a reduction in bacteria viable count of *Pseudomonas aeruginosa* when the powder was soaked for 24 h before inoculation. When soaked for 7 days before inoculation, compositions containing no strontium, 24.9 mol% and 37.4 mol% strontium oxide induced a reduction in viable counts of *Pseudomonas aeruginosa,* compared to the no-glass control. Only the glass containing 37.4 mol% strontium gave viable counts lower than the initial inoculum.

- In tests using human osteoblast-like cells, the overnight pre-treatment of scaffolds in serum-rich media was found to enhance cell adhesion after seeding.
- A mild increase in alkaline phosphatase activity was observed in human osteosarcoma G292 cells for compositions containing 6.2 mol% and 12.5 mol% strontium oxide when cultured in basal media. However, results were not conclusive.
- The presence of strontium in AWGC scaffolds enhanced the proliferation of human bone marrow-derived mesenchymal stromal cells (hBM-MSCs). Scaffolds containing 6.2 mol% strontium oxide gave the highest alkaline phosphatase activity, compared to compositions containing no strontium or 12.5 mol% strontium oxide, when cultured in osteogenic media for up to 2 weeks.
- The deposition of extracellular matrix was enhanced in scaffolds containing 6.2 mol% and 12.5 mol% strontium oxide compared to the no-strontium control when primary human bone marrow-derived mesenchymal stromal cells were cultured in osteogenic media for 4 weeks, as shown by Picroserius Red staining.

In conclusion, porous strontium-containing scaffolds could be produced via the foam replication method that gave samples with mechanical properties comparable to those of cancellous bone. The amount of strontium influenced the thermal properties, degree of sintering, crystal phases formed and apatite-forming ability of samples. Only the glass powder containing the highest amount of strontium oxide showed antimicrobial properties after soaking for 7 days, while the composition containing 6.2 mol% strontium oxide induced the highest alkaline phosphatase activity in hBM-MSCs. Therefore, no composition could be identified that could present antimicrobial properties and, at the same time, enhance the osteogenic differentiation of bone cells: low amounts of strontium were found optimal for an increase in bone regenerative properties of the material, but high strontium concentrations were required to obtain a clear antibacterial effect.

Chapter 8
Future work

The work presented in this thesis described, for the first time, the addition of strontium to the apatite-wollastonite glass-ceramic material (AWGC) used for producing porous bone scaffolds following to the foam replication method. Sample properties were investigated in three main fields, for a preliminary broad characterisation of the potential bone scaffolds: materials science, microbiology and cell biology. Future work is now required in each of these three areas, in order to better understand the material and scaffold properties and to optimise the scaffolds into the ideal construct that could guide bone regeneration.

Most characterisation took place in the materials science field. The thermal behaviour of the six materials under study was evaluated and the same heating regime was applied to all samples. Investigation on the morphology of the final scaffolds showed differences in sintering and shrinkage, as well as in crystal morphology, between the compositions considered. A study of the thermal properties of the six glasses at different heating rates, along with the determination of the optimal sintering temperature with a hot stage microscope, could allow for the design of tailored thermal treatments that could be applied to each composition for the production of well sintered scaffolds. This would also ensure a better control on the formation of crystal phases and would reduce the formation of sintering defects, thus improving the mechanical properties of samples and leading to more reproducible results, as well as reducing the effect of topography in the biological tests.
Further studies would be required to fully determine all the crystal phases that form in each composition upon heating, which depend on the thermal treatment applied. Two crystal phases were identified for all compositions, however the apatite:silicate:glass ratio was not evaluated, even though it could influence the mechanical properties of the final materials and of the porous scaffolds. In addition, the possibility of the presence of more than two crystal phases in some of the compositions, for example pseudowollastonite along with a magnesium calcium silicate or calcium silicates containing different amounts of strontium, was not fully explored. Since wollastonite, or the calcium silicate phase, is considered to be responsible for the outstanding mechanical properties of AWGC compared to other bioactive systems, it would be ideal to control the nucleation of crystal phases in the material and their final crystal size.

Micro computed tomography, scanning electron microscopy and radiopacity imaging of samples highlighted the presence of incomplete struts and defects within the scaffold structure. To overcome this, the scaffold coating process during foam replication could be improved. The process as described in the present thesis was fully manual, so some steps could be automated to ensure better repeatability, for example foam preparation, the timing of the soaking and squeezing steps and the initial drying step of the coated foams. In addition, the viscosity of the slurry was not evaluated, although it could affect the quality of the sponge coating during the soaking phase of the foam replication process: variations of viscosity with glass composition should be evaluated and the content of glass and the polymeric binder in each slurry optimised, if necessary. Only 90 pore-per-inch sponges were used in the present work. However, it is known that scaffold porosity can affect cell and bone ingrowth. Foams with larger pores could be considered, although this would hinder their mechanical properties, which therefore would have to be re-tested once the coating and sintering process has been optimised.

Regarding the mechanical properties, scaffolds were tested for compressive strength and biaxial flexural strength, which allowed for an initial evaluation of the mechanical performance of samples. However bones, especially load bearing bones, are constantly subjected to cyclic stresses, along with impacts and tensile stresses exerted by muscles. Therefore, fatigue strength, tensile strength and toughness should also be considered for a thorough characterisation of the mechanical behaviour of the novel bone-substituting implants. Only one batch of samples per composition was tested in the present thesis; however, inter-batch variability should be verified in order to ensure repeatability of the obtained mechanical properties.

Apatite formation was observed in *in vitro* simulated body fluid (SBF) tests only on the inner struts of scaffolds and low variations in ion concentration were found when discs were tested with inductively coupled plasma – optical emission spectroscopy (ICP-OES). SBF collected from porous scaffolds should therefore be tested for ion concentration, optimising the volume of solution used for soaking the samples. In addition, more time-points could be considered to better understand the short-term bioactive kinetics of apatite precipitation, as well as long-term studies in either SBF, phosphate buffered saline (PBS), tris(hydroxymethyl)aminomethane (TRIS) solution or cell culture media to evaluate the dissolution kinetics of the scaffolds.

Finally, samples were generally tested relatively shortly after being produced. Therefore, no data was gathered on the stability of the final scaffolds in terms of further precipitation and crystal growth of their crystal phases, when kept at room temperature for months or years. This information would give an indication on whether

controlled storage would be necessary for finished scaffolds and for how long scaffolds could be used before their properties significantly change.

Microbiological tests were designed to investigate the possibility that strontium could be considered an antimicrobial agent. For this reason, preliminary studies were carried out using strontium salts and the six parent glass powders instead of the final glass-ceramic porous scaffolds.
No bacterial growth inhibition could be observed in the strontium salt tests, which made the results not conclusive. It would be therefore necessary to perform further testing, either modifying the test protocol, for example reducing the concentration of the inoculum and considering shorter incubation times, or exploring whether alternative tests could be considered.
The glass powder of the sample containing 37.4 mol% strontium oxide induced a reduction in the proliferation of *Pseudomonas aeruginosa*, with a density of colony forming units (CFUs) below the concentration of the inoculum used, when the powder was dissolved in media for 1 and for 7 days. CFU reduction was also observed for glass compositions containing no strontium and 24.9 mol% strontium, when samples had their glass powders suspended in media for 7 days before inoculation. This suggested that the materials under study could present a mild antimicrobial activity and that this activity depended on the dissolution time. However, further studies would be necessary to confirm this. The ion release in microbiological culture media should be evaluated over time, which would give a better insight on the concentration of strontium and other relevant ions reached during these tests. Results would also provide reference concentrations for the salt tests.
Porous scaffolds would need to be tested, as they represent the model for the final material and approximate structure that will be in contact with bone tissue. Broth dilution assays, which would consider different dissolution time-points, could be carried out with the porous scaffolds, as well as biofilm formation tests where bacteria would be let adhere to the samples and would be cultured for a few days before being collected and evaluated.
Four bacterial species were used in the work described in the present thesis, as representative of the species most commonly detected in bone peri-prosthetic infections. However, future studies could take into consideration the use of other bacterial species and also of different strains for the species chosen.
In order to prove the efficacy of the scaffolds produced, an animal study would be required, where an infection model would be used to compare the infection rate against controls with no samples and with no-strontium scaffolds.

Finally, silver and zinc salts were tested to compare strontium with known antibacterial elements. Since silver showed inhibition of growth for all the four species tested, this would be the element of choice if antibacterial scaffolds were to be designed, provided that cytotoxicity could be avoided and that the beneficial effects of strontium on the proliferation and osteogenic differentiation of bone cells could be preserved.

Cell studies were carried out using the G292 cell line and human bone marrow-derived mesenchymal stromal cells (hBM-MSCs). In general, data presented in this work showed a high variability in the results. Because scaffolds were prepared manually, making their production process more repeatable and automated, as described above, could reduce their variability in shape, volume and porosity, which, in turn, would reduce the variability derived from the scaffolds themselves.

Different seeding methods could be tested, for example using different cell concentrations or dynamic seeding, which would ensure a more uniform distribution of cells around the scaffolds. With a dynamic method of culture, which maintains an even distribution of nutrients and oxygen within the media and around the samples, cell ingrowth within the scaffolds could also be assessed by sectioning the samples and staining them.

Cells from the G292 line were cultured for a week and results were not conclusive. Basal media was chosen in order to avoid the effect of osteogenic media overcoming the differences induced by the presence of strontium, in particular for alkaline phosphatase (ALP) activity. Considering the high proliferation rate of these cells, a lower number of cells could be seeded and then osteogenic media could be tested again, repeating the quantitative assays in particular. Alternatively, different osteoblast-like cell lines could be used and results compared.

The hBM-MSCs tested in the present work derived from a single donor. Testing of cells deriving from more donors would be preferable to confirm the optimal composition in terms of bone-regenerating potential.

Due to the reduced number of hBM-MSCs available, only two time-points could be tested: 7 and 14 days. Testing of more time-points would be required to assess the effect of the strontium scaffolds in the short and the longer term. In addition, only proliferation and ALP activity were analysed in the present work. However, a more comprehensive gene expression analysis would allow for the monitoring of other markers of osteogenic differentiation, such as osteonectin, osteocalcin, osteopontin or collagen, thus giving a more complete picture of the effect of strontium addition to AW porous scaffolds.

As with the cell line, in order to enhance cell attachment, scaffolds were pre-treated in serum-rich media overnight before seeding. However, this meant that the initial burst

ion release was not taken into account in the biological studies and therefore further testing would be required to assess whether the release from scaffolds of different compositions could affect the initial attachment and the subsequent proliferation. Finally, the use of a bioreactor that could apply mechanical loading to the samples in culture would allow to study the seeded scaffolds under more physiological conditions, as well as in the presence of a better circulation of the culture media. *In vivo* work will then be required to assess bone integration and regeneration over time after implantation.

Bibliography

1. Keating, J.F. et al. The management of fractures with bone loss. *Journal of Bone & Joint Surgery.* 2005, **87-B**(2), pp.142-150.
2. Ayoub, M.A. and El-Rosasy, M.A. Hybrid grafting of post-traumatic bone defects using beta-tricalcium phosphate and demineralized bone matrix. *European Journal of Orthopaedic Surgery & Traumatology.* 2014, **24**(5), pp.663-670.
3. Fong, K. et al. Predictors of nonunion and reoperation in patients with fractures of the tibia: An observational study. *BMC Musculoskeletal Disorders.* 2013, **14**, p.103.
4. Canadian Orthopaedic Trauma Society. Nonunion following intramedullary nailing of the femur with and without reaming. Results of a multicenter randomized clinical trial. *Journal of Bone & Joint Surgery - American Volume.* 2003, **85**(A(11)), pp.2093-2096.
5. Gomez-Barrena, E. et al. Bone fracture healing: cell therapy in delayed unions and nonunions. *Bone.* 2015, **70**, pp.93-101.
6. Faour, O. et al. The use of bone graft substitutes in large cancellous voids: Any specific needs? *Injury.* 2011, **42 Suppl 2**, pp.S87-S90.
7. American Association of Tissue Banks. *2017 Annual Report.* 2018.
8. Gazdag, A.R. et al. Alternatives to autogenous bone graft: efficacy and indications. *Journal of the American Academy of Orthopaedic Surgeons.* 1995, **3**(1), pp.1-8.
9. Giannoudis, P.V. et al. Bone substitutes: An update. *Injury.* 2005, **36 Suppl 3**, pp.S20-S27.
10. Sogal, A. and Tofe, A.J. Risk assessment of bovine spongiform encephalopathy transmission through bone graft material derived from bovine bone used for dental applications. *Journal of Periodontology.* 1999, **70**(9), pp.1053-1063.
11. Moore, W.R. et al. Synthetic bone graft substitutes. *ANZ Journal of Surgery.* 2001, **71**, pp.354-361.
12. Kokubo, T. et al. Mechanical properties of a new type of apatite-containing glass-ceramic for prosthetic application. *Journal of Materials Science.* 1985, **20**, pp.2001-2004.
13. Höland, W. and Beall, G. *Glass-ceramic technology.* Westerville, OH, U.S.A.: The American Ceramic Society, 2002.
14. Marie, P.J. Strontium ranelate: A physiological approach for optimizing bone formation and resorption. *Bone.* 2006, **38**(2 Suppl 1), pp.S10-S14.
15. Marie, P.J. et al. An uncoupling agent containing strontium prevents bone loss by depressing bone resorption and maintaining bone formation in estrogen-deficient rats. *Journal of Bone and Mineral Research.* 1993, **8**(5), pp.607-615.
16. Bonnelye, E. et al. Dual effect of strontium ranelate: Stimulation of osteoblast differentiation and inhibition of osteoclast formation and resorption in vitro. *Bone.* 2008, **42**(1), pp.129-138.
17. Guida, A. et al. Preliminary work on the antibacterial effect of strontium in glass ionomer cements. *Journal of Materials Science Letters.* 2003, **22**, pp.1401-1403.
18. Liu, J. et al. Strontium-substituted bioactive glasses *in vitro* osteogenic and antibacterial effects. *Dental Materials.* 2016, **32**(3), pp.412-422.
19. Hench, L.L. The skeletal system. In: Hench, L.L. and Jones, J.R. eds. *Biomaterials, artificial organs and tissue engineering*. Abington Hall, Abington, Cambridge CB1 6AH, England: Woodhead Publishing Limited, 2005, pp.79-89.

20. Weiner, S. and Wagner, H.D. The material bone: Structure-mechanical function relations. *Annual Review of Materials Science.* 1998, **28**, pp.271-298.
21. Olszta, M.J. et al. Bone structure and formation: A new perspective. *Materials Science and Engineering: R: Reports.* 2007, **58**(3-5), pp.77-116.
22. Currey, J.D. *Bones - Structure and mechanics.* Woodstock, Oxfordshire OX20 1SY: Princeton University Press, 2002.
23. Fratzl, P. et al. Structure and mechanical quality of the collagen-mineral nano-composite in bone. *Journal of Materials Chemistry.* 2004, **14**(14), pp.2115-2123.
24. Fratzl, P. and Weinkamer, R. Nature's hierarchical materials. *Progress in Materials Science.* 2007, **52**(8), pp.1263-1334.
25. Sommerfeldt, D.W. and Rubin, C.T. Biology of bone and how it orchestrates the form and function of the skeleton. *European Spine Journal.* 2001, **10 Suppl 2**, pp.S86-S95.
26. Rho, J.-Y. et al. Mechanical properties and the hierarchical structure of bone. *Medical Engineering & Physics.* 1998, **20**, pp.92-102.
27. Singh, I. The architecture of cancellous bone. *Journal of Anatomy.* 1978, **127**(2), pp.305-310.
28. Currey, J.D. The structure and mechanics of bone. *Journal of Materials Science.* 2012, **47**(1), pp.41-54.
29. Cooper, D.M. et al. Comparison of microcomputed tomographic and microradiographic measurements of cortical bone porosity. *Calcified Tissue International.* 2004, **74**(5), pp.437-447.
30. Karageorgiou, V. and Kaplan, D. Porosity of 3D biomaterial scaffolds and osteogenesis. *Biomaterials.* 2005, **26**(27), pp.5474-5491.
31. Hoc, T. et al. Effect of microstructure on the mechanical properties of Haversian cortical bone. *Bone.* 2006, **38**(4), pp.466-474.
32. Yaszemski, M.J. et al. Evolution of bone transplantation: Molecular, cellular and tissue strategies to engineer human bone. *Biomaterials.* 1996, **17**, pp.175-185.
33. Rezwan, K. et al. Biodegradable and bioactive porous polymer/inorganic composite scaffolds for bone tissue engineering. *Biomaterials.* 2006, **27**(18), pp.3413-3431.
34. Baino, F. and Vitale-Brovarone, C. Three-dimensional glass-derived scaffolds for bone tissue engineering: current trends and forecasts for the future. *Journal of Biomedical Materials Research - Part A.* 2011, **97**(4), pp.514-535.
35. Fu, Q. et al. Toward strong and tough glass and ceramic scaffolds for bone repair. *Advanced Functional Materials.* 2013, **23**(44), pp.5461-5476.
36. Choi, K. and Goldstein, S.A. A comparison of the fatigue behavior of human trabecular and cortical bone tissue. *Journal of Biomechanics.* 1992, **25**(12), pp.1371-1381.
37. Wolff, J. *Das Gesetz der Tranformation der Knochen*. Berlin: A. Hirchwild, 1892.
38. Wolff, J. Uber die innere Architectur der Knochen und ihre Bedeutung fur die Frange vom Knochenwachsthum. *Virchows Archiv.* 1870, **50**, pp.389-450.
39. Lee, T.C. and Taylor, D. Bone remodelling: Should we cry Wolff? *Irish Journal of Medical Science.* 1999, **168**(2).
40. Parfitt, A.M. The cellular basis of bone remodeling: The quantum concept reexamined in light of recent advances in the cell biology of bone. *Calcified Tissue International.* 1984, **36**, pp.S37-S45.
41. Schindeler, A. et al. Bone remodeling during fracture repair: The cellular picture. *Seminars in Cell & Developmental Biology.* 2008, **19**(5), pp.459-466.
42. Raggatt, L.J. and Partridge, N.C. Cellular and molecular mechanisms of bone remodeling. *Journal of Biological Chemistry.* 2010, **285**(33), pp.25103-25108.
43. McKibbin, B. The biology of fracture healing in long bones. *Journal of Bone & Joint Surgery.* 1978, **60-B**(2), pp.150-162.

44. Einhorn, T.A. The cell and molecular biology of fracture healing. *Clinical Orthopaedics and Related Research.* 1998, **355S**, pp.S7-S21.
45. Loi, F. et al. Inflammation, fracture and bone repair. *Bone.* 2016, **86**, pp.119-130.
46. Baroli, B. From natural bone grafts to tissue engineering therapeutics: Brainstorming on pharmaceutical formulative requirements and challenges. *Journal of Pharmaceutical Sciences.* 2009, **98**(4), pp.1317-1375.
47. Kneser, U. et al. Tissue engineering of bone. *Minimally Invasive Therapy & Allied Technologies.* 2002, **11**(3), pp.107-116.
48. Greenwald, A.S. et al. Bone graft substitutes: facts, fictions & applications. *Journal of Bone & Joint Surgery - American Volume.* 2001, **83-A**(Suppl. 2 Pt 2), pp.98-103.
49. Brown, J.L. et al. Bone tissue engineering. In: Ratner, B.D. et al. eds. *Biomaterials Science - An Introduction to Materials in Medicine*. Oxford, UK: Academic Press Elsevier, 2013.
50. Scabbia, A. and Trombelli, L. A comparative study on the use of a HA/collagen/chondroitin sulphate biomaterial (Biostite) and a bovine-derived HA xenograft (Bio-Oss) in the treatment of deep intra-osseous defects. *Journal of Clinical Periodontology.* 2004, **31**(5), pp.348-355.
51. Huang, J. Ceramic biomaterials for tissue engineering. In: Boccacccini, A. and Ma, P.X. eds. *Tissue engineering using ceramics and polymers*. Oxford, UK: Woodhead Publishing Elsevier, 2014.
52. McAuliffe, J.A. Bone graft substitutes. *Journal of Hand Therapy.* 2003, **16**, pp.180-187.
53. Ivarsson, I. et al. Revision of infected hip replacement: Two-stage procedure with a temporary gentamicin spacer. *Acta Orthopaedica Scandinavica.* 1994, **65**(1), pp.7-8.
54. Leunig, M. et al. A cement spacer for two-stage revision of infected implants of the hip joint. *International Orthopaedics.* 1998, **22**, pp.209-214.
55. Giannoudis, P.V. et al. Fracture healing: The diamond concept. *Injury.* 2007, **38**, pp.S3-S6.
56. Janicki, P. and Schmidmaier, G. What should be the characteristics of the ideal bone graft substitute? Combining scaffolds with growth factors and/or stem cells. *Injury.* 2011, **42 Suppl 2**, pp.S77-S81.
57. Giannoudis, P.V. et al. The diamond concept – open questions. *Injury.* 2008, **39**, pp.S5-S8.
58. Jones, J.R. Scaffolds for tissue engineering. In: Hench, L.L. and Jones, J.R. eds. *Biomaterials, artificial organs and tissue engineering*. Cambridge, UK: Woodhead Publishing Ltd, 2005.
59. Hench, L.L. et al. Bonding mechanisms at the interface of ceramic prosthetic materials. *Journal of Biomedical Materials Research Symposium.* 1971, **2**(Part 1), pp.117-141.
60. Shelby, J.E. *Introduction to Glass Science and Technology - Second Edition.* Cambridge, UK: The Royal Society of Chemistry, 2005.
61. Rawlings, R.D. Bioactive glasses and glass-ceramics. *Clinical Materials.* 1993, **14**, pp.155-179.
62. Hill, R.G. and Brauer, D.S. Predicting the bioactivity of glasses using the network connectivity or split network models. *Journal of Non-Crystalline Solids.* 2011, **357**(24), pp.3884-3887.
63. Fredholm, Y.C. et al. Strontium containing bioactive glasses: Glass structure and physical properties. *Journal of Non-Crystalline Solids.* 2010, **356**, pp.2546-2551.
64. Martin, R.A. et al. An examination of the calcium and strontium site distribution in bioactive glasses through isomorphic neutron diffraction, X-ray diffraction, EXAFS and multinuclear solid state NMR. *Journal of Materials Chemistry.* 2012, **22**(41), pp.22212-22223.

65. Hill, R. An alternative view of the degradation of bioglass. *Journal of Materials Science Letters.* 1996, **15**, pp.1122-1125.
66. Watts, S.J. et al. Influence of magnesia on the structure and properties of bioactive glasses. *Journal of Non-Crystalline Solids.* 2010, **356**(9-10), pp.517-524.
67. Deubener, J. and Höland, W. Nucleation and crystallization of glasses and glass-ceramics. In: Höland, W. and Deubener, J. eds. *Nucleation and crystallization of glasses and glass-ceramics*. Lausanne, Switzerland: Frontiers Media, 2017.
68. James, P.F. Kinetics of crystal nucleation in silicate glasses. *Journal of Non-Crystalline Solids.* 1985, **73**, pp.517-540.
69. Zanotto, E.D. and Weinberg, M.C. Trends in homogenous crystal nucleation in oxide glasses. *Physics and Chemistry of Glasses.* 1989, **30**(5), pp.186-192.
70. Yinnon, H. and Uhlmann, D.R. A kinetic treatment of glass formation - V: Surface and bulk heterogeneous nucleation. *Journal of Non-Crystalline Solids.* 1981, **44**, pp.37-55.
71. Weinberg, M.C. et al. Crystallization kinetics and the JMAK equation. *Journal of Non-Crystalline Solids.* 1997, **219**, pp.89-99.
72. Johari, G.P. and Schmelzer, J.W.P. Crystal nucleation and growth in glass-forming systems: Some new results and open problems. In: Schmelzer, J.W.P. ed. *Glass - Selected properties and crystallization*. Berlin, Germany: De Gruyter, 2014.
73. Hu, A.-M. et al. Effect of nucleation temperatures and time on crystallization behavior and properties of Li_2O–Al_2O_3–SiO_2 glasses. *Materials Chemistry and Physics.* 2006, **98**(2-3), pp.430-433.
74. Kashchiev, D. *Nucleation - Basic theory with applications.* Oxford, UK: Butterworth Heinemann, 2000.
75. Kang, S.J.L. *Sintering: Densification, grain growth, and microstructure.* 1 ed. Oxford: Elsevier Butterworth-Heinemann, 2005.
76. De Jonghe, L.C. and Rahaman, M.N. Sintering of Ceramics. In: Sōmiya, S. et al. eds. *Handbook of Advanced Ceramics*. Oxford, UK: Academic Press, 2003.
77. German, R.M. et al. Review: Liquid phase sintering. *Journal of Materials Science.* 2008, **44**(1), pp.1-39.
78. Schwartzwalder, K. and Somers, A.V. *Method of making porous ceramic articles*. US Patent no. 3 090 094. 1963.
79. Tian, J. and Tian, J. Preparation of porous hydroxyapatite. *Journal of Materials Science.* 2001, **36**, pp.3061-3066.
80. Chen, Q.Z. et al. 45S5 Bioglass-derived glass-ceramic scaffolds for bone tissue engineering. *Biomaterials.* 2006, **27**(11), pp.2414-2425.
81. Park, Y.-S. et al. Feasibility of three-dimensional macroporous scaffold using calcium phosphate glass and polyurethane sponge. *Journal of Materials Science.* 2006, **41**(13), pp.4357-4364.
82. Tripathi, G. and Basu, B. A porous hydroxyapatite scaffold for bone tissue engineering: Physico-mechanical and biological evaluations. *Ceramics International.* 2012, **38**(1), pp.341-349.
83. Bretcanu, O. et al. Simple methods to fabricate Bioglass®-derived glass-ceramic scaffolds exhibiting porosity gradient. *Journal of Materials Science.* 2008, **43**(12), pp.4127-4134.
84. Jun, I.-K. et al. Porous hydroxyapatite scaffolds coated with bioactive apatite-wollastonite glass-ceramics. *Journal of the American Ceramic Society.* 2007, **90**(9), pp.2703-2708.
85. Kokubo, T. et al. Apatite- and wollastonite-containg glass-ceramics for prosthetic application. *Bulletin of the Institute for Chemical Research, Kyoto University.* 1982, **60**(3-4), pp.260-268.
86. Hench, L.L. Bioceramics. *Journal of the American Ceramic Society.* 1998, **81**(7), pp.1705-1728.

87. Hench, L.L. Biomaterials: A forecast for the future. *Biomaterials.* 1998, **19**, pp.1419-1423.
88. Hench, L.L. et al. Bioactive glasses: Importance of structure and properties in bone regeneration. *Journal of Molecular Structure.* 2014, **1073**, pp.24-30.
89. Xynos, I.D. et al. Ionic products of bioactive glass dissolution increase proliferation of human osteoblasts and induce insulin-like growth factor II mRNA expression and protein synthesis. *Biochemical and Biophysical Research Communications.* 2000, **276**(2), pp.461-465.
90. Xynos, I.D. et al. Gene-expression profiling of human osteoblasts following treatment with the ionic products of Bioglass 45S5 dissolution. *Journal of Biomedical Materials Research.* 2001, **55**(2), pp.151-157.
91. Xynos, I.D. et al. Bioglass 45S5 stimulates osteoblast turnover and enhances bone formation In vitro: Implications and applications for bone tissue engineering. *Calcified Tissue International.* 2000, **67**(4), pp.321-329.
92. Hench, L.L. Genetic design of bioactive glass. *Journal of the European Ceramic Society.* 2009, **29**(7), pp.1257-1265.
93. Jones, J.R. et al. Bioglass and bioactive glasses and their impact on healthcare. *International Journal of Applied Glass Science.* 2016, **7**(4), pp.423-434.
94. Drago, L. et al. Bioactive glass BAG-S53P4 for the adjunctive treatment of chronic osteomyelitis of the long bones: an *in vitro* and prospective clinical study. *BMC Infectious Diseases.* 2013, **13**, p.584.
95. Fu, Q. et al. Mechanical and in vitro performance of 13-93 bioactive glass scaffolds prepared by a polymer foam replication technique. *Acta Biomaterialia.* 2008, **4**(6), pp.1854-1864.
96. Liu, X. et al. Mechanical properties of bioactive glass (13-93) scaffolds fabricated by robotic deposition for structural bone repair. *Acta Biomaterialia.* 2013, **9**(6), pp.7025-7034.
97. Montazerian, M. and Dutra Zanotto, E. History and trends of bioactive glass-ceramics. *Journal of Biomedical Materials Research - Part A.* 2016, **104**(5), pp.1231-1249.
98. Vitale-Brovarone, C. et al. High strength bioactive glass-ceramic scaffolds for bone regeneration. *Journal of Materials Science: Materials in Medicine.* 2009, **20**(2), pp.643-653.
99. Vitale-Brovarone, C. et al. Resorbable glass-ceramic phosphate-based scaffolds for bone tissue engineering: Synthesis, properties, and *in vitro* effects on human marrow stromal cells. *Journal of Biomaterials Applications.* 2011, **26**(4), pp.465-489.
100. Hench, L.L. The story of Bioglass. *Journal of Materials Science: Materials in Medicine.* 2006, **17**(11), pp.967-978.
101. Nakamura, T. et al. A new glass-ceramic for bone replacement: Evaluation of its bonding to bone tissue. *Journal of Biomedical Materials Research - Part A.* 1985, **19**(6), pp.685-698.
102. Kokubo, T. et al. Chemical reaction of bioactive glass and glass-ceramics with a simulated body fluid. *Journal of Materials Science: Materials in Medicine.* 1992, **3**, pp.79-83.
103. Kokubo, T. Bioactive glass-ceramics. In: Kokubo, T. ed. *Bioceramics and their clinical applications*. Cambridge, UK: Woodhead Publishing, 2008, pp.284-301.
104. Kokubo, T. et al. Formation of a high-strength bioactive glass-ceramic in the system MgO-CaO-SiO_2-P_2O_5. *Journal of Materials Science.* 1986, **21**, pp.536-540.
105. Ohtsuki, C. et al. Transmission electron microscopic observation of glass-ceramic A-W and apatite layer formed on its surface in a simulated body fluid. *Journal of the Ceramic Society of Japan.* 1995, **103**(5), pp.449-454.

106. Kokubo, T. Bioactive glass ceramics: properties and applications. *Biomaterials.* 1991, **12**, pp.155-163.
107. Kokubo, T. et al. Ceramics for biomedical applications. In: Sōmiya, S. et al. eds. *Handbook of advanced ceramics*. Oxford, UK: Academic Press, 2003.
108. Kokubo, T. et al. Fatigue and life-time of bioactive glass-ceramic A-W containing apatite and wollastonite. *Journal of Materials Science.* 1987, **22**, pp.4067-4070.
109. Kokubo, T. Surface chemistry of bioactive glass-ceramics. *Journal of Non-Crystalline Solids.* 1990, **120**, pp.138-151.
110. Kitsugi, T. et al. The bonding of glass ceramics to bone. *International Orthopaedics.* 1989, **13**, pp.199-206.
111. Fujita, H. et al. Porous apatite-wollastonite glass-ceramic as an intramedullary plug. *Journal of Bone & Joint Surgery.* 2000, **82-B**(614-618).
112. Ohsawa, K. et al. *In vivo* absorption of porous apatite- and wollastonite-containing glass-ceramic. *Journal of Materials Science: Materials in Medicine.* 2004, **15**, pp.859-864.
113. Kawanabe, K. et al. A-W glass ceramic as a bone substitute in cemented hip arthroplasty 15 hips followed 2-10 years. *Acta Orthopaedica Scandinavica.* 1998, **69**(3), pp.237-242.
114. Duminis, T. et al. Apatite glass-ceramics: A review. In: Höland, W. and Deubener, J. eds. *Nucleation and crystallization of glasses and glass-ceramics*. Lausanne: Frontiers Media, 2017, pp.89-103.
115. Kokubo, T. and Yamaguchi, S. Novel bioactive materials derived by Bioglass: Glass-ceramic A-W and surface-modified Ti metal. *International Journal of Applied Glass Science.* 2016, **7**(2), pp.173-182.
116. Kokubo, T. et al. Novel bioactive materials with different mechanical properties. *Biomaterials.* 2003, **24**(13), pp.2161-2175.
117. Ono, K. et al. Mechanical properties of bone after implantation of apatite-wollastonite containing glass ceramic-fibrin mixture. *Journal of Biomedical Materials Research.* 1990, **24**, pp.47-63.
118. Magallanes-Perdomo, M. et al. *In vitro* study of the proliferation and growth of human bone marrow cells on apatite-wollastonite-2M glass ceramics. *Acta Biomaterialia.* 2010, **6**(6), pp.2254-2263.
119. Xiao, K. et al. Indirect selective laser sintering of apatite-wollostonite glass-ceramic. *Proceedings of the Institution of Mechanical Engineers, Part H: Journal of Engineering in Medicine.* 2008, **222**(7), pp.1107-1114.
120. Dyson, J.A. et al. Development of custom-built bone scaffolds using mesenchymal stem cells and apatite-wollastonite glass-ceramics. *Tissue Engineering.* 2007, **13**(12), pp.2891-2901.
121. Serna, C.A. *Development of a synthetic trabecular bone graft utilizing a two phase glass-ceramic*. PhD thesis, The University of Leeds, 2016.
122. Lambert, P. Basic bacteriology. In: Elliott, T. et al. eds. *Medical microbiology and infection - Lecture notes*. Chichester, UK: Wiley-Blackwell, 2011.
123. Madigan, M.T. et al. *Brock biology of microrganisms.* Harlow, UK: Pearson Education Ltd, 2015.
124. Kohanski, M.A. et al. How antibiotics kill bacteria: from targets to networks. *Nature Reviews Microbiology.* 2010, **8**(6), pp.423-435.
125. Wang, L. et al. Bacterial growth, detachment and cell size control on polyethylene terephthalate surfaces. *Scientific Reports.* 2015, **5**, p.15159.
126. Flemming, H.C. et al. Biofilms: An emergent form of bacterial life. *Nature Reviews Microbiology.* 2016, **14**(9), pp.563-575.
127. Stoodley, P. et al. Biofilms, biomaterials, and device-related infections. In: Ratner, B.D. et al. eds. *Biomaterials Science - An Introduction to Materials in Medicine*. Oxford, UK: Academic Press Elsevier, 2013.
128. Parvizi, J. et al. Culture-negative periprosthetic joint infection. *Journal of Bone & Joint Surgery - American Volume.* 2014, **96**, pp.430-436.

129. National Joint Registry for England, Wales, Northern Ireland and the Isle of Man. *14th Annual Report - 2017.* Hemel Hempstead, Hertfordshire, UK, 2017.
130. Campoccia, D. et al. The significance of infection related to orthopedic devices and issues of antibiotic resistance. *Biomaterials.* 2006, **27**(11), pp.2331-2339.
131. Metsemakers, W.J. et al. Individual risk factors for deep infection and compromised fracture healing after intramedullary nailing of tibial shaft fractures: A single centre experience of 480 patients. *Injury.* 2015, **46**(4), pp.740-745.
132. Fernandez-Fairen, M. et al. Economical analysis on prophylaxis, diagnosis, and treatment of periprosthetic infections. *The Open Orthopaedics Journal.* 2013, **7**(Suppl 2: M9), pp.227-242.
133. Benito, N. et al. Epidemiology of prosthetic joint infection. In: Peel, T. ed. *Prosthetic joint infections*. Switzerland: Springer Nature, 2018.
134. Thakore, R.V. et al. Surgical site infection in orthopedic trauma: A case-control study evaluating risk factors and cost. *Journal of Clinical Orthopaedics and Trauma.* 2015, **6**(4), pp.220-226.
135. Metsemakers, W.-J. et al. Infection after fracture fixation of the tibia: Analysis of healthcare utilization and related costs. *Injury.* 2017, **48**(6), pp.1204-1210.
136. Arnold, W.V. et al. Bacterial biofilms and periprosthetic infections. *Journal of Bone & Joint Surgery - American Volume.* 2013, **95-A**(24), pp.2224-2229.
137. Nelson, C.L. et al. Is aseptic loosening truly aseptic? *Clinical Orthopaedics and Related Research.* 2005, **437**, pp.25-30.
138. Parvizi, J. et al. Aseptic loosening of total hip arthroplasty: Are they all truly aseptic? *The Journal of Arthroplasty.* 2010, **25**(3), p.e24.
139. Parvizi, J. et al. Aseptic loosening of total hip arthroplasty: Infection always should be ruled out. *Clinical Orthopaedic and Related Research.* 2011, **469**(5), pp.1401-1405.
140. Drago, L. and Vecchi, E.D. Microbiological diagnosis of implant-related infections: Scientific evidence and cost/benefit analysis of routine antibiofilm processing. In: Drago, L. ed. *A modern approach to biofilm-related orthopaedic implant infections*. Switzerland: Springer Nature, 2017.
141. Benito, N. et al. Time trends in the aetiology of prosthetic joint infections: a multicentre cohort study. *Clinical Microbiology and Infection.* 2016, **22**(8), pp.732.e1-732.e8.
142. Sandoe, J. Bone and joint infections. In: Elliott, T. et al. eds. *Medical microbiology and infection - Lecture notes*. Chichester, UK: Wiley-Blackwell, 2011.
143. Haddad, F.S. et al. Prosthetic joint infections and cost analysis? In: Drago, L. ed. *A modern approach to biofilm-related orthopaedic implant infections*. Switzerland: Springer Nature, 2017.
144. Meija, J. et al. Atomic weights of the elements 2013 (IUPAC Technical Report). *Pure and Applied Chemistry.* 2016, **88**(3), pp.265-291.
145. Querido, W. et al. The effects of strontium on bone mineral: A review on current knowledge and microanalytical approaches. *Micron.* 2016, **80**, pp.122-134.
146. Habibovic, P. and Barralet, J.E. Bioinorganics and biomaterials: Bone repair. *Acta Biomaterialia.* 2011, **7**(8), pp.3013-3026.
147. Cabrera, W.E. et al. Strontium and bone. *Journal of Bone and Mineral Research.* 1999, **14**(5), pp.661-668.
148. Dahl, S.G. et al. Incorporation and distribution of strontium in bone. *Bone.* 2001, **28**(4), pp.446-453.
149. Pors Nielsen, S. The biological role of strontium. *Bone.* 2004, **35**(3), pp.583-588.
150. Marie, P.J. et al. Mechanisms of action and therapeutic potential of strontium in bone. *Calcified Tissue International.* 2001, **69**(3), pp.121-129.

151. Gentleman, E. et al. The effects of strontium-substituted bioactive glasses on osteoblasts and osteoclasts in vitro. *Biomaterials.* 2010, **31**(14), pp.3949-3956.
152. Saidak, Z. and Marie, P.J. Strontium signaling: Molecular mechanisms and therapeutic implications in osteoporosis. *Pharmacology & Therapeutics.* 2012, **136**(2), pp.216-226.
153. Canalis, E. et al. The divalent strontium salt S12911 enhances bone cell replication and bone formation *in vitro*. *Bone.* 1996, **18**(6), pp.517-523.
154. Brennan, T.C. et al. Osteoblasts play key roles in the mechanisms of action of strontium ranelate. *British Journal of Pharmacology.* 2009, **157**(7), pp.1291-1300.
155. Zhu, L.L. et al. Induction of a program gene expression during osteoblast differentiation with strontium ranelate. *Biochemical and Biophysical Research Communications.* 2007, **355**(2), pp.307-311.
156. Santocildes-Romero, M.E. et al. The osteogenic response of mesenchymal stromal cells to strontium-substituted bioactive glasses. *Journal of Tissue Engineerig and Regenerative Medicine.* 2015, **9**(5), pp.619-631.
157. Fromigué, O. et al. Essential role of nuclear factor of activated T cells (NFAT)-mediated Wnt signaling in osteoblast differentiation induced by strontium ranelate. *Journal of Biological Chemistry.* 2010, **285**(33), pp.25251-25258.
158. Rybchyn, M.S. et al. An Akt-dependent increase in canonical Wnt signaling and a decrease in sclerostin protein levels are involved in strontium ranelate-induced osteogenic effects in human osteoblasts. *Journal of Biological Chemistry.* 2011, **286**(27), pp.23771-23779.
159. Caudrillier, A. et al. Strontium ranelate decreases receptor activator of nuclear factor-KappaB ligand-induced osteoclastic differentiation in vitro: Involvement of the calcium-sensing receptor. *Molecular Pharmacology.* 2010, **78**(4), pp.569-576.
160. Hurtel-Lemaire, A.S. et al. The calcium-sensing receptor is involved in strontium ranelate-induced osteoclast apoptosis. New insights into the associated signaling pathways. *Journal of Biological Chemistry.* 2009, **284**(1), pp.575-584.
161. da Rosa, J.A. et al. Strontium ranelate effect on the repair of bone defects and molecular components of the cortical bone of rats. *Brazilian Dental Journal.* 2016, **27**(5), pp.502-507.
162. Meunier, P.J. et al. Effects of long-term strontium ranelate treatment on vertebral fracture risk in postmenopausal women with osteoporosis. *Osteoporosis International.* 2009, **20**(10), pp.1663-1673.
163. Meunier, P.J. et al. The effects of strontium ranelate on the risk of vertebral fracture in women with postmenopausal osteoporosis. *The New England Journal of Medicine.* 2004, **350**(5), pp.459-468.
164. Reginster, J.Y. et al. Long-term treatment of postmenopausal osteoporosis with strontium ranelate: Results at 8 years. *Bone.* 2009, **45**(6), pp.1059-1064.
165. Reginster, J.Y. et al. Effects of long-term strontium ranelate treatment on the risk of nonvertebral and vertebral fractures in postmenopausal osteoporosis: Results of a five-year, randomized, placebo-controlled trial. *Arthritis & Rheumatism.* 2008, **58**(6), pp.1687-1695.
166. Reginster, J.Y. et al. Strontium ranelate reduces the risk of nonvertebral fractures in postmenopausal women with osteoporosis: Treatment of Peripheral Osteoporosis (TROPOS) study. *Journal of Clinical Endocrinology & Metabolism.* 2005, **90**(5), pp.2816-2822.
167. Kaufman, J.M. et al. Efficacy and safety of strontium ranelate in the treatment of osteoporosis in men. *Journal of Clinical Endocrinology & Metabolism.* 2013, **98**(2), pp.592-601.
168. Compston, J. Strontium ranelate lives to fight another day. *Maturitas.* 2014, **78**(2), pp.75-76.

169. Abrahamsen, B. et al. Nationwide registry-based analysis of cardiovascular risk factors and adverse outcomes in patients treated with strontium ranelate. *Osteoporosis International.* 2014, **25**(2), pp.757-762.
170. Cooper, C. et al. Ischaemic cardiac events and use of strontium ranelate in postmenopausal osteoporosis: A nested case-control study in the CPRD. *Osteoporosis International.* 2014, **25**(2), pp.737-745.
171. Vestergaard, P. New strategies for osteoporosis patients previously managed with strontium ranelate. *Therapeutic Advances in Musculoskeletal Disease.* 2014, **6**(6), pp.217-225.
172. European Medicines Agency. *Protelos - Procedural steps taken and scientific information after the authorisation.* (EMA/668725/2016). London, United Kingdom, 2016.
173. European Medicines Agency. *Protelos/Osseor to remain available but with further restrictions.* (EMA/235924/2014). London, United Kingdom, 2014.
174. European Medicines Agency. *PRAC recommends suspending use of Protelos/Osseor (strontium ranelate).* London, United Kingdom, 2014.
175. European Medicines Agency. *Recommendation to restrict the use of Protelos/Osseor (strontium ranelate).* (EMA/235924/2014). London, United Kingdom, 2013.
176. Reginster, J.Y. et al. The position of strontium ranelate in today's management of osteoporosis. *Osteoporosis International.* 2015, **26**(6), pp.1667-1671.
177. O'Donnell, M.D. et al. Materials characterisation and cytotoxic assessment of strontium-substituted bioactive glasses for bone regeneration. *Journal of Materials Chemistry.* 2010, **20**(40), pp.8934-8941.
178. Gorustovich, A.A. et al. Osteoconductivity of strontium-doped bioactive glass particles: a histomorphometric study in rats. *Journal of Biomedical Materials Research - Part A.* 2010, **92**(1), pp.232-237.
179. Lao, J. et al. Strontium-delivering glasses with enhanced bioactivity: A new biomaterial for antiosteoporotic applications? *Chemistry of Materials.* 2008, **20**, pp.4969-4973.
180. Isaac, J. et al. Effects of strontium-doped bioactive glass on the differentiation of cultured osteogenic cells. *European Cells and Materials.* 2011, **21**, pp.130-143.
181. Hesaraki, S. et al. Physico-chemical and in vitro biological evaluation of strontium/calcium silicophosphate glass. *Journal of Materials Science: Materials in Medicine.* 2010, **21**(2), pp.695-705.
182. Zhang, W. et al. Effects of strontium in modified biomaterials. *Acta Biomaterialia.* 2011, **7**(2), pp.800-808.
183. Qiu, K. et al. Effect of strontium ions on the growth of ROS17/2.8 cells on porous calcium polyphosphate scaffolds. *Biomaterials.* 2006, **27**(8), pp.1277-1286.
184. Zhang, C. et al. Architectures of strontium hydroxyapatite microspheres: solvothermal synthesis and luminescence properties. *Langmuir.* 2009, **25**(23), pp.13591-13598.
185. Hao, J. et al. Novel bioresorbable strontium hydroxyapatite membrane for guided bone regeneration. *Clinical Oral Implants Research.* 2015, **26**(1), pp.1-7.
186. Vickers, W.O.M. *The effect of strontium substitution on apatite-wollastonite glass-ceramics*. PhD thesis, The University of Leeds, 2013.
187. Tian, M. et al. In vivo study of porous strontium-doped calcium polyphosphate scaffolds for bone substitute applications. *Journal of Materials Science: Materials in Medicine.* 2009, **20**(7), pp.1505-1512.
188. Zreiqat, H. et al. The incorporation of strontium and zinc into a calcium-silicon ceramic for bone tissue engineering. *Biomaterials.* 2010, **31**(12), pp.3175-3184.

189. Landi, E. et al. Sr-substituted hydroxyapatites for osteoporotic bone replacement. *Acta Biomaterialia.* 2007, **3**(6), pp.961-969.
190. Zhu, Y. et al. Composition–structure–property relationships of the CaO–MxOy–SiO2–P2O5 (M = Zr, Mg, Sr) mesoporous bioactive glass (MBG) scaffolds. *Journal of Materials Chemistry.* 2011, **21**(25), pp.9208-9218.
191. Wu, C. et al. Strontium-containing mesoporous bioactive glass scaffolds with improved osteogenic/cementogenic differentiation of periodontal ligament cells for periodontal tissue engineering. *Acta Biomaterialia.* 2012, **8**(10), pp.3805-3815.
192. Wang, X. et al. Synthesis and characterization of hierarchically macroporous and mesoporous CaO-MO-SiO_2-P_2O_5 (M=Mg, Zn, Sr) bioactive glass scaffolds. *Acta Biomaterialia.* 2011, **7**(10), pp.3638-3644.
193. Molino, G. et al. Electrophoretic deposition of spray-dried Sr-containing mesoporous bioactive glass spheres on glass-ceramic scaffolds for bone tissue regeneration. *Journal of Materials Science.* 2017, **52**(15), pp.9103-9114.
194. Zhang, J. et al. Three-dimensional printing of strontium-containing mesoporous bioactive glass scaffolds for bone regeneration. *Acta Biomaterialia.* 2014, **10**(5), pp.2269-2281.
195. Dabsie, F. et al. Does strontium play a role in the cariostatic activity of glass ionomer? Strontium diffusion and antibacterial activity. *Journal of Dentistry.* 2009, **37**(7), pp.554-559.
196. Alkhraisat, M.H. et al. Loading and release of doxycycline hyclate from strontium-substituted calcium phosphate cement. *Acta Biomaterialia.* 2010, **6**(4), pp.1522-1528.
197. Brauer, D.S. et al. Bactericidal strontium-releasing injectable bone cements based on bioactive glasses. *Journal of the Royal Society Interface.* 2012, **10**(78), p.20120647.
198. Fernandes, J.S. et al. Intrinsic antibacterial borosilicate glasses for bone tissue engineering applications. *ACS Biomaterials Science & Engineering.* 2016, **2**(7), pp.1143-1150.
199. Ravi, N.D. et al. Strontium-substituted calcium deficient hydroxyapatite nanoparticles: Synthesis, characterization, and antibacterial properties. *Journal of the American Ceramic Society.* 2012, **95**(9), pp.2700-2708.
200. Fielding, G.A. et al. Antibacterial and biological characteristics of silver containing and strontium doped plasma sprayed hydroxyapatite coatings. *Acta Biomaterialia.* 2012, **8**(8), pp.3144-3152.
201. Geng, Z. et al. Strontium incorporation to optimize the antibacterial and biological characteristics of silver-substituted hydroxyapatite coating. *Materials Science and Engineering C.* 2016, **58**, pp.467-477.
202. Geng, Z. et al. Incorporation of silver and strontium in hydroxyapatite coating on titanium surface for enhanced antibacterial and biological properties. *Materials Science and Engineering C.* 2017, **71**, pp.852-861.
203. Allan, I. et al. Antibacterial activity of particulate Bioglass® against supra- and subgingival bacteria. *Biomaterials.* 2001, **22**, pp.1683-1687.
204. Hu, S. et al. Study on antibacterial effect of 45S5 Bioglass. *Journal of Materials Science: Materials in Medicine.* 2009, **20**(1), pp.281-286.
205. Drago, L. et al. *In vitro* antibiofilm activity of bioactive glass S53P4. *Future Microbiology.* 2014, **9**(5), pp.593-601.
206. Drago, L. et al. Antimicrobial activity and resistance selection of different bioglass S53P4 formulations against multidrug resistant strains. *Future Microbiology.* 2015, **10**(8), pp.1293-1299.
207. Coraça-Huber, D.C. et al. Efficacy of antibacterial bioactive glass S53P4 against *S. aureus* biofilms grown on titanium discs in vitro. *Journal of Orthopaedic Research.* 2014, **32**(1), pp.175-177.

208. Munukka, E. et al. Bactericidal effects of bioactive glasses on clinically important aerobic bacteria. *Journal of Materials Science: Materials in Medicine.* 2008, **19**(1), pp.27-32.
209. Leppäranta, O. et al. Antibacterial effect of bioactive glasses on clinically important anaerobic bacteria *in vitro*. *Journal of Materials Science: Materials in Medicine.* 2008, **19**(2), pp.547-551.
210. Cabal, B. et al. A new biocompatible and antibacterial phosphate free glass-ceramic for medical applications. *Scientific Reports.* 2014, **4**, p.5440.
211. Moya, J.S. et al. Glass powders with a high content of calcium oxide: A step towards a “green” universal biocide. *Advanced Engineering Materials.* 2011, **13**(6), pp.B256-B260.
212. Maier, S.K. et al. Long-chain polyphosphate causes cell lysis and inhibits bacillus cereus septum formation, which is dependent on divalent cations. *Applied and Environmental Microbiology.* 1999, **65**(9), pp.3942-3949.
213. Liu, L. et al. Antibacterial property expressed by a novel calcium phosphate glass. *Journal of Biomedical Materials Research - Part B: Applied Biomaterials.* 2014, **102**(3), pp.423-429.
214. Yin, H. et al. Fabrication and characterization of strontium-doped borate-based bioactive glass scaffolds for bone tissue engineering. *Journal of Alloys and Compounds.* 2018.
215. Lao, J. et al. New strontium-based bioactive glasses: physicochemical reactivity and delivering capability of biologically active dissolution products. *Journal of Materials Chemistry.* 2009, **19**(19), pp.2940-2949.
216. Kargozar, S. et al. Synthesis, physico-chemical and biological characterization of strontium and cobalt substituted bioactive glasses for bone tissue engineering. *Journal of Non-Crystalline Solids.* 2016, **449**, pp.133-140.
217. Strobel, L.A. et al. Novel strontium-doped bioactive glass nanoparticles enhance proliferation and osteogenic differentiation of human bone marrow stromal cells. *Journal of Nanoparticle Research.* 2013, **15**, pp.1780-1788.
218. Kim, T.-G. and Park, B. Synthesis and growth mechanisms of one-dimensional strontium hydroxyapatite nanostructures. *Inorganic Chemistry.* 2005, **44**, pp.9895-9901.
219. Zhang, W. et al. Synthesis of nanosize single-crystal strontium hydroxyapatite via a simple sol-gel method. *Ceramics International.* 2014, **40**(10), pp.16061-16064.
220. Du, J. and Xiang, Y. Effect of strontium substitution on the structure, ionic diffusion and dynamic properties of 45S5 Bioactive glasses. *Journal of Non-Crystalline Solids.* 2012, **358**(8), pp.1059-1071.
221. Coble, R.L. Effects of particle-size distribution in initial-stage sintering. *Journal of the American Ceramic Society.* 1973, **56**(9), pp.461-466.
222. Ma, J. and Lim, L.C. Effect of particle size distribution on sintering of agglomerate-free submicron alumina powder compacts. *Journal of the European Ceramic Society.* 2002, **22**, pp.2197-2208.
223. Yeh, T.-S. and Sacks, M.D. Effect of particle size distribution on the sintering of alumina. *Journal of the American Ceramic Society.* 1988, **71**(12), pp.C-484-C-487.
224. Sun, C. et al. Effect of particle size gradation on the performance of glass-ceramic 3D printing process. *Ceramics International.* 2017, **43**(1), pp.578-584.
225. Murphy, E.J. et al. Cytotoxicity of aluminum silicates in primary neuronal cultures <Murphy_Cytotoxicity of AlSi in neuronal cultures_Neurosci_1993.pdf>. *Neuroscience.* 1993, **57**(2), pp.483-490.
226. Di Virgilio, A.L. et al. Response of UMR 106 cells exposed to titanium oxide and aluminum oxide nanoparticles. *Journal of Biomedical Materials Research - Part A.* 2010, **92**(1), pp.80-86.

227. Lin, W. et al. Cytotoxicity and cell membrane depolarization induced by aluminum oxide nanoparticles in human lung epithelial cells A549. *Toxicological & Environmental Chemistry.* 2008, **90**(5), pp.983-996.
228. Lönnroth, E.-C. and Dahl, J.E. Cytotoxicity of dental glass ionomers evaluated using dimethylthiazol diphenyltetrazolium and neutral red tests. *Acta Odontologica Scandinavica.* 2009, **59**(1), pp.34-39.
229. Ohgushi, H. et al. Al2O3 doped apatite-wollastonite containing glass ceramic provokes osteogenic differentiation of marrow stromal stem cells. *Journal of Biomedical Materials Research - Part A.* 1999, **44**(4), pp.381-388.
230. Fredholm, Y.C. et al. Influence of strontium for calcium substitution in bioactive glasses on degradation, ion release and apatite formation. *Journal of the Royal Society Interface.* 2012, **9**(70), pp.880-889.
231. Brink, M. The influence of alkali and alkaline earths on the working range for bioactive glasses. *Journal of Biomedical Materials Research.* 1997, **36**, pp.109-117.
232. Linati, L. et al. Qualitative and Quantitative Structure-Property Relationships Analysis of Multicomponent Potential Bioglasses. *Journal of Physical Chemistry B.* 2005, **109**, pp.4989-4998.
233. Cannillo, V. et al. Thermal and physical characterisation of apatite/wollastonite bioactive glass-ceramics. *Journal of the European Ceramic Society.* 2009, **29**(4), pp.611-619.
234. Likitvanichkul, S. and Lacourse, W.C. Apatite–wollastonite glass-ceramics Part I Crystallization kinetics by differential thermal analysis. *Journal of Materials Science.* 1998, **33**, pp.5901-5904.
235. Hill, R.G. et al. The influence of strontium substitution in fluorapatite glasses and glass-ceramics. *Journal of Non-Crystalline Solids.* 2004, **336**(3), pp.223-229.
236. Fujikura, K. et al. Influence of strontium substitution on structure and crystallisation of Bioglass® 45S5. *Journal of Materials Chemistry.* 2012, **22**(15), pp.7395-7402.
237. Lotfibakhshaiesh, N. et al. Bioactive glass engineered coatings for Ti6Al4V alloys: Influence of strontium substitution for calcium on sintering behaviour. *Journal of Non-Crystalline Solids.* 2010, **356**(44-49), pp.2583-2590.
238. Baino, F. et al. 3-D high-strength glass-ceramic scaffolds containing fluoroapatite for load-bearing bone portions replacement. *Materials Science and Engineering C.* 2009, **29**(6), pp.2055-2062.
239. Brovarone, C.V. et al. Macroporous bioactive glass-ceramic scaffolds for tissue engineering. *Journal of Materials Science: Materials in Medicine.* 2006, **17**(11), pp.1069-1078.
240. Lyckfeldt, O. and Ferreira, J.M.F. Processing of porous ceramics by 'Starch consolidation'. *Journal of the European Ceramic Society.* 1998, **18**, pp.191-140.
241. Vitale-Brovarone, C. et al. Macroporous glass-ceramic materials with bioactive properties. *Journal of Materials Science: Materials in Medicine.* 2004, **15**, pp.209-217.
242. Deville, S. et al. Freeze casting of hydroxyapatite scaffolds for bone tissue engineering. *Biomaterials.* 2006, **27**(32), pp.5480-5489.
243. Fu, Q. et al. Freeze-cast hydroxyapatite scaffolds for bone tissue engineering applications. *Biomedical Materials.* 2008, **3**(2), p.025005.
244. Sepulveda, P. et al. Bioactive sol-gel foams for tissue repair. *Journal of Biomedical Materials Research - Part A.* 2002, **59**, pp.340-348.
245. Jones, J.R. et al. Optimising bioactive glass scaffolds for bone tissue engineering. *Biomaterials.* 2006, **27**(7), pp.964-973.
246. Jones, J.R. and Hench, L.L. Effect of surfactant concentration and composition on the structure and properties of sol-gel-derived bioactive glass foam

scaffolds for tissue engineering. *Journal of Materials Science.* 2003, **38**, pp.3783-3790.
247. Yue, S. et al. Evaluation of 3-D bioactive glass scaffolds dissolution in a perfusion flow system with X-ray microtomography. *Acta Biomaterialia.* 2011, **7**(6), pp.2637-2643.
248. Hwa, L.C. et al. Recent advances in 3D printing of porous ceramics: A review. *Current Opinion in Solid State and Materials Science.* 2017, **21**(6), pp.323-347.
249. Suwanprateeb, J. et al. Mechanical and *in vitro* performance of apatite-wollastonite glass ceramic reinforced hydroxyapatite composite fabricated by 3D-printing. *Journal of Materials Science: Materials in Medicine.* 2009, **20**(6), pp.1281-1289.
250. Zhou, Z. et al. Printability of calcium phosphate: calcium sulfate powders for the application of tissue engineered bone scaffolds using the 3D printing technique. *Materials Science and Engineering C.* 2014, **38**, pp.1-10.
251. British Standards Institution. BS EN ISO 6872:2015. *Dentistry - Ceramic materials.* BSI, 2015.
252. Khalili, A. and Kromp, K. Statistical properties of Weibull estimators. *Journal of Materials Science.* 1991, **26**, pp.6741-6752.
253. Lu, C. et al. Fracture statistics of brittle materials: Weibull or normal distribution. *Physical Review E.* 2002, **65**(6), p.067102.
254. British Standards Institution. BS ISO 23317:2014. *Implants for surgery - In vitro evaluation for apatite-forming ability of implant materials.* BSI, 2014.
255. Kokubo, T. and Takadama, H. How useful is SBF in predicting in vivo bone bioactivity? *Biomaterials.* 2006, **27**(15), pp.2907-2915.
256. Vitale-Brovarone, C. et al. Feasibility and tailoring of bioactive glass-ceramic scaffolds with gradient of porosity for bone grafting. *Journal of Biomaterials Applications.* 2010, **24**(8), pp.693-712.
257. Vitale-Brovarone, C. et al. Foam-like scaffolds for bone tissue engineering based on a novel couple of silicate-phosphate specular glasses: synthesis and properties. *Journal of Materials Science: Materials in Medicine.* 2009, **20**(11), pp.2197-2205.
258. Baino, F. et al. Optimization of composition, structure and mechanical strength of bioactive 3-D glass-ceramic scaffolds for bone substitution. *Journal of Biomaterials Applications.* 2013, **27**(7), pp.872-890.
259. Shahid, S. et al. Glass ionomer cements: effect of strontium substitution on esthetics, radiopacity and fluoride release. *Dental Materials.* 2014, **30**(3), pp.308-313.
260. Baino, F. and Vitale-Brovarone, C. Bioactive glass and glass–ceramic foam scaffolds for bone tissue restoration. In: Netti, P.A. ed. *Biomedical foams for tissue engineering applications*. Cambridge, UK: Woodhead Publishing Limited, 2014, pp.213-248.
261. Boccaccini, A.R. et al. Sintering, crystallisation and biodegradation behaviour of Bioglass®-derived glass-ceramics. *Faraday Discussions.* 2007, **136**, pp.27-44.
262. Li, W. et al. Preparation and characterization of PHBV microsphere/45S5 bioactive glass composite scaffolds with vancomycin releasing function. *Materials Science and Engineering C.* 2014, **41**, pp.320-328.
263. Vitale-Brovarone, C. et al. Bioactive glass-derived trabecular coating: a smart solution for enhancing osteointegration of prosthetic elements. *Journal of Materials Science: Materials in Medicine.* 2012, **23**(10), pp.2369-2380.
264. Erol, M.M. et al. Copper-releasing, boron-containing bioactive glass-based scaffolds coated with alginate for bone tissue engineering. *Acta Biomaterialia.* 2012, **8**(2), pp.792-801.
265. Fu, H. et al. In vitro evaluation of borate-based bioactive glass scaffolds prepared by a polymer foam replication method. *Materials Science and Engineering C.* 2009, **29**(7), pp.2275-2281.

266. Vitale-Brovarone, C. et al. 3D-glass-ceramic scaffolds with antibacterial properties for bone grafting. *Chemical Engineering Journal.* 2008, **137**(1), pp.129-136.
267. Boccardi, E. et al. Characterisation of Bioglass based foams developed via replication of natural marine sponges. *Advances in Applied Ceramics.* 2015, **114**(Sup1), pp.S56-S62.
268. Wang, H. et al. Bio-templated synthesis of mesoporous bioactive glass with a hierarchical pore structure. *Materials Letters.* 2012, **76**, pp.237-239.
269. Li, X. et al. Hierarchically porous bioactive glass scaffolds synthesized with a PUF and P123 cotemplated approach. *Chemistry of Materials.* 2007, **19**, pp.4322-4326.
270. Fiorilli, S. et al. Electrophoretic deposition of mesoporous bioactive glass on glass-ceramic foam scaffolds for bone tissue engineering. *Journal of Materials Science: Materials in Medicine.* 2015, **26**(1), p.21.
271. Ni, S. et al. A novel bioactive porous $CaSiO_3$ scaffold for bone tissue engineering. *Journal of Biomedical Materials Research - Part A.* 2006, **76**(1), pp.196-205.
272. Kunjalukkal Padmanabhan, S. et al. Wollastonite/hydroxyapatite scaffolds with improved mechanical, bioactive and biodegradable properties for bone tissue engineering. *Ceramics International.* 2013, **39**(1), pp.619-627.
273. Massera, J. and Hupa, L. Influence of SrO substitution for CaO on the properties of bioactive glass S53P4. *Journal of Materials Science: Materials in Medicine.* 2014, **25**(3), pp.657-668.
274. Kapoor, S. et al. Thermo-mechanical behaviour of alkali free bioactive glass-ceramics co-doped with strontium and zinc. *Journal of Non-Crystalline Solids.* 2013, **375**, pp.74-82.
275. Bellucci, D. et al. Role of magnesium oxide and strontium oxide as modifiers in silicate-based bioactive glasses: Effects on thermal behaviour, mechanical properties and in-vitro bioactivity. *Materials Science and Engineering C.* 2017, **72**, pp.566-575.
276. Bellucci, D. et al. Mg- and/or Sr-doped tricalcium phosphate/bioactive glass composites: synthesis, microstructure and biological responsiveness. *Materials Science and Engineering C.* 2014, **42**, pp.312-324.
277. Prado, M.O. et al. Isothermal sintering with concurrent crystallization of polydispersed soda-lime-silica glass beads. *Journal of Non-Crystalline Solids.* 2003, **331**(1-3), pp.145-156.
278. Prado, M.O. et al. Non-isothermal sintering with concurrent crystallization of polydispersed soda-lime-silica glass beads. *Journal of Non-Crystalline Solids.* 2003, **331**(1-3), pp.157-167.
279. Liu, X. et al. Bioactive borosilicate glass scaffolds: improvement on the strength of glass-based scaffolds for tissue engineering. *Journal of Materials Science: Materials in Medicine.* 2009, **20**(1), pp.365-372.
280. Tulliani, J.-M. et al. Semiclosed-cell mullite foams: Preparation and macro- and micromechanical characterization. *Journal of the American Ceramic Society.* 1999, **82**(4), pp.961-968.
281. Fostad, G. et al. Loadable TiO2 scaffolds - A correlation study between processing parameters, micro CT analysis and mechanical strength. *Journal of the European Ceramic Society.* 2009, **29**(13), pp.2773-2781.
282. Roohani-Esfahani, S.I. et al. Effects of bioactive glass nanoparticles on the mechanical and biological behavior of composite coated scaffolds. *Acta Biomaterialia.* 2011, **7**(3), pp.1307-1318.
283. Bernardo, E. Micro- and macro-cellular sintered glass-ceramics from wastes. *Journal of the European Ceramic Society.* 2007, **27**(6), pp.2415-2422.
284. Karamanov, A. and Pelino, M. Evaluation of the degree of crystallisation in glass-ceramics by density measurements. *Journal of the European Ceramic Society.* 1999, **19**, pp.649-654.

285. Hing, K.A. et al. Characterization of porous hydroxyapatite. *Journal of Materials Science: Materials in Medicine.* 1999, **10**, pp.135-145.
286. Morsy, R. et al. Synthesis of microcrystalline wollastonite bioceramics and evolution of bioactivity. *Silicon.* 2017, **9**(4), pp.489-493.
287. Ni, S. et al. Comparison of osteoblast-like cell responses to calcium silicate and tricalcium phosphate ceramics in vitro. *Journal of Biomedical Materials Research - Part B: Applied Biomaterials.* 2007, **80**(1), pp.174-183.
288. Salman, S.M. et al. The effect of strontium oxide replacing calcium oxide on the crystallization and thermal expansion properties of Li_2O-CaO-SiO_2 glasses. *Ceramics International.* 2015, **41**(1), pp.137-143.
289. Salman, S.M. et al. Crystallization behaviour and properties of multicomponent strontium-containing lithia calcia silicate glasses. *Ceramics International.* 2010, **36**(8), pp.2307-2314.
290. Wu, C. et al. The effect of strontium incorporation into $CaSiO_3$ ceramics on their physical and biological properties. *Biomaterials.* 2007, **28**(21), pp.3171-3181.
291. Bellucci, D. and Cannillo, V. A novel bioactive glass containing strontium and magnesium with ultra-high crystallization temperature. *Materials Letters.* 2018, **213**, pp.67-70.
292. Otsuki, B. et al. Pore throat size and connectivity determine bone and tissue ingrowth into porous implants: three-dimensional micro-CT based structural analyses of porous bioactive titanium implants. *Biomaterials.* 2006, **27**(35), pp.5892-5900.
293. Fujibayashi, S. et al. Osteoinduction of porous bioactive titanium metal. *Biomaterials.* 2004, **25**(3), pp.443-450.
294. Chen, J. et al. Micro-CT based modelling for characterising injection-moulded porous titanium implants. *International Journal for Numerical Methods in Biomedical Engineering.* 2017, **33**(1), p.e02779.
295. Lin, A.S.P. et al. Microarchitectural and mechanical characterization of oriented porous polymer scaffolds. *Biomaterials.* 2003, **24**, pp.481-489.
296. Moore, M.J. et al. Quantitative analysis of interconnectivity of porous biodegradable scaffolds with micro-computed tomography. *Journal of Biomedical Materials Research - Part A.* 2004, **71**(2), pp.258-267.
297. Zidek, J. et al. Accurate micro-computed tomography imaging of pore spaces in collagen-based scaffold. *Journal of Materials Science: Materials in Medicine.* 2016, **27**(6), p.110.
298. Sandino, C. et al. A finite element study of mechanical stimuli in scaffolds for bone tissue engineering. *Journal of Biomechanics.* 2008, **41**(5), pp.1005-1014.
299. Zhang, J. et al. RhBMP-2-loaded calcium silicate/calcium phosphate cement scaffold with hierarchically porous structure for enhanced bone tissue regeneration. *Biomaterials.* 2013, **34**(37), pp.9381-9392.
300. Sa, Y. et al. Physicochemical properties and mineralization assessment of porous polymethylmethacrylate cement loaded with hydroxyapatite in simulated body fluid. *Materials Science and Engineering C.* 2016, **61**, pp.190-198.
301. Cunningham, E. et al. Hydroxyapatite bone substitutes developed via replication of natural marine sponges. *Journal of Materials Science: Materials in Medicine.* 2010, **21**(8), pp.2255-2261.
302. Meininger, S. et al. Strength reliability and in vitro degradation of three-dimensional powder printed strontium-substituted magnesium phosphate scaffolds. *Acta Biomaterialia.* 2016, **31**, pp.401-411.
303. Baino, F. and Vitale-Brovarone, C. Mechanical properties and reliability of glass-ceramic foam scaffolds for bone repair. *Materials Letters.* 2014, **118**, pp.27-30.
304. Jones, J.R. et al. Non-destructive quantitative 3D analysis for the optimisation of tissue scaffolds. *Biomaterials.* 2007, **28**(7), pp.1404-1413.

305. Yue, S. et al. Synchrotron X-ray microtomography for assessment of bone tissue scaffolds. *Journal of Materials Science: Materials in Medicine.* 2010, **21**(3), pp.847-853.
306. Liu, X. et al. Bone regeneration in strong porous bioactive glass (13-93) scaffolds with an oriented microstructure implanted in rat calvarial defects. *Acta Biomaterialia.* 2013, **9**(1), pp.4889-4898.
307. Fu, Q. et al. Bioinspired strong and highly porous glass scaffolds. *Advanced Functional Materials.* 2011, **21**(6), pp.1058-1063.
308. Renghini, C. et al. Micro-CT studies on 3-D bioactive glass-ceramic scaffolds for bone regeneration. *Acta Biomaterialia.* 2009, **5**(4), pp.1328-1337.
309. Renghini, C. et al. Microstructural characterization and in vitro bioactivity of porous glass-ceramic scaffolds for bone regeneration by synchrotron radiation X-ray microtomography. *Journal of the European Ceramic Society.* 2013, **33**(9), pp.1553-1565.
310. Baino, F. et al. Using porous bioceramic scaffolds to model healthy and osteoporotic bone. *Journal of the European Ceramic Society.* 2016, **36**(9), pp.2175-2182.
311. Shen, Y. et al. Bone regeneration: importance of local pH - strontium-doped borosilicate scaffold. *Journal of Materials Chemistry.* 2012, **22**(17), pp.8662-8670.
312. Oliveira, J.M. et al. Macroporous hydroxyapatite scaffolds for bone tissue engineering applications: physicochemical characterization and assessment of rat bone marrow stromal cell viability. *Journal of Biomedical Materials Research - Part A.* 2009, **91**(1), pp.175-186.
313. Hildebrand, T. et al. Direct three-dimensional morphometric analysis of human cancellous bone: Microstructural data from spine, femur, iliac crest, and calcaneus. *Journal of Bone and Mineral Research.* 1999, **14**(7), pp.1167-1174.
314. Chen, Y. et al. Micro-CT based finite element models of cancellous bone predict accurately displacement once the boundary condition is well replicated: A validation study. *Journal of Mechanical Behavior of Biomedical Materials.* 2017, **65**, pp.644-651.
315. Kim, Y.J. and Henkin, J. Micro-computed tomography assessment of human alveolar bone: bone density and three-dimensional micro-architecture. *Clinical Implant Dentistry and Related Research.* 2015, **17**(2), pp.307-313.
316. Hambli, R. Micro-CT finite element model and experimental validation of trabecular bone damage and fracture. *Bone.* 2013, **56**(2), pp.363-374.
317. Hench, L.L. Repair of skeletal tissue. In: Hench, L.L. and Jones, J.R. eds. *Biomaterials, artificial organs and tissue engineering*. Abington Hall, Abington, Cambridge CB1 6AH, England: Woodhead Publishing Limited, 2005, pp.119-128.
318. Akhter, M.P. et al. Transmenopausal changes in the trabecular bone structure. *Bone.* 2007, **41**(1), pp.111-116.
319. Bruker microCT. *Introduction to porosity analysis*. Method note. Kontich, Belgium: Bruker.
320. American Society for Testing and Materials. ASTM F2883-11. *Characterisation of ceramic and mineral based scaffolds used for tissue-engineered medical products (TEMPs) and as device for surgical implant applications.* ASTM International, 2011.
321. Wu, Z.Y. et al. Melt-derived bioactive glass scaffolds produced by a gel-cast foaming technique. *Acta Biomaterialia.* 2011, **7**(4), pp.1807-1816.
322. Dong, J. et al. In vivo evaluation of a novel porous hydroxyapatite to sustain osteogenesis of transplanted bone marrow-derived osteoblastic cells. *Journal of Biomedical Materials Research - Part A.* 2001, **57**(2), pp.208-216.
323. Fan, X. et al. Part I: porosity dependence of the Weibull modulus for hydroxyapatite and other brittle materials. *Journal of Mechanical Behavior of Biomedical Materials.* 2012, **8**, pp.21-36.

324. Muhamad Nor, M.A.A. et al. Preparation and characterization of ceramic foam produced via polymeric foam replication method. *Journal of Materials Processing Technology.* 2008, **207**(1-3), pp.235-239.
325. Barbieri, L. et al. The microstructure and mechanical properties of sintered celsian and strontium-celsian glass-ceramics. *Materials Research Bulletin.* 1995, **30**(1), pp.27-41.
326. Jallot, E. Correlation between hydroxyapatite osseointegration and Young's modulus. *Medical Engineering & Physics.* 1998, **20**, pp.697-701.
327. Meixner, D.L. and Cutler, R.A. Sintering and mechanical characteristics of lanthanum strontium manganite. *Solid State Ionics.* 2002, **146**, pp.273-284.
328. Poh, P.S.P. et al. Fabrication and in vitro characterization of bioactive glass composite scaffolds for bone regeneration. *Biofabrication.* 2013, **5**(4), p.045005.
329. Meganck, J.A. et al. Biaxial flexure testing of calcium phosphate bioceramics for use in tissue engineering. *Journal of Biomedical Materials Research - Part A.* 2005, **72**(1), pp.115-126.
330. Fan, X. et al. Weibull modulus and fracture strength of highly porous hydroxyapatite. *Journal of Mechanical Behavior of Biomedical Materials.* 2013, **20**, pp.283-295.
331. Zocca, A. et al. 3D-printed silicate porous bioceramics using a non-sacrificial preceramic polymer binder. *Biofabrication.* 2015, **7**(2), p.025008.
332. Chung, S.M. et al. Flexural strength of dental composite restoratives: comparison of biaxial and three-point bending test. *Journal of Biomedical Materials Research - Part B: Applied Biomaterials.* 2004, **71**(2), pp.278-283.
333. Xu, Y. et al. Comparative study of flexural strength test methods on CAD/CAM Y-TZP dental ceramics. *Regenerative Biomaterials.* 2015, **2**(4), pp.239-244.
334. Liu, D.-M. Control of pore geometry on influencing the mechanical property of porous hydroxyapatite bioceramic. *Journal of Materials Science Letters.* 1996, **15**, pp.419-421.
335. Barralet, J.E. et al. Preparation of macroporous calcium phosphate cement tissue engineering scaffold. *Biomaterials.* 2002, **23**, pp.3063-3072.
336. Barralet, J.E. et al. Effect of porosity reduction by compaction on compressive strength and microstructure of calcium phosphate cement. *Journal of Biomedical Materials Research - Part A.* 2002, **63**(1), pp.1-9.
337. Chen, Q. et al. Modelling of the strength-porosity relationship in glass-ceramic foam scaffolds for bone repair. *Journal of the European Ceramic Society.* 2014, **34**(11), pp.2663-2673.
338. Sriranganathan, D. et al. Strontium substituted bioactive glasses for tissue engineered scaffolds: The importance of octacalcium phosphate. *Journal of Materials Science: Materials in Medicine.* 2016, **27**(2), p.39.
339. Pan, H.B. et al. Strontium borate glass: potential biomaterial for bone regeneration. *Journal of the Royal Society Interface.* 2010, **7**(48), pp.1025-1031.
340. Arcos, D. et al. A new quantitative method to evaluate the in vitro bioactivity of melt and sol-gel-derived silicate glasses. *Journal of Biomedical Materials Research - Part A.* 2003, **65A**(3), pp.344-351.
341. Peltola, T. et al. Calcium phosphate formation on porous sol-gel-derived SiO2 and CaO-P_2O_5-SiO_2 substrates in vitro. *Journal of Biomedical Materials Research - Part A.* 1999, **44**(1), pp.12-21.
342. Pereira, M.M. et al. Effect of texture on the rate of hydroxyapatite formation on gel-silica surface. *Journal of the American Ceramic Society.* 1995, **78**(9), pp.2463-2468.
343. O'Donnell, M.D. and Hill, R.G. Influence of strontium and the importance of glass chemistry and structure when designing bioactive glasses for bone regeneration. *Acta Biomaterialia.* 2010, **6**(7), pp.2382-2385.

344. Maçon, A.L.B. et al. A unified in vitro evaluation for apatite-forming ability of bioactive glasses and their variants. *Journal of Materials Science: Materials in Medicine.* 2015, **26**, p.115.
345. Watts, D.C. Radiopacity vs. composition of some barium and strontium glass composites. *Journal of Dentistry.* 1987, **15**, pp.38-43.
346. Lachowski, K.M. et al. Study of the radio-opacity of base and liner dental materials using a digital radiography system. *Dentomaxillofacial Radiology.* 2013, **42**(2), p.20120153.
347. Romieu, G. et al. Calcium-strontium mixed phosphate as novel injectable and radio-opaque hydraulic cement. *Acta Biomaterialia.* 2010, **6**(8), pp.3208-3215.
348. Mohan, B.G. et al. Strontium calcium phosphate for the repair of leporine (*Oryctolagus cuniculus*) ulna segmental defect. *Journal of Biomedical Materials Research - Part A.* 2013, **101**(1), pp.261-271.
349. Philpott, A. et al. Predictive outcomes of revision total hip replacement- A consecutive series of 1176 patients with a minimum 10-year follow-up. *Maturitas.* 2014, **77**(2), pp.185-190.
350. Bozic, K.J. et al. The epidemiology of revision total knee arthroplasty in the United States. *Clinical Orthopaedics and Related Research.* 2010, **468**(1), pp.45-51.
351. Bozic, K.J. et al. The epidemiology of revision total hip arthroplasty in the United States. *Journal of Bone & Joint Surgery - American Volume.* 2009, **91**(1), pp.128-133.
352. Gundtoft, P.H. et al. The "true" incidence of surgically treated deep prosthetic joint infection after 32,896 primary total hip arthroplasties: a prospective cohort study. *Acta Orthopaedica.* 2015, **86**(3), pp.326-334.
353. Gwam, C.U. et al. Current epidemiology of revision total hip arthroplasty in the United States: National inpatient sample 2009 to 2013. *Journal of Arthroplasty.* 2017, **32**(7), pp.2088-2092.
354. Getzlaf, M.A. et al. Multi-disciplinary antimicrobial strategies for improving orthopaedic implants to prevent prosthetic joint infections in hip and knee. *Journal of Orthopaedic Research.* 2016, **34**(2), pp.177-186.
355. Schleheck, D. et al. *Pseudomonas aeruginosa* PAO1 preferentially grows as aggregates in liquid batch cultures and disperses upon starvation. *PLoS One.* 2009, **4**(5), p.e5513.
356. Matuschek, E. et al. Development of the EUCAST disk diffusion antimicrobial susceptibility testing method and its implementation in routine microbiology laboratories. *Clinical Microbiology and Infection.* 2014, **20**(4), pp.O255-O266.
357. Walter, C. et al. Moderate effect of enamel matrix derivative (Emdogain® Gel) on *Porphyromonas gingivalis* growth in vitro. *Archives of Oral Biology.* 2006, **51**, pp.171-176.
358. Jaiswal, S. et al. Preparation and rapid analysis of antibacterial silver, copper and zinc doped sol-gel surfaces. *Colloids and Surfaces B Biointerfaces.* 2012, **94**, pp.170-176.
359. Malachová, K. et al. Antibacterial and antifungal activities of silver, copper and zinc montmorillonites. *Applied Clay Science.* 2011, **53**(4), pp.642-645.
360. Liu, M. et al. Biosorption of strontium from simulated nuclear wastewater by *Scenedesmus spinosus* under culture conditions: adsorption and bioaccumulation processes and models. *International Journal of Environmental Research and Public Health.* 2014, **11**(6), pp.6099-6118.
361. Peng, S. et al. In vivo anabolic effect of strontium on trabecular bone was associated with increased osteoblastogenesis of bone marrow stromal cells. *Jurnal of Orthopaedic Research.* 2010, **28**(9), pp.1208-1214.
362. Watanakunakornl, C. and Tisone, J.C. Synergism between vancomycin and gentamicin or tobramycin for methicillin-susceptible and methicillin-resistant *Staphylococcus aureus* strains. *Antimicrobial Agents and Chemotherapy.* 1982, **22**(5), pp.903-905.

363. Sabath, L.D. et al. Susceptibility of *Staphylococcus aureus* and *Staphylococcus epidermidis* to 65 Antibiotics. *Antimicrobial Agents and Chemotherapy.* 1976, **9**(6), pp.962-969.
364. Johnson, A.P. et al. Gentamicin resistance in clinical isolates of *Escherichia coli* encoded by genes of veterinary origin. *Journal of Medical Microbiology.* 1994, **40**, pp.221-226.
365. Woolfrey, B.F. et al. Evaluation of the AutoMicrobic system for susceptibility testing of *Pseudomonas aeruginosa* to gentamicin, tobramycin, and amikacin. *Journal of Clinical Microbiology.* 1984, **19**(4), pp.502-505.
366. Bloomfield, S.F. and Uso, E.E. The antibacterial properties of sodium hypochlorite and sodium dichloroisocyanurate as hospital disinfectants. *Journal of Hospital Infection.* 1985, **6**, pp.20-30.
367. Gorriti, M.F. et al. *In vitro* study of the antibacterial activity of bioactive glass-ceramic scaffolds. *Advanced Engineering Materials.* 2009, **11**(7), pp.B67-B70.
368. Kargozar, S. et al. Strontium- and cobalt-substituted bioactive glasses seeded with human umbilical cord perivascular cells to promote bone regeneration via enhanced osteogenic and angiogenic activities. *Acta Biomaterialia.* 2017, **58**, pp.502-514.
369. Pouria, A. et al. Physicochemical properties and cellular responses of strontium-doped gypsum biomaterials. *Bioinorganic Chemistry and Applications.* 2012, **2012**, p.976495.
370. Taherkhani, S. and Moztarzadeh, F. Influence of strontium on the structure and biological properties of sol-gel-derived mesoporous bioactive glass (MBG) powder. *Journal of Sol-Gel Science and Technology.* 2016, **78**(3), pp.539-549.
371. Maleki-Ghaleh, H. et al. Effect of tricalcium magnesium silicate coating on the electrochemical and biological behavior of Ti-6Al-4V alloys. *PLoS One.* 2015, **10**(9), p.e0138454.
372. Frith, J. and Genever, P. Transcriptional control of mesenchymal stem cell differentiation. *Transfusion Medicine and Hemotherapy.* 2008, **35**, pp.216-227.
373. Montalbano, G. et al. Synthesis of bioinspired collagen/alginate/fibrin based hydrogels for soft tissue engineering. *Materials Science and Engineering: C.* 2018, **91**, pp.236-246.
374. Gentile, P. et al. Multilayer Nanoscale Encapsulation of Biofunctional Peptides to Enhance Bone Tissue Regeneration In Vivo. *Advanced Healthcare Materials.* 2017, **6**(8), p.1601182.
375. Pittenger, M.F. et al. Multilineage potential of adult human mesenchymal stem cells. *Science.* 1999, **284**(5411), pp.143-147.
376. Jones, E.A. et al. Isolation and characterization of bone marrow multipotential mesenchymal progenitor cells. *Arthritis & Rheumatism.* 2002, **46**(12), pp.3349-3360.
377. Kern, S. et al. Comparative analysis of mesenchymal stem cells from bone marrow, umbilical cord blood, or adipose tissue. *Stem Cells.* 2006, **24**(5), pp.1294-1301.
378. Ayobian-Markazi, N. et al. Comparison of cell viability and morphology of a human osteoblast-like cell line (SaOS-2) seeded on various bone substitute materials: An *in vitro* study. *Dental Research Journal.* 2012, **9**(1), pp.86-92.
379. Kharaziha, M. and Fathi, M.H. Improvement of mechanical properties and biocompatibility of forsterite bioceramic addressed to bone tissue engineering materials. *Journal of the Mechanical Behavior of Biomedical Materials.* 2010, **3**(7), pp.530-537.
380. Kalantari, E. et al. Nanostructured monticellite: An emerging player in tissue engineering. *Materials Today: Proceedings.* 2018, **5**(7), pp.15744-15753.
381. Naddaf Dezfuli, S. et al. Fabrication of biocompatible titanium scaffolds using space holder technique. *Journal of Materials Science: Materials in Medicine.* 2012, **23**(10), pp.2483-2488.

382. Mobini, S. et al. Bioactivity and biocompatibility studies on silk-based scaffold for bone tissue engineering. *Journal of Medical and Biological Engineering.* 2013, **33**(2), pp.207-214.
383. Bakhtiari, L. et al. Investigation of biphasic calcium phosphate/gelatin nanocomposite scaffolds as a bone tissue engineering. *Ceramics International.* 2010, **36**(8), pp.2421-2426.
384. Aboudzadeh, N. et al. Fabrication and characterization of poly(D,L-lactide-co-glycolide)/hydroxyapatite nanocomposite scaffolds for bone tissue regeneration. *Journal of Biomedical Materials Research - Part A.* 2010, **94**(1), pp.137-145.
385. Borhan, S. et al. Evaluation of colloidal silica suspension as efficient additive for improving physicochemical and in vitro biological properties of calcium sulfate-based nanocomposite bone cement. *Journal of Materials Science: Materials in Medicine.* 2010, **21**(12), pp.3171-3181.
386. Mobini, S. et al. Synthesis and characterisation of gelatin–nano hydroxyapatite composite scaffolds for bone tissue engineering. *Advances in Applied Ceramics.* 2013, **107**(1), pp.4-8.
387. Fernandes, G. et al. The effect of ascorbic acid on bone cancer cells in vitro. *Cogent Biology.* 2017, **3**(1), p.1288335.
388. Sharifianjazi, F. et al. Formation of apatite nano-needles on novel gel derived SiO_2-P_2O_5-CaO-SrO-Ag_2O bioactive glasses. *Ceramics International.* 2017, **43**(17), pp.15214-15220.
389. Yang, X.B. et al. Human osteoprogenitor growth and differentiation on synthetic biodegradable structures after surface modification. *Bone.* 2001, **29**(6), pp.523-531.
390. Blaker, J.J. et al. In vitro evaluation of novel bioactive composites based on Bioglass-filled polylactide foams for bone tissue engineering scaffolds. *Journal of Biomedical Materials Research - Part A.* 2003, **67**(4), pp.1401-1411.
391. Yang, X.B. et al. Evaluation of human bone marrow stromal cell growth on biodegradable polymer/bioglass composites. *Biochemical and Biophysical Research Communications.* 2006, **342**(4), pp.1098-1107.
392. Karakoti, A.S. et al. Rare earth oxides as nanoadditives in 3-D nanocomposite scaffolds for bone regeneration. *Journal of Materials Chemistry.* 2010, **20**(40), pp.8912-8919.
393. Jones, J.R. et al. Extracellular matrix formation and mineralization on a phosphate-free porous bioactive glass scaffold using primary human osteoblast (HOB) cells. *Biomaterials.* 2007, **28**(9), pp.1653-1663.
394. Midha, S. et al. Bioactive glass foam scaffolds are remodelled by osteoclasts and support the formation of mineralized matrix and vascular networks in vitro. *Advanced Healthcare Materials.* 2013, **2**(3), pp.490-499.
395. Vitale-Brovarone, C. et al. Development of glass-ceramic scaffolds for bone tissue engineering: Characterisation, proliferation of human osteoblasts and nodule formation. *Acta Biomaterialia.* 2007, **3**(2), pp.199-208.
396. Bielby, R.C. et al. Time- and concentration-dependent effects of dissolution products of 58S sol-gel bioactive glass on proliferation and ifferentiation of murine and human osteoblasts. *Tissue Engineering.* 2004, **10**(7/8), pp.1018-1026.
397. Pryce, R.S. and Hench, L.L. Dissolution characteristics of bioactive glasses. *Key Engineering Materials.* 2003, **240-242**, pp.201-204.
398. Nishimura, M. et al. Cytological properties of stromal cells derived from giant cell tumor of bone (GCTSC) which can induce osteoclast formation of human blood monocytes without cell to cell contact. *Journal of Orthopaedic Research.* 2005, **23**, pp.979-987.
399. Thakur, S. et al. Effect of strontium substitution on the cytocompatibility and 3-D scaffold structure for the xSrO-(10-x) MgO-60SiO_2-20CaO-10 P_2O_5 ($2 \leq x \leq$

8) sol-gel glasses. *Journal of Materials Science: Materials in Medicine.* 2017, **28**(6), p.89.
400. Farag, M.M. et al. Study of the dual effect of gamma irradiation and strontium substitution on bioactivity, cytotoxicity, and antimicrobial properties of 45S5 bioglass. *Journal of Biomedical Materials Research - Part A.* 2017, **105**(6), pp.1646-1655.
401. Weng, L. et al. Binary doping of strontium and copper enhancing osteogenesis and angiogenesis of bioactive glass nanofibers while suppressing osteoclast activity. *ACS Applied Materials & Interfaces.* 2017, **9**(29), pp.24484-24496.
402. Pautke, C. et al. Characterization of osteosarcoma cell lines MG-63, Saos-2 and U-2 OS in comparison to human osteoblasts. *Anticancer Research.* 2004, **24**, pp.3743-3748.
403. Clover, J. and Gowen, M. Are MG-63 and HOS TE85 human osteosarcoma cell lines representative models of the osteoblastic phenotype? *Bone.* 1994, **15**(6), pp.585-591.
404. Lauvrak, S.U. et al. Functional characterisation of osteosarcoma cell lines and identification of mRNAs and miRNAs associated with aggressive cancer phenotypes. *British Journal of Cancer.* 2013, **109**(8), pp.2228-2236.
405. Schumacher, M. et al. A novel strontium(II)-modified calcium phosphate bone cement stimulates human-bone-marrow-derived mesenchymal stem cell proliferation and osteogenic differentiation in vitro. *Acta Biomaterialia.* 2013, **9**(12), pp.9547-9557.
406. Yang, F. et al. Strontium enhances osteogenic differentiation of mesenchymal stem cells and in vivo bone formation by activating Wnt/catenin signaling. *Stem Cells.* 2011, **29**(6), pp.981-991.
407. Birgani, Z.T. et al. Human mesenchymal stromal cells response to biomimetic octacalcium phosphate containing strontium. *Journal of Biomedical Materials Research - Part A.* 2016, **104**(8), pp.1946-1960.
408. Lin, K. et al. Enhanced osteoporotic bone regeneration by strontium-substituted calcium silicate bioactive ceramics. *Biomaterials.* 2013, **34**(38), pp.10028-10042.
409. Montesi, M. et al. Sr-substituted bone cements direct mesenchymal stem cells, osteoblasts and osteoclasts fate. *PLoS One.* 2017, **12**(2), p.e0172100.
410. Sila-Asna, M. et al. Osteoblast differentiation and bone formation gene expression in strontium-inducing bone marrow mesenchymal stem cell. *Kobe Journal of Medical Sciences.* 2007, **53**(1), pp.25-35.
411. Xie, H. et al. Microenvironment construction of strontium–calcium-based biomaterials for bone tissue regeneration: the equilibrium effect of calcium to strontium. *Journal of Materials Chemistry B.* 2018.
412. Wornham, D.P. et al. Strontium potently inhibits mineralisation in bone-forming primary rat osteoblast cultures and reduces numbers of osteoclasts in mouse marrow cultures. *Osteoporosis International.* 2014, **25**(10), pp.2477-2484.
413. Aimaiti, A. et al. Low-dose strontium stimulates osteogenesis but high-dose doses cause apoptosis in human adipose-derived stem cells via regulation of the ERK1/2 signaling pathway. *Stem Cell Research & Therapy.* 2017, **8**(1), p.282.
414. Li, Z. et al. Strontium-calcium coadministration stimulates bone matrix osteogenic factor expression and new bone formation in a large animal model. *Journal of Orthopaedic Research.* 2009, **27**(6), pp.758-762.
415. Arepalli, S.K. et al. Enhanced bioactivity, biocompatibility and mechanical behavior of strontium substituted bioactive glasses. *Materials Science and Engineering C.* 2016, **69**, pp.108-116.
416. Dalby, M.J. et al. The control of human mesenchymal cell differentiation using nanoscale symmetry and disorder. *Nature Materials.* 2007, **6**(12), pp.997-1003.
417. Dalby, M.J. et al. Harnessing nanotopography and integrin-matrix interactions to influence stem cell fate. *Nature Materials.* 2014, **13**(6), pp.558-569.

418. Hu, D. et al. The combined effects of nanotopography and Sr ion for enhanced osteogenic activity of bone marrow mesenchymal stem cells (BMSCs). *Journal of Biomaterials Applications.* 2017, **31**(8), pp.1135-1147.
419. Engler, A.J. et al. Myotubes differentiate optimally on substrates with tissue-like stiffness: pathological implications for soft or stiff microenvironments. *Journal of Cell Biology.* 2004, **166**(6), pp.877-887.
420. Engler, A.J. et al. Matrix elasticity directs stem cell lineage specification. *Cell.* 2006, **126**(4), pp.677-689.
421. Dawson, J.I. et al. Concise review: bridging the gap: bone regeneration using skeletal stem cell-based strategies - Where are we now? *Stem Cells.* 2014, **32**(1), pp.35-44.
422. Bonab, M.M. et al. Aging of mesenchymal stem cell in vitro. *BMC Cell Biology.* 2006, **7**, p.14.
423. Yameen, Z. et al. Multilineage differentiation potential of bone and cartilage cells derived from explant culture. *The Open Stem Cell Journal.* 2009, **1**, pp.10-19.
424. O'Donnell, M.D. Predicting bioactive glass properties from the molecular chemical composition: glass transition temperature. *Acta Biomaterialia.* 2011, **7**(5), pp.2264-2269.
425. Hill, R.G. and Brauer, D.S. Predicting the glass transition temperature of bioactive glasses from their molecular chemical composition. *Acta Biomaterialia.* 2011, **7**(10), pp.3601-3605.
426. Magdeski, J.S. The porosity dependence of mechanical properties of sintered alumina. *Journal of the University of Chemical Technology and Metallurgy.* 2010, **45**(2), pp.143-148.
427. Sabree, I. et al. Mechanical properties of porous ceramic scaffolds: Influence of internal dimensions. *Ceramics International.* 2015, **41**(7), pp.8425-8432.

Appendix A

License numbers for re-print permission

Figure 1.1: 4375600706304

Figure 1.5: 4342661368996

Figure 1.8: Permission granted via email.

Text of the email:

Dear Lucia

The Royal Society of Chemistry hereby grants permission for the use of the material specified below in the work described and in all subsequent editions of the work for distribution throughout the world, in all media including electronic and microfilm. You may use the material in conjunction with computer-based electronic and information retrieval systems, grant permissions for photocopying, reproductions and reprints, translate the material and to publish the translation, and authorize document delivery and abstracting and indexing services. The Royal Society of Chemistry is a signatory to the STM Guidelines on Permissions (available on request).

Please note that if the material specified below or any part of it appears with credit or acknowledgement to a third party then you must also secure permission from that third party before reproducing that material.
Please ensure that the published article carries a credit to The Royal Society of Chemistry in the following format:
[Original citation] – Reproduced by permission of The Royal Society of Chemistry

and that any electronic version of the work includes a hyperlink to the article on the Royal Society of Chemistry website.

Regards

Gill Cockhead
Publishing Contracts & Copyright Executive

Gill Cockhead
Publishing Contracts & Copyright Executive
Royal Society of Chemistry,
Thomas Graham House,
Science Park, Milton Road,
Cambridge, CB4 0WF, UK
Tel +44 (0) 1223 432134

Figure 1.9: 4343081177655
Figure 1.11: 4344410020489
Figure 1.12: 4346530466548
Figure 1.13: 4346571129688
Figure 1.14: 4346631183230
Figure 1.15: 4346631484105
Figure 1.16: 4346780319578
Figure 1.17: 4347870718313